Dissertation
submitted to the
Combined Faculties for the Natural Sciences and for Mathematics
of the Rupertus Carola University of
Heidelberg, Germany
for the degree of
Doctor of Natural Sciences

presented by

Diplom-Physicist: **Holger Kreckel**
born in: Bad Marienberg

Oral examination: 22.07.2003

Internal Excitations of Stored Triatomic Hydrogen Molecular Ions

Referees: **Prof. Dr. Andreas Wolf**
Prof. Dr. H.-Jürgen Kluge

Kurzfassung

Interne Anregungen gespeicherter dreiatomiger Wasserstoffmolekülionen

Das dreitatomige Wasserstoffmolekülion H_3^+ ist das einfachste polyatomare Molekül, neben seiner fundamentalen Bedeutung für die Quantenchemie ist es einer der Eckpfeiler molekularer Prozesse in interstellaren Wolken. Die dissoziative Elektronen-Rekombination (DR) von H_3^+ wurde bereits oft untersucht, dennoch ist sie Gegenstand einer langwierigen Kontroverse. Moderne Ionen-Speicherringe, ausgestattet mit Elektronenkühlern, stellen eine relativ saubere Umgebung für DR Messungen dar, vorausgesetzt man kann die rotatorischen and vibratorischen Bewegungen der Molekülionen kontrollieren. Hier werden Messungen mit zwei Methoden vorgestellt, um die internen Anregungen von H_3^+ am Speicherring TSR des Max-Planck-Institut für Kernphysik nachzuweisen; die Coulomb Explosion Imaging-Technik (CEI) bestätigt die Vibrations-Kühlung durch spontanen Zerfall nach zwei Sekunden Speicherzeit, während DR Fragment Imaging Messungen die Existenz von hoch angeregten Rotations-Zuständen mit bis zu 1 eV (12000 K) Energie belegen. Ein umfassendes rovibronisches Relaxationsmodell basierend auf theoretischen Berechnungen der Übergangswahrscheinlichkeiten wurde erstellt, um die experimentellen Befunde zu erklären. Für zukünftige Experimente wurde eine Tieftemperatur-22-Pol Ionenfalle aufgebaut, die zur Präparation rovibronisch kalter H_3^+-Ionen genutzt werden kann.

Abstract

Internal Excitations of Stored Triatomic Hydrogen Molecular Ions

The triatomic hydrogen molecular ion H_3^+ is the simplest polyatomic molecule, besides its fundamental importance for quantum chemistry, it is one of the cornerstones of molecular processes in interstellar clouds. The dissociative electron recombination (DR) of H_3^+ is much studied, but still subject to a long-standing controversy. Modern ion storage rings equipped with electron coolers provide a relatively clean environment for DR measurements, given that the vibrational and rotational motion of the molecular ions can be controlled. Measurements using two different experimental approaches are presented, which were used to monitor H_3^+ internal excitations at the ion storage ring TSR of the Max-Planck-Institut für Kernphysik; the Coulomb explosion imaging technique confirmed vibrational cooling due to spontaneous decay within 2 s of storage, while DR fragment imaging measurements indicated the existence of highly excited rotational states with energies up to 1 eV (12000 K) after more than 10 s. A comprehensive rovibrational excitation model, based on theoretical calculations of transition probabilities can explain the experimental observations. For future experiments, a cryogenic 22-pole ion trap was constructed, which is capable of preparing rovibrationally cold H_3^+ ions.

Contents

Chapter 1
Introduction

This work is dedicated to the triatomic molecular ion H_3^+, the most simple polyatomic molecule. The structural simplicity of three protons bound together by two electrons is contrasted by a variety of surprising details of molecular properties and reaction dynamics. Due to their fundamental nature H_3^+ and its instable neutral counterpart H_3 are much studied in experiment and theory and both are widely used as benchmark systems for accurate quantum mechanical calculations on polyatomic molecules.

Since hydrogen is by far the most abundant element – it accounts for 70% of the mass of the universe – triatomic hydrogen is not as exotic as it might seem at first glance. A very effective formation reaction renders H_3^+ the dominant ion in cold hydrogen plasmas, a fact that led to its early discovery by J. J. Thomson in 1911 [Tho11].

In the literature on triatomic hydrogen many superlatives can be found regarding its outstanding role and the scientific achievements that have been accomplished: the simplest polyatomic ion, the only known polyatomic excimer (H_3), the most accurately known polyatomic potential, the best examined chemical reaction ($H+H_2 \rightarrow H_2+H$) are a few examples and indeed many aspects in that context are known with tremendous precision. It is all the more surprising that a seemingly simple process like the electron recombination $H_3^+ + e^-$ followed by the dissociation into neutral fragments is still far from being understood. Besides a long-standing search for the mechanism that drives the recombination process, many experiments were carried out to determine the rate coefficient for this reaction. Unfortunately the results of these measurements obtained by a variety of different techniques disagree by as much as four orders of magnitude.

The controversy does not end in the laboratory since H_3^+ is supposed to be the basis of the ion-molecule reaction networks in interstellar space where it was recently observed by means of infrared spectroscopy [Geb96, McC98]. The electron recombination is the dominant destruction mechanism for H_3^+ in diffuse interstellar clouds and the discrepancy for its rate coefficient translates directly into a large uncertainty for the size of these

objects.

One of the major difficulties in experiments with H_3^+ is to keep track of rovibrational excitations of the molecule, since the degree of excitation might influence the outcome of the experiment. It was suggested that the discrepancy of the measured rate coefficients might stem from different internal excitation schemes in the various experimental environments. In this work methods to monitor and control the rovibrational excitations of H_3^+ are presented and developed that might eventually point the way to state-specific recombination measurements.

The thesis is divided into three parts, the first part "Motivation and Theory" gives a brief introduction into the physics and scientific history of triatomic hydrogen. The role of H_3^+ in interstellar chemistry is explained and the process of dissociative recombination is introduced as well as some of the symmetry properties relevant to dipole transitions.

Part II, "Storage Ring Experiments" begins with an account of molecular physics at heavy ion storage rings. Two experimental techniques are described that are employed here for diagnostics of internal excitation: *Coulomb explosion imaging (CEI)* and *Dissociative recombination (DR) fragment imaging*. Results obtained by these techniques for H_3^+ are presented and analyzed by a comprehensive rovibrational excitation model.

The last part "Development of a 22-Pole Ion Trap" describes steps being taken in order to account for the experience gained in the storage ring experiments. The goal that is pursued in these developments is to study fundamental reactions of H_3^+ in ground- and excited states under controlled conditions and in particular to come to a profound understanding of the DR reaction dynamics on a microscopic level through detailed comparison with advanced theoretical calculations. In this part the principles of trapping and guiding of ions in radio frequency fields are indicated and the construction of a cryogenic 22-Pole trap as an ion source for the TSR storage ring is described. First results demonstrating the functionality of the trap are presented.

The script closes with conclusions and perspectives for measurements that are under preparation and will be possible in the near future.

Part I

Motivation and Theory

Chapter 2
Triatomic hydrogen

2.1 A brief history

In the scientific history of triatomic hydrogen, there are many intersections between the neutral and the ionic species. The first documented evidence for the existence of triatomic hydrogen dates back to 1911 [Tho11]. It was J.J. Thomson who observed a mass three component in the rudimentary version of a mass spectrum coming from a hydrogen discharge. At that time the existence of H_3^+ seemed to be the only explanation for a singly charged molecule of mass three, although it contradicted all contemporary theories of chemical bonding. Consequently, when deuterium was found some years later the discoverer doubted his own postulation, since the formation of HD^+ appeared to be a much more logical explanation. In retrospect it is quite obvious that Thomson saw H_3^+ because it is actually hard to purge a hydrogen plasma from H_3^+ at moderate temperatures.
First calculations by Coulson [Cou35] in 1935 already indicated the equilateral triangular shape that is commonly accepted nowadays and even the calculated bond length was close to modern high accuracy calculations. However, his work found little acceptance, and in 1938 Hirschfelder predicted a nonlinear C_{2v} nuclear geometry [Hir38, Wat00], but in the 60s computer calculations [Chr64] reestablished the picture of a triangular molecule. The theoretical understanding that we have today on triatomic hydrogen owes much to the work of J.T. Hougen and J.K.G. Watson, who pinned down the symmetry properties and classification scheme of the energy levels in a series of papers [Hou62, Hou63, Wat84]. In the 70s Carney and Porter presented an *ab initio* potential surface [Car74] and calculated rovibrational energy levels based on this surface [Car76, Car80]. They could demonstrate that the potential is highly anharmonic and their work played a key role in the first experimental observation of a vibrational bending mode transition in the laboratory by Takeshi Oka [Oka80] in 1980.
The first experimental evidence of the triangular shape was derived with the Coulomb

explosion imaging technique in 1978 [Gai78], a more recent experiment of the same type – but aiming at vibrational diagnostics – will be discussed in detail later in this work. The experimental value for the binding energy of H_3^+ is (4.37±0.02) eV, determined by Cosby and Helm in 1986 [Cos88]. Three years later Wolfgang Ketterle and coworkers used the close correlation between H_3^+ and H_3 Rydberg states to perform a measurement of the second fundamental of H_3^+ [Ket89], the so-called breathing mode vibration.
Soon after the first observation of a spectrum in the laboratory, the search in interstellar space began, because the first models of the chemistry of interstellar clouds [Her73] had identified H_3^+ as the most important reaction agent for the creation of larger molecules. Since in this case both electronic and rotational spectroscopy are useless, for the ion possesses neither any stable electronically excited states nor a permanent dipole moment, one had to resort to vibrational spectroscopy in the infrared which eventually led to the discovery of H_3^+ in dense [Geb96] and diffuse [McC98] interstellar clouds in 1996 and 1998, respectively. The significance of H_3^+ in interstellar environments and the mystery that is related to the electron recombination in diffuse clouds will be discussed in the next chapter. In the last two decades H_3^+ was detected in several planetary atmospheres and probably in the remnants of supernova SN1987A [Mil92] and it is even used today to monitor the magnetic flux in Jupiter's ionosphere [Con93, Con00].
The formation of neutral H_3 in hydrogen plasmas was suggested already in 1927 by another eminent physicist Gerhard Herzberg at the age of 23 [Her27]. It took more than 50 years until Herzberg himself eventually reported a Rydberg spectrum of H_3, giving the first experimental evidence for its existence [Her79]. Ironically it seems that Herzberg was not even looking for the neutral version, since the spectrum was taken in the frame of a campaign to detect H_3^+. The ground state of neutral H_3 is repulsive, but Rydberg states exist – described by one electron attached to a H_3^+ core – that are stable from the point of view of nuclear structure but decay radiatively with lifetimes of less than $1\,\mu s$. In that sense H_3 is an excimer and it is the only polyatomic molecule known so far to show this behaviour [Her79].

2.2 Structure and potential surface

The central theorem of quantum chemistry is the Born-Oppenheimer approximation [Bor27, Bor51]. It makes use of the mass difference between electrons and nuclei, assuming the electrons to adapt instantaneously to changes in the nuclear configuration. This approach allows the electronic Schrödinger equation to be solved for a number of points parametrized by the set of nuclear coordinates $\{R_a\}$. The results are usually fitted

by an analytical function yielding an electronic potential energy surface (PES) $E_{elec}(\{R_a\})$ that is inserted into the nuclear Hamiltonian, which consists of the nuclear kinetic energy term, the electronic energy and the nuclear repulsion

$$H_{nucl} = -\sum_{a=1}^{N} \frac{\hbar}{2\,M_a} \nabla_a^2 + E_{elec}(\{R_a\}) + \sum_{a=1}^{N} \sum_{b>a}^{N} \frac{Z_a Z_b\, e^2}{R_{ab}}\,, \tag{2.1}$$

with M_a denoting the mass of nucleus a and Z_a, Z_a and R_{ab} standing for the charge state and distance of nuclei a and b. Eventually the nuclear Schrödinger equation is formulated

$$H_{nucl}\ \Psi_{nucl} = E\,\Psi_{nucl}\,, \tag{2.2}$$

and solved to gain the eigenfunctions or nuclear wave functions, describing molecular vibration and rotation

$$\Psi_{nucl} = \Psi_{nucl}(\{R_a\})\,. \tag{2.3}$$

One of the key problems of quantum mechanical calculations therefore arises from the solution of the electronic problem and the determination of the electronic energies, since any however elaborate calculation of molecular dynamics or spectroscopic frequencies is restricted to the accuracy of the underlying PES. For the triatomic hydrogen ion, a milestone was reached when Meyer, Botschwina and Burton (MBB) published an *ab initio*

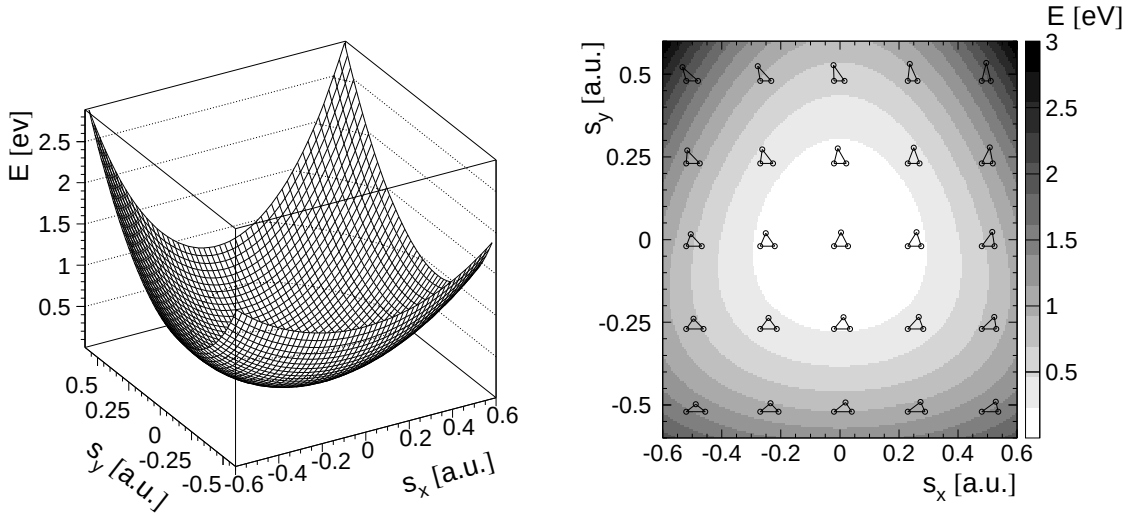

Figure 2.1: *H_3^+ potential energy surface plotted in symmetry coordinates (see chapter 5) $s_x = (2r_{12} - r_{23} - r_{31})/\sqrt{6}$ and $s_y = (r_{23} - r_{31})/\sqrt{2}$, defining the shape of the molecule, while the circumference was kept fixed at the equilibrium value. The triangles in the representation on the right-hand side indicate the geometry of the molecule at a given (s_x, s_y) point in the diagram. Potential surface according to Prosmiti* et al. *[Pro97].*

surface [Mey86] (actually one parameter was adjusted to match the experimental value of the ν_2 fundamental [Wat00]) that was designed to yield high accuracy in the equilibrium region (see Fig. 2.1) and is still the basis of most modern calculations. One of them is the probably most accurate potential surface for a polyatomic ion to date, calculated by Cencek *et al.* [Cen98, Jaq98] including non-Born-Oppenheimer and relativistic corrections. The minimum of this potential indicates an equilateral triangular geometry with a side length of $1.65035\,a_0$.

For the understanding of dissociation and dynamical processes it is necessary to extend the calculations to large internuclear distances corresponding to high energies. This project is complicated by the presence of two dissociation channels ($H_2 + H^+$ and $H_2^+ + H$) and the fact that H_3^+ can sample linear geometries already at energies above $10000\,cm^{-1}$ (see Fig. 2.2). Recent calculations by Tennyson *et al.* [Pro97, Pol00] use an energy switching approach [Var96] to combine potentials that are supposed to be accurate for different energy intervals to yield a *global* potential surface suited both for the treatment of spectroscopy and dynamical processes.

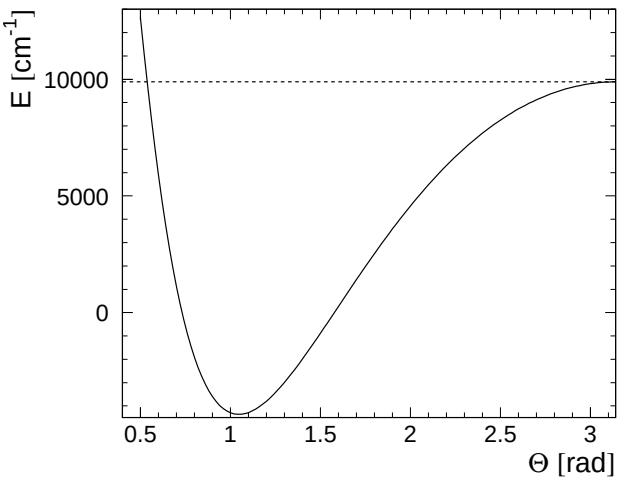

Figure 2.2: *The barrier to linearity. A special representation of the H_3^+ potential surface, where two H-H bonds are forced to be equal, while their length is varied to yield the minimum energy for a given angle Θ between them. The broken line indicates the asymptotic energy for Θ=180°. (Potential surface taken from [Pro97], zero point energy set to 4362 cm^{-1}, according to [Roe94]).*

The benchmark test for the quality of an electronic surface calculation is the comparison with spectroscopy. For the calculation of nuclear wave functions and transition energies the variational approach of Sutcliffe and Tennyson has been very successful [Sut87].

Nowadays theoretical calculations for rovibrational transition frequencies below the barrier to linearity are in excellent agreement ($\delta E \leq 0.1\,\mathrm{cm}^{-1}$) with the experimental lines. Accurate predictions for states above $10000\,\mathrm{cm}^{-1}$ are still a challenge to theory, partly due to the inherent problems with the potential surface at higher energies, as discussed above, and partly because the standard basis sets are not appropriate for the treatment of linear geometries [Nea96].

Chapter 3
Interstellar H_3^+

The space between the stars is filled by a mixture of gaseous and particulate matter and photons. In our galaxy the interstellar medium (ISM) accounts for 10% of the total mass [Dul84] and its main constituent is hydrogen either in atomic or molecular form. Although the average number density of the ISM is as low as $1\,\mathrm{cm}^{-3}$, it is known today, that the distribution is highly inhomogeneous and can reach $10^6\,\mathrm{cm}^{-3}$ in dense clouds. It is in these massive, cold objects where the formation of stars is supposed to occur. In this context the existence of molecules is key to the agglomeration of matter since they provide cooling mechanisms at low temperatures, where radiative emission from atoms becomes ineffective.

In the last decades the field of interstellar chemistry has been rapidly evolving; while in 1964 only four interstellar molecules were known, until today 123 molecules were detected in the ISM (as of 04/2003, a list can be found at `http://www.cv.nrao.edu/~awootten/allmols.html`). All of these molecules are either neutrals or positively, singly charged ions, ranging in size from diatomics to organic molecules consisting of up to 13 atoms. Recently even the emission spectrum of glycol aldehyde (CH_2OHCHO), a simple sugar, has been identified by a radio telescope [Hol00], nourishing the conjectures on biologically relevant molecules in the ISM.

The rich chemistry of interstellar clouds appears surprising in the first place, because of the adverse conditions prevailing in these objects. Owing to the low densities and cold temperatures (10-100 K) ternary collisions and endothermic processes, as well as reactions where a significant reaction barrier has to be overcome, are ruled out. Under these conditions exothermic ion-neutral reactions dominate, where the neutral reactant is polarized by the field of the ion and an attractive dipole potential is formed. One of the major reaction agents driving the formation of many more complex molecules is H_3^+, its role in interstellar clouds will be the subject of this chapter.

The first quantitative model for the gas phase chemistry of interstellar clouds was pre-

sented by Herbst and Klemperer in 1973 [Her73]. In this model about 100 reactions were considered for 35 species, while the UMIST database for astrochemistry 1999 counts 4113 gas-phase reactions for 396 species [LeT00]. Nevertheless, not all molecules can be formed in the gas phase; the most prominent exception is also the most abundant molecule by far, namely molecular hydrogen. When two H atoms collide there is no force that would glue them together long enough for a photon to be emitted and the molecule to be stabilized. Therefore the only feasible mechanism seems to be the synthesis on the surface of dust grains [Wil02], however, although this conclusion seems to be commonly accepted, it is actually based on falsification of alternative pathways rather than on a stringent argumentation.

Once that molecular hydrogen is available, the first step in the formation of H_3^+ is the ionization of H_2 by cosmic rays (cr)

$$H_2 + (cr) \longrightarrow H_2^+ + e^- + (cr), \tag{3.1}$$

followed by the well-known exothermic formation reaction

$$H_2^+ + H_2 \longrightarrow H_3^+ + H \qquad + 1.7\,\mathrm{eV}, \tag{3.2}$$

which occurs with a rate that approaches the Langevin rate[1] , implying that H_2^+ will be depleted rapidly and converted into H_3^+ [Her00]. The removal of H_3^+ can proceed via two independent pathways, firstly through proton transfer reactions of the type

$$H_3^+ + X \longrightarrow XH^+ + H_2\,. \tag{3.3}$$

where X can stand for either atomic or molecular reactants, and secondly by dissociative recombination (DR) with free electrons

$$H_3^+ + e^- \rightarrow \begin{cases} H + H + H \\ H_2 + H\ . \end{cases} \tag{3.4}$$

The efficiency of the latter process depends critically on the DR rate coefficient at low temperatures and on the density of free electrons in the gas phase which is supposed to

1 The Langevin rate is essentially an approximation of the maximum ion-neutral collision rate, assuming a reaction probability of 1 if the reactants can overcome the centrifugal barrier and ignoring the repulsive part of the potential. The rate is given by

$$k = \frac{1}{4\pi\,\epsilon_0}\,2\pi e \left(\frac{\alpha}{\mu}\right)^{1/2},$$

where α is the polarizability of the neutral collision partner and μ is the reduced mass. Note that the Langevin rate is temperature-independent.

differ by several orders of magnitude between dense and diffuse clouds. In the next two sections relatively simple model calculations will be employed to predict the H_3^+ number density in dense and diffuse clouds and compare them to the astronomically observed column densities.

3.1 Dense interstellar clouds

The fractional abundance of free electrons in interstellar clouds is maintained by the ionization of elements like carbon, sulphur, silicon, iron, and magnesium that can be ionized by ultraviolet starlight. In dense clouds this process is hindered by two factors, namely by the low abundance of these elements in the gas phase (many of these elements can be absorbed on dust grains [Her00]) and by the fact that dense clouds are too opaque for ultraviolet light to penetrate into the inner regions. Assuming a total H_2 density of $n(H_2)=10^5\,cm^{-3}$ and the typical fractional electron abundance in dense clouds [Her00] of $n(e)/n(H_2) \approx 10^{-8}$ combined with a fast DR rate coefficient at 30 K of $\alpha = 5\times10^{-7}\,cm^3\,s^{-1}$ the H_3^+ destruction rate through DR is obtained

$$r_{DR} = \alpha \cdot n(H_3^+) \cdot n(e) \approx n(H_3^+) \cdot 5 \times 10^{-10}\,s^{-1}\,. \tag{3.5}$$

On the other hand, the most important chemical reaction to remove H_3^+ is the formation of HCO^+

$$H_3^+ + CO \longrightarrow HCO^+ + H_2\,, \tag{3.6}$$

where the fractional abundance of CO in dense clouds derived from direct observations [Bla00] is in the range $n(CO)/n(H_2)= (2-5)\times10^{-4}$ and the rate coefficient for the reaction (Eq. 3.6) is [Ani86] $k_{CO} = 2 \times 10^{-9}\,cm^3\,s^{-1}$, yielding a substantially higher destruction rate of

$$r_{CO} = k_{CO} \cdot n(H_3^+) \cdot n(CO) \approx n(H_3^+) \cdot 5 \times 10^{-8}\,s^{-1}\,. \tag{3.7}$$

These values indicate that chemical reactions are much more effective in removing H_3^+ from dense clouds than electron recombination, even if a high DR rate coefficient of $5 \times 10^{-7}\,cm^3\,s^{-1}$ is adopted. Furthermore in a simple model calculation the H_3^+ number density can be estimated, as the dominant destruction rate is known[2] from Eq. 3.7, as well as the formation rate according to Eq. 3.1, given by the number density of H_2 multiplied by the cosmic ray ionization rate ζ. Equating both rates and thus assuming equilibrium

2 The next largest process would be the reaction with atomic oxygen, which has a rate of about 1/3 of the CO term [Oka99], all other reactions are much less important.

conditions yields

$$\zeta\, \mathrm{n(H_2)} \approx \mathrm{k}_{CO}\, \mathrm{n(H_3^+)}\, \mathrm{n(CO)}. \tag{3.8}$$

In models of dense clouds the fractional abundance of carbon-monoxide agrees with the aforementioned observations at values about $\mathrm{n(CO)/n(H_2)} \approx 2 \times 10^{-4}$, hence together with the cosmic ray ionization rate of 3×10^{-17} [Oka99] Eq. 3.8 is reduced to

$$\mathrm{n(H_3^+)} \approx 10^{-4}\,\mathrm{cm^{-3}}\ . \tag{3.9}$$

Consequently, the H_3^+ number density is independent of the total density of the cloud. This finding can be used to determine the size of the cloud along the path of sight, if the column density[3] $\mathrm{N(H_3^+)}$ is known, since the column can be calculated by

$$\mathrm{L} = \frac{\mathrm{N(H_3^+)}}{\mathrm{n(H_3^+)}.} \tag{3.10}$$

Typical H_3^+ column densities in dense clouds are about $\mathrm{N(H_3^+)} \approx 5 \times 10^{14}\,\mathrm{cm^{-2}}$ which together with the number density of Eq. 3.9 results in a column length of 1.5 parsec, which is similar to the linear extension of the observed clouds on the sky. Furthermore the ratio between the column densities of H_3^+ and H_2 is compatible with modern cloud models, just as the observed temperatures of 25-50 K [Oka99]. In conclusion, the H_3^+ detections in dense molecular clouds do not conflict with theoretical models.

3.2 Diffuse interstellar clouds

Along the same line of reasoning the H_3^+ abundances in diffuse interstellar clouds can be estimated. In diffuse clouds the fractional ionization is much higher that in dense clouds, due to a higher "metallicity" (in astronomy every element heavier than helium is considered metallic) in the gas phase – especially atomic carbon that can be ionized by 11.3 eV photons is supposed to be an effective source for free electrons – and the penetrability to starlight. From the fractional abundance of atomic carbon an approximated value of the electron density can be derived $\mathrm{n(e)/n(H_2)} \approx 5 \times 10^{-4}$ [Bla00] which is more than four orders of magnitude higher than in dense clouds. Thus the destruction rate due to DR in diffuse clouds can be calculated assuming again a DR rate coefficient of $\alpha = 5 \times 10^{-7}\,\mathrm{cm^3\,s^{-1}}$ and a H_2 number density of $\mathrm{n(H_2)} = 10^3\,\mathrm{cm^{-3}}$

$$\mathrm{r}_{DR} = \alpha \cdot \mathrm{n(H_3^+)} \cdot\ \mathrm{n(e)} \approx \mathrm{n(H_3^+)} \cdot 2.5 \times 10^{-7}\,\mathrm{s^{-1}}\ , \tag{3.11}$$

3 The column density is defined as the number of molecules in a $1\,\mathrm{cm^2}$ cross section along the path of sight $\mathrm{N} = \int_0^L n\, dl$. It can be derived from astronomical observations once the temperature and thus the rotational partition function can be determined [Win74].

which should be much faster than competing chemical reactions (note that the numerical result from Eq. 3.7 scales with the total CO number density – which would be much lower here – and thus can not be compared directly). Consequently the H_3^+ number density given by

$$\zeta\, n(H_2) \approx \alpha\, n(H_3^+)\, n(e)\,, \tag{3.12}$$

results in

$$n(H_3^+) \approx 1.2 \times 10^{-7}\,cm^{-3}\,, \tag{3.13}$$

which is two to three orders of magnitude lower than in dense clouds. If this approximation is taken serious, the observation of H_3^+ in diffuse interstellar matter would be rather unlikely even with modern techniques. Surprisingly, the first detection in the diffuse interstellar medium towards Cygnus OB2 No. 12 [McC98, Geb99] revealed a column density $N(H_3^+) = 3.8 \times 10^{14}\,cm^{-2}$ that is as high as in dense clouds. Using Eq. 3.10 the column length would be 1 kpc, implying that the biggest part of the 1.7 kpc distance to Cygnus OB2 No. 12 would be filled with H_3^+!

The outcome of the estimate seems unphysical and thus the discrepancy must come from n(e), α or ζ. In a very recent observation of H_3^+ towards ζ Persei [McC03], a somewhat lower column density $N(H_3^+) = 8 \times 10^{13}\,cm^{-2}$ was measured. The authors also adopted an H_3^+ DR rate coefficient that is a factor of two lower than the previously accepted value (the new value is an outcome of a storage ring measurement at CRYRING/Stockholm, see next chapter), but still the resulting H_3^+ number density is too high to be reproduced by the above outlined model calculations. Therefore they propose that the cosmic ray ionization rate towards ζ Persei is higher by a factor of 40 compared to the standard value used above.

3.3 More aspects of interstellar H_3^+

As a consequence of the importance of H_3^+ as a proton-donor in the ISM and the low temperatures prevailing there, subtle effects concerning internal excitation or isotope exchange reactions may have significant influence on the whole reaction network; two examples will be given below.

3.3.1 Deuterium fractionation

In cold interstellar clouds the slight differences in zero point energy of hydrogen-bearing molecules compared to their deuterated isotopomers can lead to large isotopic enrichment.

In general the exchange of a hydrogen atom by a deuteron will lead to stronger bonding and thus energy is gained. For example the reaction

$$H_3^+ + HD \longrightarrow H_2D^+ + H_2\,, \tag{3.14}$$

is exothermic by 232 K [Ger02b]. For the backward reaction to occur the same amount of energy has to be invested and if one assumes the products to thermalize at cloud temperatures between 10 and 50 K before undergoing the next reactive collision, the backward reaction is extremely unlikely. Actually, the same is true for the next steps of deuteration, the exchange reactions

$$H_2D^+ + HD \longrightarrow D_2H^+ + H_2\,, \tag{3.15}$$

$$D_2H^+ + HD \longrightarrow D_3^+ + H_2\,, \tag{3.16}$$

are exothermic by 189 K and 235 K, respectively. This reaction chain will be used in the third part of this work to test the functionality of the cryogenic ion trap. In interstellar clouds the natural atomic deuterium fraction of D/H$= 1.5\times10^{-5}$ is substantially enhanced for triatomic hydrogen and the ratio H_2D^+/H_3^+ can reach values of several percent at temperatures below 25 K [Mil00]. Since the chemistry of the deuterated species with respect to other atoms or molecules is roughly unchanged, the deuteration can thus be transported into more complex molecules via the typical proton-exchange reactions.
More than ten deuterated species have already been detected in the ISM, among them two doubly deuterated molecules (NHD_2 and D_2CO), and very recently even fully deuterated ammonia (ND_3) has been found [Lis02]. The abundance of the deuterated molecules is often enhanced by a factor of 100 to 1000 compared to the cosmic D/H ratio. The reason for these large factors are believed to lie in the energetics of the forward and backward reactions, and again triatomic hydrogen is supposed to play a major role since it is supposed to be the most effective ion reacting with HD and thus carrying deuterium into the chemical network.
Unfortunately there is only little laboratory data on the reaction rates at the relevant temperatures; e.g., in theoretical cloud models the deuteration of H_3^+ (Eq. 3.14) was assumed to proceed with the Langevin cross section. This assumption was corrected only recently, when Gerlich *et al.* [Ger02b] analyzed the H_3^++HD $\leftrightarrow$ H_2D^++H_2 reaction system at 10 K measured in a 22-pole ion trap (see Part III of this work) and came to the conclusion that the forward reaction is slower by a factor of five, while the backward reaction is about five orders of magnitude faster than previously assumed. The new values result in distinctly lower isotope enrichment for practically all deuterated species and thus aggravate the discrepancy between astronomical observations and cloud models.

To resolve this problem more detailed measurements at low temperatures are needed as well as a better understanding of the interplay between dust grains and the gaseous phase in the ISM.

3.3.2 Possible cosmic masers

Due to the lack of a permanent dipole moment, pure rotational transitions in H_3^+ are in principle forbidden. This means on the other hand that rotationally excited states can have very long lifetimes, as will be demonstrated in chapter 8. A particular feature arises for the (J, G)=(4,4) and (3,1) levels (for quantum numbers, see chapter 5) which accidentally happen to lie close together. While the upper state (4,4) can decay only into (3,1), the (3,1) state has two rather efficient radiative pathways into lower states. Black [Bla98, Bla00] pointed out that this situation will lead to a natural population inversion – if the collision rate in the medium is low enough – and thus could give rise to a cosmic maser at 217.78 GHz. This maser line is yet to be seen in the ISM but Black suggests that in molecular gas around active galactic nuclei observations might eventually be successful.

Chapter 4
Dissociative recombination

The capture of a free electron by a molecular cation followed by the dissociation into neutral fragments is called dissociative recombination (DR)

$$AB^+ + e^- \longrightarrow A + B\,, \tag{4.1}$$

where the neutral fragments A and B can be either atomic or molecular. The DR process is important in various fields from atmospheric [Bar70] to interstellar physics (see previous chapter) and in fusion plasmas [Jan99]. The first DR measurements were stimulated by studies of atmospheric air glows. In 1931 Kaplan proposed that two emission lines of the night sky measured by Lord Rayleigh could be due to the production of excited atomic oxygen through the DR of O_2^+ [Kap31]. Today it is known that the DR of O_2^+ is indeed responsible for auroral greenline emission from the $O(^1D)\leftarrow O(^1S)$ transition at 557.7 nm [Pev01].

The first theoretical treatments predicted extremely low DR rates since they assumed that the process involves coupling between electronic and nuclear motion which was supposed to render the process slow (a review on the development of DR theory can be found in [Bat94]). Nevertheless, when the first experiments yielded high DR rates measured in the afterglow of various gases [Bio49], the theoretical position had to be thought over and in 1950 Bates proposed a DR mechanism [Bat50a, Bat50b] – initiated by the capture of the electron in a doubly excited dissociative state – that is referred to as *crossing mode* DR today. In the meantime it was necessary to introduce further DR mechanisms to explain the experimental evidence for various molecular ions.

Many different techniques were applied to measure DR rate coefficients, branching ratios and reaction kinetics in the last decades. While the majority of the early experiments were performed in microwave-driven discharges, in the 80s molecular beam experiments were developed and the 90s saw the advent of electron cooler rings.

In this chapter the different DR mechanisms will be described briefly, for the sake of

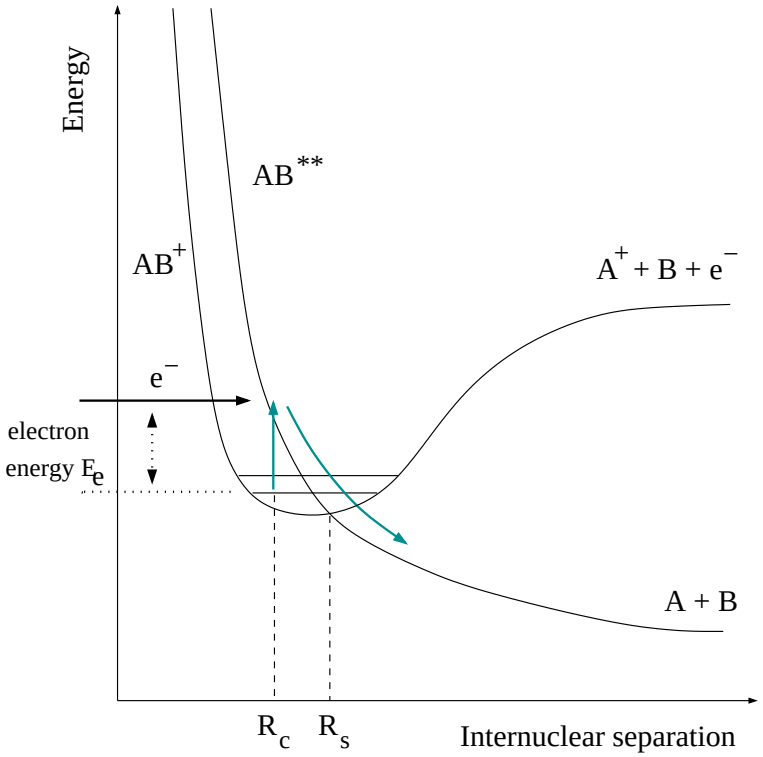

Figure 4.1: *Sketch of the direct mechanism of dissociative recombination.*

simplicity diatomic potential curves will be used as examples. Furthermore the special and most controversial case, namely the DR of H_3^+ will be introduced.

4.1 Crossing mode DR

The direct mechanism

The direct mechanism depends on a favourable crossing of the ionic ground state by a neutral repulsive state at low energies. In Fig. 4.1 the potential curve of the initial molecular ion AB^+ is plotted together with an incoming electron of energy E_e; the zero-point of the energy scale is set to be equal to the ground state energy of the ion. The direct DR process can be understood as a two-step process, first the capture of the free electro into the doubly excited repulsive state AB^{**} and second the stabilization of the neutral system by dissociation. From this simple picture a few handwaving arguments can be developed.

Following the ansatz of Bardsley to derive a simple mathematical formulation [Bar70],

the two-step mechanism corresponds to the separation of the cross section in two terms

$$\sigma(E) = \sigma_{cap}(E)\, S(E)\,, \tag{4.2}$$

where σ_{cap} is the cross section for electron capture, while $S(E)$ is the so-called survival factor, describing the competition between stabilization of the neutral complex (resulting in the dissociation of the molecule) and autoionization that restores the initial situation $AB^+ + e^-$. The capture itself is described by the electronic matrix element $V(R)$, coupling the nuclear wave function of the ion $\langle\zeta_{AB^+}(R)|$ to that of the doubly excited state $|\zeta_{AB^{**}}(R)\rangle$. The capture cross section can be written

$$\sigma_{cap}(E) = \frac{2\,\pi^3}{\hbar m E}\ \frac{r}{2}\ |\langle\zeta_{AB^+}(R)|V(R)|\zeta_{AB^{**}}(R)\rangle|^2\,, \tag{4.3}$$

with E denoting the energy of the electron and the factor r representing the ratio of the multiplicities of the two states. It is divided by two, to account for the two possible spin orientations of the incoming electron. In many cases this formula can be simplified by replacing $|\zeta_{AB^{**}}(R)\rangle$ by a delta function at the internuclear distance R_c of the electron capture (for details concerning this approximation and the configuration interaction matrix element $V(R)$, see [Bar70] and references therein)

$$\zeta_{AB^{**}}(R) = \left(\frac{1}{U'}\right)^{(1/2)}\ \delta(R - R_c)\,, \tag{4.4}$$

where U' is the slope of the potential curve of the doubly excited state AB^{**} at R_c. Together with the introduction of the capture width $\Gamma_c = (2\pi/\hbar)|V(R_c)|^2$ the capture cross section becomes

$$\sigma_{cap}(E) = \frac{\pi^2}{mE}\ \frac{r}{2}\ \frac{\Gamma_c}{U'}\ |\zeta_{AB^+}(R_c)|^2\,. \tag{4.5}$$

It can be seen that the probability for electron capture scales with the capture width and the inverse of the slope of the repulsive state. Furthermore the electron capture is most likely at distances R_c within the molecular vibrations of the initial ion. However, the most significant dependence – since observable in experiments – is the dependence upon the electron energy

$$\sigma_{cap} \sim 1/E\ . \tag{4.6}$$

The electron capture goes hand in hand with a transition from a free to a bound state and thus the electron deposits its energy. The neutral complex AB^{**} is therefore equipped with excess energy that will lead to autoionization – the reverse process of electron capture – if it cannot be converted into other degrees of freedom. The energy can either be carried away by the emission of a photon (radiative recombination) or transfered into nuclear

motion resulting in the dissociation of the molecule. In most cases, it turns out that photon emission is too slow to be competitive and thus the stabilization of the complex through dissociation is a better candidate. Once the internuclear distance R_s is reached, the energy of the repulsive state is lower than the ionic potential curve and autoionization is energetically forbidden (in the frame of the Born-Oppenheimer approximation). In that sense R_s is the "point of no return", and the time interval that is needed to reach this point has to be compared with the average lifetime against autoionization if one wants to decide which process is more efficient. It is convenient to define the survival factor

$$S = \frac{A(st)}{A(st) + A(ai)} \tag{4.7}$$

where $A(ai)$ stands for the autoionization rate and $A(st)$ is the rate of stabilization of the neutral complex. The lifetime of autoionizing states is typically of the order of 10^{-14} s, while the stabilization by dissociation is usually completed after 10^{-15} to 10^{-16} s and thus S is often close to unity which makes direct DR a fast process [Bar70], given a curve crossing at low energy occurs. Typical recombination rates for diatomic molecular ions undergoing direct DR are of the order of $\alpha \sim 10^{-7}\,\mathrm{cm^3\,s^{-1}}$, for polyatomic ions α can be higher by one order of magnitude.
In the case of atomic recombination, this very stabilization process is not available and consequently the DR rates of molecular ions are several orders of magnitude faster than atomic radiative or dielectronic recombination rates. Also, in contrast to atomic recombination the process depicted in Fig. 4.1 has no resonant character, because the energy gap between the ionic and the neutral state varies smoothly for different values of R_c.

The indirect mechanism

Nevertheless resonances in DR cross sections at low energies have been observed. The cause of these structures is the indirect DR mechanism that is depicted in Fig. 4.2. Here, the electron is first captured in a Ryberg state AB^* of the ion, which then interacts with the repulsive state AB^{**} to eventually dissociate the molecule. Consequently, indirect DR can be described as a three-step process

$$AB^+ + e^- \longrightarrow AB^* \longrightarrow AB^{**} \longrightarrow A + B\,, \tag{4.8}$$

where the interaction between Rydberg state AB^* and repulsive state AB^{**} is called *predissociation*. It involves coupling between electronic and vibronic degrees of freedom (breakdown of the Born-Oppenheimer principle) and because of this coupling the indirect process was supposed to be very slow for diatomic molecules. However, indirect DR

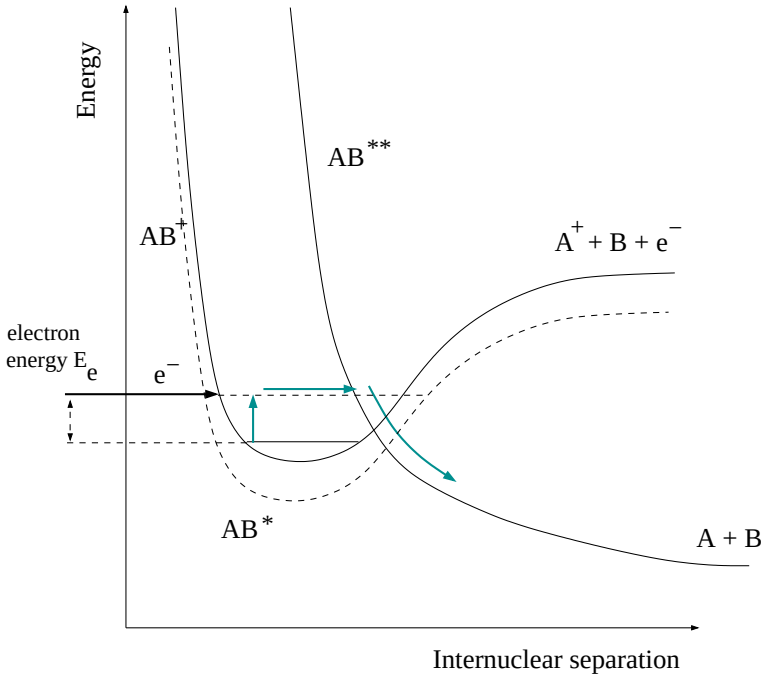

Figure 4.2: *Sketch of the indirect mechanism of dissociative recombination.*

proceeds through radiationless one-electron transitions while direct DR requires a two-electron process for the electron capture. Direct and indirect DR can interfere both constructively and destructively, causing resonance structures in the DR cross section at low energies. Today, Rydberg resonances have been clearly identified in the DR of molecular hydrogen and can be reproduced by appropriate theoretical treatments. State-of-the-art is the Multichannel Quantum Defect theory (MQDT) [Giu80], which is capable of treating direct and indirect DR simultaneously and was applied successfully to several diatomic molecules.

4.2 Tunneling mode DR

The mechanisms discussed in the last section rely on the existence of a repulsive neutral state that crosses the ionic potential at low energy. For a long time the absence of such a curve crossing was interpreted as an indicator for a vanishing DR cross section. Again this position had to be corrected when the first experimental results of non-crossing species were published. The two most striking examples of molecular ions that lack a curve crossing in their ground state but still recombine at a substantial rate are HeH^+ and H_3^+. For HeH^+ the theoretical prediction of the DR rate coefficient of $10^{-11}\,cm^3\,s^{-1}$ based on radiative recombination, was contradicted by the first results from merged beam tech-

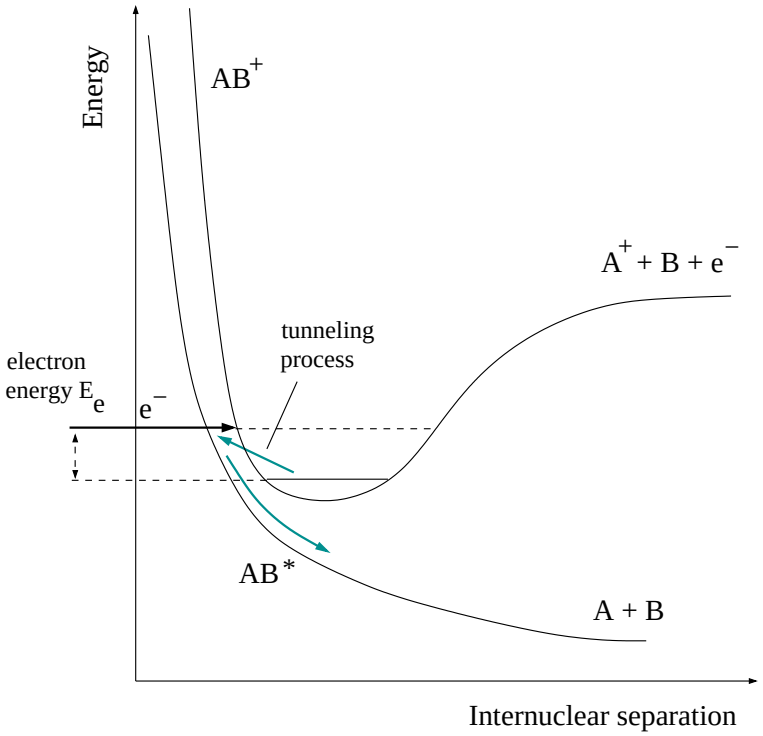

Figure 4.3: *Sketch of tunneling mode dissociative recombination.*

niques, showing a rate of $10^{-8}\,\mathrm{cm^3\,s^{-1}}$ at 300 K accompanied with resonance structures at low energies [You89]. A few years later, storage ring measurements supported the finding of a fast DR process [Tan93] as well as the presence of deep window resonances below 1 eV [Mow95]. Two different theoretical approaches were pursued, Sarpal *et al.* used the R-Matrix method [Sar94] to perform a calculation for $^4HeH^+$, while Guberman applied a refined version of MQDT where the interaction is driven by the nuclear kinetic operator (implying a breakdown of the Born-Oppenheimer approximation) to $^3HeH^+$ [Gub94].
Both calculations agreed on the non-crossing mechanism that is depicted in Fig. 4.3. Here the electron capture goes hand-in-hand with a tunneling process through the classically forbidden region into the repulsive state AB*. The tunneling process is supposed to show a strong mass dependence and to be effective only for hydrogen-containing ions. The poor tunneling probability can be partly compensated by the fact that only radiationless single-electron transitions are needed in contrast to direct DR.
Both calculations stressed the importance of intermediate Rydberg states leading to resonance structures and both succeeded in reproducing the overall magnitude of the cross section, however, they predicted different channels to be important. Further storage ring experiments measuring the final product channels by imaging techniques (imaging results for H_3^+ will be presented later in this work) favoured Gubermans MQDT approach

[Sem96].
The situation for H_3^+ is similar to that of HeH^+ in the sense that no curve crossing at low energies is found but still H_3^+ recombines rapidly with electrons; consequently, the tunneling mechanism was proposed to drive the DR of H_3^+, too.

4.3 DR of H_3^+

In the last chapter the implications of H_3^+ dissociative recombination on interstellar chemistry were discussed. The outstanding role of H_3^+ was recognized already in the early seventies and consequently in the last decades the DR of triatomic hydrogen was a much studied process, both experimentally and theoretically. A full account of all the published work on H_3^+ DR is beyond the scope of this script, reviews can be found in [Lar00, Dal94]. The DR process of ground state H_3^+ can be described by

$$H_3^+ + e^- \rightarrow \begin{cases} H(1s) + H(1s) + H(1s)\,, \\ H_2(v) + H(1s)\ . \end{cases} \tag{4.9}$$

In the three-body channel the kinetic energy release is fixed at 4.76 eV, while in the two-

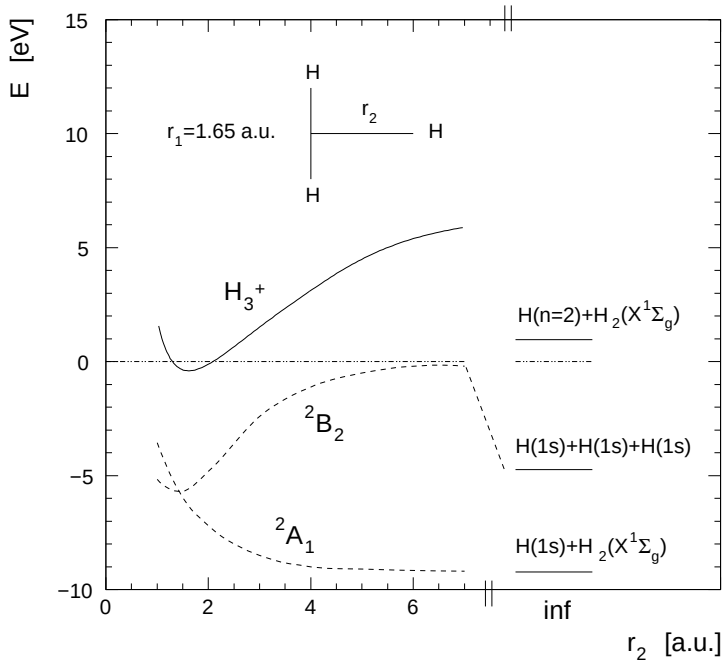

Figure 4.4: *Molecular potentials relevant for the DR of H_3^+ as a function of the Jacobi coordinate r_2 for the geometry indicated in the inset. The dashed curves represent neutral H_3 states, the correlated final-state energies are also plotted (in the two-body channel for the rovibrational ground state of H_2).*

body channel it can vary, depending on the vibrational excitation of the $H_2(v)$ product between 9.23 eV ($v = 0$) and 4.92 eV ($v = 14$). In Fig. 4.4 the relevant H_3 potentials are plotted together with the H_3^+ ground state and the final-state energies. The first electronically excited product state H(n=2)+$H_2(X^1\Sigma_g)$ opens at 0.96 eV above the energy of the H_3^+ ground state.

The overall reaction probability at a certain temperature (usually 300 K) is expressed in terms of the thermal rate coefficient α [$cm^3\,s^{-1}$]. This coefficient multiplied by the electron density gives the rate of dissociation. In the last thirty years more than twenty measurements of $\alpha(300\,K)$ have been published (even more have been performed); the results – despite small individual error bars – are spread over four orders of magnitude from $\sim 10^{-11}$ to $\sim 10^{-7}\,cm^3\,s^{-1}$.

A thorough understanding of the DR process would also imply insight into the dissociation dynamics and product states. Thus, besides the rate coefficient, the branching ratio of the two channels and the product states and dynamics are of interest and have been investigated experimentally. Below the experimental efforts and theoretical developments will be summarized.

4.3.1 Experimental studies

Rate coefficient measurements

The first measurement cited in most reviews (although there had been stationary afterglow studies with hydrogen plasmas by Biondi and Brown more than fifty years ago, see [Bio49, Pla02]) came from a microwave-afterglow/mass-spectrometer apparatus and yielded a value of $\alpha = 2.3\times10^{-7}\,cm^3\,s^{-1}$ at 300 K [Leu73]. This outcome was confirmed by molecular beam methods and further afterglow experiments in the next years until Adams and Smith in a flowing afterglow/langmuir probe (FALP) measurement in 1984 found no evidence for recombination at all. They concluded that the rate coefficient was immeasurably small and gave an upper limit of $2 \times 10^{-8}\,cm^3\,s^{-1}$ [Ada84]. This new evidence for a slow recombination process was strongly supported by Michels and Hobbs [Mic84] who published a theoretical treatment of the direct DR of H_3^+ that suggested a very low rate coefficient and in the following years the upper limit for α was reduced in a series of papers to $2 \times 10^{-11}\,cm^3\,s^{-1}$ (see e.g. [Smi87]). Subsequently, the explanation for the high rate coefficients observed in the other experiments was supposed to lie in undefined vibrational excitation. This uncertainty was overcome by Amano in 1988 who used an infrared absorption technique to measure the loss of $v = 0$ ions directly [Ama88], resulting in a high rate of $1.8 \times 10^{-7}\,cm^3\,s^{-1}$. In 1993 the first storage ring experiment with H_3^+

was carried out at CRYRING/Stockholm [Lar93], yielding a cross section as a function of electron collision energy (the storage ring technique will be discussed in detail in chapter 6) corresponding to a thermal rate coefficient at 300 K of $\alpha = 1.15 \times 10^{-7}\,\mathrm{cm^3\,s^{-1}}$ [Sun94]. In this experiment, the H_3^+ ions were supposed to be in the vibrational ground state, since the storage times were long enough to allow for radiative cooling.

Shortly afterwards two publications by Smith and Španel withdrew the claim of a immeasurably low α and announced that experiment and theory was "reconciled" and the "controversy resolved" by further studies in a flowing afterglow that showed a dependence of the rate coefficient on the vibrational excitation and for $v = 0$ their new value was $\alpha = (1-2) \times 10^{-8}\,\mathrm{cm^3\,s^{-1}}$ [Smi93b, Smi93a]. A misinterpretation of the CRYRING data lead them to the conclusion that this value was in agreement with the storage ring result which was actually one order of magnitude higher.

To date three storage rings (CRYRING/Sweden, TARN II/Japan, ASTRID/Denmark) have published cross sections for H_3^+ DR and all three agree within their resolution at $\alpha \approx 1 \times 10^{-7}\,\mathrm{cm^3\,s^{-1}}$. The role of internal excitation in storage ring experiments with H_3^+ was scrutinized in several experiments at the TSR of the MPI für Kernphysik. These experiments – which will be presented in this work – led to the conclusion that ion sources capable of producing rovibrationally cold H_3^+ are needed to achieve reliable results. The latest development in that context is a measurement at CRYRING, using an expansion ion source that gave a rate coefficient that was lower by a factor of 2 ($\alpha \approx 6.8 \times 10^{-8}\,\mathrm{cm^3\,s^{-1}}$) compared to the previous experiments [McC03].

In the meantime the discrepancy among the afterglow results remains unresolved despite serious efforts [Gou95]. Moreover, recent experiments in a stationary afterglow detected a strong dependence of α on the partial pressure of H_2 in the plasma and give a very low upper limit of $\alpha < 3 \times 10^{-9}\,\mathrm{cm^3\,s^{-1}}$ in apparent contradiction to all other measurements performed in the last decade [Pla02].

Branching ratio

The branching between the two channels of Eq. 4.9 was measured for the first time in a merged beam experiment in 1983 by Mitchell *et al.* [Mit83]. Two- and three-body breakup were differentiated by the means of a grid with a finite transmission that was positioned in front of the detector. It was found that the three-body channel dominates at low energies, however, no detailed account of the vibrational excitation of the H_3^+ ions could be given. More than ten years later Datz *et al.* carried out a storage ring measurement utilizing the same grid technique and finding a branching ratio of

$$H_3^+ + e^- \rightarrow \begin{cases} H + H + H & \rightarrow \quad 75\,\% \\ H_2 + H\,. & \rightarrow \quad 25\,\% \end{cases}, \tag{4.10}$$

that is constant up to 0.5 eV electron energy, while the two-body channel dominates for energies between 1 and 10 eV. A simple statistical model was introduced by Strasser *et al.* that agrees well with the experimental data [Str01b].

Dissociation dynamics, product states

At the TSR two different aspects of the DR dynamics of H_3^+ have been examined. First the vibrational excitation of the H_2 fragment in the two-body channel (results will be presented later in this work) and second the energy sharing between the fragments in the three-body breakup. The measurements were performed by the DR fragment imaging technique – revealing also information on the internal energy of the H_3^+ ion prior to dissociation, which will be discussed in detail in chapter 6.4. The three-body dynamics were analyzed using Dalitz plots [Dal53], that represent the three-dimensional momentum space without phase space contortions. A dominance of linear dissociation geometries was found, although a different measurement using the Coulomb explosion imaging technique (CEI) clearly demonstrated the triangular shape of the initial H_3^+ ion circulating in the ring (see Fig. 4.5 and [Str01a] for details). It should be noted that the experiment – as will be seen in chapter 7.4 – gave hints for significant rotational excitation of the H_3^+ ions, correspondingly the measurement is likely to reflect a mixture of many different dissociating states.
That uncertainty was avoided by a series of remarkable experiments carried out by Müller *et al.*. They succeeded to excite state-selectively H_3 Rydberg states by laser excitation and record their dissociation patterns. The various Dalitz plots they inferred for the three-body breakup show rich structures that depend critically on the rovibrational state that was chosen [Mül99b, Mül99a]. In addition they could show that the vibrational excitation of the H_2 fragment in the two-body channel is heavily influenced by the rotational state of the excited H_3 molecule

Isotopomers: DR of H_2D^+, D_2H^+ and D_3^+

All deuterated species of triatomic hydrogen have been subject to DR measurements of one kind or the other. At the CRYRING facility a systematic comparison of the thermal (300 K) rate coefficient of H_3^+ [Sun94], H_2D^+ [Lar96] and D_3^+ [LeP98] was initiated that revealed a clear isotope effect as it was found that: $\alpha(H_3^+) = 1.15 \times 10^{-7}\,\mathrm{cm^3\,s^{-1}}$,

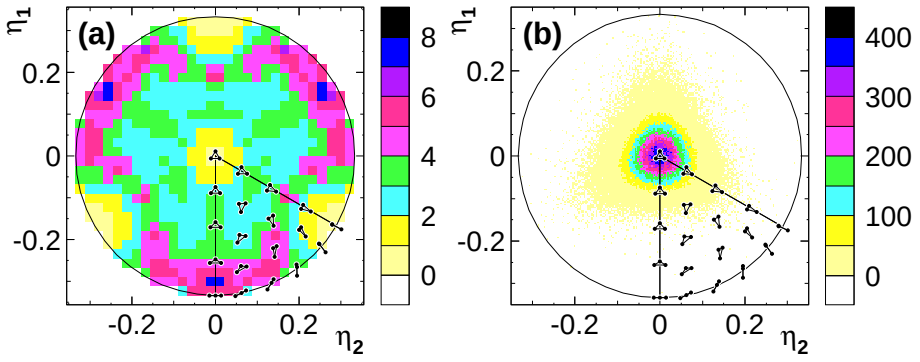

Figure 4.5: *(a) Intensity plot of the three-body dissociation geometry in Dalitz coordinates that are defined by* $\eta_1 = (2E_3 - E_2 - E_1)/3E_k$ *and* $\eta_2 = (E_2 - E_1)/\sqrt{3}E_k$*, where* E_1*,* E_2*,* E_3 *are the respective kinetic energies of the three fragments and* E_k *is the total kinetic energy. The small triangles represent the shape of the momentum triangle associated with the* η_1*,* η_2 *coordinates. The three-dimensional kinetic energies were reconstructed from a projected distance measurement (for details see [Str02]). (b) Coulomb explosion imaging measurement of the shape of vibrationally cold* H_3^+ *ions extracted from the TSR storage ring after vibrational relaxation (the CEI method and results for* H_3^+ *will be discussed in detail in chapter 6.5 and 7, see also [Kre02].) Picture taken from [Str01a].*

$\alpha(H_2D^+) = 6 \times 10^{-8}\,cm^3\,s^{-1}$ and $\alpha(D_3^+) = 2.7 \times 10^{-8}\,cm^3\,s^{-1}$. However, all of these measurements were performed using hot filament ion sources and in the light of the experiences made at the TSR in the last years and the new measurement at CRYRING with $\alpha(H_3^+) = 6.8 \times 10^{-8}\,cm^3$ [McC03], it seems likely that the older values are heavily influenced by rotational excitation. Several afterglow experiments with D_3^+ are reported (a review can be found in [Pla02]), the observed rate coefficient tends to be of the same order as the H_3^+ value determined with the same apparatus.

The branching ratio between two- and three-body breakup was also measured for the H_2D^+ case at CRYRING, the outcome showed that in 73 % of all dissociation events three fragments emerged, a result that resembles the observations for the H_3^+ case (75 % three-body).

A comparison of the dissociation geometries for all four isotopic variants of triatomic hydrogen (tritium-containing molecules not included) derived from DR imaging measurements at the TSR is about to be published [Str03].

4.3.2 Theoretical studies

The first theoretical treatments were carried out by Kulander and Guest [Kul79] and Michels and Hobbs [Mic84]. Both were still committed to the spirit of Bates' direct

recombination mechanism and thus were looking for low-energy curve crossings between the ionic ground state and repulsive neutral states. Since no favourable crossing was found, it was concluded that vibrationally relaxed H_3^+ should recombine extremely slow. Michels and Hobbs pointed out that for vibrationally excited ions with $v \geq 3$ the situation is altered by a neutral state crossing at about $\sim 1\,\mathrm{eV}$. They estimated that H_3^+ in these vibrationally excited states would recombine two orders of magnitude faster than the ground state.

The first successful description of H_3^+ DR was also performed for the direct mechanism but focused on energies above 1 eV. In that region doubly excited H_3 states exist that can be accessed by electronic couplings as seen in standard direct DR cases. The cross section measured in storage rings shows a prominent peak at high electron energies that is attributed to the opening of these channels. Orel and Kulander evaluated the strength of the electronic couplings and employed a wave packet method that gave reasonable agreement with the experiment at high energy [Ore93] but – as expected – could not explain high recombination rates at low energy.

In order to tackle the low-energy DR Schneider *et al.* [Sch00] chose a method that was stimulated by the successful modeling of the non-crossing DR in HeH^+ [Gub94]. They combined the MQDT approach of Guisti [Giu80] with a wave packet propagation method to estimate the influence of indirect DR via so-called "closed channels". The calculation was carried out in two dimensions only, and other severe approximations were used (autoionization was neglected), nevertheless it showed that the indirect mechanism prevails and in this two-dimensional estimate it raised the cross section by two orders of magnitude. Although a huge discrepancy between experiment and theory remained this step has to be considered an important interim success.

A major progress was made when Kokoouline *et al.* introduced Jahn-Teller couplings into the treatment and at the same time performed the first full dimensional calculation in hyperspherical coordinates [Kok01]. Although H_3^+ was known to be a model system of the symmetry-distorting Jahn-Teller effect since a long time [Por68], its relevance to enhance the electron recombination had not been realized. In a first publication an upper bound of $\alpha \leq 1.2 \times 10^{-8}\,\mathrm{cm^3\,s^{-1}}$ was derived (lower bound $3.4 \times 10^{-10}\,\mathrm{cm^3\,s^{-1}}$), representing for the first time a theoretical description that advanced close to the range that was covered by most modern experiments. In addition the preference of the three-body channel was correctly predicted as well as the broad vibrational distribution of the H_2 molecules in the two-body breakup (presented in chapter 7.4).

Very recently, the calculation has been revised and a missing factor of π^2 was corrected that catapulted upper and lower bound one order of magnitude upwards [Kok03]. In

fact, the latest prediction of $\alpha(300\,\mathrm{K}) = 7.2 \times 10^{-8}\,\mathrm{cm}^3\,\mathrm{s}^{-1}$ does exceed (slightly) for the first time the latest storage ring result of $6.8 \times 10^{-8}\,\mathrm{cm}^3\,\mathrm{s}^{-1}$ [McC03]. At this point the evidence seems overwhelming that the true mechanism of H_3^+ dissociative recombination is finally found.

Chapter 5
Symmetry and selection rules

The point group symmetry of an equilateral triangle is called C_{3v}, the group comprises three classes of symmetry operations, the first class consists of the trivial unity operation (E) alone, the second class contains two rotations of 120° (C_3) and 240° (C_3^2), respectively, the third class is formed by three reflections (σ_1, σ_2 , σ_2). The effects of these six operations are illustrated in Fig. 5.1.

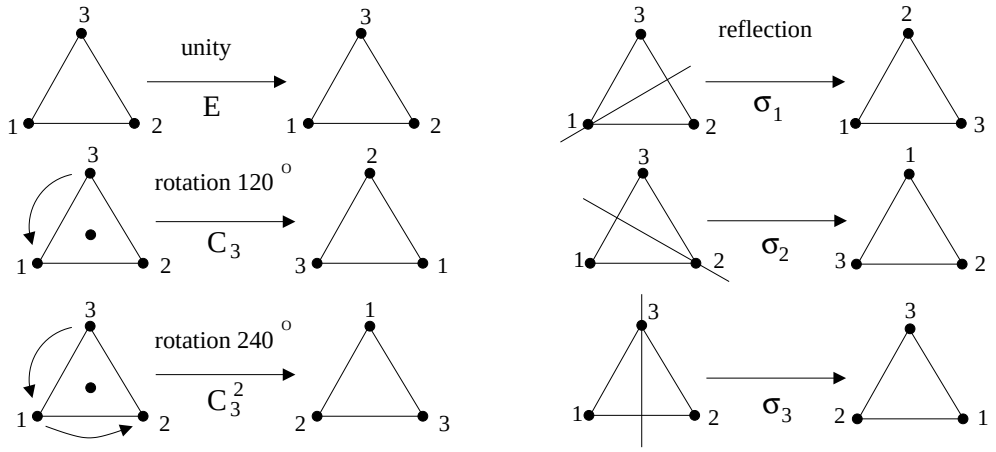

Figure 5.1: *The symmetry operations of the C_{3v} group*

The C_{3v} group is restricted to two dimensions and therefore it cannot account for the full symmetry of the three-dimensional molecule, but it is sufficient for an educative treatment of vibrational modes, since the three protons are always found in one plane.

5.1 Vibrational modes

To describe the positions of the three protons in space, $3N = 9$ nuclear coordinates are needed. Three of them can be chosen to define the center of mass of the molecule and

three more coordinates describe the rotation of the molecular frame of reference with respect to a space-fixed coordinate system. The remaining three coordinates are connected with the three internal degrees of freedom of a triatomic molecule. The choice of these coordinates is arbitrary, but the vibrational modes are best described in normal coordinates which diagonalize the Hamilton operator and thus decouple the vibrations. The normal

C_{3v}	E	$2C_3$	$3\sigma_v$
A_1	1	1	1
A_2	1	1	-1
E	2	-1	0

C_{3v}	A_1	A_2	E
A_1	A_1	A_2	E
A_2		A_1	E
E			$A_1 + A_2 + E$

Table 5.1: *Character and multiplication table of the C_{3v} point group.*

coordinates are linear combinations of the three internuclear distances and they transform according to one of the irreducible representations of the C_{3v} symmetry group. The number of irreducible representations is equal to the number of classes of the group, for C_{3v} one finds two one-dimensional representations of A_1 and A_2 symmetry, respectively, and a two-dimensional representation of E symmetry. The characters are given in Table 5.1, the dimension of the respective representations are equal to the character of the unity operation E of that representation. In a more thorough analysis [Inu98, Kre00] one can show, that the first normal mode connected with vibrational motion is of A_1 symmetry and is formed by the sum of the three internuclear distances (and a normalization factor)

$$s_a = \frac{1}{\sqrt{3}}(r_{12} + r_{23} + r_{31}). \tag{5.1}$$

The other two vibrational modes are degenerate and both transform according to the two-dimensional E representation

$$s_x = \frac{1}{\sqrt{6}}(2r_{12} - r_{23} - r_{31}), \tag{5.2}$$

$$s_y = \frac{1}{\sqrt{2}}(r_{23} - r_{31}) \ . \tag{5.3}$$

By varying one of the coordinates and keeping the other two fixed, one can create illustrative pictures of the geometry of the vibrational motion that is connected with a change in this coordinate. The three normal mode oscillations are shown in Fig. 5.2. The s_a mode is a symmetric stretch of the whole molecule that leaves the triangular shape undisturbed. Throughout this motion the center of positive charge and the center of negative charge coincide, and thus no dipole moment is formed. This mode is commonly referred to as "breathing mode". The other two oscillations deform the equilateral shape

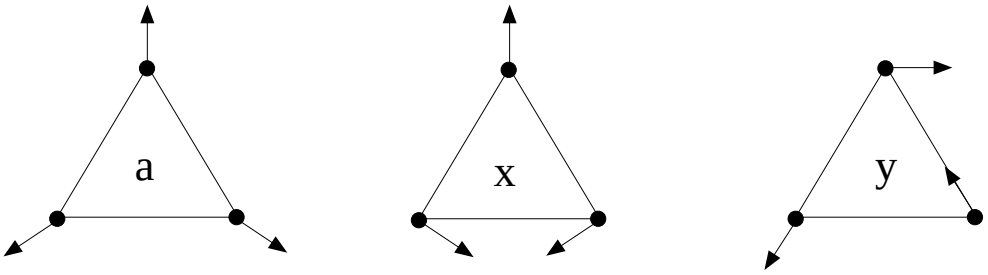

Figure 5.2: *The normal modes of* H_3^+.

of the triangle and give rise to the temporary formation of a dipole moment. Therefore these two degenerate "bending modes" s_x and s_y are infrared-active, while the breathing mode s_a is not.

The breathing mode quantum number (and sometimes also the mode itself) is conventionally labeled ν_1. Since the s_x and s_y modes are degenerate, they are practically indistinguishable (as long as the harmonic approximation is valid) because their frequencies are the same by definition. For degenerate modes one may consider any superposition of arbitrary phase, in Fig. 5.3 two combinations with s_y out of phase by +90° ($\nu+$) and -90° ($\nu-$) are shown.

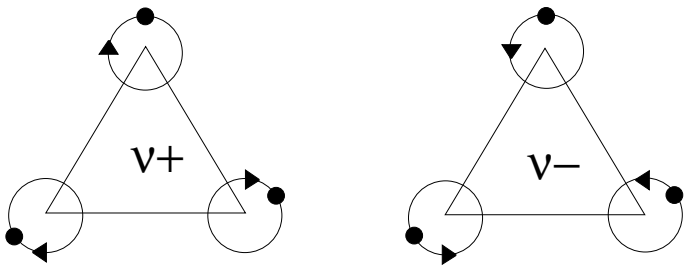

Figure 5.3: *Vibrational angular momentum.*

Obviously the circular motion of the nuclei around their equilibrium position carries angular momentum, therefore the bending mode excitation is usually labeled ν_2^l, where ν_2 counts the number of quanta (the energy), while l stands for the vibrational angular momentum (l ranges from $-\nu_2$ to $+\nu_2$ in steps of two). Consequently H_3^+ vibrational states are characterized by three quantum numbers $(\nu_1, {\nu_2}^l)$, e.g. $(0, 0^0)$ defines the vibrational ground state, $(1, 0^0)$ the first breathing mode, etc.

5.2 Rotationless decay

Dipole transitions between vibrational states are governed by selection rules that arise from molecular symmetries. As mentioned before the states with A_1 symmetry like the ground state for example have no dipole moment, therefore pure breathing transitions are dipole forbidden. States with E symmetry do have a dipole and therefore $E \leftrightarrow E$ transitions as well as $A \leftrightarrow E$ transitions are allowed [Ten95a].

In a harmonic picture also transitions with ν_2 and l quantum numbers changing by more than one would be forbidden. But since H_3^+ is a rather anharmonic molecule these transitions do occur, although there is a preference for transitions with Δl being small [Ten95a]. In Fig. 5.4 the H_3^+ vibrational level scheme is plotted together with inverse Einstein A coefficients for the most efficient decay routes from a rotationless approach by Dinelli *et al.* [Din92]. In this calculation wave functions for $J = 0$ were combined with the dipole surface to achieve vibrational band intensities, which are constant for a particular vibrational

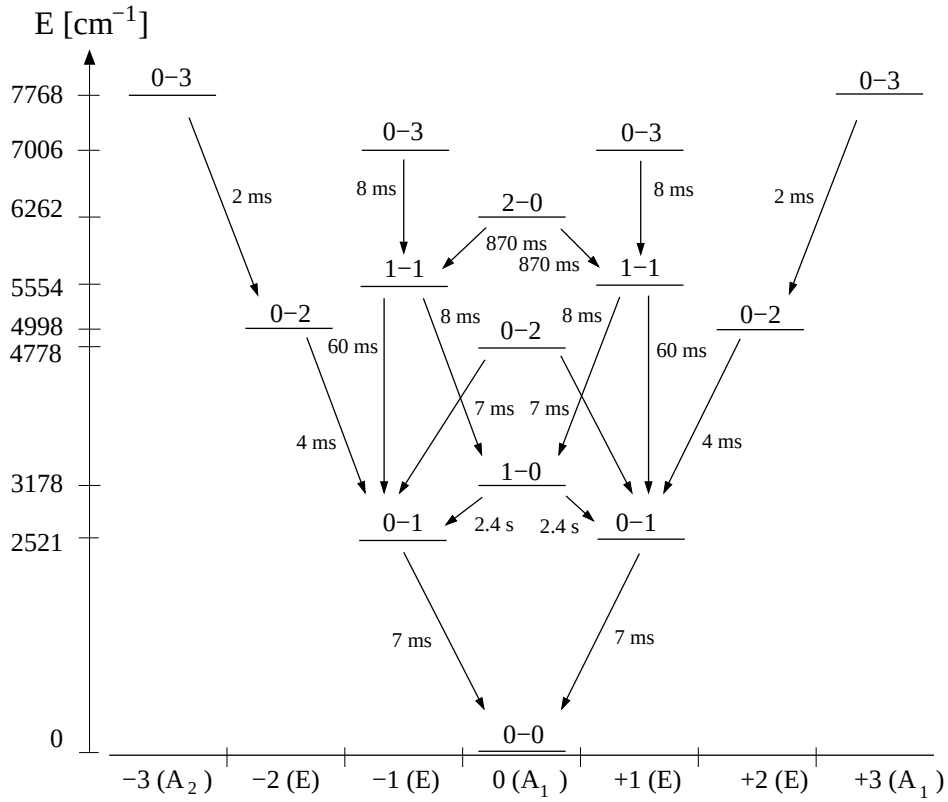

Figure 5.4: *H_3^+ vibrational levels and their decay constants for rotationless transitions (J=0) as calculated from Einstein coefficients of [Din92]. Level scheme adapted from [Ten95a]. On the abscissa the value and sign of l are given, followed by the symmetry label of the state. The levels themselves are tagged with $\nu_1 - \nu_2$ quantum numbers.*

transition. Based on this constant, rovibrational transition probabilities can be approximated by calculating the so-called Hönl-London factor [Her50]. In a harmonic picture the vibrational band intensities can be determined from the derivative of the dipole moment at equilibrium [Wil80], but in modern methods – often employing internal coordinates – the choice of the axes of the dipole surface is crucial, and Le Sueuer *et al.* could show that the rules for axes definition proposed by Eckart yield good separation between rotational and vibrational motion [LeS92]. For the moment the Einstein coefficients derived by this method will be interpreted as average decay constants of vibrational states for the limit J→0.

The most long-lived states in the diagram are the two pure breathing excitations $(1,0^0)$ and $(2,0^0)$ with lifetimes of 1.2 s and 0.4 s respectively. Based on these calculations most storage ring measurements of the dissociative recombination of H_3^+ were made after several seconds of storage to allow for vibrational cooling to the ground state.

5.3 Rovibrational selection rules for dipole transitions

To appoint selection rules between internal states of a molecule, one has to find good quantum numbers. Two rigorously good quantum numbers for any molecule are parity $P = \pm$ and the total angular momentum F. These quantum numbers arise from the invariance of the Hamiltonian under rotation and inversion in space. For any dipole transition the following rules hold [May97]

$$\triangle F = 0, \pm 1 \qquad (F = 0 \not\leftrightarrow F = 0)\,, \tag{5.4}$$

$$\triangle P \neq 0 \qquad (\pm \longleftrightarrow \mp)\,. \tag{5.5}$$

The total angular momentum is the sum of the motional angular momentum J and the nuclear spin angular momentum I ($F = J+I$), the coupling between both is the hyperfine interaction which in the case of H_3^+ is very small in the equilibrium region [McN95]. Therefore to a good approximation one can separate F into J and I and expand the dipole transition rules to

$$\triangle I = 0\,, \tag{5.6}$$

$$\triangle J = 0, \pm 1 \qquad (J = 0 \not\leftrightarrow J = 0)\,. \tag{5.7}$$

The three spin-$\frac{1}{2}$ components of the protons can couple to a total spin of $I = \frac{1}{2}$ (para-H_3^+) or $I = \frac{3}{2}$ (ortho-H_3^+), the selection rule $\triangle I = 0$ therefore rules out spin-conversion between the two species.

Further selection rules arise from the symmetry of the H_3^+ molecule. To tackle the problem of rotation-vibrational transitions one has consider the *complete nuclear permutation inversion group* (CNPI) S_3^* of the molecule [Bun98] which will be introduced in the following paragraph.

5.3.1 The complete nuclear permutation inversion group S_3^*

In the last section the C_{3v} group was used to describe the symmetry labels of the H_3^+ vibrational states. This group consists of 3 classes of geometrical operations depicted in Fig. 5.1. The same classification can be made by replacing the C_{3v} elements by permutations of the three protons. The reflections σ_1, σ_2 and σ_3 can be replaced by the proton interchanges (23), (13) and (12). Analogously the rotations C_3 and C_3^2 have the same effect as a cyclic permutation of the three protons (132) and (123), respectively.

The proton interchanges and permutations (together with the unity operation E, which is unaffected) form a symmetry group like the geometrical operations of C_{3v}. The new group is called S_3=$\{E$,(123),(132),(12),(23),(31)$\}$ and it has the same character table and the same multiplication table as C_{3v} (Tab. 5.1), revealing that both groups are isomorphous. S_3 is called the *complete nuclear permutation group* (CNP) [Bun98].

In addition one has to take into account the inversion operation E^*. The center of inversion is defined as the center of mass of the molecule and thus the application of the E^* operation inverts the spatial coordinates of a given nucleus or electron

$$E^*(x_i, y_i, z_i) = (-x_i, -y_i, -z_i). \tag{5.8}$$

Together with the unity operation E^* forms the inversion group $\mathsf{E} = \{E, E^*\}$. Both elements of this group commute with any possible permutation operation. The CNPI group of a molecule is the direct product of the CNP group with E. In the case of H_3^+ we obtain

$$\begin{aligned} S_3^* &= S_3 \otimes \mathsf{E} && (5.9)\\ &= \{E, (123), (132), (12), (23), (31), E^*, (123)^*, (132)^*, (12)^*, (23)^*, (31)^*\}. && (5.10) \end{aligned}$$

Since the elements of the two product groups commute, one can derive the character table of the new CNPI group S_3^* by simply multiplying the respective characters of the product tables (see Tab. 5.2).

Similarly the multiplication table of S_3^* is constructed (Tab. 5.3) by applying the rules

S_3	E	2(123)	3(12)
A_1	1	1	1
A_2	1	1	-1
E	2	-1	0

$\otimes$

E	E	E^*
A'	1	1
A''	1	-1

$=$

S_3^*	E	2(123)	3(12)	E^*	2(123)*	3(12)*
A_1'	1	1	1	1	1	1
A_1''	1	1	1	-1	-1	-1
A_2'	1	1	-1	1	1	-1
A_2''	1	1	-1	-1	-1	1
E'	2	-1	0	2	-1	0
E''	2	-1	0	-2	1	0

Table 5.2: *Character table of the S_3^* group.*

for multiplication of representations with $'$ and $''$ [Wag98]

$$' \times ' = ' \qquad '' \times '' = '$$
$$' \times '' = '' \qquad '' \times ' = ''$$

to the multiplication table of S_3 (or C_{3v}, see Tab. 5.1).
With the help of these tools, restrictions on the quantum numbers of the H_3^+ wave function can be formulated, and approximate selection rules are derived.

S_3^*	A_1'	A_2'	E'	A_1''	A_2''	E'
A_1'	A_1'	A_2'	E'	A_1''	A_2''	E''
A_2'		A_1'	E'	A_2''	A_1''	E''
E'			$A_1' + A_2' + E'$	E''	E''	$A_1'' + A_2'' + E''$
A_1''				A_1'	A_2'	E'
A_3''					A_1'	E'
E''						$A_1' + A_2' + E'$

Table 5.3: *Multiplication table of the S_3^* group.*

5.3.2 The approximation of separable wave functions

The following considerations will be based on the assumption that the total wave function can be separated into four components

$$\Phi_{total} = \Phi_{el} \;\; \Phi_v \; \Phi_r \; \Phi_{ns} \; , \tag{5.11}$$

with Φ_{el} being the electronic part of the wave function, Φ_v and Φ_r describing the nuclear motion (vibrational and rotational, respectively) and Φ_{ns} representing the nuclear spin wave function. The decoupling of Φ_{ns} relies on the weakness of the hyperfine interaction (as discussed above) and spin-spin interactions. The separation of the electronic wave function from the nuclear motion is the basis of the Born-Oppenheimer approximation [Bor27, Bor51]. Furthermore to examine the effects of the S_3^* operations on the wave function, one divides the nuclear motion term into vibrational Φ_v and rotational Φ_r wave functions. To achieve approximate selection rules one assumes the following quantum numbers to be good:

- ν_1, ν_2 and l, the three vibrational quantum numbers,
- J, the total motional angular momentum,
- K, the projection of J onto the normal vector of the molecular plane.

Using these quantum numbers the rovibrational wave function can be written $|\nu_1, \nu_2, l\rangle|J, K\rangle$. The effects of the operations of the S_3^* permutation group on this wave function have been investigated by Watson [Wat84]. He finds three characteristic equations

$$(123)|\nu_1, \nu_2, l\rangle|J, K\rangle| \;=\; e^{2\pi i(K-l)/3}|\nu_1, \nu_2, l\rangle|J, K\rangle \, , \tag{5.12}$$

$$E^*|\nu_1, \nu_2, l\rangle|J, K\rangle \;=\; (-1)^K|\nu_1, \nu_2, l\rangle|J, K\rangle \, , \tag{5.13}$$

$$(23)|\nu_1, \nu_2, l\rangle|J, K\rangle \;=\; (-1)^J|\nu_1, \nu_2, -l\rangle|J, -K\rangle \; . \tag{5.14}$$

Dipole transitions are described by the electric dipole moment operator μ which is unaffected by the exchange of identical particles. Using Eq. 5.12 and $|\nu_1, \nu_2, l\rangle = |\Phi_v\rangle$ one can show

$$\langle\Phi_v|\langle J, K|\mu|J', K'\rangle|\Phi_v'\rangle \;=\; \langle\Phi_v|\langle J, K|(123)^{-1}(123)\mu(123)^{-1}(123)|J', K'\rangle|\Phi_v'\rangle \, , \tag{5.15}$$

$$=\; \langle\Phi_v|\langle J, K|e^{-2\pi i(K-l)/3} \; \mu \; e^{2\pi i(K-l)/3}|J', K'\rangle|\Phi_v'\rangle \, , \tag{5.16}$$

$$=\; \langle\Phi_v|\langle J, K| \; \mu \; |J', K'\rangle|\Phi_v'\rangle \; e^{2\pi i(K-K'+l-l')/3} \, , \tag{5.17}$$

$$\Longrightarrow \qquad 1 \;=\; e^{2\pi i(K-K'+l-l')/3} \, . \tag{5.18}$$

This equation defines the selection rule $\triangle(K-l) = 3n$ (n being integral). To account for this relation a new quantum number is introduced $G = (K-l)$, and the selection rule is simplified $\triangle G = 3n$. In fact this selection rule also implies the conservation of nuclear spin ($\triangle I = 0$), since there is a connection between the quantum number G and nuclear spin [McC01, Wat84]:

$$\text{ortho-}H_3^+ \iff G = 0 \; mod \; 3\,, \tag{5.19}$$

$$\text{para-}H_3^+ \iff G \neq 0 \; mod \; 3\,. \tag{5.20}$$

The second property (Eq. 5.13) is a restatement of the requirement of parity change in dipole transitions $\triangle K = \text{odd}$, the parity is given by $(-1)^K$ [McN95].
The last operation (Eq. 5.14) is also less "informative" than the first one (see Watson: "An introduction to the spectroscopy of H_3^+"[Wat00]), but an extended version can be used to symmetrize the approximate wave functions with respect to (23).
Finally, the following approximate selection rules for dipole transitions can be summarized

- $\triangle K = 2n+1$,
- $\triangle J = 0, \pm 1; \quad J = 0 \not\leftrightarrow J = 0$,
- $\triangle G = 3n$, $\triangle I = 0$.

Another interesting outcome of the separation of the wave function is the forbidden rovibrational ground state of H_3^+ (with $\nu_1 = \nu_2 = J = 0$). Since H_3^+ is a fermionic system, the Pauli principle implies that the total wave function changes sign under the interchange of two protons, whereas it is left unchanged under a cyclic permutation (because a cyclic permutation is effectively the same as the product of two subsequent proton interchanges). In Tab. 5.2 one finds that the total wave function has to be of A_2' or A_2'' symmetry. For bosonic systems (like D_3^+) the wave function is supposed to be unchanged under both types of operations, and therefore A_1' and A_1'' apply.
The H_3^+ ground state electronic wave function Φ_{el} belongs to the totally symmetric A_1' representation [Sch74], and the rovibrational ground state $\Phi_{rv}^0 \equiv \Phi_r^0 \; \Phi_v^0$ has the same symmetry. From the multiplication table of S_3^* (Tab. 5.3) it can be seen that the direct product of two A_1' representations will again be of A_1' symmetry. If the nuclear spin of the three protons is aligned to $\frac{3}{2}$ then Φ_{ns}^0 is also unaffected by any interchange of nuclei and thus has A_1' symmetry. For the para-state of H_3^+ with nuclear spin $\frac{1}{2}$ the E' representation is valid. Correspondingly, the symmetry of a rovibronic (rotational-vibrational-electronic) ground state with ortho nuclear spin configuration would be

$$\Gamma(\Phi_{el}^0) \otimes \Gamma(\Phi_{rv}^0) \otimes \Gamma(\Phi_{ns-ortho}^0) = A_1' \otimes A_1' \otimes A_1' = A_1'. \tag{5.21}$$

which is forbidden by the Pauli principle, whereas the para-configuration is ruled out by the intrinsic relation between the G quantum number – which is zero for the $(J = K = l = 0)$ rovibrational ground state – and nuclear spin (Eq. 5.19, 5.20). As a consequence the state $(\nu_1 = \nu_2 = J = 0)$ that one would naively refer to as the energetically lowest H_3^+ state, does not exist in reality. Thus in addition to the vibrational zero point energy that lifts the ground state 4363 cm^{-1} [Jaq98] above the minimum of the potential surface, another 64 cm^{-1} [Pol99] have to be added, attributed to "rotational zero point energy".

In a more precise treatment of the interplay between nuclear spin and molecular symmetry, the nuclear spin statistical weight of the six representations of the rovibrational wave functions can be derived [Wat84] for both fermionic (e.g. H_3^+) and bosonic (e.g. D_3^+) systems.

$\Gamma_{el,rv}$	Bosons (general)	$I = 1$ (D_3^+)	Fermions (general)	$I = \frac{1}{2}$ (H_3^+)
A_1', A_1''	N_1	10	N_2	0
A_2', A_2''	N_2	1	N_1	4
E', E''	N_3	8	N_3	2

$$N_1 = (2I+1)(2I+2)(2I+3)/6$$
$$N_2 = (2I+1)(2I)(2I-1)/6$$
$$N_3 = (2I)(2I+1)(2I+2)/3$$

Table 5.4: *Nuclear spin statistical weights of rovibronic levels (according to [Wat84])*

From Table 5.4 it becomes clear that the forbidden rovibrational ground state of H_3^+ is only a special case of a more general rule, namely that all rovibronic states with A_1' and A_1'' symmetry have zero statistical weight. It was noted before that the para-H_3^+ states are of E symmetry, and from the table it can be seen that they are fourfold degenerate, while the states with A_2 symmetries correspond to doubly degenerate ortho-H_3^+.

The selection rules and assignments given above are important for understanding the rovibrational levels and the spectroscopy of H_3^+, but they do not necessarily have to be implemented in state-of-the-art calculations. As pointed out before, the most successful method to achieve rovibrational transition energies and probabilities, is the variational approach of Sutcliffe and Tennyson [Sut87], where all rovibrational levels and wave functions are calculated variationally. The quantum numbers for these levels are assigned

afterwards, if possible, because for higher energies many assignments are not unambigous [Nea96]. In addition, theoretical tables of H_3^+ energy levels often contain non-existing states like the forbidden ground state ($J = 0,\ v = 0$) and to calculate transitions between the states, only the rigorous dipole selection rules ($\Delta J = 0,\ \pm 1$) are taken into account, since all other selection rules based on molecular symmetry are valid only within certain approximations.

The most comprehensive linelist for H_3^+ was calculated by Neale *et al.*, it consists of about ~ 3 million transitions, and it will be used in chapter 8 to create a detailed model of the rovibrational decay of H_3^+.

Part II

Storage Ring Experiments

Chapter 6
Storage ring techniques for molecular physics experiments

6.1 General aspects

The development of heavy-ion storage rings for atomic physics started in the eighties and the first ring that became operational was the Test Storage Ring (TSR) at the Max-Planck-Institut für Kernphysik in Heidelberg in 1988 [Jae88]. The TSR has a circumference of 55.4 m and a magnetic rigidity of 1.6 Tm. Two years later the first experiment at the Test Accumulation Ring for the Numatron Accelerator Facility (TARN II, 78 m, 6.1 Tm) of the University of Tokyo, Japan was performed and in 1991 the Aarhus Storage Ring Denmark (ASTRID, 40 m , 1.6 Tm) in Aarhus, Denmark and the Experimental Storage Ring (ESR, 108 m, 10 Tm) at Darmstadt, Germany followed. In 1992 the Cryogenic Ion source ring (CRYRING, 51.6 m, 1.4 Tm) at Stockholm, Sweden completed the field (ion storage rings with a small component in atomic physics were not considered in this list). A common feature to all of the above mentioned devices is the use of an electron cooler to improve the quality of the ion beam.

The focus during the design of most of the storage rings was upon research with highly charged ions and the creation of high-quality (crystalline) ion beams. Molecular physics, which appeared as a minor field of use for these machines at first, started in 1993, when measurements with molecular ions were published nearly simultaneously by groups from three different storage rings (TARN II [Tan93], TSR [For93], CRYRING [Lar93]). Today there are three magnetic cooler rings active in molecular physics: ASTRID, CRYRING and TSR (TARN II has been shut down).

Before the special benefit of storage rings for experiments with molecular ions are discussed, the general advantages of the storage ring technique are summarized:

- *Effective increase of the ion current.* In many single-pass experiments where processes with small cross sections are examined, only a negligible fraction of the ion current is used, while the unaffected part of the beam is dumped somewhere in the vacuum system. In an ion storage ring, the particles that are passing the interaction region unaffected will just be recirculated and come back for the next pass every few microseconds. This "recycling" of the ion beam can improve the efficiency of using a given number of ions enormously.

- *Simple detection schemes.* One of the advantages that all experiments with fast beams have in common is the applicability of relatively simple detection schemes. For example in an experiment of radiative recombination of atomic ions, where the initial ion A^{i+} captures an electron $A^{i+} + e^- \rightarrow A^{(i-1)+} + h\nu$, the trajectory of the new product ion $A^{(i-1)+}$ in a storage ring will differ only slightly from the beam trajectory (since the reaction energy is much smaller than the beam energy) and an appropriately positioned detector will easily record all recombination events without having to cover the whole 4π solid angle.

- *Long lifetime of the ion beam.* The lifetime of an ion beam in a storage ring (that means the time by which the beam current is reduced by a factor $1/e$) like the TSR can range from 2.5 days for protons down to a few seconds for singly charged slow molecules. In that time the decay of excited states that were produced in the ion source can be observed, states can be pumped by laser transitions and cooling procedures can be applied.

- *Electron cooling.* Modern electron coolers produce ion beams with very low divergence, energy spread and diameter, and in addition the electrons may serve as a target for recombination or detachment experiments. As a consequence of the kinematic compression (see section 6.4.1) collision energies between the electrons and the ion beam in the frame of reference of the ions can be adjusted with millielectronvolt precision, allowing experiments with a resolution that is superior to most other techniques.

For molecular physics there is an additional benefit from the long lifetimes of the stored beam. Since the level spacing between molecular vibrations and rotations is small compared to electronic excitations, and the production of molecular ions in standard sources involves the ionization of a target gas, it necessarily goes hand in hand with an excitation of internal degrees of freedom of the molecular ion. To carry out a meaningful experiment it is often desired to prepare the ion beam at least in the ground vibrational

state, because many elementary processes are known to depend critically on vibrational excitations. Therefore complicated sources and measurements were set up and often a substantial part of a typical molecular beam experiment consists of the preparation of an internally cold ion beam. For infrared active molecules the radiative lifetimes of vibrational states are usually of the order of milliseconds, and thus after storage of several seconds in a storage ring all the vibrations have vanished and a vibrationally cold ion beam can be prepared without further efforts. On the other hand, at short storage times also excited states are present and the time evolution of their population can be followed by appropriate experimental techniques.

6.2 Basic operation

A heavy ion storage ring consists of a magnetic structure with dipole sections where the ion beam is bent, straight sections where quadrupole and sextupole magnets are situated to focus the beam and keep it inside the acceptance, and an ultrahigh vacuum system ($\approx 10^{-11}$ mbar) that is crucial to minimize interactions between the ion beam and residual gas which limit the storage time. Fig. 6.1 shows an outline of the TSR storage ring together with the Coulomb explosion imaging beamline.
To bend a charged particle on a curvature ρ in a dipole field, the centrifugal force mv^2/ρ has to be equal to the Lorentz force given by qBv, where B denotes the strength of the magnetic field and q the charge of the particle. Solving this equation for the parameters which are associated to storage ring properties gives

$$B\rho = \frac{mv}{q}\,. \tag{6.1}$$

The product of B and ρ is called the ring rigidity and the maximum rigidity is one of the characteristic properties of an ion storage ring. The maximum values of $B\rho$ for the rings that are involved in molecular physics are typically around 1.5 Tm. Clearly, there is no principle q/m limit for magnetic rings because every particle can be brought around a given curvature if only the velocity is chosen low enough. In practice the loss processes that dominate the lifetime of the ion beam become stronger with decreasing energy (in the energy range relevant here) and thus practical limits are imposed on the charge to mass ratio.
The TSR has a maximum rigidity of 1.6 Tm and since molecules are normally singly charged the maximum velocity that the ring can hold for a molecule of mass number A is

$$v_{max} = \frac{qB\rho}{m} = \frac{e \cdot 1.6\,\mathrm{Tm}}{u}\frac{1}{A} \approx 0.5\,c\,\frac{1}{A}\,. \tag{6.2}$$

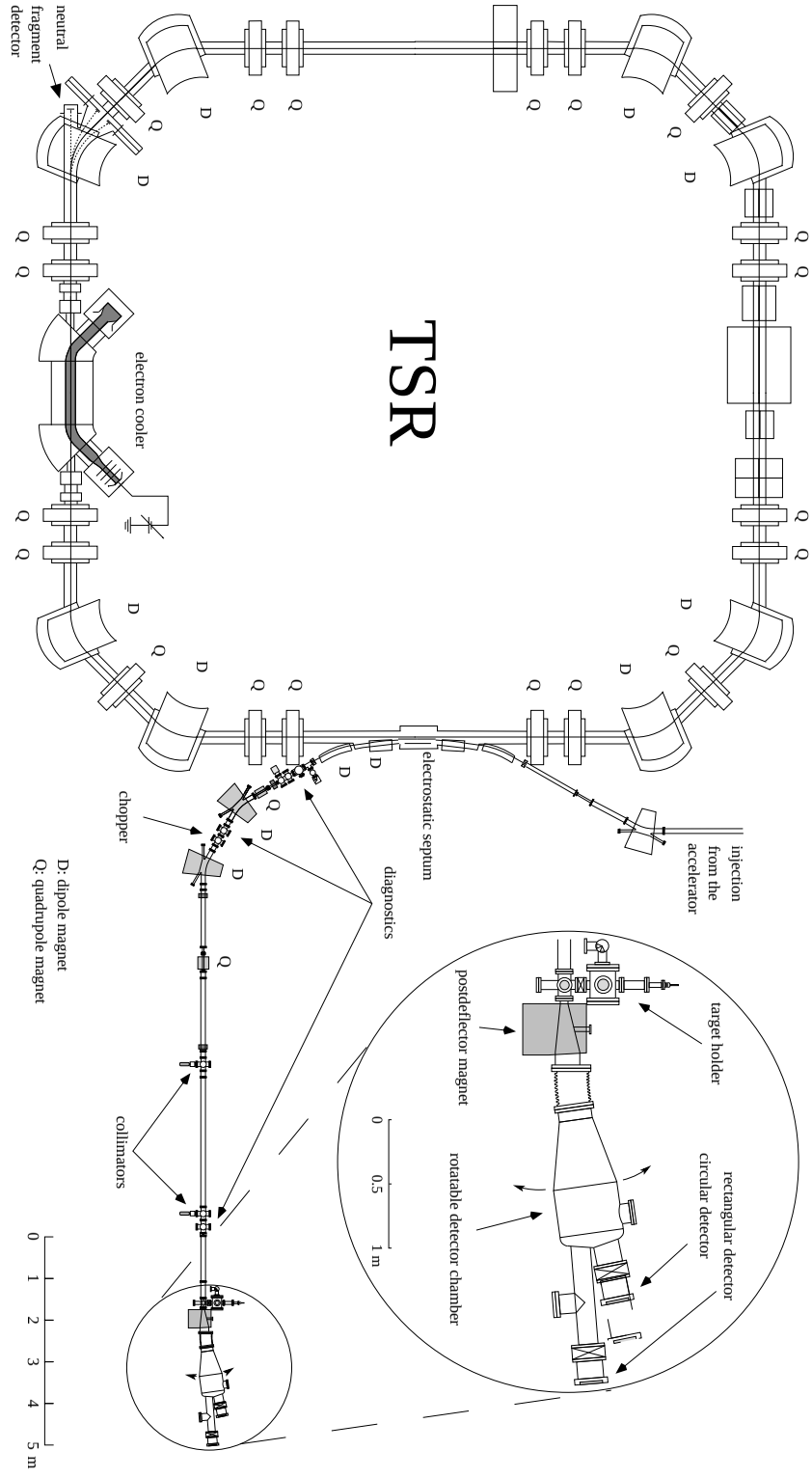

Figure 6.1: *Drawing of the TSR storage ring with the Coulomb explosion imaging (CEI) beamline. The magnified region shows the CEI target chamber, the separation magnet and the two imaging detectors.*

Coulomb explosion imaging experiments for example require energies above 70 keV/u to strip off the binding electrons (see section 6.5) and therefore the ring rigidity limits the upper mass for CEI experiments to about $A = 40$ corresponding to a total kinetic energy of 2.8 MeV. For other experiments less severe restrictions may apply, but the low charge state of molecular ions is a common limitation for both acceleration and storage. The ion current I_{ion} in the storage ring can be expressed in terms of the number of ions N_{ion} with charge q multiplied by the revolution frequency f

$$I_{ion} = N_{ion}\ q\ f. \tag{6.3}$$

For example, in a typical H_3^+ experiment at the TSR with a beam energy of 1.5 MeV and thus a revolution frequency of 177 kHz, an ion current of 1 μA would result in $3.5{\times}10^7$ stored molecules.

The ion beam is injected into the ring by fast ramped magnets and in a filling procedure where the number of particles that can be transferred to the ring corresponds to a cut-out of the ion beam over several lengths of the ring circumference (multiturn injection). Thus the phase space volume of the ring is filled efficiently using stacking methods. At the TSR it has been shown, that the current in the ring can be increased by a factor of 30 by using this multi-turn injection scheme [Bis90].

6.3 Molecular ion beam production

At the Max-Planck-Institut für Kernphysik three different accelerators are used to produce molecular ion beams. Two of them are utilizing the Van De Graaff principle, where a high voltage platform is charged to several million Volt by a rotating pelletron chain. One of them, the so-called MP-Tandem needs a negative precursor ion that is fragmented at the high voltage platform. While a multitude of positive molecular ions have been produced successfully in this mode of operation (e.g. CH^+, OH^+, CH_2^+, $C_2H_2^+$ NH_2^+, DCO^+, D_2CO^+, LiH^+), it is clearly not well suited for triatomic hydrogen. The first H_3^+ beamtime [Kno97] at the TSR was carried out with a single-ended Van De Graaff accelerator that can go up to 3 MeV in energy. In this apparatus the ion source is enclosed in the isolation gas filled steel tank of the accelerator and thus not easily accessible.

Since 1999 most of the molecular ion beams are delivered by the new High Current Injector (Hoch-Strom-Injektor, HSI) [vHa98]. The first stage of the HSI consists of two Radio-frequency Quadrupole (RFQ) benches (see Fig. 6.2) that bunch, focus and accelerate an incoming DC beam. By using the two RFQs alone a fixed energy of 500 keV/u (≈ 0.03 c) is achieved. The quality that makes these structures predestined for high currents is the

fact that the quadrupole fields focus the ion beam all the way through the accelerator and thus the tendency of strong slow beams to blow up due to intra-beam repulsion can be compensated. For flexibility the second stage is composed of a variable system of seven gap resonators with a maximum end energy of 1.8 MeV/u ($\approx$ 0.057 c). From the HSI the ion beam is directed through the MPI post accelerator to the storage ring. In the post accelerator the energy can be boosted further if necessary, which is only rarely the case for molecular beams. The drawback of the HSI is a limitation on the q/m value of 1/9, which effectively restricts its use for singly charged molecules to mass 9 or lighter; nevertheless since the research at the TSR in recent years has been focused on a detailed understanding of small molecules, the HSI has become the working horse for nearly all the beamtimes with positive (H_2^+, HD^+, D_2^+, H_3^+, H_2D^+, D_2H^+, D_3^+, HeH^+, He_2^+) molecular ions. Furthermore the HSI was recently used to produce a LiH_2^- beam, for the first negative ion experiment at the TSR.

The standard ion source used at the HSI is a hot filament source called CHORDIS [Kel89] (for Cold or HOt Reflex Discharge Ion Source). It can be mounted to either of the two source ports that are connected to a 60° mass analyzing magnet. The initial degree of internal excitation that molecular ions possess upon injection into the ring is determined by the conditions in the ion source, thus if one wants to start with a cold molecular ion beam, one has to connect a cold ion source to one of the two ports (the development of a new type of storage ion source is described in the third part of this thesis).

In the next sections the experimental techniques that are employed for molecular beamtimes at the TSR are introduced.

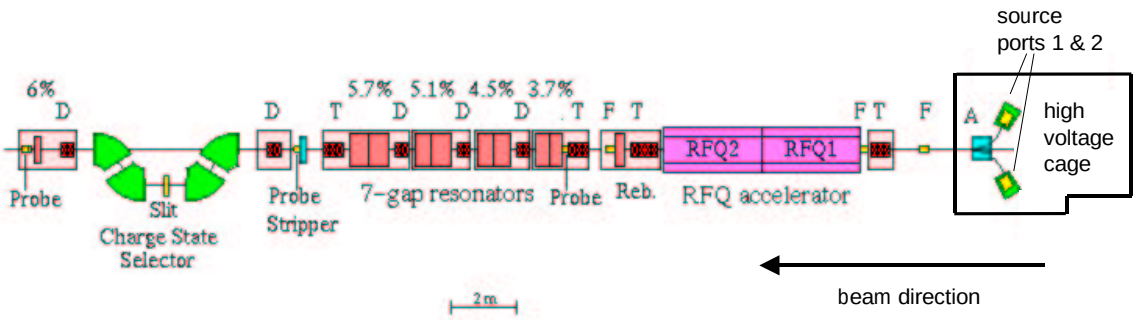

Figure 6.2: *Sketch of the HSI High Current Injector with the two RFQ structures and the variable seven gap arrangement. The ion velocity is given in percentage of the speed of light at various points.*

6.4 Dissociative recombination measurements

Dissociative recombination in storage ring experiments takes place inside the electron cooler (see Fig. 6.3), where a cold electron beam and the stored ion beam are merged. Since the products of recombination events are neutral, they pass the next dipole magnet and can easily be collected by appropriate detector systems.

6.4.1 Electron-ion merged beams

The central device of the TSR storage ring is the electron cooler, where a cold electron beam is used as a coolant for the ion beam or alternatively as a precision target for collision experiments. The electron cooler is located in the middle of one of the straight sections of the TSR (see Figures 6.1 and 6.3). The interaction region where the ion beam and the electron beam are superimposed has a length of 1.5 m. A thermal cathode that is located in one of the arms of the cooler produces the electrons which are accelerated by a set of electrodes and guided on spiral trajectories by magnetic fields. To phase-space cool the ion beam, the energy of the electrons is adjusted such, that the velocities of the ion beam and the electron beam coincide. The ions are circulating in the ring with typical frequencies of 100-200 kHz and in each revolution they may undergo Coulomb interactions with the electron bath in the cooler. Since the electrons are produced in the cathode for one passage before they are dumped in a collector, they may withdraw heat from the system and thus cool the ion beam. Eventually the ion temperature will be determined by the temperature of the electron beam.
In order to minimize the energy spread of the electrons and thus the temperature of the beam, the accelerating and guiding fields inside the cooler have to meet special requirements. The initial temperature of the electrons can be divided into a transverse component or *transverse temperature* $T_\perp$ and a *longitudinal temperature*[1] $T_\parallel$ with respect to the normal vector of the surface. The initial transverse temperature is exclusively determined by cathode properties and operating conditions $T_{\perp i} = T_{ca}$, a typical value for $k_B T_{ca}$ is $\sim$110 meV. The cathode is located in a relatively strong magnetic field that is released during the acceleration, resulting in a widening of the spiral trajectories and thus in an increased electron beam diameter. This field reduction is done in a adiabatic fashion, leading to an *adiabatic expansion* of the electron beam. The ratio of the transverse temperature $kT_\perp$ before and after the expansion is given by

$$T_\perp = \frac{B}{B_i} T_{\perp i} \ , \tag{6.4}$$

1 Usually the temperatures are expressed in terms of the corresponding energy $k_B T$ in meV.

where the inverse of the above ratio $\alpha = B_i/B$ is called expansion factor. At the TSR electron cooler the maximum expansion factor of 30 consequently reduces the transverse temperature to 4 meV.
The longitudinal beam temperature is defined as

$$T_{\parallel} = \frac{m}{k_B}\left(\langle v_{\parallel}^2\rangle - \langle v_{\parallel}\rangle^2\right) , \tag{6.5}$$

its initial value is found to be smaller than the cathode temperature [Jan90]

$$T_{\parallel i} = 2(1-\pi/4)\, T_{ca} \;\approx\; 0.429\, T_{ca} \; . \tag{6.6}$$

Nevertheless the relevant longitudinal electron temperature is that regarded from the reference system of the circulating ion beam and therefore one has to consider the transformation of $T_{\parallel i}$ into the moving coordinate system of the ions. According to a calculation that can be found in [Jan90], the longitudinal temperature in the comoving reference frame is given by

$$T_{\parallel f} = \frac{k_B\, T_{ca}^2}{2eV}, \tag{6.7}$$

where V denotes the accelerating potential, showing that the relevant temperature is reduced with increasing acceleration voltage. Realistic values for the potential V are of the order of keV and thus theoretically $T_{\parallel f}$ can be in the μeV regime. However, this estimation is valid only in the case of a fully adiabatic expansion that is in reality hindered by correlations between the electrons, limiting the longitudinal temperature around $\sim$0.1 meV.
As mentioned above, after several seconds of electron cooling the temperature of the ion beam is essentially given by the temperature of the electron beam, this implies that also a small mismatch between the velocity of the electrons and the ions is corrected. In other words the electron beam can slowly change the energy of the ion beam, an effect that is referred to as *beam dragging*. This effect may cause problems, when collision experiments with the electron cooler are carried out. In that case the electron energy usually has to be varied, in order to measure energy-dependent cross sections. These energy scans have to be performed carefully, because a long-time exposure of the ions with electrons of a different velocity will eventually lead to a change in the ion beam energy. To minimize the dragging, special measurement schemes are implemented, typically the ion beam is precooled for several seconds by an electron beam with cooling energy $E = 0$ (ion and electron velocities are matched) and then the electron energy jumps repeatedly for short periods ($\sim$20 ms) between the measurement energy, the cooling energy and a reference value that is usually needed for normalization. With this so-called "wobbling" procedure

it is ensured that the ion beam energy stays at the desired value during the scan of the measurement energy.
The cooling of the coasting ion beam goes hand in hand with a reduction of the beam emittance that also results in a reduction of the beam diameter. A well-cooled ion beam can be smaller than 1 mm in diameter, a fact that is very useful in imaging experiments, as will be seen in the next chapter.

6.4.2 DR cross section measurements

In ion storage rings, DR cross sections are measured as a function of the detuning of the electron energy with respect to the ion beam. For that purpose a solid state detector, situated in the neutral chamber downstream of the electron cooler, can be used to count the neutral fragments with nearly 100 % detection efficiency. The rate coefficient at a given relative electron energy E can be calculated from the count rate R, the electron density $n_e(E)$, the number of ions stored N_{ion} and a geometrical factor $\eta = L_c/L$, describing the length of the merging region in the electron cooler L_c with respect to the length L of the storage ring

$$\alpha(E) = \frac{R(E)}{\eta\, n_e(E)\, N_{ion}}. \tag{6.8}$$

The rate coefficient is related to the cross section by the relative electron velocity

$$\alpha(v) = \sigma(v)\, v\,, \tag{6.9}$$

thus for energies larger than the electron temperature, the cross section can be obtained by a simple division of the rate coefficient. For small energies, however, the measured rate coefficient will be determined by the exact distribution of the electron velocities convoluted with the cross section. As discussed in the last section, the electron temperature has different longitudinal and transversal components, resulting in a well-defined flattened maxwellian velocity distribution; using this information, the DR cross section can be deconvoluted from the measured rate coefficient (details can be found in [Kro02, Lan02] and references therein).

6.4.3 Principles of DR fragment imaging

Instead of counting the neutral fragments with energy-sensitive devices, they can also be detected with imaging detectors, yielding the relative impact positions, which can be related to the kinetic energy released in the reaction. If the product states of the neutral

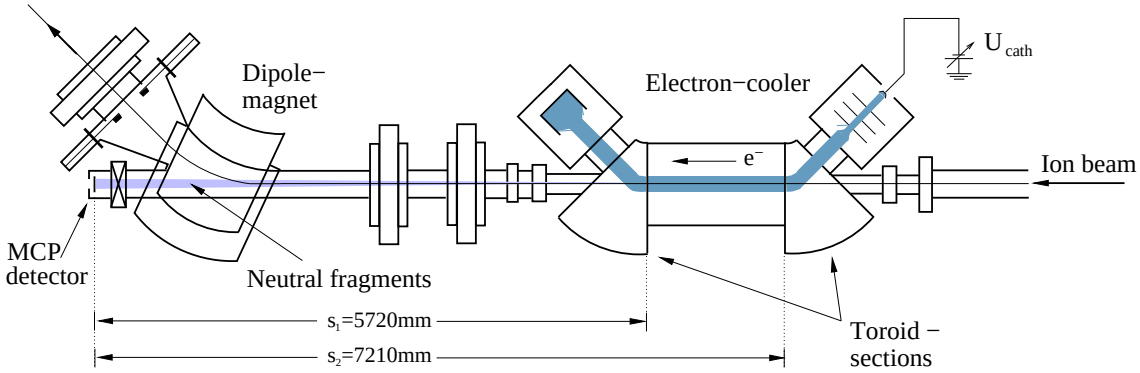

Figure 6.3: *Picture of the electron cooler together with the position-sensitive MCP detector of the fragment imaging setup.*

fragments are known (e.g. in the three-body breakup of H_3^+, where three H(1s) atoms emerge, Eq. 4.9), the kinetic energy release determined by this means reveals information on the initial state of the molecular ion. If, on the other hand, the products can be internally excited (e.g. the H_2 molecule in the two-body breakup of H_3^+), the kinetic energy distributions can also be used to infer the degree of excitation in the products.

As mentioned above, a certain amount of energy is set free during the electron recombination of a molecular ion in the cooler (see Fig. 4.1, 4.2, 4.3), either as pure kinetic energy or as a mixture of kinetic E_{kin} and internal energy of the neutral fragments, thus depending on the size of E_{kin} (in the range of eV), the beam energy E_{beam} (typically MeV) and the product masses, the neutral fragments will reach distances of several millimeters up to centimeters until they reach the detector (see Fig. 6.3).

To understand the measurement principle, it is useful to consider the DR of a diatomic molecule. Fig. 6.4 shows the result of a dissociation process of two atomic fragments and respective velocities. Due to momentum conservation, the velocities will be anti-parallel and after a flight distance S (which is in the case of the TSR electron cooler between 5720 and 7210 mm) they have gained the mutual distance

$$d = S \cdot \frac{m_1 + m_2}{\sqrt{m_1\, m_2}} \left(\frac{E_{kin}}{E_{beam}} \right)^{-1/2} . \tag{6.10}$$

Since the orientation of the molecule in the cooler prior to recombination is unknown, there will in general be an angle between the line along the distance d and the detector plane. The measured distance D is smaller than d according to

$$D = d \sin \Theta , \tag{6.11}$$

where Θ stands for the angle between the internuclear axis and the normal vector of the detector. If the angle Θ was known, it would be possible to deduce from the measure-

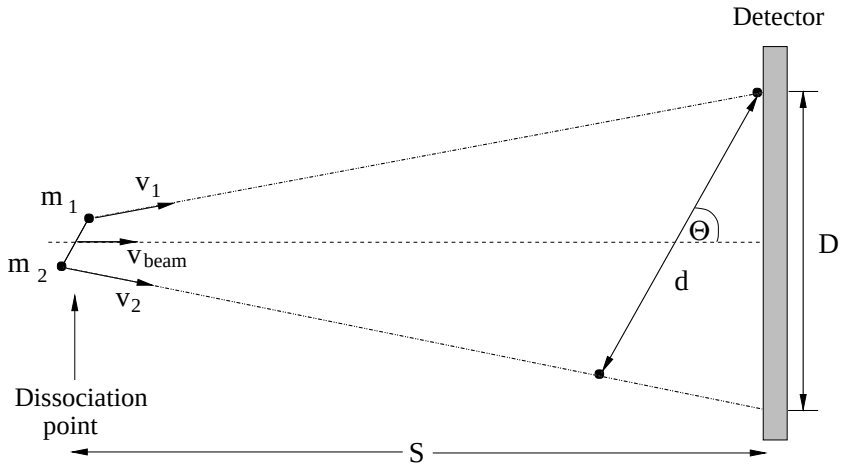

Figure 6.4: *Dissociation process of a diatomic molecule. The kinetic energy release (KER) results in fragment velocities v_1 and v_2 and after a flight distance S the projected distance $D = d \sin\Theta$ will be measured.*

ment of the fragment separation the KER. For all experiments presented in this work the electron and ion velocity are matched (E_e=0), in this case Θ is determined exclusively by the orientation of the molecules in the cooler, which is supposed to be isotropic [Zaj95, Ami96]. At an electron energy $E_e \neq 0$ anisotropies may be induced because the recombination might be favoured in certain orientations of the molecule with respect to the electron velocity in the reference frame of the ions.

A second difficulty arises from the extension of the electron cooler. The interaction region, where ion and electron beam overlap collinearly, has a length of 1.5 m, and therefore the exact position of the recombination is not known. Taking into account this additional uncertainty and assuming an isotropic dissociation, the expected projected distance distribution can be calculated [Ami96]

$$P_i(D) = \begin{cases} \dfrac{1}{(s_2 - s_1)\ \delta_i} \left(\arccos \dfrac{D}{s_2\, \delta_i} - \arccos \dfrac{D}{s_1\, \delta_i} \right) \\ \qquad \text{for } 0 \leq D \leq s_1 \delta_i \\ \dfrac{1}{(s_2 - s_1)\ \delta_i} \arccos \dfrac{D}{s_2\, \delta_i} \\ \qquad \text{for } s_1\, \delta_i \leq D \leq s_2\, \delta_i \\ 0 \qquad \text{otherwise,} \end{cases} \tag{6.12}$$

with s_1, s_2 denoting the distances to the cooler endpoints (Fig. 6.3) and δ_i being determined by the kinetic energy release $E_{kin,i}$ for the dissociation of one particular molecular

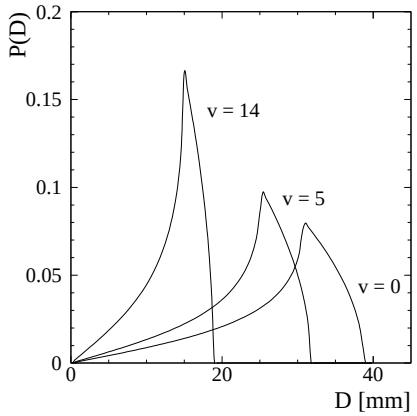

Figure 6.5: *Exemplary projected distance distributions (normalized) for the 2-body breakup of $H_3^+ + e^-$ in $H_2(v)$ and H. The curves represent three different vibrational states for the H_2 product molecule, corresponding to 9.21 eV (v=0), 7.32 eV (v=5) and 4.92 eV (v=14) KER. The beam energy is set to 1.43 MeV, the detector-cooler distances s_1, s_2 are set to the appropriate values for the TSR setup and the dissociation is assumed to be isotropic.*

state into atomic ground state products with masses m_1 and m_2

$$\delta = \frac{m_1 + m_2}{\sqrt{m_1\, m_2}} \left(\frac{E_{kin,i}}{E_{beam}}\right)^{-1/2} . \tag{6.13}$$

If several states contribute the measurement will yield a superposition of the specific $P_i(D)$ distributions weighted with the respective branching ratios b_i

$$P(D) = \sum_i b_i\, P_i(D) . \tag{6.14}$$

The above described kinematics for the dissociation of a diatomic molecule can be applied in the same way to the 2-body breakup of any polyatomic molecular ion, if one allows for the presence of internal energy also in the reaction products. As seen before (chapter 4.3) the DR of H_3^+ has a two-body and a three-body channel

$$H_3^+ + e^- \rightarrow \begin{cases} H + H + H \\ H_2(v) + H\ . \end{cases} \tag{6.15}$$

For the recombination of ground state H_3^+ the KER in the three-body-channel amounts to 4.76 eV. This value is fixed, because not enough energy is available to excite one of the three atomic products. If more than 4.76 eV are seen in DR imaging spectra, the excess energy was brought into the reaction by the inital H_3^+ ion. Consequently the three-body channel can be used to determine the degree of internal excitation of the H_3^+ ions in the ring (as will be seen in the next chapter).

In the two-body case, the binding energy of the H_2 fragment in its particular vibrational state has to be added. Therefore the kinetic energy release $E_{kin,i}$ ranges from 9.23 eV (v=0) to 4.92 eV (v=14). Three exemplary projected distance distributions for the 2-body channel of H_3^+ DR are plotted in Fig. 6.5. The calculated functions can be used to fit the measured distribution, and thus to derive the contributions of the vibrational states of H_2 in the two-body breakup.

6.4.4 Experimental setup

DR imaging setup

The DR imaging detector is located in a vacuum chamber straight ahead of the electron cooler section (see Fig. 6.3). The detector itself (the imaging setup is sketched in Fig. 6.6) consists of two *multi channel plates* (MCP) in chevron geometry and a phosphor screen. Particles hitting the MCP will start an electron avalanche that is further accelerated towards the phosphor screen where the impact of the electron cloud creates a light spot that is recorded with a CCD camera. The 25 Hz image frequency of the camera is low

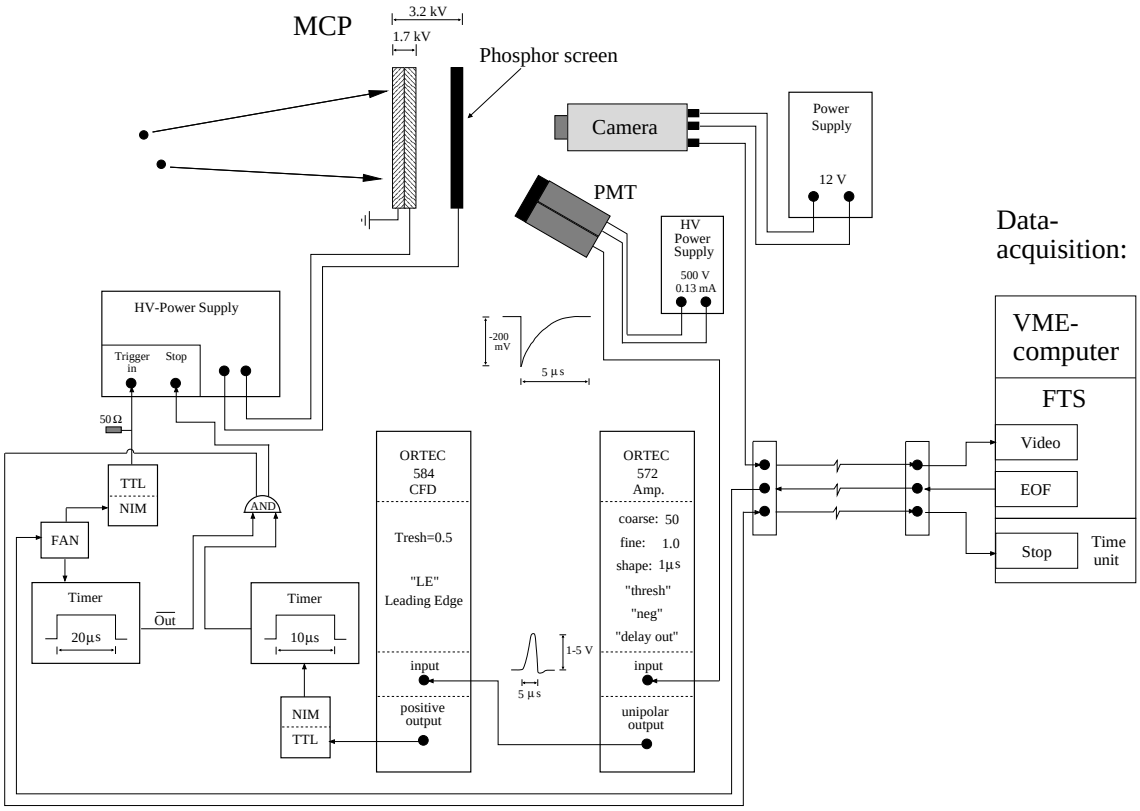

Figure 6.6: *Sketch of the DR fragment imaging setup*

compared to the particle rates at the detector, which are usually of the order of kHz, and therefore simple recording of the phosphor would yield an overwhelming number of fragments from different recombination events per camera frame that would be impossible to analyze. To be able to measure the breakup of a single molecule at a time, the fast signal of a photomultiplier (PMT) pointing towards the detector is used to switch off the high voltage of the phosphor screen as soon as a particle hit is detected. It takes several microseconds for the PMT signal to be processed in the electronics and the high voltage to be switched off, a time that is long enough to accumulate all fragments of a recombination event that generally arrive at the detector within a few hundred nanoseconds, and still short enough to discriminate efficiently against double events in a single camera frame.
After an event detection by the PMT the camera frame is read out by a VME computer, and the phosphor screen is set to high voltage again. The switching of the voltage may induce noise signals in the PMT or the associated electronics that create fake events and switch off again the phosphor immediately. Therefore a delay of 20 μs was introduced and combined with the PMT signal (see Fig. 6.6) to forbid a direct deactivation of the screen voltage. More detailed descriptions of the detector can be found in references [Kro02, Ami96, Lan99].

6.5 Coulomb explosion imaging

6.5.1 Measurement principle

Information on the structure of small molecules is almost exclusively derived from the comparison of spectroscopic data to theoretical structure calculations. In some cases this approach may be hindered by experimental difficulties – for example the number of molecules that are required to get a clean signal – or the lack of a quantum-mechanical calculation.
The Coulomb explosion imaging (CEI) technique is based on the foil-induced fragmentation of molecules followed by the measurement of the asymptotic fragment velocities (see Fig. 6.7) in all three dimensions. For studies of molecular structure this measurement allows one to draw direct conclusions on the initial molecular wave function without theoretical input, while in other cases, where the wave functions are well known, they can be used for time-dependent analysis to monitor vibrational excitation [Ami98]. A more physical picture of the Coulomb explosion is shown in Fig. 6.8. The potential energy of a diatomic molecular ion is plotted together with the squared wave functions of the vibrational ground state and the first excited state. The fast stripping process is depicted by a

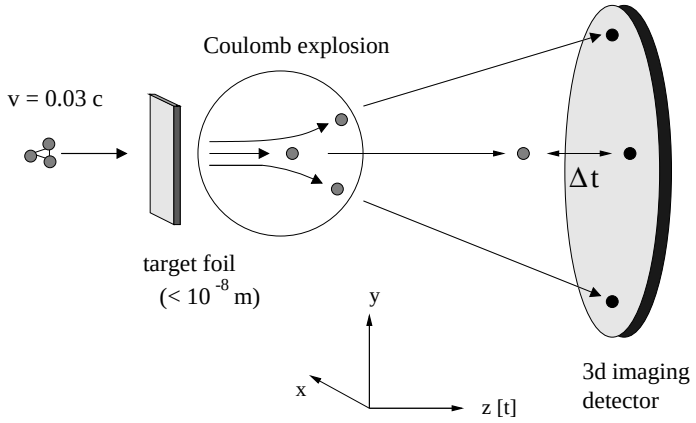

Figure 6.7: *Sketch of the CEI method. Molecular ions at MeV energies are directed towards a thin carbon foil that strips off the binding electrons and initiates the Coulomb explosion. The fragment velocities are recorded with a 3D imaging detector*

vertical jump to the pure $1/r$ Coulomb potential that is followed by the fast dissociation (Coulomb explosion). The measured kinetic energy release distribution is a transformed image of the initial molecular wave function.

The CEI method was pioneered in the seventies at the Weizmann Institute of Science (Rehovot, Israel) [Gem75, Vag76b, Vag76a]. In 1978 it was used to produce the first experimental evidence for the equilateral shape of H_3^+ [Gai78]. In the nineties the foil effects that occur during the passage of the nuclei through the foil were more thoroughly analyzed and a Monte-Carlo simulation was written to take the various effects like multiple scattering and charge exchange into account [Zaj90, Zaj92a, Zaj92b]. The CEI principle was merged with the storage ring technique in 1996 [Wes96] when a CEI setup was installed at the slow extraction beamline of the TSR storage ring at the Max-Planck-Institut für Kernphysik [Wes98], allowing to store molecular ions for variable times before the measurement.

6.5.2 TSR Coulomb explosion beamline

The idea behind a Coulomb explosion beamline at an ion storage ring is to make use of the long storage times either to prepare ground state ions for well-defined molecular structure examinations, or to monitor the time evolution of the vibrational decay after the injection of the ions into the ring. In combination with DR measurements the CEI setup – serving as a vibrational diagnostics – is ideally suited for vibrational state-specific DR investigations [Ami98, Ami99].

The CEI method benefits from the availability of fast ion beams and thin foils. The

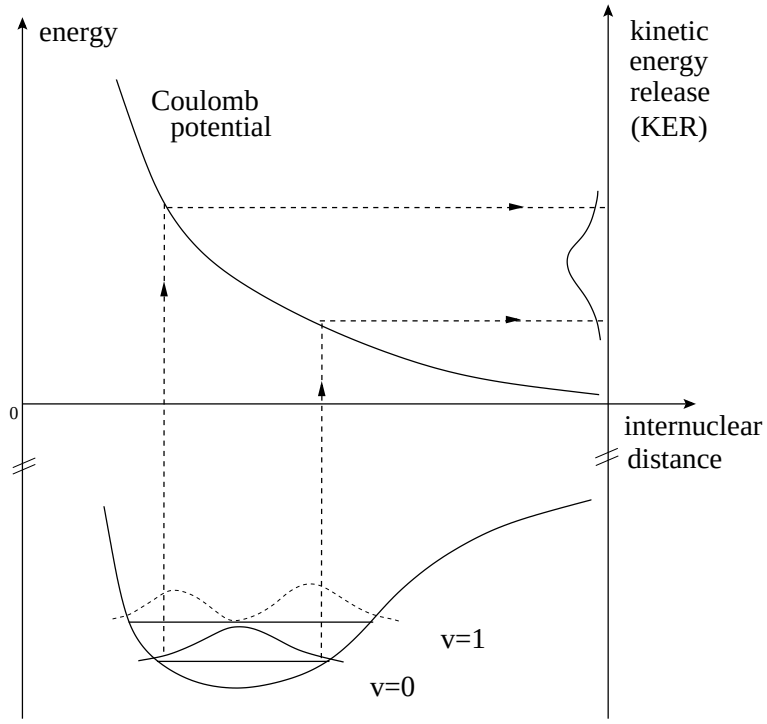

Figure 6.8: *CEI principle for a diatomic molecule. The fast stripping process corresponds to a vertical transition to the pure Coulomb curve, followed by the dissociation of the positively charged fragments along the well-known Coulomb potential*

molecular ions are accelerated to MeV energies and injected into the storage ring. In the injection-extraction section of the TSR (see Fig. 6.1) a small part of the circulating ion beam is continuously extracted and guided into the CEI beamline, where the ion beam is collimated and directed towards the target foil (Fig. 6.9). The targets that are currently used are made of diamond like carbon (DLC) [Lie97, Lev00] and have a thickness of $\approx 5\,\mathrm{nm}$. Typical rates at this stage are of the order of kHz. A fast beam chopper with a switching time of $\approx 50\,\mathrm{ns}$ allows for the measurement of single molecules.

Furthermore, the TSR setup permits a mode of operation where the storage ring is by-passed and the ions are directly guided into the CEI beamline. In this mode it takes the ions a few microseconds to travel from the ion source to the detector, and thus it is often used to check and optimize source conditions.

At a velocity of $0.03\,\mathrm{c}$ the flight time of the nuclei through the foil is about $5\times10^{-16}\,\mathrm{s}$, in this time the binding electrons are stripped off while the nuclear conformation of the impinging molecule is preserved, since the time scales of vibrational and rotational motion are considerably longer ($10^{-12}\,\mathrm{s}$ and $10^{-14}\,\mathrm{s}$, respectively). Most of the Coulomb explosion itself happens outside of the target foil in the vacuum. Already of few micrometer

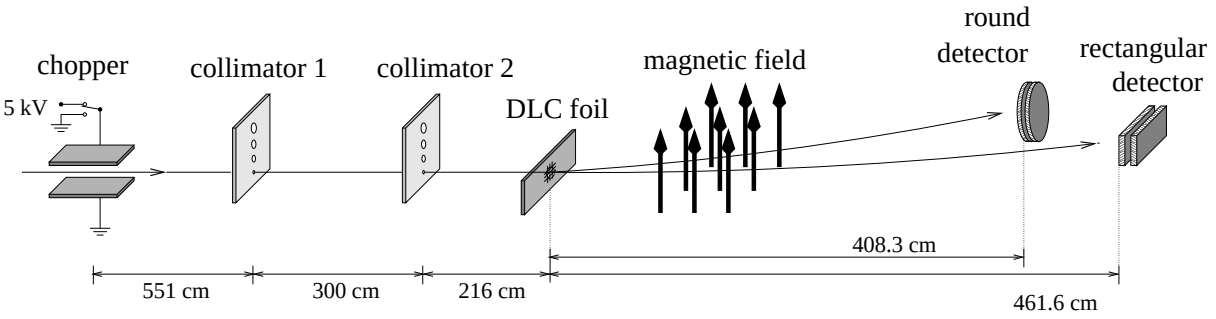

Figure 6.9: *Sketch of the functional parts of the CEI beamline. The extracted ion beam is collimated and directed towards the target foil. After the stripping process the fragments are mass selected by a dipole magnet and detected by multi channel plates. A fast high voltage beam chopper allows for the measurement of single molecules.*

behind the foil practically all the potential energy is converted into kinetic energy and the fragments have reached asymptotic velocities.
To be able to separate different atomic fragments for heteronuclear molecules a dipole magnet is used. After a flight distance of 4.6 m the nuclei have gained typical distances of a few centimeter which are measured with a 3D imaging detector that consists of two systems of multi channel plates (MCP) combined in a rotatable detector chamber. The MCPs are equipped with phosphor screens that convert the electron bunches which are initiated by the impinging particles in light spots that are recorded with CCD cameras. The camera information is used to measure the spatial distance of the fragments on the detector. The time information is collected by anode strips that are situated on the backside of the phosphor screen. The anode signals are amplified, discriminated and digitized by dedicated CAMAC modules and processed by a VME computer system that compounds the camera and anode information to fully correlated 3D events. Details concerning the detector and the measurement scheme can be found elsewhere [Wes98].

6.5.3 Monte-Carlo simulation

For comparison between experimental results and theoretical calculations a Monte-Carlo simulation is used. The simulation is based on a computer program employing classical trajectory calculations that was written by Zajfman et al. and is described in several publications [Zaj90, Zaj92a, Zaj92b].
The program needs two input files: firstly information on the physical properties of the target foil has to be provided and secondly a sample of molecular conformations of the desired molecular ion has to be prepared. This sample is usually based on theoretical calculations of the molecular wave function. In a first step the passage through the foil

including multiple scattering and charge exchange effects is simulated. The output is a distribution of asymptotic velocities. The second part simulates the efficiencies of the CEI detector and the result of this simulation is directly compared to measured velocity distributions.

It has to be mentioned that not all existing foil effects are properly treated in the simulation. A charged particle traversing a target foil will induce a polarization field that can interact with other particles. One of the consequences of the polarization is the "wake-effect". In a naive picture the leading particle will drag behind an electron cloud that attracts the following particles and thus tends to align the fragments [Gar00]. This effect will be most pronounced if a light particle trails a heavy-particle with high charge state that creates a strong polarization field. In order to discriminate against this unwanted effect usually the class of events that is supposed to be influenced by the wake effect is cut away both in the experimental and simulated data.

Currently the implementation of the polarization forces in the Monte-Carlo simulation is underway. Several tests with diatomic molecules like H_2^+, HD^+ and CH^+ have been carried out and the comparison with a preliminary version of the new simulation looks very promising [Buh02], but the full verification for polyatomic molecules has not yet been made.

6.5.4 CEI to monitor vibrational excitation

The CEI method is sensitive to changes in the distribution of internuclear distances. It is clear from Fig 6.8 that a change in the fractional vibrational excitation of the circulating ion beam will translate into changes in the measured velocity distribution.

In this respect the TSR facility offers an unique environment for Coulomb explosion experiments. One of the advantages of storage rings that has already been discussed is the possibility to wait for radiative cooling to the ground vibrational state and make experiments with a well-defined ion beam. CEI experiments at the TSR benefit in addition from the fact that the ion beam is injected at high energies and there is no further ramping of the energy inside the storage ring needed. Therefore a beam of internally excited ions can be injected from the ion source within a few μs into the ring and the vibrational cooling can be followed starting right from the creation of the ions. For ions with well-known wave functions the velocity distributions for different vibrational states can be simulated by feeding the Monte-Carlo routine with theoretical calculations. These distributions can then be fitted to the measured velocity distribution for different storage times and populations of the vibrational states as a function of storage time can be derived as fit

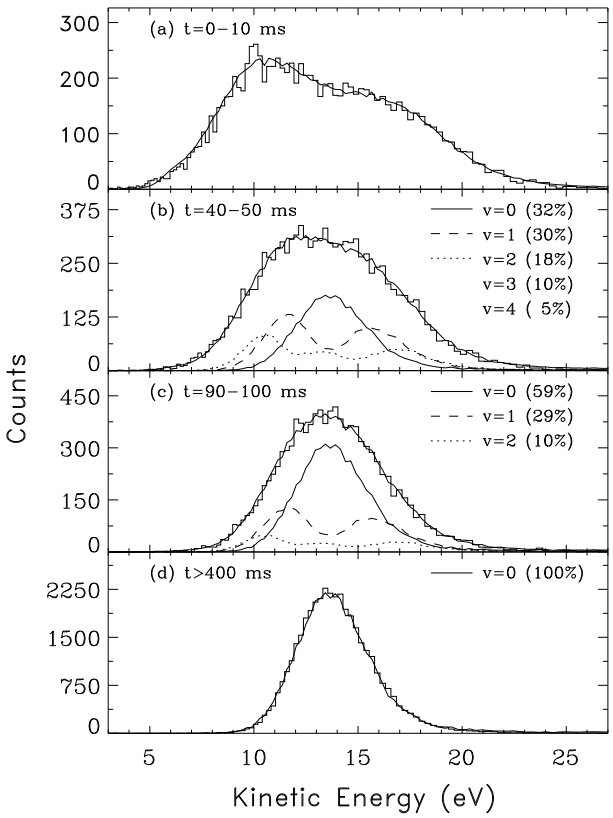

Figure 6.10: *CEI kinetic energy distributions for HD^+ as a function of storage time. The solid lines represent superpositions of simulated molecular wave functions for different vibrational states. Picture taken from [Ami99].*

parameters.

The applicability of CEI to monitor vibrational cooling has been beautifully verified for HD^+ (see Fig 6.10), where the decay of vibrational states could be detected in the first 300 ms after injection and lifetimes of single vibrational modes could be determined [Ami98, Ami99].

Chapter 7
Coulomb explosion and recombination fragment imaging of H_3^+

In this chapter the results of CEI and DR fragment imaging for H_3^+ will be presented. The information that can be provided by both techniques is in some sense complementary, for the CEI method is sensitive to vibrational excitation only, while the DR imaging can give insight into the initial rotational excitation of H_3^+ and the product states.

7.1 Beam conditions and data taking

For both experiments, the H_3^+ ions were produced with the CHORDIS ion source, and accelerated to 1.43 MeV (2.86 MeV for the CEI experiment with D_3^+) by the RFQ structures of the High Current Injector. The ions were stored in the TSR for 8 s (CEI H_3^+) and 10 s (DR H_3^+, CEI D_3^+), respectively.

CEI beamtime

In the Coulomb explosion experiment during the storage time a small fraction of the beam was peeled off and guided into the CEI beamline. A diamond like carbon (DLC) foil with a thickness of 0.7 μg/cm^2 (corresponding to 50Å absolute thickness, measured in an independent beamtime) was used as a target. Precise imaging of H_3^+ wave functions was one of the goals. Therefore best possible resolution required to increase the target-detector distance from 2965 mm to 4608 mm for this beamtime. Since in the case of H_3^+ the fully correlated spatially- and time-resolved distances of three identical particles have to be measured at the same detector, special care was taken to prevent cross-talk between

the anode strips that are responsible for the timing information. For that purpose novel fast amplifier boards were developed [Sch99] and implemented for the first time.

In addition the detector was operated in an interlaced mode that allows for data acquisition with 50 Hz, thus in comparison to the standard 25 Hz mode of the CCD camera nearly a factor of two was gained in terms of statistics.

In one week of beamtime ca. 3 million good events were recorded. From the online analysis, it was obvious that the distributions for H_3^+ changed significantly during the first 2 s of storage and then became stationary; therefore the focus was set on short storage times. All data with storage time $t > 2$ s will henceforth be called "cold data".

In the same beamtime we switched for one day to D_3^+ at the same velocity (consequently the energy was doubled to 2.86 MeV), and since the whole setup was already prepared and the system ran smoothly for 24 h, the data set is smaller by a factor of less than three only. As expected, the vibrational cooling was slower for D_3^+, here the measured distributions became stationary ("cold") after 5 s of storage.

For H_3^+ a second CEI measurement was performed without storage, in which the ion beam was guided directly into the CEI beamline. In this mode of operation, it takes the ions about 10 μs to travel the 100 m distance from the ion source to the detector, thus they can be scrutinized just after their production.

DR imaging beamtime

The fragment imaging data of H_3^+ was the first data sample taken in the framework of a campaign that was started in order to understand the dissociation dynamics of triatomic hydrogen. In that context imaging experiments with all isotopomers (H_3^+, H_2D^+, D_2H^+, D_3^+) were carried out, which are partly available in journal publications [Str01a, Str02] and will be described in detail in the forthcoming works of D. Strasser [Str04] and L. Lammich [Lam04].

For the DR measurements the ion beam was superimposed by an electron beam at the same velocity. The transverse and longitudinal electron temperatures were 6 meV and 0.1 meV, respectively, and the electron beam diameter was 35 mm. After 3 s the phase-space cooling of the ion beam was completed yielding an ion beam of $\sim$0.8 mm diameter.

7.2 Coulomb explosion imaging of H_3^+

7.2.1 Coordinates

The observables of CEI experiments are the relative asymptotic velocities of the fragments. In the case of H_3^+ the velocities between the three protons are denoted by v_{12}, v_{23} and v_{31}. Furthermore the orientation of the plane that is spanned by the three protons with respect to the detector plane is of interest, which is characterized by the azimuthal angle Θ (see Fig 7.1). The normal vector $\vec{n}$ of the molecular plane can be calculated from the

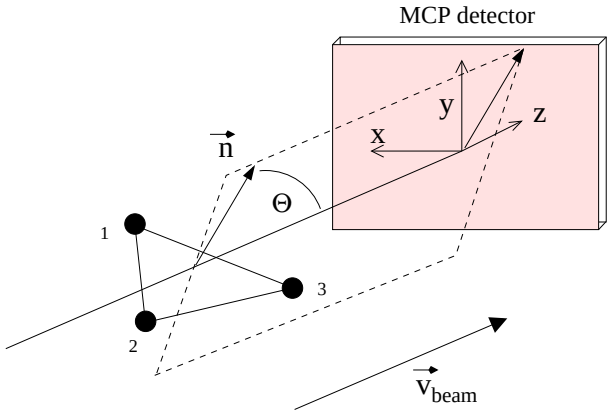

Figure 7.1: *Definition of the azimuthal angle Θ, $\vec{n}$ stands for the normal vector of the molecular plane.*

velocity vectors

$$\vec{n} = \frac{\vec{v_{12}} \times \vec{v_{23}}}{|\vec{v_{12}}| \cdot |\vec{v_{23}}|}. \tag{7.1}$$

With that definition the cosine of the angle Θ is the z-component of the normal vector

$$\cos\,\Theta = n_z. \tag{7.2}$$

In chapter 5 the normal coordinates of H_3^+ have been introduced. These coordinates are linear combinations of internuclear distances. To represent the outcome of CEI experiments new coordinates in velocity space have to be defined that can still account for the molecular symmetry. The coordinates of choice are linear combinations of relative fragment velocities, that are adapted from the normal coordinates

$$v_a = (v_{12} + v_{23} + v_{31})/\sqrt{3}, \tag{7.3}$$

$$v_x = (2\,v_{12} - v_{23} - v_{31})/\sqrt{6}, \tag{7.4}$$

$$v_y = (v_{23} - v_{31})/\sqrt{2}, \tag{7.5}$$

where v_{ij} stands for the velocity between the fragments i and j in atomic units[1]. Because of the radial symmetry of the Coulomb force, it can still be assumed that changes in the v_a coordinate are connected with breathing mode excitations while the v_x and v_y coordinates are associated to the doubly degenerate bending mode.
In order to discriminate against possible target polarization effects (see chapter 6.5.3), in all steps of the analysis (except stated otherwise) a cut of $|\cos\Theta|>0.8$ was applied, assuring that the normal axis of the molecular plane is almost parallel to the normal axis of the detector. In addition a cut was introduced that required the center-of-mass of the event at the detector plane to be within specific limits, to suppress false coincidences and large angle scattering. After the cuts $\sim 4.5 \times 10^5$ fully correlated events remained, representing probably the largest CEI data sample ever taken for a single molecule. For D_3^+ the same cuts were applied, which yielded a data set of 2×10^5 events.

7.2.2 CEI velocity distributions

The beam conditions are described in section 7.1. Now we consider the events which have there been identified as "cold data", corresonding to storage times > 2 s.
The equilateral triangular shape of the H_3^+ ion with a side length of 1.65 Bohr radii is well established theoretically and supported by the excellent agreement between theory and spectroscopy [Wat00, Lin01]. The CEI data must reveal both the shape and the bond length of the molecule within the accuracies that can be achieved and therefore these two aspects may serve as a first consistency check.
From the inlay in Fig. 7.2 it can be seen, that the average asymptotic velocity between two protons amounts to 0.0440 a.u. This mean velocity reflects the bond length of the molecule that is converted into kinetic energy by the repulsive Coulomb potential. To take all the possible permutations into account, the distribution plotted in Fig. 7.2 was exchange-symmetrized.
To derive this velocity one has to calculate the potential energy that is stored in the triangular conformation of the nuclei prior to the removal of the binding electrons. The total energy is the sum of the potential energy between the respective protons. If one considers two singly charged particles $r_{12} = 1.65$ a.u. apart, the electrostatic energy amounts to

$$E_{pot12} = \frac{1}{4\pi\epsilon_0}\frac{e^2}{r_{12}} = 16.5\,eV\,. \tag{7.6}$$

1 atomic velocity unit: 1 a.u. = 1 c·α, where c is the speed of light and α the fine structure constant.

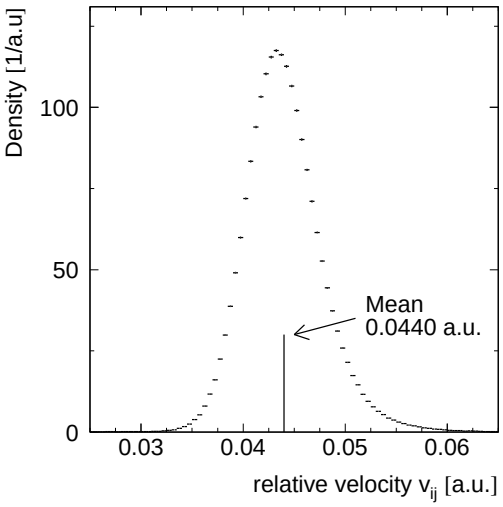

Figure 7.2: *Distribution of the relative fragment velocities v_{ij}, symmetrized for each possible permutation of the three protons. Only events with storage times $> 2\,s$ are considered.*

In the triangular lattice of the H_3^+ ion, this potential energy is contained three times in the respective proton pairings, thus the total potential energy of the nuclear repulsion is $E_{total} = 49.5\,\text{eV}$. In a first order approximation of the Coulomb explosion process this repulsion would result in an accelerated motion away from the center of the triangle, preserving the equilateral shape (Fig. 7.3b).
The kinetic energy will be equally shared between the three protons, thus the absolute value of the velocity vector $\vec{v_1}$ of the first proton away from the center of the triangle is

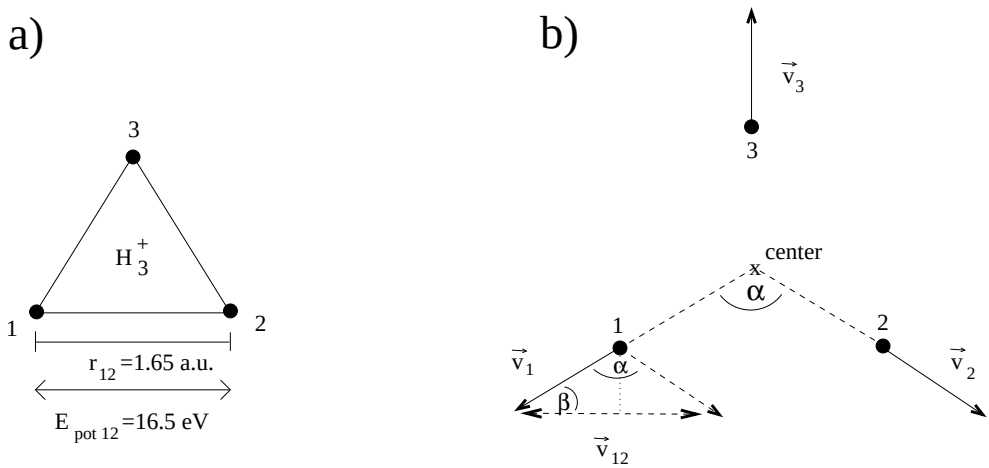

Figure 7.3: *a) The equilibrium structure of H_3^+. b) Picture of a dissociating H_3^+ ion after asymptotic velocities have been reached.*

given by

$$v_1 = \sqrt{\frac{2\,E_{total}}{3\,m_{proton}}} = 0.0257\,\text{a.u.} \tag{7.7}$$

In Fig. 7.3(b) it can be seen that for the equilibrium geometry the angle α between $\vec{v_1}$ and $\vec{v_2}$ is 120°, and consequently β is 30°. The cosine of β is equal to $v_{12}/2$ divided by v_1 and thus v_{12} can be determined

$$\cos\beta = \frac{v_{12}}{2\,v_1} \qquad \Rightarrow \qquad v_{12} = 2\,v_1\,(\cos 30°) = \sqrt{3}\,v_1 \;= 0.0445\,\text{a.u.}, \tag{7.8}$$

in good agreement with the CEI result of Fig. 7.2.

Molecular shape

To demonstrate the triangular shape of the molecule, the symmetry coordinates formed from the fragment velocities have to be analyzed. Whereas the symmetric v_a coordinate fixes the size of the triangle, the shape is specified by the asymmetric coordinates v_x and v_y. For a given value of v_a the pair of coordinates (v_x, v_y) corresponds to a fragmentation into a particular triangular shape. The expectation value of v_a can be calculated from the average value of v_{12} under the assumption of an isotropic explosion starting from

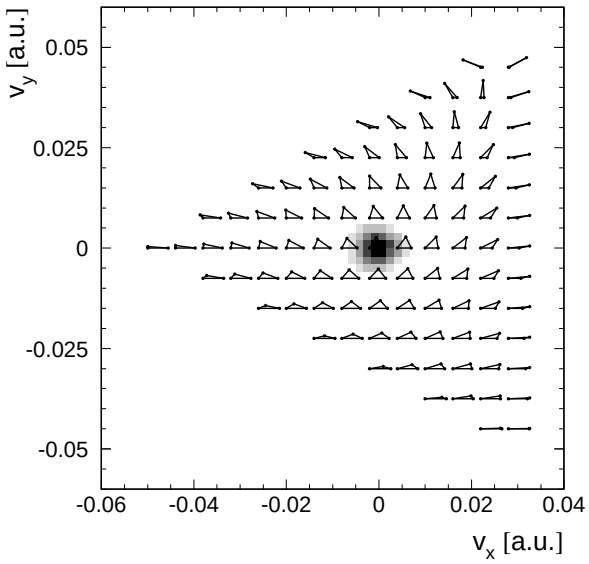

Figure 7.4: *Density plot of v_y against v_x. Only events where the symmetric coordinate v_a is centered around the equilibrium value $0.075 < v_a < 0.076$ (in a.u.) are plotted. The small triangles represent the 3-dimensional pattern of the fragments impinging on the detector, projected onto the molecular plane.*

the equilibrium geometry that implements $v_{12} = v_{23} = v_{31}$. According to Eq. 7.3 the expectation value for the symmetric stretch coordinate in velocity units is $v_a = \frac{1}{\sqrt{3}}(3\,v_{12}) = 0.076$ a.u. Fig. 7.4 shows a density plot of the CEI data for v_y against v_x. To be able to attribute the position in the plot with a particular triangular shape, only a small slice in the v_a coordinate is considered with $0.075 < v_a < 0.076$ (a.u.). The small triangles represent the various possible triangular conformations, ranging from linear geometries in the outer parts to an equilateral triangle in the middle of the plot. The accumulation of the experimental events in the center is a manifestation of the equilateral fragmentation geometry and hence of the corresponding shape of the H_3^+ ion.

7.2.3 Comparison with molecular structure calculations

For a more detailed comparison of the CEI results with theoretical calculations, a Monte-Carlo simulation of the Coulomb explosion of H_3^+ was performed, using rotationless ($J = 0$) wave functions that were provided by J. Tennyson. The wave functions were calculated with the DVR3D [Ten95b] program, implementing the potentials and nonadiabatic corrections of Polyansky and Tennyson [Pol99].

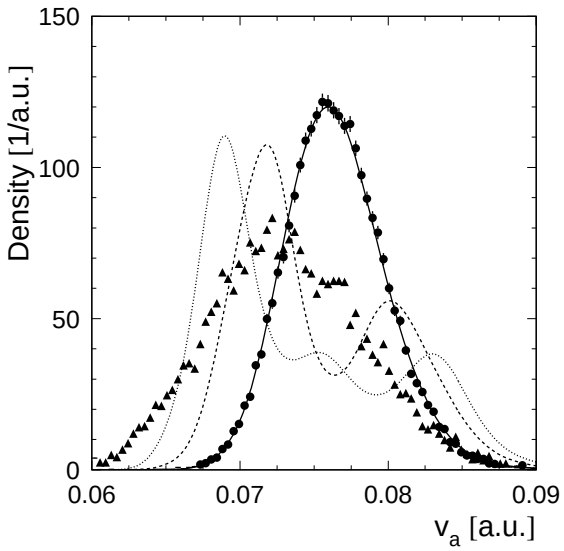

Figure 7.5: *Comparison of simulated v_a distributions with experimental data for two different times. The solid, dashed and dotted lines show the simulated distribution for the ground vibrational state $(0,0^0)$, the first breathing mode $(1,0^0)$ and the second breathing mode $(2,0^0)$, respectively. The experimental distributions are represented by solid circles for storage times $t > 2\,s$ and triangles for $t < 10\,\mu s$ (direct transfer from accelerator).*

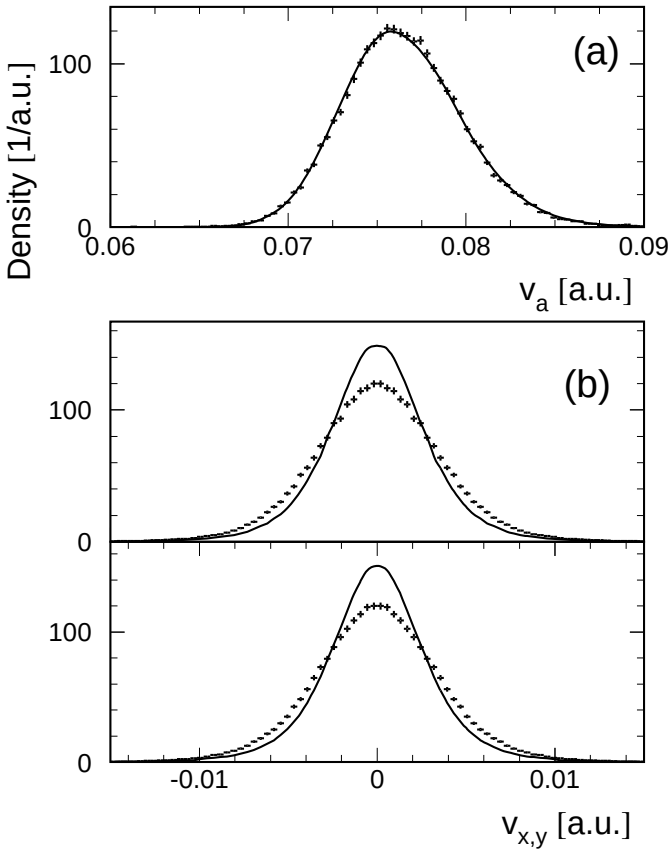

Figure 7.6: *Asymptotic velocity distributions derived by CEI of H_3^+ (normalized) for (a) the breathing coordinate v_a and (b) the bending coordinates v_x, v_y using data for storage times $> 2s$ (crosses), compared to simulated ground state distributions (full lines).*

The first step is to check how the "cold distribution" with storage times of more than 2 s compares to the simulation in the breathing mode coordinate. If there were any long-lived vibrational excitations, they should primarily be visible in this representation.
In Fig. 7.5 the output of the Monte-Carlo simulation is plotted in the v_a coordinate for the ground vibrational state and the first two breathing excitations. The experimental distribution is superimposed for long storage times ($t > 2$ s), and directly after acceleration. The latter measurement is achieved by bypassing the storage ring and transferring the ions directly from the accelerator to the CEI beamline (as described in section 7.1). The excellent agreement between the ground state and the experimental distribution for long storage times confirms the end of vibrational cooling after 2 s, resulting in a distribution that suggests that only the vibrational ground state is populated.
The v_a mode represents only one of the molecule's three internal degrees of freedom.

In Fig. 7.6 the comparison between "cold data" and simulation is made for all three symmetry coordinates. While for the breathing mode experiment and theory are in good agreement – as seen above – there is a distinct deviation for both bending modes. In order to explain this discrepancy, one has to remember that the CEI simulation does not take into account the internal kinetic energy that the nuclei may posses upon entrance of the foil, since only spatial wave functions are used to create the input file for the simulation. To include the initial momenta properly, a full quantum mechanical calculation would be required.

effect\origin	ZPE in v_a	ZPE in v_x	ZPE in v_y	Sim.	Sim. + ZPE	Exp.
$\langle v_a \rangle$	$v_a^0 \cdot$ 0.002	$v_a^0 \cdot$ 0.0005	$v_a^0 \cdot$ 0.0005	0.0765	0.0765	0.0767
σ_a	1.1×10^{-4}	2.42×10^{-4}	2.42×10^{-4}	0.0034	0.0034	0.0034
$\langle v_x \rangle$	0	0	0	$\sim 10^{-9}$	$\sim 10^{-9}$	$\sim 10^{-9}$
σ_x	0	0.0013	0.0013	0.0031	0.0037	0.0037
$\langle v_y \rangle$	0	0	0	$\sim 10^{-9}$	$\sim 10^{-9}$	$\sim 10^{-9}$
σ_y	0	0.0013	0.0013	0.0031	0.0036	0.0036

Table 7.1: *Tabulation of the effects of the zero point energies (ZPE) in the three different modes on the paramters of the velocity distributions (see Appendix A), where $\langle v_i \rangle$ stands for the mean and σ_i for the width of the respective distribution and v_a^0 denotes the mean value of the "undisturbed" breathing mode velocity $v_a^0 = 0.076$. For the calculation including the ZPE, the shifts of the mean values $\langle v_i \rangle$ are added and the contributions to the widths σ_i are added quadratically. All velocities in atomic units.*

A calculation of the size of this effect in different coordinates is performed in a harmonic approximation in Appendix A. The outcome of this estimate can be seen in Tab. 7.1. It shows the contributions of the initial zero point energies in all three coordinates to the mean values and variances of the three experimental distributions. Column (Sim.) shows the results of the simulation alone. In column (Sim. + ZPE) the harmonic corrections are added to the parameters of the simulated velocity distributions and comparison to the experimental values reveals that the ZPE can well account for the observed widths σ_x and σ_y in the bending mode coordinates, while all other parameters are practically unaffected.

It should be noted that a similar effect was seen in the Coulomb explosion data on HD^+, there the initial kinetic energy could be included into the Monte-Carlo simulation by a procedure that was adapted to the diatomic case and can not be applied easily to polyatomic ions [Ami99].

7.2.4 Vibrational cooling

The CEI simulation can be used to visualize the effect that the presence of vibrationally excited H_3^+ molecules in the stored ion beam will have on the measured velocity distributions. In Fig. 7.7(a) simulated distributions in the symmetric v_a coordinate are shown for the ground state ($0,0^0$) and the first ($1,0^0$) and second ($2,0^0$) breathing excitations. A considerable fraction of excited molecules in this mode would result in a shift to lower velocities and – more importantly – a broadening of the whole distribution. Excitations in the bending modes $v_{x,y}$ were found to have very little influence on the breathing coordinate; in a perfectly harmonic system the modes would be completely decoupled and the presence of bending excitations would not affect the v_a distribution at all.

In Fig. 7.7(b) simulated distributions in the asymmetric coordinates v_x and v_y are plot-

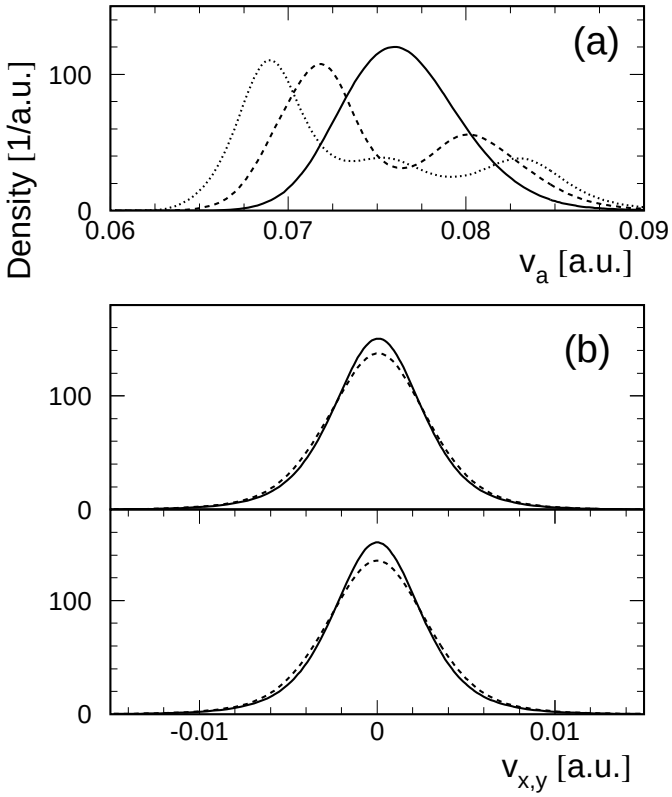

Figure 7.7: *Simulated asymptotic velocity distributions (normalized) for (a) the breathing coordinate v_a and the ground state $(0,0^0)$ (solid line) as well as the lowest breathing-excited levels $(1,0^0)$ (dashed line) and $(2,0^0)$ (dotted line), and for (b) the bending coordinates $v_{x,y}$ and the ground state $(0,0^0)$ (solid line) as well as the lowest bending-excited level $(0,1^1)$ (dashed line).*

ted. Here the vibrational ground state is compared to the first excited bending mode $(0,1^1)$, although it has to be mentioned that the wave functions of E symmetry (see Fig. 5.4) are not unambiguous in the rotationless calculation, which yields different results for different parities of the rovibrational state [Ten01]. Since the CEI results are not sensitive to particular rotational states and thus do not reveal exact quantum numbers, any superposition of odd and even parity is allowed. For the first bending state $(0,1^1)$ however, both distributions are indistinguishable on the scale of Fig. 7.7(b) which is meant to demonstrate the magnitude of change one has to expect for low-lying excitations, thus only the wave function with even parity is plotted. Generally, as seen in Fig. 7.7(b), the existence of bending excitations will result in a broadening of the v_x and v_y distributions. The simulation results for $v_{x,y}$ assuming breathing excitation but no bending excitation, show no difference with those for the $(0,0^0)$ ground state.

The simulated velocity distributions can help to interpret the time-dependent CEI results.

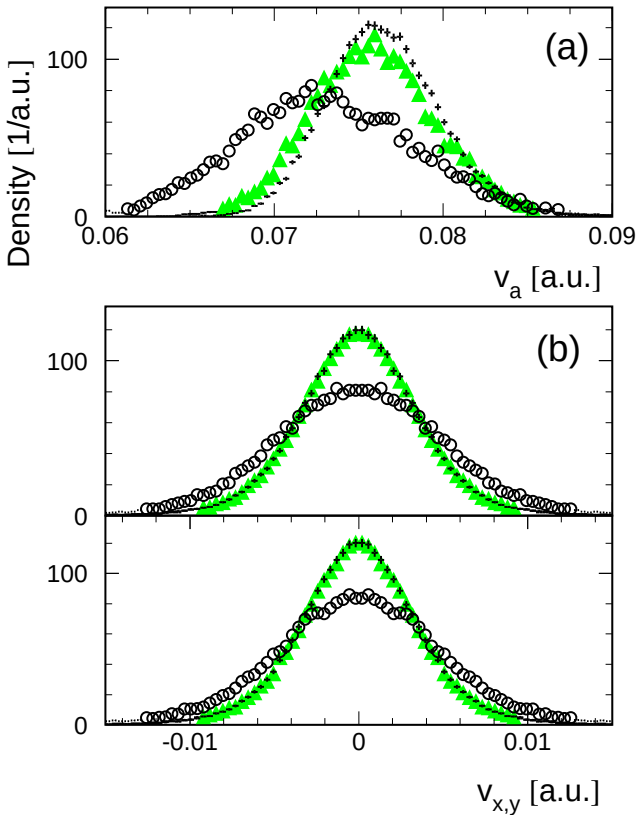

Figure 7.8: *Asymptotic velocity distributions (normalized) for (a) the breathing coordinate v_a and (b) the bending coordinates v_x, v_y as measured directly after acceleration of the H_3^+ beam (open circles) and after storage times of 30–50 ms (shaded triangles) and $> 2\,s$ (crosses).*

In Fig. 7.8 the measured distributions are plotted for three different storage time slices, namely for >2 s, 30-50 ms and directly after acceleration.
In the breathing coordinate (Fig. 7.8(a)) the expected shift to lower energies together with a broadening of the distribution due to the presence of excited states can clearly be identified for short times. As discussed above, the distribution for $t > 2$ s is in very good agreement with the simulated vibrational ground state.
The infrared-active bending modes, depicted in Fig. 7.8(b), also follow the expected behaviour. Since the lifetimes of these excitations are distinctly shorter than those of the metastable breathing modes, the distribution for t>2 s and for the interval 30-50 ms already coincide, while for the undelayed experiment, with an ion beam coming directly from the ion source a wider velocity distribution is observed.

Time dependence of the fragment velocity width

To get a more quantitative picture of the vibrational cooling in the different modes, one may consider the time-dependent width of the velocity distributions. In Fig. 7.9 the RMS width of the v_a distribution is plotted as a function of storage time. At this stage the focus is on the time behaviour alone and the precise shape of the distribution is not

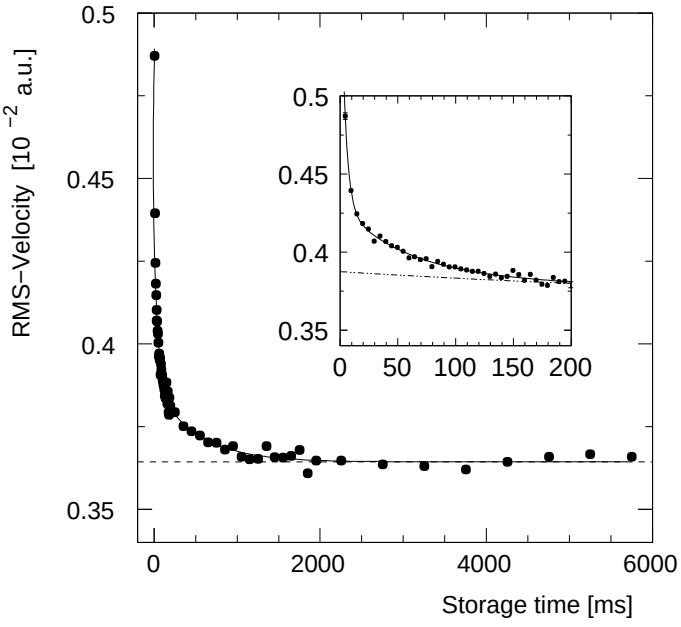

Figure 7.9: *Root-mean-square width of the v_a distribution as a function of the storage time with a fitted three-component exponential (resulting time constants (500±60) ms, (53±6) ms and (4.0±0.5) ms). The short-time behaviour (inset) clearly shows the influence of two shorter time constants beside the long-lived component of 500 ms (broken line).*

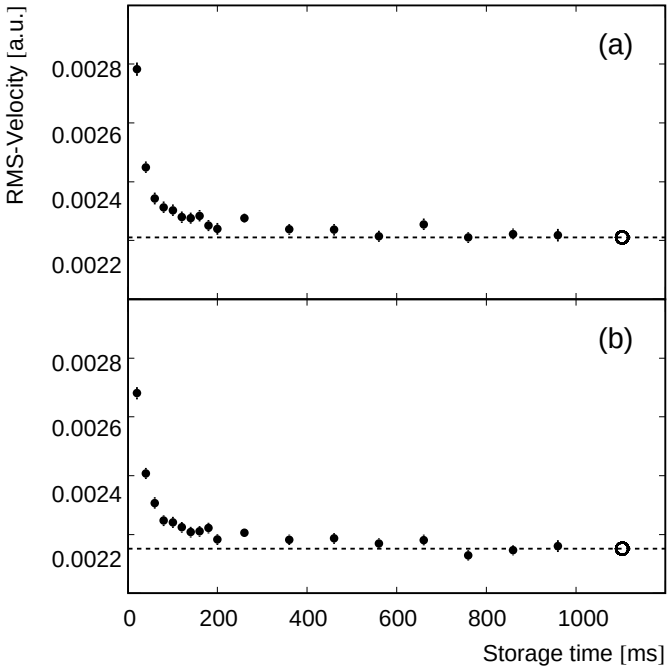

Figure 7.10: *Root-mean-square width derived from the velocity distributions of the asymmetric coordinates v_x (a) and v_y (b) for different storage time intervals up to 200 ms. The mean r.m.s. widths of the distribution observed for storage times between 2 and 6 s are shown by the open circles.*

crucial, therefore all the molecular orientations are included (no cut in $|\cos\Theta|$) in the plot and possible target polarization effects (that are storage time independent) may also influence the absolute scale of the width. The experimental points are fitted by a three-component exponential function (solid line) with time constants (500 ± 60) ms, (53 ± 6) ms and (4.0 ± 0.5) ms. The inset illustrates the fact that two additional components are needed besides the most long-lived constant to describe the decay at short times.

From the rotationless calculation of level lifetimes by Dinelli *et al.* [Din92] (see also level scheme in chapter 5.2) it seems obvious that the first two breathing levels $(1,0^0)$ and $(2,0^0)$ are the only ones to have lifetimes distinctly longer than 10 ms, namely 1.18 s and 0.38 s, respectively. Therefore it is tempting to attribute the two longer time constants of 500 ms and 53 ms to the decay of the two metastable breathing states. Although at this point it is not admissible to make a clear assignment of lifetimes for these states, it should be noted that in both cases the rotationless calculation predicts longer decay constants (by a factor of $\sim$2.6 for $(1,0^0)$ and $\sim$8 for $(2,0^0)$) than those resulting from the exponential fit.

For the infrared-active bending mode excitations $v_{x,y}$ the predicted lifetimes are much shorter. Fig. 7.10 shows a fast initial decay with a time constant of <10 ms in agreement with the theoretical prediction and a slight further decrease of the width after ∼50 ms. This slow component can be explained by the presence of breathing mode excitations since the decoupling of the modes is not perfect, and by the population of intermediate states that are part of the cascade from the metastable states to the ground state (see level scheme Fig. 5.4).

Time dependence of level populations

In a more thorough analysis the functional shapes of the wave functions have to be taken into account to derive time-dependent populations. For this purpose the Monte-Carlo generated distributions can be fitted to the experimental velocity distributions. For the asymmetric modes $v_{x,y}$ this procedure is hindered by several aspects. Firstly, as discussed above, the agreement between simulation and experiment in these coordinates (see Fig. 7.6) is poor, since the internal kinetic energy of the nuclei plays a significant role for the shape of the distribution (see App. A). Secondly, for wave functions with E symmetry the parity is not determined and thus the wave function is not unambiguous since it can consist of superpositions with negative and positive parity. Finally, the decay constants of all the bending excitations are of similar magnitude and the many states that one would have to include in the fit would be indistinguishable on the basis of the statistics available in the short time interval of the bending mode decay.
For the breathing coordinate v_a the situation is different. As demonstrated above (App. A) in this coordinate the initial kinetic energy of the nuclei plays a negligible role and consequently the simulation for the vibrational ground state practically coincides with the measurement for long storage times (Fig. 7.6). Furthermore the parity of states with A_1 symmetry, like e.g. the ground state and all pure breathing excited levels, is even and thus the rotationless wave function is well-determined. Also the number of states is manageable, since from the consideration of the RMS of the v_a distribution above, it seems adequate to include only these states of $v = 1$ and 2 in addition to $v = 0$ for $t > 30$ ms.
In order to raise the sensitivity for small contributions, it turned out to be necessary to replace the simulated ground state distribution by a smooth function fitted to the "cold data", since the simulation displays small deviations from the experiment that are hardly visible in Fig. 7.6 but still disturb the fit for excited state fractions in some critical time bins. In addition the population of the second breathing mode was artificially set to zero for t>600 ms to suppress unphysical fluctuations. Note that in contrast to the first

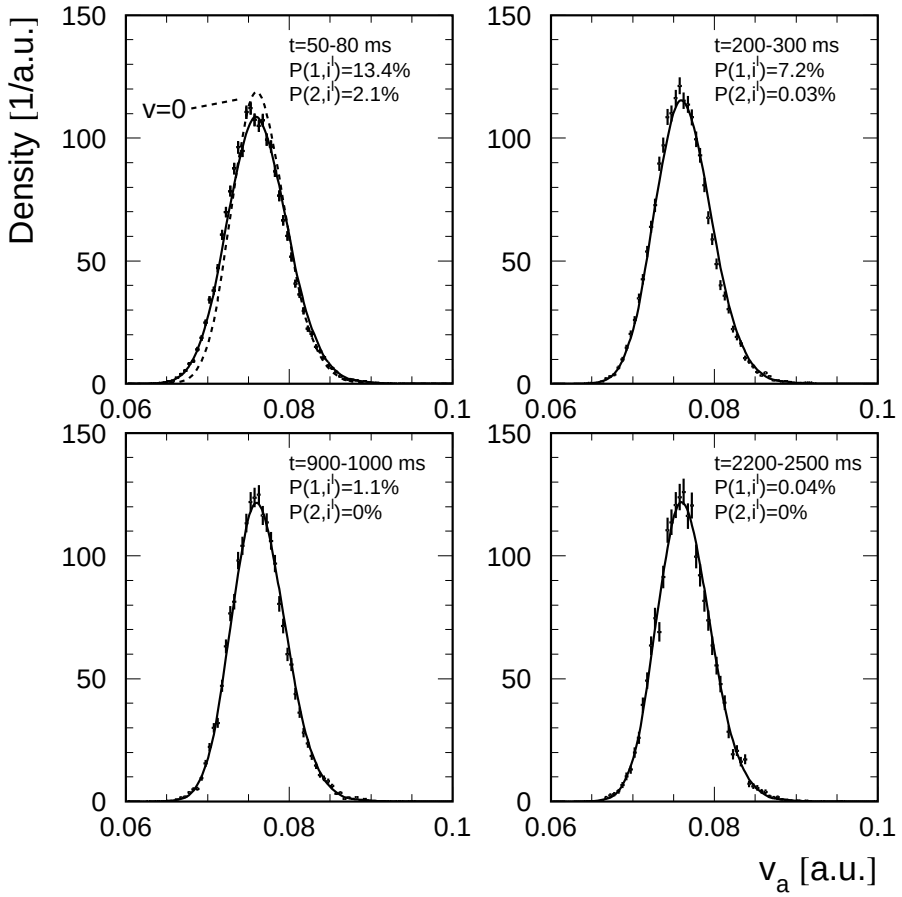

Figure 7.11: *Exemplary fits of the experimental v_a distribution by a superposition of the simulated distributions of the ground state $(0,0^0)$ and the two first breathing modes $(1,0^0)$ and $(2,0^0)$. The populations of the two excited modes are given in percent, $P(1,i^j)$ ($P(2,i^j)$) denoting all states with ν_1=1 (ν_1=2) and arbitrary values i,j for the bending mode quantum numbers. In the first picture, a fit of the vibrational ground state alone is plotted for comparison.*

breathing excitation, the fitted population of the second breathing mode can for shorter times be influenced by even higher-lying excitations and bending excited levels that are present in the same time interval. In Fig. 7.11 four exemplary fits are depicted, and the time-intervals as well as the populations of the first two breathing modes are given.

The time-dependent populations for the two breathing modes derived by this procedure are plotted in Fig. 7.12. For the first 20 ms the interference of non-breathing excited states was too high for a reliable fit to be performed, hence the first time bin used is 20-50 ms.

The dashed lines represent exponential functions with decay constants according to the

rotationless calculations of Dinelli *et al.* [Din92] and a constant factor fitted to the data for longer times (t> 500 ms for the first breathing mode, t> 70 ms for the second breathing mode). The discrepancy between experiment and theory is evident, in both cases the calculated time constants are longer than the decay of the experimentally derived populations. Hints towards the reason for the divergence come from both experiment and theory. In an independent measurement of dissociative recombination at the TSR it was shown that the stored H_3^+ ions host significant rotational energy (see next chapter), that could be approximated by a Boltzmann distribution with a temperature of 0.23 eV ($\sim$ 2700 K). A comparison of the rotationless lifetimes with rotation-vibrational state specific transitions from a comprehensive calculation by Neale *et al.* [Nea96] revealed that the presence of rotational excitation is likely to speed up the vibrational decay. In chapter 8 the line list of Neale *et al.* will be used to create a refined model of the vibrational decay to gain a better understanding of the CEI results.

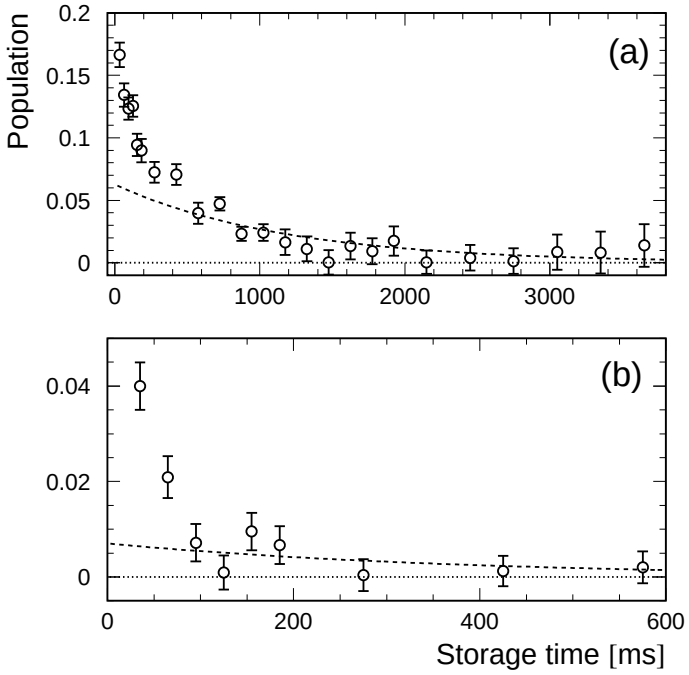

Figure 7.12: *Population fractions for (a) the first excited breathing level* $(1,0^0)$ *and (b) the second level* $(2,0^0)$*, obtained by fitting superpositions of the simulated distributions from Fig. 7.7(a) to the measured* v_a *velocity distributions for storage time bins centered at the indicated data points. The dashed lines show single-component exponentials for the rotationless calculated decay time constants of the* $(1,0^0)$ *and* $(2,0^0)$ *levels and a constant scaling factor fitted to the data at* $t > 500$ *ms for* $(1,0^0)$ *and* $t > 70$ *ms for* $(2,0^0)$*.*

7.3 Coulomb explosion imaging of D_3^+

Coulomb explosion data of D_3^+ were taken with the same target and detector settings used for the H_3^+ beamtime. Analogously to the H_3^+ measurement the beam was produced in the CHORDIS ion source and accelerated to $\sim 480\,\mathrm{keV}$ per nucleon by the RFQ accelerator. Storage times up to 10 s were measured.

7.3.1 CEI velocity distributions

For both isotopomers H_3^+ and D_3^+ the same electronic potential energy surface applies (within the Born-Oppenheimer approximation), and since the molecular geometry and average bond length is determined by the minima of the electronic potential, the molecular equilibrium structure is supposed to be the same for both ions. Thus the mean value of the nuclear wave function is the same. However, the extension of the wave function (the width) will vary with the atomic masses.

This means that the average kinetic energy that is set free from the Coulomb explosion is the same in both cases, but since the CEI method measures the asymptotic velocities, the mean value of the v_a distribution and all widths are expected to be shifted by $1/\sqrt{2}$ with respect to the H_3^+ case, while the bending mode coordinates v_x and v_y are centered around zero anyway in both cases. This effect can be seen in Fig. 7.13 and Tab. 7.2, where the cold data is compared to simulated distributions (for H_3^+, see Fig. 7.6). In contrast to H_3^+, a constant scaling factor for the beam energy had to be introduced because the velocities from the unscaled simulation were shifted by 0.6 %. However, this correction is in the range of the uncertainty of $\sim 1\,\%$ of the beam energy if the beam is delivered from the RFQ-accelerator and is not phase-space-compressed by the electron cooler. The wave functions that were used as input for the simulation were provided by J. Tennyson and stem from the same type of calculation used for H_3^+. Parallel to H_3^+ the same features are seen, namely agreement for the breathing mode coordinate v_a and distinct deviations

	H_3^+ Exp.	H_3^+ Sim.	(H_3^+ Exp.)/$\sqrt{2}$	(H_3^+ Sim.)/$\sqrt{2}$	D_3^+ Exp.	D_3^+ Sim.
$\langle v_a \rangle$	0.0765	0.0765	0.0541	0.0541	0.0545	0.0544
$\sigma(v_a)$	0.0034	0.0034	0.0024	0.0024	0.0022	0.0021
$\sigma(v_x)$	0.0037	0.0031	0.0026	0.0022	0.0021	0.0018
$\sigma(v_y)$	0.0037	0.0031	0.0026	0.0022	0.0021	0.0018

Table 7.2: *Comparison of the cold velocity distributions of H_3^+ and D_3^+. All values in a.u., the mean values $\langle v_x \rangle$, $\langle v_y \rangle$ are all $\leq 2 \times 10^{-9}$ a.u..*

– caused by initial kinetic energy not accounted for in the simulation – for the bending modes v_x and v_y.

The factor connecting the widths of the respective distributions is somewhat greater than $\sqrt{2}$ both in experiment and simulation, revealing the fact that the D_3^+ wave functions are already narrower, corresponding to the lower zero point energies. The deviation caused by the initial kinetic energy seems to be a little reduced for D_3^+, this could have to do with the lower zero point energies that translate into lower average kinetic energy of the nuclei.

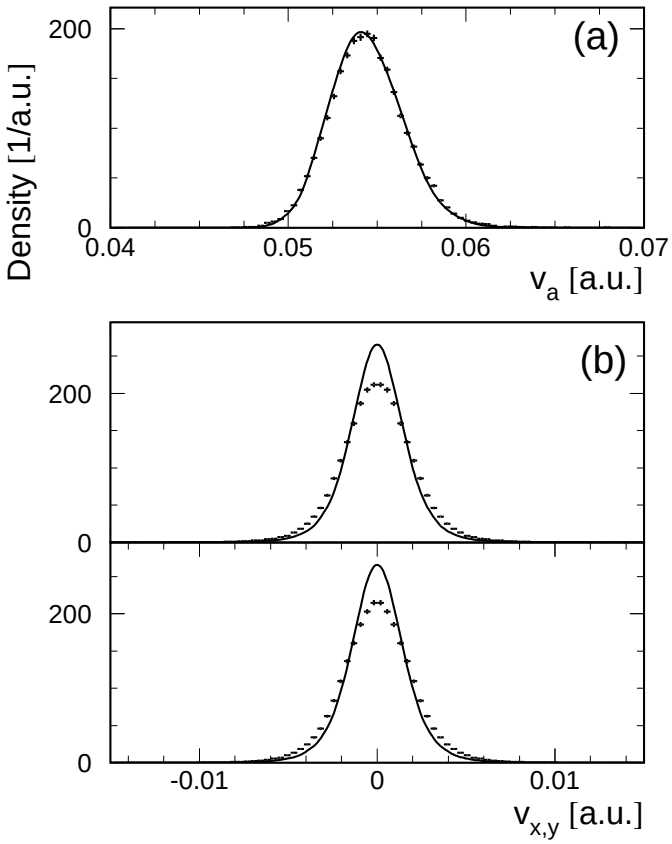

Figure 7.13: *Asymptotic velocity distributions derived by CEI of D_3^+ (normalized) for (a) the breathing coordinate v_a and (b) the bending coordinates v_x, v_y using data for storage times $> 5\,s$ (crosses), compared to simulated distributions (full lines).*

7.3.2 Vibrational cooling

Fig. 7.14 shows the time-dependence of the RMS-width of the breathing mode coordinate v_a with respect to storage time (to compare with H_3^+: Fig. 7.9, in analogy to the H_3^+ case no cut in $|\cos\Theta|$ was applied for this step of the analysis). The data points are fitted by a three component exponential with time constants of (1.67±0.27) s, (135±25) ms and (8±2) ms), respectively.

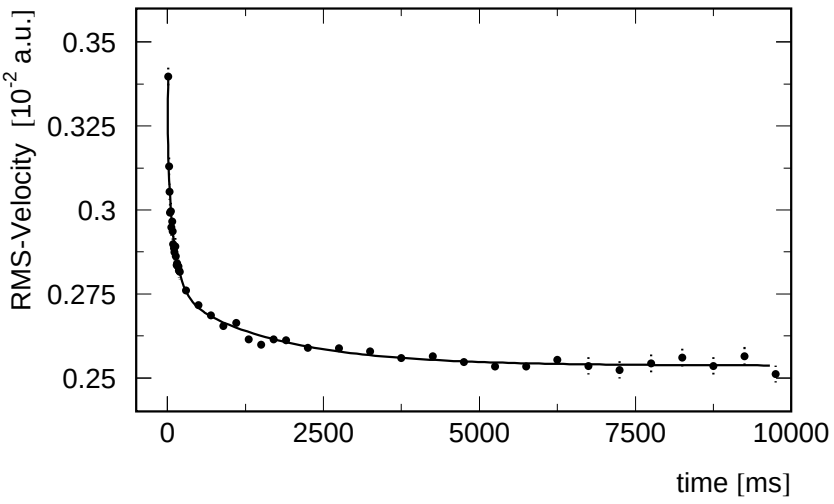

Figure 7.14: *Root-mean-square width of the v_a distribution measured by CEI of D_3^+ as a function of the storage time with a fitted three-component exponential (resulting time constants (1.67±0.27) s, (135±25) ms and (8±2) ms).*

No theoretical predictions of vibrational lifetimes of D_3^+ are available. Nevertheless, for a rough analysis, lifetimes can be estimated from the H_3^+ calculations. The Einstein coefficient of spontaneous decay can be calculated knowing the dipole matrix element μ_{if} and the frequency ν of the transition

$$A_{if} = \frac{64\,\pi^4}{3\,h\,c^3}|\mu_{if}|\,\nu^3. \tag{7.9}$$

If one assumes the matrix elements for H_3^+ and D_3^+ to be of similar size, then the transition probability is proportional to $\sim \nu^3$. Taking the values of the band origin of the first breathing mode excitation[2] $\nu(H_3^+) = 3187\,\mathrm{cm}^{-1}$ and $\nu(D_3^+) = 2301\,\mathrm{cm}^{-1}$, the lifetime for D_3^+ is longer by a factor of ≈ 2.6. The same factor holds true for the second

2 For consistency all values were taken from the same publication [Mey86], which is not the most recent one, but more than sufficient in accuracy for this simple estimate.

decay constant	$\tau(D_3^+)$ [ms]	$\tau(H_3^+)$ [ms]	$\tau(D_3^+)/\tau(H_3^+)$
1	1670 ± 270	500 ± 60	3.3
2	135 ± 25	53 ± 6	2.5
3	8 ± 2	4 ± 0.5	2.0

Table 7.3: *Comparison of the decay constants derived from a three-component exponential fit to the storage time dependent velocity widths of the v_a coordinate for H_3^+ and D_3^+.*

breathing mode ($\nu(H_3^+) = 6268\,cm^{-1}$, $\nu(D_3^+) = 4555\,cm^{-1}$) and the first bending mode ($\nu(H_3^+) = 2120\,cm^{-1}$, $\nu(D_3^+) = 1833\,cm^{-1}$).

However, to do a comparison between both ions additional information is needed. Because it is known that rotations will influence the vibrational lifetimes, a comparison would make sense only if the average rotational excitation produced by the ion source is comparable for both ions. Fortunately this seems to be the case, for DR fragment imaging experiments (see chapter 7.4) yielded values of ~0.23 eV of rotational energy for H_3^+ and ~0.3 eV for D_3^+

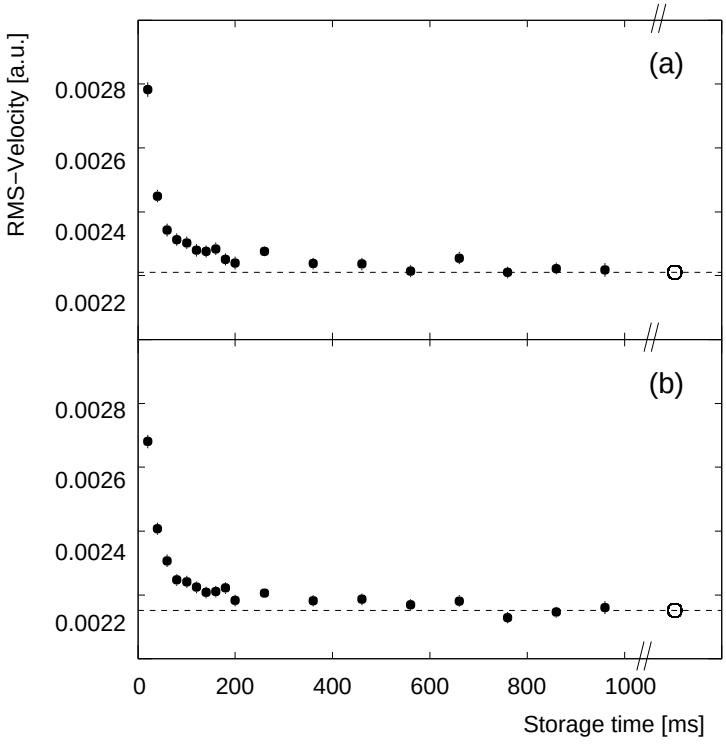

Figure 7.15: *Root-mean-square width derived from the D_3^+ velocity distributions of the asymmetric coordinates v_x (a) and v_y (b) for different storage time intervals up to 1000 ms. The mean r.m.s. widths of the distribution observed for storage times between 5 and 10 s are shown by the open circles.*

(the uncertainty of both numbers is roughly 0.03 eV) [Str02]. Furthermore the relaxation model presented in chapter 8 indicates that differences in the absolute value at these high energies are only of minor influence.

The observed decay constants for D_3^+ are larger by factors between 2.0 and 3.3 compared to the H_3^+ fit, in reasonable agreement with the simple estimate above (see Tab. 7.3).

The cooling of the bending modes is depicted in Fig. 7.15 (to be compared to Fig. 7.10, note the different scale at the abscissa). As expected also the bending level decay is somewhat slower for D_3^+ than for H_3^+.

To extract meaningful lifetimes of the two first breathing excited levels, the same procedure as used for H_3^+ was applied: the velocity distributions of the two breathing excited levels were simulated and fitted to the experimental data for various time slices. The ground state distribution was replaced by a smooth function fitted to the data for long storage times ($t > 5$ s), to avoid unphysical effects caused by small deviations between simulation and "cold data". Again a comparison to the H_3^+ data (Fig. 7.12) shows longer relaxation times for D_3^+, as expected. In chapter 8 the time-dependent populations of Fig.

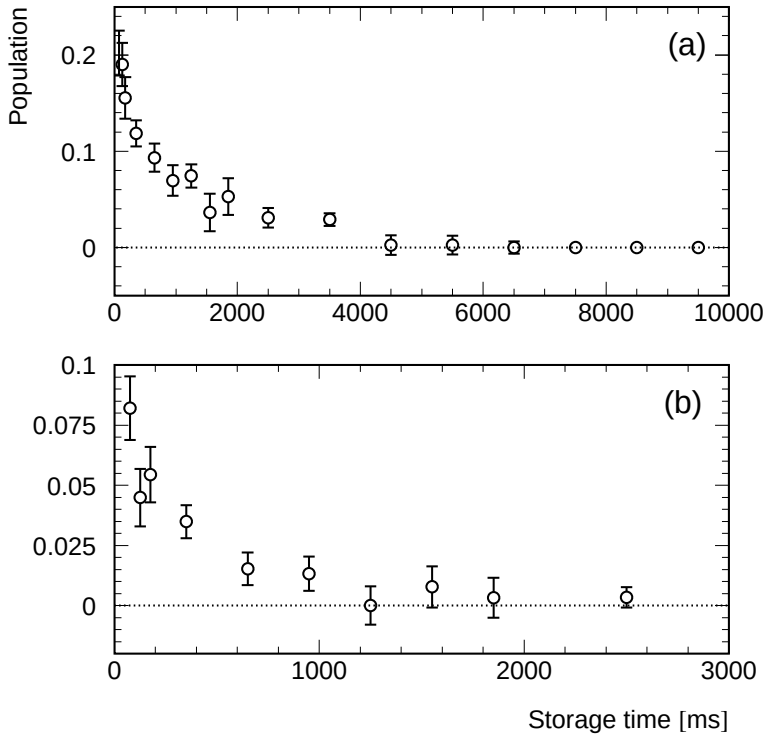

Figure 7.16: *Population fractions for (a) the first excited breathing level $(1, 0^0)$ and (b) the second level $(2, 0^0)$ of D_3^+, obtained by fitting superpositions of the simulated distributions to the measured v_a velocity distributions for storage time bins centered at the indicated data points.*

7.16 will be compared to an adjusted version of the H_3^+ rovibrational relaxation model.

7.4 DR fragment imaging of H_3^+

The DR imaging measurements give insight not only into the dissociation pattern (analyzed with Dalitz plots, see Fig. 4.5), they also reveal information on the internal excitation of the initial ion and the products (see chapter 6.4.3). In this chapter the emphasis will be set upon these aspects that are crucial for understanding the CEI results and for the definition of the initial conditions of the relaxation model that will be presented in the next chapter.
As mentioned before, the DR of ground state H_3^+ can proceed via two pathways

$$H_3^+ + e^- \rightarrow \begin{cases} H(1s) + H(1s) + H(1s) & +4.76\,\text{eV}\,, \\ H_2(v) + H(1s)\,, & +(4.92 \ldots 9.23)\,\text{eV}\,, \end{cases} \tag{7.10}$$

in the three-body breakup the energy release is fixed at 4.76 eV, since the hydrogen atoms are in a well-defined atomic state. Assuming that the H_3^+ ion has a certain amount of internal energy stored either in vibrational or rotational motion, this energy will be transferred into kinetic energy of the products and consequently a measurement of their momentum is a measurement of the internal energy of the H_3^+ molecule prior to electron recombination.
In the two-body channel the picture is more complicated, here the binding energy of the H_2 molecule is also available (4.49 eV for the ground state), but this binding energy again depends on the degree of internal excitation of the H_2 molecule. Considering only vibrational excitation for both the initial H_3^+ ion ($v = 0$) and the H_2 product, the kinetic energy release in this channel may vary between 9.23 eV (H_2 in $v = 0$) and 4.92 eV (H_2 in $v = 14$).
The situation is altered, if the H_3^+ ion brings more than 0.96 eV into the reaction, lifting the total available energy to 10.2 eV; above this threshold the hydrogen atom can be excited to the H(2s) state (see level scheme Fig. 4.4). Since in this case nearly all the energy is absorbed by the electronic excitation, one would expect a very small kinetic energy release corresponding to low fragment momenta.

7.4.1 Two-body breakup

For the analysis of the two-body events, two different sources of background have to be considered. The first are the inevitable residual gas collisions in the cooler section which

create 2 neutral and 1 charged particle. The second sort of background stems from the finite detection efficiency of the MCP detector. At MeV energies the efficiency is estimated to be ∼0.6; from this value it is obvious that for many three-particle breakups not all fragments will be detected. To discriminate against both background sources one can benefit from the sharp ion beam diameter after electron cooling. In order to identify a two-body event originating from the breakup into H_2 and H the mass-weighted distances have to yield a center of mass that lies within the limits of the beam diameter defined by the ion beam direction in the electron cooler and its angular divergence. The position of the ion beam center of mass at the detector is evaluated from the observed center-of-mass positions of the three-body events, since this measurement is basically free of background and wrong assignments (see section 7.4.2).

The first step is to assign the masses to the two fragments, because from the raw data it is not clear if a light spots stems from the impact of H_2 or H, but momentum conservation for the two-body decay implies that the heavier fragment has to be closer to the center of mass. At this stage the sample is still contaminated by three-body events with one particle undetected and residual gas events.

To surpress this background a strict center-of-mass (CM) cut was applied and only events with storage times greater than 3 s were considered, to make sure that the phase space cooling is finished and the beam diameter has reached the final value of ~ 0.8 mm. With these two restrictions the data sample was reduced to ~ 48000 two-body events, leaving enough statistics for the projected distance distribution (see Fig. 7.17(a)). Further improvement was achieved, by subtracting the distance distribution for a class of events lying outside the CM cut from the two-body distribution. The subtracted distribution was scaled by a factor that was derived by fitting it to the data at large distances D that cannot be achieved by the KER available.

The distribution resulting from this procedure was fitted for D>10 mm by projected distance functions of the kind depicted in Fig. 6.5 including all 14 vibrational states neutral H_2 can host and deriving relative populations as fit parameters. The outcome of the fit is shown in Fig. 7.17(a) together with three sample shapes of the fitted functions. It can be seen that the fit reproduces the measured shape excellently for D>10 mm, while below this limit a shoulder appears that cannot be sampled by any of the fitted functions. The relative populations plotted in Fig. 7.17(b) show a broad distribution peaking around $v = 5$. The shape of this distribution is in good agreement with a statistical model published by Strasser *et al.* [Str01b]. Furthermore the peak position is in agreement with a recent ab initio theoretical DR calculation of Kokoouline *et al.* [Kok01].

The shoulder at small distances was found to be independent of the cuts that were applied

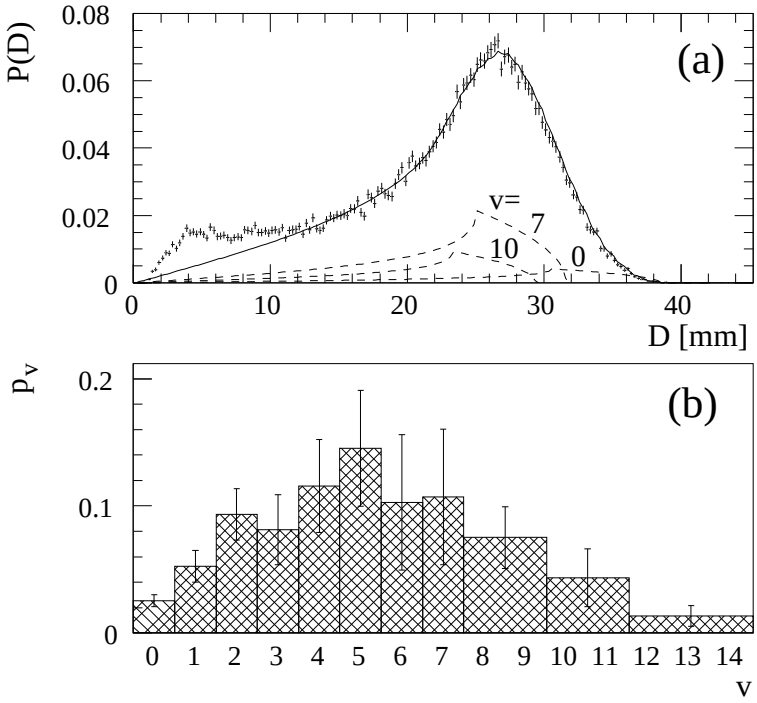

Figure 7.17: *(a) Projected distance distribution of the two-body breakup $H_3^+ + e^- \rightarrow H_2(v) + H$ for storage times >3s. The data was CM cut and fitted for D>10mm with functions according to Eq. 6.12. Three sample shapes for v=0,7,10 are plotted (dashed lines). (b) Relative populations of the H_2 vibrational states obtained from the fits. Rotational excitation was not taken into account, for histogram bins spanning more than one unit in v, the relative populations were set to be equal in the fitting routine. Picture taken from [Str01a]*

and also of different electron cooler settings. From this experimental evidence – together with the results of the three-body breakup, presented below – the most likely explanation is the presence of highly excited rotational states (vibrational excitation is ruled out by the CEI results) with up to $\sim$1eV rotational energy that lifts the total energy available above 10.2 eV, allowing the dissociation to proceed through the H(n=2)+H_2 ($^1\Sigma_g^+$) channel where the greatest part of the energy would be converted in electronic excitation rather than in kinetic energy.

Measurements with a storage ion source that will be presented in chapter 12 showed a dependence of the intensity in the shoulder on the source conditions while the storage ring and cooler parameters remained unchanged, supporting strongly the conjecture that the appearance of the shoulder is connected to internal excitation transferred to H_3^+ in the formation process. This interpretation is also backed by the existence of long-lived, highly excited rotational states in the model of H_3^+ rovibrational decay introduced in chapter 8 and by the prediction of Kulander and Guest [Kul79] that the H(n=2) channels

will absorb all the flux as soon as they are energetically accessible. The rotational energy is not taken into account in the fitting procedure (Fig. 7.17 (b)), neither for the initial H_3^+ state, nor for the H_2 product, thus the relative populations are assumed to be accurate within $\triangle$v=$\pm$1.

7.4.2 Three-body breakup

In contrast to the two-body breakup, the three-body data is practically background free, since random coincidences with residual gas events will most likely be rejected by a strict center of mass cut, reducing the three-body data set to $\sim$67000 events. Also, since in this case the outcome are three identical particles, no identification of the fragments is needed. However, the analysis is complicated by the fact that the expected distance distributions cannot be treated by analytical expressions like in the two-body case, since the energy sharing between the three fragments is only restricted – but not fully determined – by momentum conservation. The center of mass is calculated from the particle coordinates x_i, y_i at the detector

$$X = (x_1 + x_2 + x_3) \tag{7.11}$$

$$Y = (y_1 + y_2 + y_3) \ , \tag{7.12}$$

The distributions of the CM value were found to be Gaussian-shaped with a width of σ_x=0.6 mm and σ_y=0.4 mm [Str02].
In the three-body case the observables – apart from the angular correlations represented in the Dalitz plot, see Fig. 4.5 – are the projected squared distances R_i^2 in the CM frame that are related to the transverse kinetic energy per fragment by

$$R_i^2 = (x_i - X)^2 + (y_i - Y)^2 = (S\, v_{\perp,i}/v_{beam})^2 = 3S^2 E_{\perp,i}/E_{beam} \tag{7.13}$$

where $v_{\perp,i}$ and $E_{\perp,i}$ stand for the transverse velocity and kinetic energy of fragment i and S is the distance from the point of dissociation to the detector. The total transverse kinetic energy is obtained by summing over all fragments

$$R^2 = \sum_i R_i^2 = 3S^2 \, \frac{E_\perp}{E_{beam}} \tag{7.14}$$

A Monte-Carlo simulation was performed to investigate the projection of the fragment velocities onto the detector plane. For a first step the recombination was assumed to start from rovibrationally cold H_3^+ and zero-energy electrons, thus the total KER was kept fixed at 4.76 eV. The simulation used randomized dissociation geometries in an isotropically

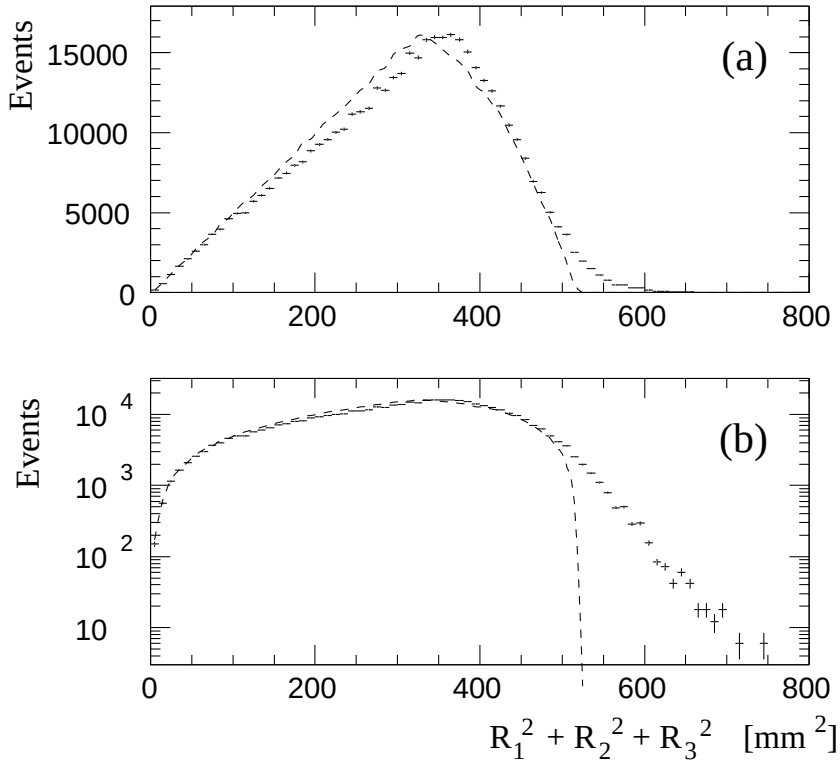

Figure 7.18: *Projected squared distance distribution of the three-body breakup $H_3^+ + e^- \rightarrow H + H + H$ in linear (a) and logarithmic (b) scale. Only storage times >3 s are plotted and a 1-sigma CM cut was applied. The dashed line represents the outcome of a rotationless Monte-Carlo simulation for randomized dissociation geometries and isotropic orientation.*

oriented dissociation plane. Experimental parameters like the finite length of the electron cooler and the position resolution of the detector were included, as well as the fact that hits with distances of less than 1 mm can not be resolved.

The experimental distribution is plotted in Fig. 7.18 as well as the result of the Monte-Carlo simulation (dashed lines). While the shape of the distributions show an overall qualitative agreement, they also differ distinctly. It can be shown that the shape for R^2 , 500 mm^2 is heavily depending on the dissociation geometry [Str01b], and indeed a detailed analysis of the dissociation dynamics using Dalitz type coordinates [Str01a] show a preference of linear geometries. Therefore part of the differences in the form of the distribution might be attributed to a dominance of certain dissociation patterns, that is not included in the simulation.

To draw conclusions on the internal excitation of the H_3^+ ions – being in the focus of this work – the high distance part with $R^2 > 500$ mm^2 is more informative. As mentioned above, the three-body breakup starting from the H_3^+ ground state into three (1s) hydrogen atoms is connected with a well defined KER of 4.76 eV. This energy, assuming a dissoci-

ation at the entrance of the electron cooler that yields the maximum flight time, would result in a R^2 value of $(517 \pm 10)\,\mathrm{mm}^2$. The experimental distribution shows a tail beyond that limit, that cannot be explained by experimental artefacts or special dissociation patterns, since it reflects the maximum KER that is available. In Fig. 7.18(b) the excess energy can be seen even more pronounced in logarithmic scale, revealing the functional form to be exponential.

To reproduce the high energy tail, the Monte-Carlo simulation was refined to include a rotational Boltzmann distribution. The rotational energy levels as a function of the total angular momentum J and its projection onto the molecular symmetry axis K were approximated by a simplified symmetric top formula [Kro92]

$$E_{rot} = B\,J(J+1) - (B/2)\,K^2\,, \tag{7.15}$$

with $B = 0.533\,10^{-2}\,\mathrm{eV}$ chosen such, that Eq. 7.15 is in fair agreement ($\triangle E{=}\pm 10\,\mathrm{cm}^{-1}$ for states below $1200\,\mathrm{cm}^{-1}$) with the result of variational calculations of the rotational energy levels [Pol99]. The outcome of the simulation for three different temperatures is compared to the experimental distribution in Fig. 7.19 At a Boltzmann temperature of 0.23 eV the simulation can reproduce the high energy tail (see Fig. 7.19(b)) and it also improves the agreement at lower distances significantly (Fig. 7.19(a)). This finding is interpreted by the existence of long-lived rotational states with an average energy around 0.23 eV, and with the highest rotational energies being as high as 1 eV. This amount of

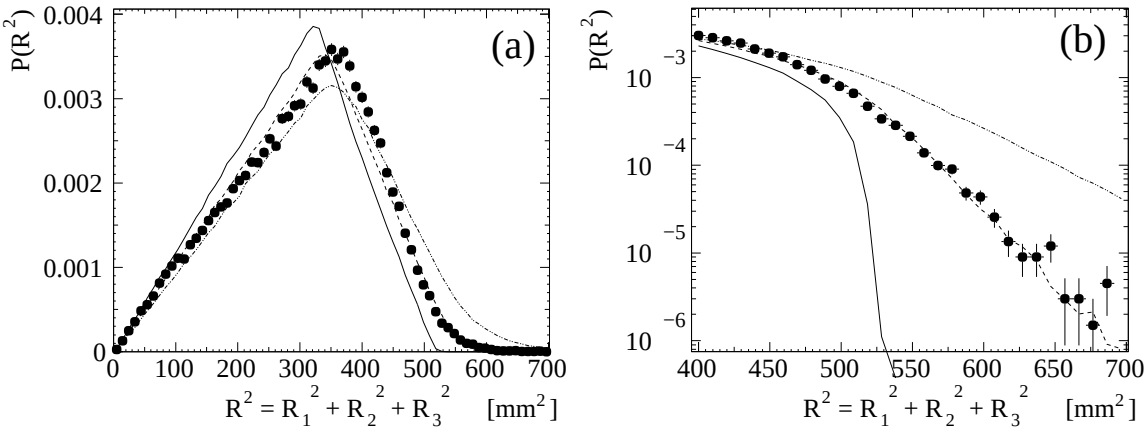

Figure 7.19: *Distribution of the total squared projected distance for the three-body breakup. Also plotted are Monte-Carlo simulations for three different Boltzmann temperatures of 0 eV (solid line), 0.23 eV (dashed line) and 0.5 eV (dotted line). The agreement of the excess energy tail with the simulation for 0.23 eV temperature is shown in logarithmic scale (b).*

excess energy is needed to explain the extension of the tail in the three-body channel as well as the excitation of the H(2s) atomic state in the two-body breakup, that manifests itself in the shoulder at small distances (see Fig. 7.17).
Evidence for the existence of long-lived rotational states comes also from a model of H_3^+ rovibrational decay that will be introduced in the next chapter.

Chapter 8
Rovibrational relaxation model

The last chapter raised results that await a physical explanation. The combination of DR imaging and CEI measurements implies that the molecular ions in the storage ring are vibrationally cold already after 2 s of storage, while they host rotational excitations up to 1 eV for much longer times. In this chapter it will be examined, if this behaviour can be explained by theoretical predictions.
In order to set up a complete model of the rotational and vibrational cooling of H_3^+, detailed information of all the states that are involved and all the possible transitions is required. Fortunately in the case of H_3^+ this data is available in the form of a linelist that was calculated at University College London by Neale *et al.* [Nea96] mainly for the interpretation of spectroscopic measurements.

8.1 The UCL linelist for H_3^+

The linelist of Neale *et al.* considers all H_3^+ states below 15000 cm^{-1} and $J \leq 20$. Between these states 3.19 million transitions were calculated, restricted only by rigorous dipole selection rules ($\triangle J = 0, \pm 1$). Since spectroscopical applications were in the focus of that work, the weakest transitions with an Einstein A-coefficient of less than 10^{-7} were removed, leaving ~3 million transitions.
Table 8.1 shows an excerpt of the comprehensive linelist, where J' and E' denote the angular momentum quantum number and the energy of the upper state, likewise J'' and E'' stand for the lower state, ω is the transition energy, A_{if} stands for the Einstein coefficient of spontaneous decay, and g denotes the spin degeneracy. For H_3^+ g should be either 2 or 4, but the method used for the calculation did not make these assignments. Most of the transitions with $E'' < 5000$ and $J', J'' < 10$ were assigned with a dedicated algorithm starting from a few hand-assigned states. However, since the number of states increases drastically with energy, this procedure left the vast majority of the ~3 million

J'	E' (cm^{-1})	J''	E'' (cm^{-1})	ω (cm^{-1})	A_{if} (s^{-1})	g
10	5559.156	9	2702.08	2857.0759	0.1864E+01	2
8	7425.172	8	4567.275	2857.8973	0.1001E-01	2
6	6650.963	5	3793.033	2857.9299	0.2614E+02	2
11	7592.384	11	4734.082	2858.3022	0.4208E-06	8/3
5	6679.233	4	3820.803	2858.4294	0.7224E+02	4
9	7074.147	10	4215.239	2858.9074	0.1016E-06	8/3
7	6736.544	7	3877.035	2859.5084	0.1871E-03	2
12	7494.607	12	4634.287	2860.3195	0.1253E-04	8/3
7	7436.699	6	4575.975	2860.7237	0.3921E+02	2
2	7703.346	1	4842.568	2860.7781	0.5750E-02	2
7	7317.772	7	4456.901	2860.8705	0.2691E+00	2
8	5257.293	9	2396.415	2860.8785	0.1084E-01	2
11	7157.95	10	4296.621	2861.3287	0.2814E-01	8/3
5	6529.265	4	3667.123	2862.1418	0.2532E+02	2

Table 8.1: *Excerpt from the UCL linelist [Nea96]. Only states with $E'' \leq 5000\,cm^{-1}$ were chosen.*

transitions unassigned. In this case the degeneracy was set to $g = 8/3$, which is a compromise between the possible values 4 and 2, taking into account the fact that there are roughly twice as many E states ($g = 2$) than A_2 states ($g = 4$) [Sid92, Mil90]. The calculation was performed using the DVR3D program [Ten95b] that employs the method of discrete variable representation. The underlying effective potential surface is that of Dinelli *et al.* [Din95], the dipole surfaces were taken from ab initio calculations of Röhse *et al.* [Roe94]. The error of the energies was estimated to be $\sim 0.05\,cm^{-1}$ in the region below $5000\,cm^{-1}$, $\sim 0.2\,cm^{-1}$ at $10000\,cm^{-1}$ and $1\,cm^{-1}$ at $15000\,cm^{-1}$. The whole list is availabe in 16 files via FTP in directory `ftp://ftp.tampa.phys.ucl.ac.uk/pub/astrodata/h3+`. Further details are given in the original publication [Nea96].

As can be seen from Tab. 8.1 the only quantum number that is given to label rovibrational states is the angular momentum J, while for a complete characterization of H_3^+ states besides the vibrational quantum numbers ν_1, ν_2, l also $G = |K - l|$ is needed (see chapter 5). As a consequence it turns out to be extremely difficult to derive information on vibrational cooling and specific properties of the rotational states involved from the linelist alone.

One of the goals of a model for rovibrational decay would be to get a better understanding

of the influence of rotational excitation on the vibrational lifetimes that were measured with the CEI method. For that purpose in particular, the breathing excited states would have to be treated separately. Fortunately, the identification of vibrational states was made possible by another publication of Dinelli *et al.* [Din97] which is based on the same potential surface, where all the energy levels up to $9000\,\mathrm{cm}^{-1}$ and $J \leq 9$ are assigned.

8.2 Modelling the rovibrational cooling of H_3^+

For a complete model of the rovibrational cooling of H_3^+ starting from an initial (not necessarily thermal) distribution, one has to set up a system of differential equations that connects all the levels according to their spontaneous decay rates. In a first step, a PERL script was written that goes through the line list and extracts all the energy levels. The criterion for two energy levels found in the list to be different was that either the energy has to differ by more than $0.01\,\mathrm{cm}^{-1}$, or the J quantum number has to be not equal. The search was restricted to $12000\,\mathrm{cm}^{-1}$ ($\sim$17200 K), since in any event for the states above $9000\,\mathrm{cm}^{-1}$ no assignment could be made. In that way the number of relevant transitions for the model was reduced from $\sim$3 million to $\sim$245,000.

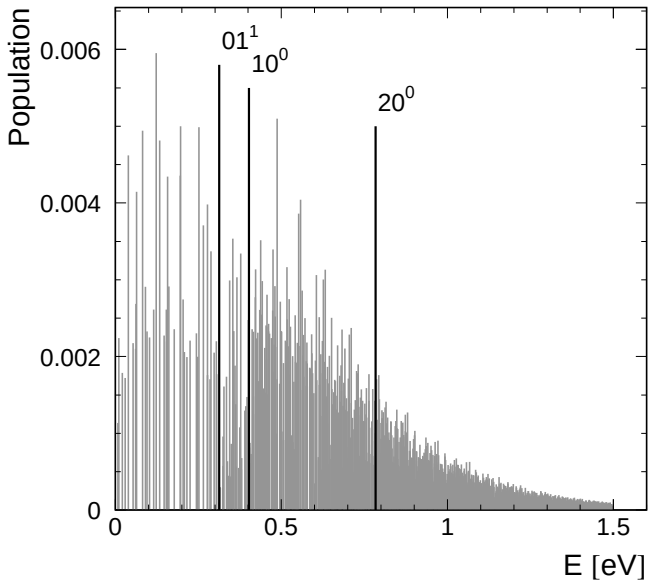

Figure 8.1: *Stick diagram of all the H_3^+ levels up to $12000\,\mathrm{cm}^{-1}$. The length of the bar gives the relative population according to a Boltzmann distribution with 0.23 eV temperature. The three black lines indicate the opening of the first vibrational bending mode ($0,1^1$), the first breathing mode ($1,0^0$) and the second breathing mode ($2,0^0$), respectively.*

To determine initial state populations as a starting condition for the model, a reasonable assumption on the distribution has to be made. As the DR fragment imaging results could be reproduced by including a Boltzmann weigthed rotational excitation with a temperature of 0.23 eV, the same distribution was chosen as initial condition for the model. In Fig. 8.1 all the states taken into consideration are plotted as a stick diagram, representing their relative populations including the $(2J+1)$ multiplicity and the spin degeneracy. Note that especially in the high energy region many states overlap, so that the fractional contribution of higher energies cannot be judged from this plot. Also indicated in the diagram are the openings of the first bending $(0,1^1)$ and breathing vibrations $(1,0^0)$ as well as the onset of the second breathing mode $(2,0^0)$.

The lifetime of each state i was derived by sorting out all the transitions from the UCL list with this particular state as the upper level. The lifetime T_i was caculated as the reciprocal of the sum over the corresponding Einstein A coefficients

$$T_i = \frac{1}{\sum_f A_{if}} \,. \tag{8.1}$$

For states without decay route in the list the lifetime was set to $9.99 \cdot 10^6$ s, since all transitions with Einstein A coefficients $< 10^{-7}\,\mathrm{s}^{-1}$ were discarded from the UCL files.

In addition all n transitions with state i as lower level were grouped into a vector, completing the differential equation for the time-dependent population of that particular state

$$\frac{d\,P(i)}{d\,t} = -\frac{1}{T_i} P(i) + \sum_{k=1}^{n} P(k) \cdot A_{ki} \,. \tag{8.2}$$

Since H_3^+ has no dipole moment, the coupling to the ambient 300 K black-body radiation of the storage ring is very weak and is neglected at this stage (see next section). The complete set of differential equations for the ~2500 states was brought into a FORTRAN compatible syntax (see Tab. 8.2) and compiled into the DRKSTP routine of the CERN program library [Ers94]. This routine employs the *Runge-Kutta* method for numerical integration of first-order differential equations [Zur65, Hil56].

In Fig. 8.2 the result of a calculation up to 60 s is plotted. To simplify the interpretation the states were filled into histograms with a bin size of ~6.5 meV. In contrast to the stick diagram of Fig. 8.1, in this representation the integration of the shaded area gives meaningful results. Comparing the initial distribution of Fig. 8.2 (a) with Fig. 8.1 the opening of the first vibrational mode is more pronounced, as well as the fractional population of highly excited states. Also the cutoff at 12000 cm^{-1} corresponding to ~1.5 eV is clearly visible.

```
f(1)   =  -pop(1)*1.000001000001e-07        ⟵ decay
          +pop(1454)*0.1738E-03  ⎫
          +pop(1788)*0.2517E-02  ⎪
                    ⋮            ⎬          ⟵ feeding
          +pop(1880)*0.2073E+01  ⎪
          +pop(1892)*0.1904E+00  ⎭
f(2)   =  -pop(2)*1.000001000001e-07
       =  +pop(1471)*0.5318E+00
                    ⋮
          +pop(111)*0.9863E+02
   ⋮                ⋮
f(2545)=  -pop(2545)*199.0456761176
```

Table 8.2: *Excerpt from the set of differential equations to be compiled into the DRKSTP cernlib routine, where* `pop(i)` *stands for the population of state i and the real numbers are the inverse lifetimes or feeding rates, respectively, extracted from the UCL linelist.*

The average energy of the initial distribution amounts to 0.74 eV[1] and decreases in the following time bins due to fast initial decay to 0.31 eV after 10 s, while it is reduced only slightly to 0.29 eV after 60 s. This behaviour is compatible with the observation of the DR fragment imaging experiments, where an excess energy of ∼0.3 eV temperature was found to be stable up to 40 s [Str02]. In retrospect the choice of the initial temperature is confirmed by this finding, while the choice of a Boltzmann distribution is motivated by simplicity and the fact that the KER of the long-lived rotational states could be approximated by a Boltzmann distribution. However, the detailed distribution of internal states produced in the ion source is beyond the resolution of the DR experiment.

8.3 Vibrational cooling of H_3^+ and D_3^+

To distinguish between rotational and vibrational states, and to derive lifetimes for the vibrational breathing modes, the assignments given in [Din97] were used. For the first

1 The average energy is higher than the initial 0.23 eV temperature, because the density of states increases dramatically with energy and the high-lying rotational states have large multiplicity factors $(2J+1)$

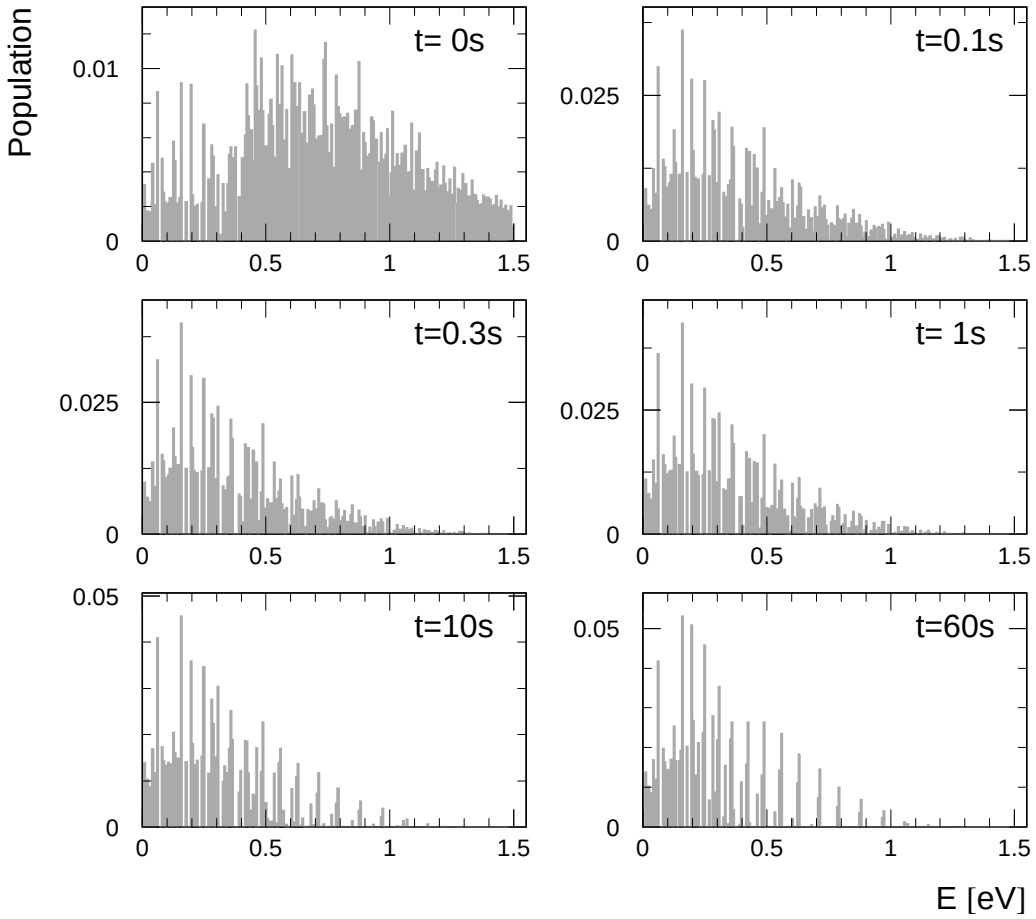

Figure 8.2: *Rovibrational energy distributions (relative populations in ~6.5 meV bins) starting with an initial thermal distribution (t=0 s) for a temperature of 0.23 eV; later distributions after 0.1 s, 0.3 s, 1 s, 10 s and 60 s.*

breathing mode, all levels with $\nu_1 = 1$ and energies below $9000\,\mathrm{cm}^{-1}$ were identified, namely all states with vibrational quantum numbers $(1,0^0)$, $(1,1^{\pm1})$, $(1,2^0)$ and $(1,2^{\pm2})$, amounting to 248 states in total. Distinctly less states were found for the second breathing mode; since its band origin is at $6323\,\mathrm{cm}^{-1}$ while the assignable region ends at $9000\,\mathrm{cm}^{-1}$, the effective energy range is much smaller. Thus only 73 states with quantum numbers $(2,0^0)$ and $(2,1^{\pm1})$ were identified. As a consequence the lifetime prediction of the model is expected to be less reliable for the second breathing mode, because especially high-lying rotational states sitting on top of the vibrational excitation are not included.

In Fig. 8.3 time-dependent distributions are plotted for the same initial temperature of

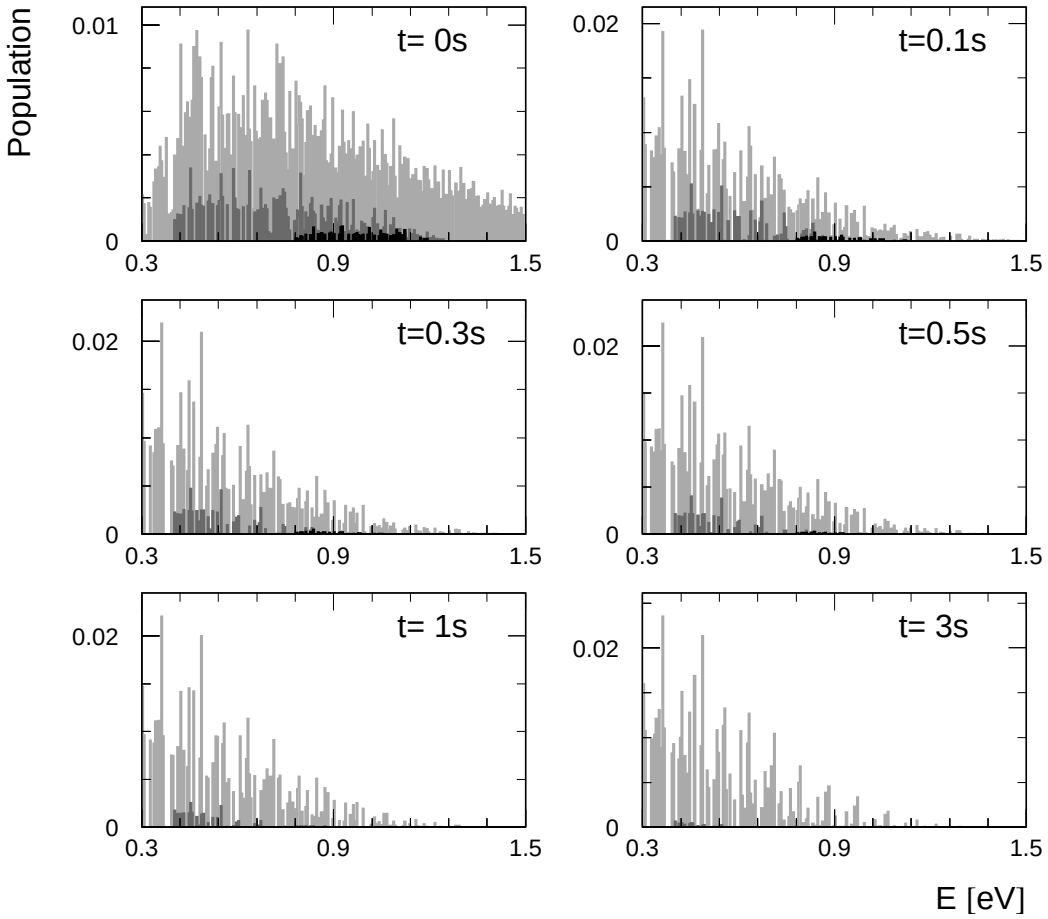

Figure 8.3: *Rovibrational energy distributions (relative populations in ~5 meV bins) starting with an initial thermal distribution (t=0 s) for a temperature of 0.23 eV. Only the energy and time range relevant to vibrational excitation is plotted. All rovibrational levels are drawn as light shaded areas, the states with assigned breathing quantum numbers $\nu_1 = 1$ (darker shaded areas) and $\nu_1 = 2$ (black areas) are superimposed.*

0.23 eV as above. Note that the scale of the abscissa was changed to the energy range from 0.3 eV to 1.5 eV relevant to vibrational excitation. The assigned levels with breathing mode excitation $\nu_1 = 1$ and $\nu_1 = 2$ are plotted in dark grey and black, respectively. In the initial distribution a considerable population of 13.7 % is found for the first breathing mode, while the second breathing mode has a fraction of 2 % (in comparison to Ref. [Kre02], the model has been revised and additional states with breathing and bending excitation ($2,1^{\pm 1}$) were assigned, raising the fractional initial population from 1.6 % to 2 %).

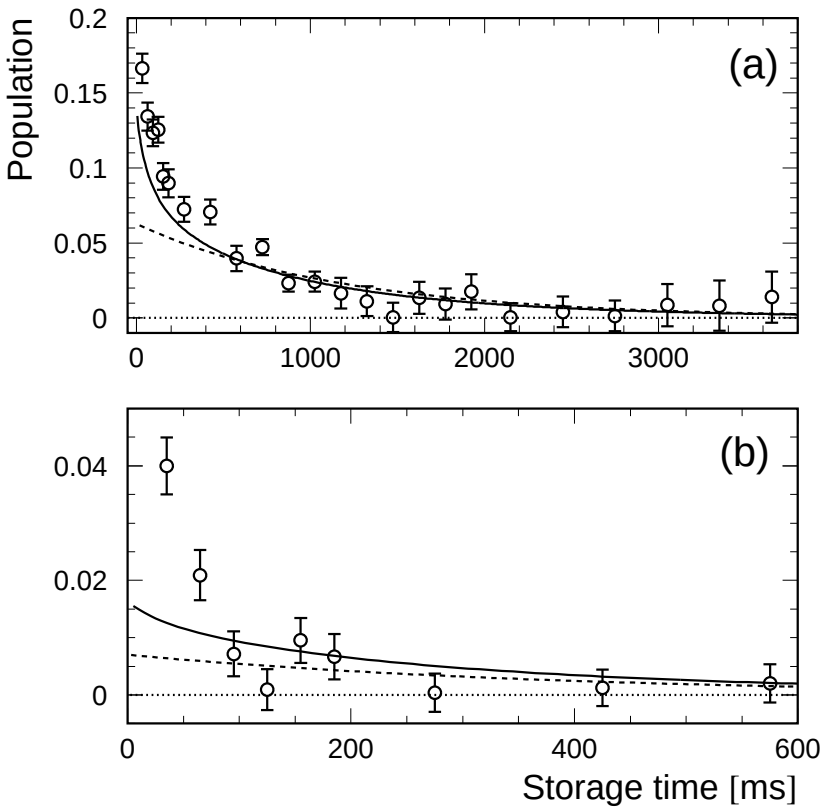

Figure 8.4: *Population fractions for the first (a) and second (b) breathing level, obtained with the CEI method. The solid lines show the unscaled results of the rovibrational relaxation model (initial temperature 0.23 eV). The dashed lines show single-component exponentials for the rotationless decay time constants of the (1,0^0) and (2,0^0) levels and a constant scaling factor fitted to the data at t> 500 ms for (1,0^0) and t> 70 ms for (2,0^0). A zero line (dotted) is drawn for clarity.*

It can be seen that both fractions are rapidly decreasing with time and while for the first breathing mode a population of 0.4 % still exists after 3 s, the second breathing mode has dropped to 0.07 % already after 1 s. From the rotationless calculations [Din92, Ten95a] as well as from the UCL linelist it is obvious and conclusive that the two breathing excitations are the most long-lived vibrational modes due to the lack of a dipole moment. One conclusion from the decay behaviour is therefore that the later distributions in Fig. 8.2 are essentially free of vibrational excitation and consist purely of rotational states. The nature of these long-lived states as well as their lifetimes will be discussed in the next section.

In order to compare the vibrational lifetimes to the experimental values from the CEI

measurement, the breathing mode populations were integrated for various time slices. The result is shown in Fig. 8.4 for both breathing modes together with the single-component exponential of the rotationless calculation [Din92]. The populations predicted by the new model were left unscaled and can be directly compared to the CEI result, while the purely exponential decay curves for the rotationless decay constants of 1.18 s $(1,0^0)$ and 0.38 s $(2,0^0)$ were fitted to the data, varying a constant factor for the vertical scale. In both cases the new model is closer to the experimental values, furthermore the decay of the first breathing mode even quantitatively agrees well with the measurement, given the uncertainties inherent in the choice of the exact initial distribution. However, both curves are lower than the measured populations at short times, indicating that a higher initial temperature or a non-thermal distribution might prevail. Unfortunately the restricted model space renders checks at higher temperatures useless, since already a decay curve for an initial Boltzmann distribution of 0.3 eV is practically indistinguishable from the present one.

For the second breathing mode the agreement is much worse, especially at short times. The key problem here has already been addressed before, namely the limited energy range for which assignments are available. This restriction is supposed to influence the short time behaviour in particular, since highly-excited states that might lead to fast decay are not included. In addition, also the experimental values are less reliable for the second breathing mode, firstly because the simulated curve for $v_1 = 2$ is broader than for $v_1 = 1$

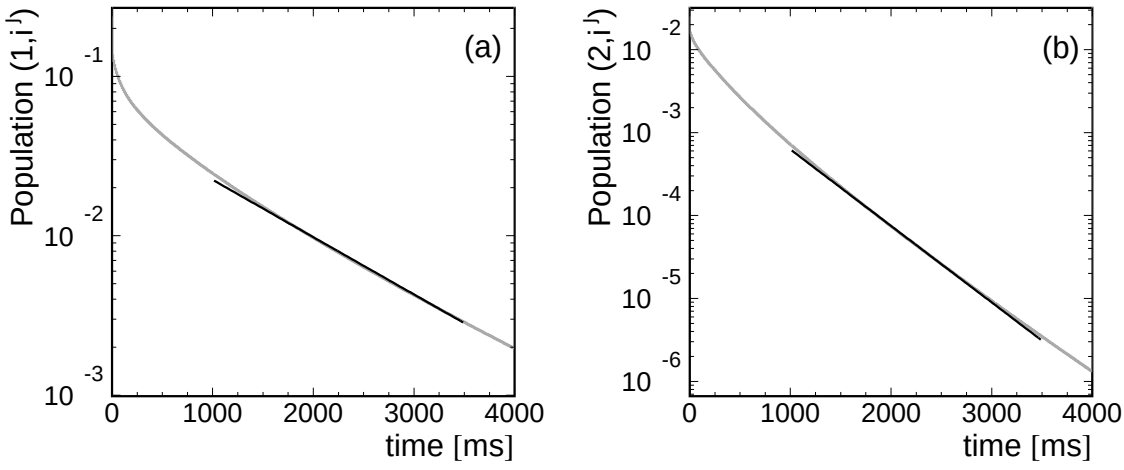

Figure 8.5: *Result of the relaxation model (grey) for the decay of the first (a) and second breathing mode (b) in logarithmic scale. An exponential function (black line) was fitted to the asymptotic curves from 1500-3500 ms, revealing asymptotic lifetimes of 1.2 s for the first breathing level and 470 ms for the second level.*

and any short-lived contribution from higher excitations $v_1 > 2$ will likely be attributed to the second breathing mode. Secondly, the focus for the second breathing mode is at shorter times anyway, where also bending mode excitations may still be present and disturb the fitting.

From the above results the tendency of vibrational decay to speed up in the presence of rotational excitations, seems obvious. It is interesting to note that for the reverse effect, namely the existence of nominally forbidden rotational lines through intensity stealing from vibrational modes, H_3^+ is a classic case [Bun98]. However, a consistency check can be done if one compares the outcome of the rotationless calculation with the predictions of the complete model for long times. After the fast initial decay both calculations should merge (as can be seen already in Fig. 8.4 at longer times) and yield similar asymptotic lifetimes for both breathing modes.

In Fig. 8.5 the decay curves for both breathing excitations are plotted in logarithmic scale, together with single-component exponentials fitted to the curves for 1500-3500 ms. The fit yields lifetimes of 1.2 s for the first level $(1,i^j)$ (i,j arbitrary), and 470 ms for the second $(2,i^j)$. Compared to the values of the rotationless calculation of 1.18 s and

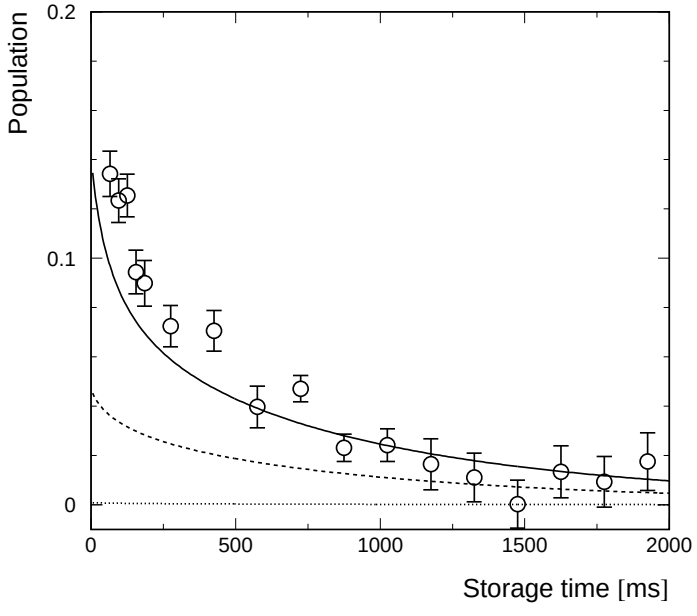

Figure 8.6: *Measured population fraction for the first breathing level. The lines show the unscaled results of the rovibrational relaxation model for different starting conditions. The solid line stands for an initial temperature of 0.23 eV, the dashed line for 0.1 eV and the dotted line represents room temperature or 0.026 eV.*

380 ms, respectively, the agreement is excellent, given the complexity of the system and the accuracy of the rotationless approach [LeS92].

The necessity to assume starting conditions with temperatures of at least 0.23 eV can be demonstrated by applying the relaxation model to different Boltzmann distributions. In Fig. 8.6 three different temperatures are compared to the CEI results. Obviously the highest temperature comes closer to the experiment than the other two curves of 0.1 eV and 0.026 eV. Even after scaling the curves with a constant factor, the decay would be slower than observed if low initial temperatures are used. The latter value – corresponding to room temperature or 300 K – coincides in this representation with a zero line. At this point the argument could be turned around. Believing the transitions of the UCL linelist, the relatively short breathing mode lifetimes measured by CEI give clear evidence for substantial rotational excitation.

Vibrational cooling of D_3^+

In chapter 7 time-dependent populations of the $(1,0^0)$ and $(2,0^0)$ breathing levels were derived also for the D_3^+ isotopomer. Due to a lack of detailed theoretical information on vibrational lifetimes of D_3^+, a simple formula was used to estimate that the H_3^+ lifetimes should be scaled by a factor ~ 2.6 to respect the different level spacings. The same simple estimate was used to scale the outcome of the rovibrational relaxation model to D_3^+.

However, since the initial population assumed in the model is calculated for the particular level structure of H_3^+, the initial populations of D_3^+ can not be well accounted for. In order to check whether the adjusted time behaviour of the model is in agreement with the experimental decay, a constant factor was fitted to the model curve, allowing the initial population of both levels to be adjusted to the experiment. The result is plotted in Fig. 8.7, showing that the time dependence of both levels is well described by the model.

This finding is not surprising, because the model includes several hundreds of states, so that a difference in the coupling strengths of particular rovibrational states is likely to be washed out by statistics. It should be noted, that with this method only the time behaviour can be checked, and while the agreement in Fig. 8.7 is obviously better than in the case of H_3^+ (see Fig. 8.4), it carries substantially less information and must be considered less valuable, because in the case of H_3^+ unscaled results of the rovibrational model are plotted.

Concerning the second breathing mode, one aspect is remarkable; the initial population is distinctly higher (8 %) compared to H_3^+ (4 %), the reason for this enhancement might lie in the difference of the breathing mode level energies for both isotopomers. A simple

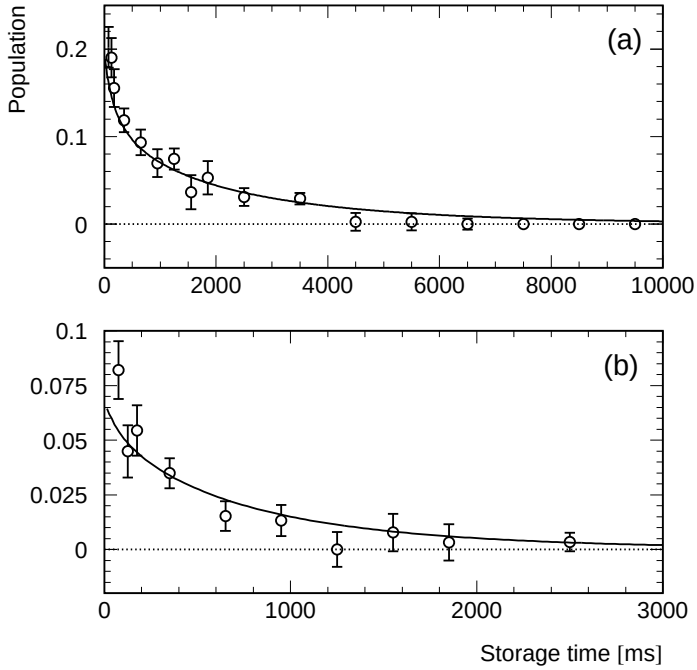

Figure 8.7: *Population fractions for the first (a) and second (b) breathing level of D_3^+, obtained with the CEI method. The solid lines show the results of the rovibrational relaxation model for H_3^+ (initial temperature 0.23 eV) that were scaled by a factor 2.6 on the time axis. To account for the difference in the initial populations of both levels with respect to H_3^+ the curves were multiplied by a constant factor that was fitted to the experimental data. A zero line (dotted) is drawn for clarity.*

calculation of the ratio of the expected populations of the $(2,0^0)$ vibrational band origin (energies given in chapter 7.3.2) in a 0.23 eV Boltzmann distribution gives

$$\frac{n(2,0^0)[D_3^+]}{n(2,0^0)[H_3^+]} \approx \frac{\exp\left(-\dfrac{E(2,0^0)[D_3^+]}{\langle E\rangle}\right)}{\exp\left(-\dfrac{E(2,0^0)[H_3^+]}{\langle E\rangle}\right)} = \exp(-2.5+3.4) \approx 2.5\,, \tag{8.3}$$

explaining qualitatively the enhanced population. This result should not be over-interpreted, since a similar calculation for the first breathing mode gives a factor of 1.6 which is not found in the data (although the initial population is slightly higher for D_3^+ there, too). For a more detailed comparison, a comprehensive linelist for D_3^+ would be required.

8.4 Long-lived rotational states

Besides the predictions for the vibrational lifetimes, the relaxation model reveals another very interesting aspect. In the DR fragment imaging experiments two strong hints for considerable rotational excitation was found. Firstly the excess energy tail in the three-body breakup and secondly the shoulder in the two-body breakup that was attributed to a new channel, namely to $H_3^+ + e^- \Rightarrow H(n=2) + H_2(^1\Sigma_g^+)$, which is energetically open only if at least 0.96 eV internal energy is brought into the system. Both features were found to be stable for storage times up to 10 s for H_3^+ and a similar measurement with D_3^+ showed that the excess energy (temperature 0.3 eV) as well as the shoulder in the two-body channel survived even 40 s of storage [Str02].

As pointed out before, these findings are well reproduced by the relaxation model, where the average energy from 10 s to 60 s was approximately stable at 0.3 eV. In addition high-lying rotational states were found, that might transfer enough energy in the system to electronically excite atomic hydrogen. After 60 s of radiative cooling (see Fig. 8.2) still roughly 1 % of the total population is in states with energies ≥ 0.96 eV that is needed for the electronic excitation. However, the shoulder in the two-body breakup (Fig. 7.17) contains an estimated fractional intensity of 5 % of the DR signal. This comparison implies that the relative rate coefficient for rotationally excited states might be distinctly higher than those of the lower states, or especially the ground state.

To learn about the character of the long-lived states and the lifetimes one can expect, it is

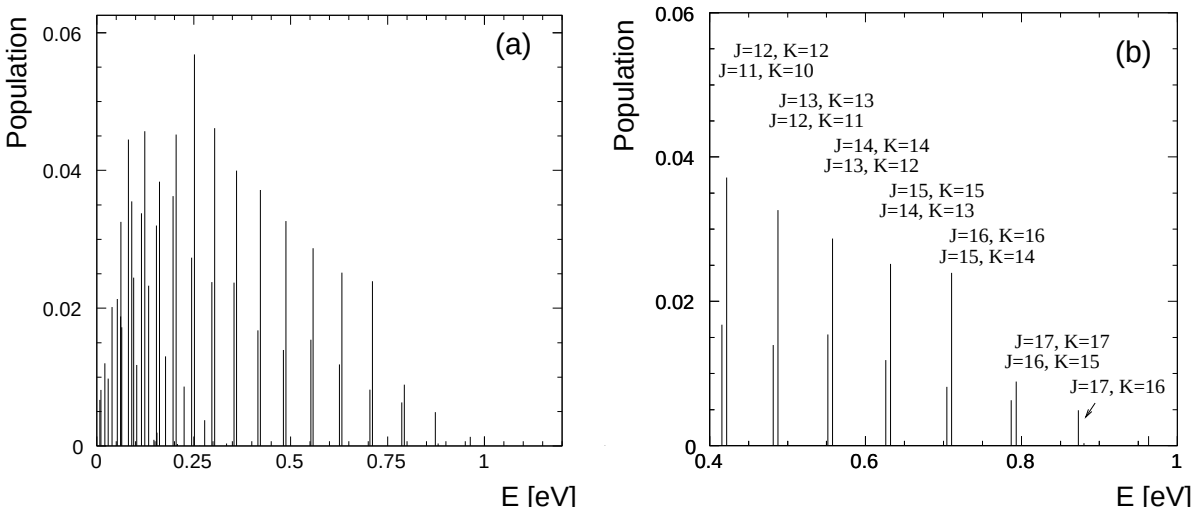

Figure 8.8: *(a) Stick diagram of the energy distribution resulting from the relaxation model after a time of 1800 s. The initial temperature was again set to 0.23 eV. (b) High energy region, including assignment of the doublet structures arising from the long-lived rotational states.*

useful to do a calculation for times that are not accessible in a storage ring measurement. In Fig. 8.8(a) the energy distribution for a relaxation time of 1800 s is plotted. It can be seen that the number of states has decreased, while the average energy is still as high as 0.26 eV. Compared to the distribution after 10 s where the mean energy was already at 0.3 eV – but distributed among many states – it means that the energy is essentially trapped in a few metastable states.

Tab. 8.3 summarizes all states with a population $\geq$0.01 % after 1800 s. Although only 48 states are above that threshold, they account for 99.98 % of the total population. For many of these states no decay route was found in the UCL linelist, and thus a lower limit for the lifetime of $>1 \cdot 10^7$ s is given (since the list contains no transitions with an Einstein coefficient $<1 \cdot 10^{-7}\,\mathrm{s}^{-1}$, see section 8.1).

All the states listed are purely rotationally excited ($\nu_1 = \nu_2 = l = 0$), and thus the assignment is complete with the rotational quantum numbers J, K and the spin degeneracy g. As mentioned before, the states were assigned according to a publication [Din97] that contains all states up to $9000\,\mathrm{cm}^{-1}$ and $J < 12$. The K values for the high J states were identified from the systematics that is observed from $J = 10$ to $J = 18$ where always the two highest possible K states $K = J$ and $K = (J - 1)$ survive. The pattern manifests itself in characteristic double peak structures that are visible in the high energy part of the spectrum (see Fig. 8.8(b)). This feature does not come as a surprise, for if the rotational axis is parallel to the molecular axis ($J \approx K$), no dipole-moment is induced by the rotation, while with decreasing K the triangular symmetry may be distorted and a small dipole-moment appears.

Summing up the implications of the rovibrational model, it can be stated that the vibrational decay observed by CEI can be reproduced within the uncertainties of the shape of the initial distribution, and that the substantial rotational excitation that was seen in the DR imaging data after several ten seconds of storage is backed theoretically. In addition, the existence of rotational states with energies as high as 1 eV, that is assumed to be responsible for the shoulder in the distance distribution of the two-body breakup (see Fig. 7.17) is confirmed.

At presence the model is limited by the unsatisfactory knowledge of the detailed initial excitation and the fact the the assignment ends at $9000\,\mathrm{cm}^{-1}$. For both points improvements are difficult to achieve. Experimentally it seems advantageous to go for ion sources that produce internally cold molecules rather than to invest more time in the calibration of the CHORDIS source in particular, and theoretically the extension of the assignment may be impossible since the quantum numbers are no longer well defined.

E (cm^{-1})	P (%)	T_i (s)	J	K	g	E (cm^{-1})	P (%)	T_i (s)	J	K	g
64.13	0.67	>1.00e+07	1	1	2	1647.26	4.52	>1.00e+07	8	8	2
86.96	0.81	>1.00e+07	1	0	4	1972.80	2.73	>1.00e+07	8	7	2
169.30	1.20	2.38e+06	2	2	2	2242.20	0.38	9.21e+02	8	6	4
237.36	0.98	1.76e+06	2	1	2	2030.64	5.69	>1.00e+07	9	9	4
315.35	2.02	>1.00e+07	3	3	4	2396.41	2.38	>1.00e+07	9	8	2
428.02	2.13	5.65e+04	3	2	2	2702.08	0.04	4.54e+02	9	7	2
494.77	1.88	2.65e+04	3	1	2	2451.61	4.61	>1.00e+07	10	10	2
516.88	1.72	1.35e+04	3	0	4	2856.73	2.37	>1.00e+07	10	9	4
502.04	3.25	>1.00e+07	4	4	2	2909.48	4.00	>1.00e+07	11	11	2
658.72	4.45	1.68e+04	4	3	4	3352.99	1.68	>1.00e+07	11	10	2
768.48	2.45	5.51e+03	4	2	2	3403.54	3.72	3.40e+06	12	12	4
833.59	1.18	1.63e+03	4	1	2	3884.33	1.39	>1.00e+07	12	11	2
729.01	3.55	>1.00e+07	5	5	2	3933.14	3.26	5.97e+05	13	13	$\frac{8}{3}$
928.98	3.38	4.62e+04	5	4	2	4450.10	1.54	3.98e+06	13	12	$\frac{8}{3}$
1080.49	2.33	5.52e+04	5	3	4	4497.68	2.87	1.13e+05	14	14	$\frac{8}{3}$
1187.11	0.09	4.87e+02	5	2	2	5049.24	1.19	5.08e+05	14	13	$\frac{8}{3}$
1250.31	0.19	2.99e+02	5	1	2	5096.75	2.52	2.31e+04	15	15	$\frac{8}{3}$
995.88	4.57	>1.00e+07	6	6	4	5681.54	0.82	9.96e+04	15	14	$\frac{8}{3}$
1238.45	3.20	1.57e+05	6	5	2	5730.16	2.39	5.38e+03	16	16	$\frac{8}{3}$
1430.72	1.30	2.30e+03	6	4	2	6345.43	0.63	2.06e+04	16	15	$\frac{8}{3}$
1679.79	0.03	1.10e+02	6	2	2	6397.84	0.89	1.45e+03	17	17	$\frac{8}{3}$
1302.14	3.84	>1.00e+07	7	7	2	7042.36	0.49	5.22e+03	17	16	$\frac{8}{3}$
1586.59	3.63	>1.00e+07	7	6	4	7099.83	0.04	4.39e+02	18	18	$\frac{8}{3}$
1818.14	0.86	1.64e+03	7	5	2	7768.97	0.13	1.34e+03	18	17	$\frac{8}{3}$

Table 8.3: *Metastable rotational states of H_3^+, where E is the energy, P the population after 1800 s, T_i the lifetime, J the angular momentum quantum number, K the projection of J onto the molecular symmetry axis and g denotes the spin degeneracy. All states with population $\geq$0.01% after 1800 s (starting from a 0.23 eV Boltzmann distribution) are listed. Note that all the states are purely rotational, e.g. $\nu_1 = \nu_2 = 0$ and especially $K = G$. The states listed account for 99.98 % of the total population.*

8.5 Radiative heating

So far only relaxation due to spontaneous decay was considered. This approach is justified for conditions prevailing in a storage ring by the weakness of the coupling of the H_3^+ molecule to ambient (300 K) radiation, and especially for the decay from temperatures as high as 0.23 eV (~2700 K) this approximation is very good. However, in order to check whether the exposure of cold H_3^+ to 300 K blackbody radiation for several ten seconds – like in storage ring experiments – leads to radiative heating, the model was extended to include radiation induced transitions. The main purpose of this extension is to verify, whether a cold H_3^+ beam, e.g. created by special ion sources (see Part III of this work), would remain cold during the storage time, or if the state populations would change significantly on the time scale of the storage times that can be achieved in the ring.
The probability per second that a molecule absorbs a photon can be expressed in terms of the spectral energy density $\rho(\nu)$ times the Einstein-B coefficient of induced absorption

$$\frac{d}{dt}P_{12} = B_{12}\,\rho(\nu). \tag{8.4}$$

For a stationary field, the B_{12} Einstein coefficient can be related to that of spontaneous emission A_{21} [Dem98], which is given in the UCL linelist

$$B_{12} = A_{21}\frac{c^3}{8\,\pi\,\nu^3\,h}\,\frac{g_2}{g_1}\ , \tag{8.5}$$

where ν is the transition frequency and g_2, g_1 are the statistical weights of the upper and lower state, respectively. Induced emission is neglected, since the time scale of radiative heating is of interest rather than the precise level populations of the system approaching equilibrium. To calculate the spectral energy density, Planck's radiation law is used

$$\rho(\nu) = \frac{8\,\pi\nu^2}{c^3}\,\frac{h\,\nu}{e^{h\nu/kT}-1}. \tag{8.6}$$

The model was restricted to states below 8000 cm^{-1} (11500 K) for this calculation in order to reduce the number of transitions to ~15600 and the number of states to 693.
Fig. 8.9 shows the result of the model for an initial temperature of 100 K prior to injection in the ring and a blackbody temperature of 300 K. It can be seen that at a starting temperature of 100 K (a) only a few states carry significant contributions. The five lowest-lying states (see also Tab. 8.3) together account for 99.1 % of the total population. The distributions after 10 s (b) and 100 s (c) are practically indistuingishable from the initial distribution, revealing the weak effect of radiative heating at 300 K, as expected. After 1 hour exposure to 300 K radiation (Fig. 8.9 (d)) a slight heating effect becomes visible

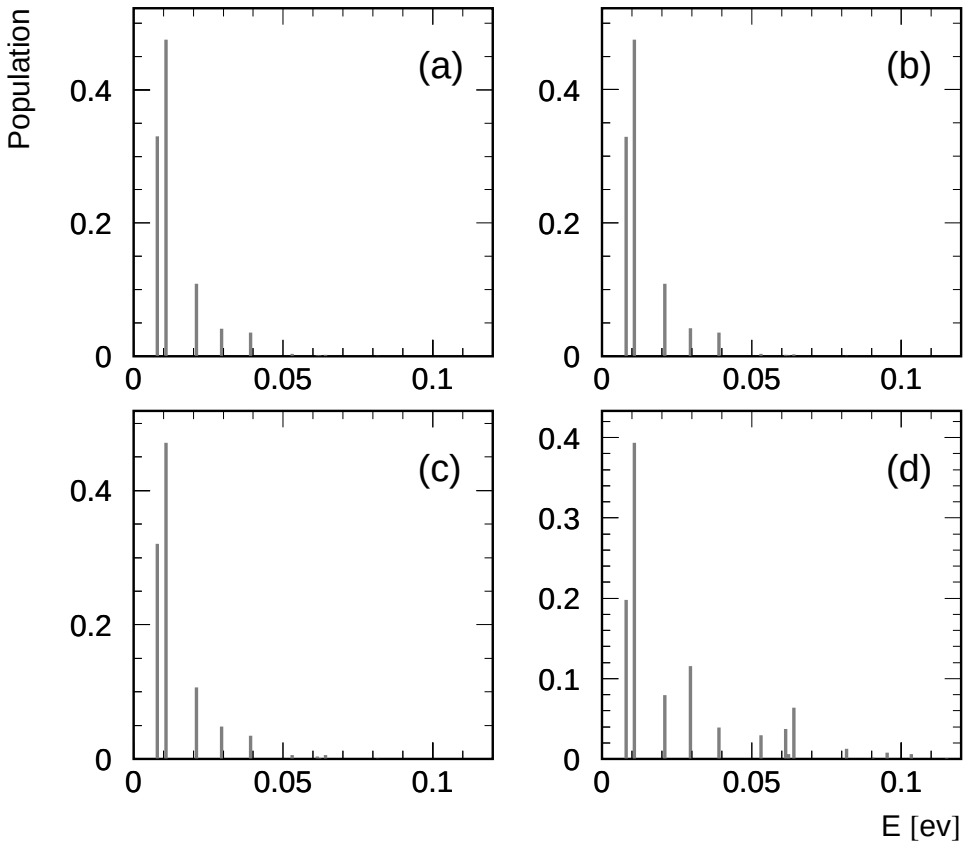

Figure 8.9: *Stick diagram of the H_3^+ level population at a temperature of 100 K (a) and after exposure to blackbody radiation of 300 K for 10 s (b), 100 s (c) and 3600 s (d), respectively.*

as a shift to higher energies occurs. The summed population of the five lowest states is reduced to 98.1 % after 100 s, while it drops to 82.6 % after 1 hour.
For comparison in Fig. 8.10 (a) the equilibrium distribution for a Boltzmann temperature of 300 K is plotted together with the outcome of the model for an initial temperature of 100 K and 10 hours of exposure to a 300 K radiation field (b). The structural similarity of both distributions serves as a consistency check of the model, while the disagreement in the absolute values reveals that equilibrium is not entirely reached after 10 hours.
This result indicates that the influence of 300 K background radiation is negligible on the time scales of seconds to minutes that can be achieved in storage ring experiments. Nevertheless, it is interesting to examine which transitions are the most effective in removing population from the lowest states. For that purpose the twenty fastest transitions starting from the five energetically lowest states and assuming a 300 K radiation field are

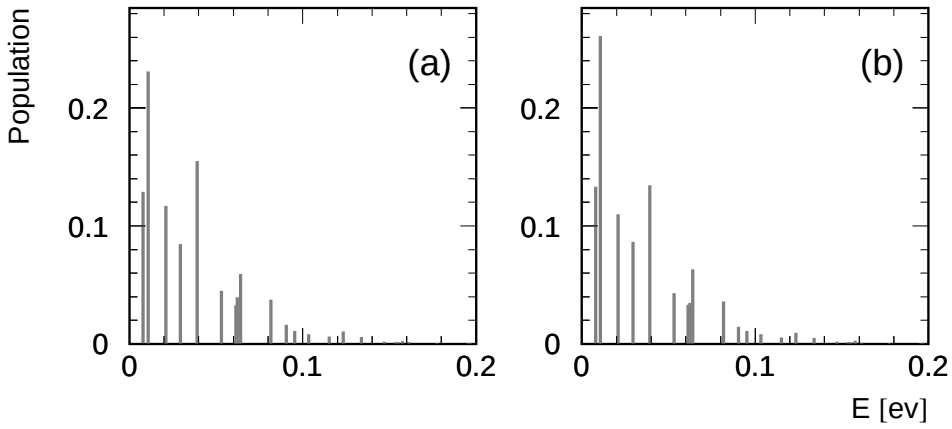

Figure 8.10: *Comparison of the equilibrium distribution for a Boltzmann temperature of 300 K (a) and the result of the model for an initial temperature of 100 K and exposure to 300 K radiation for 10 hours (b).*

listed in Tab. 8.4. The last column of the table represents the transition rate in seconds given by the product of the Einstein coefficient B_{12} times the radiation density $\rho(\nu)$ at the corresponding transition frequency. Remarkably, only one of these transitions is purely rotational, while the majority proceeds through the first vibrational bending mode excitation (01^1).

This behaviour reflects the fact that pure rotational transitions are strongly suppressed. For a vibrational excitation from the low-lying states photons with an energy $> 3000\,\mathrm{K}$ are needed and thus the Einstein coefficients of these transitions have to be greater by several orders of magnitude – compared to pure rotational transitions – since they have to compensate for the exponentially decreasing spectral density of the 300 K radiation field at higher temperatures. Once a photon has been absorbed and a bending mode excitation has been created, it will decay rapidly to the vibrational ground state again and therefore this process creates only a negligible fraction of temporal vibrational excitation; on the other hand higher rotational states can be populated by this cascade.

One of the implications of this aspect is that even small intensity stray light at high temperatures might heat up the ions in the storage ring much more effectively than the ambient room temperature background radiation. A possible source of stray light could be hot filament vacuum gauges situated at several places in the ring. In the next paragraph therefore an estimate of the influence of the ion gauges on the ion temperature will be made.

E'' (cm^{-1})	J''	G''	U''	E' (cm^{-1})	J'	G'	U'	$\nu_1\nu_2^l$	$B_{12}\cdot\rho(\nu)$ (s^{-1})
64.13	1	1	0	2521.42	0	1	1	01^1	4.544451e-04
64.13	1	1	0	2609.55	1	1	1	01^1	3.308968e-04
64.13	1	1	0	2755.58	2	1	-1	01^1	1.919355e-04
64.13	1	1	0	2790.35	2	1	1	01^1	1.893854e-04
86.96	1	0	0	2616.70	1	0	-1	01^1	6.927503e-04
86.96	1	0	0	2812.87	2	0	1	01^1	3.108134e-04
169.30	2	2	0	2548.18	1	2	1	01^1	8.063910e-04
169.30	2	2	0	2723.97	2	2	1	01^1	2.146782e-04
169.30	2	2	0	2931.38	3	2	-1	01^1	1.973984e-04
169.30	2	2	0	2992.44	3	2	1	01^1	8.358818e-05
237.36	2	1	0	2609.55	1	1	1	01^1	4.107492e-04
237.36	2	1	0	2755.58	2	1	-1	01^1	4.762785e-04
237.36	2	1	0	2790.35	2	1	1	01^1	1.084216e-04
237.36	2	1	0	3002.91	3	1	-1	01^1	4.868542e-05
237.36	2	1	0	3063.48	3	1	1	01^1	1.589145e-04
315.35	3	3	0	516.89	3	0	0	00^0	4.549292e-05
315.35	3	3	0	2614.28	2	3	1	01^1	1.210311e-03
315.35	3	3	0	2876.85	3	3	1	01^1	1.579356e-04
315.35	3	3	0	3145.28	4	3	-1	01^1	1.693406e-04
315.35	3	3	0	3233.38	4	3	1	01^1	4.487614e-05

Table 8.4: *List of the 20 strongest transitions for 300 K radiation heating up the 5 lowest-lying states of H_3^+. E'', J'', G'', U'' and E', J', G', U' denote the energies and rotational quantum numbers (as discussed in chapter 5) of the lower and upper state, respectively. The vibrational quantum numbers $\nu_1\nu_2^l$ of the upper state are also given, while all the lower states are in the vibrational ground state ($\nu_1'' = \nu_2'' = l'' = 0$).*

Possible influence of ion gauges

The TSR storage ring is an ultra high vacuum machine with a typical residual gas pressure of 3×10^{-11} mbar. In order to measure the base pressure reliably 8 hot filament ion gauges of the Bayard-Alpert type are installed at various locations in the ring. These instruments have thin filaments that are operated with a power between 12 and 30 Watt and therefore illuminate their surrounding similar to a light bulb. The part of the 55.4 m storage ring that is affected by the light directly is rather small ($\sim$0.4 m), but as seen above only little intensity of light at temperatures that are in the range of vibrational excitations can contribute substantially to the radiative heating of H_3^+.

The tungsten filament in a light bulb can reach 3000 K [Har72]; since the power of the ion gauges is somewhat smaller, a value of 2000 K is adapted for the filament temperature. The total energy density of a thermionic emitter can be calculated by integrating Planck's formula over all frequencies

$$I_{total} = \int_0^\infty \frac{8\,\pi h\nu^3}{c^3} \frac{1}{e^{h\nu/kT}-1}\, d\nu\,, \tag{8.7}$$

$$= \frac{8\,\pi h}{c^3} \int_0^\infty \frac{\nu^3}{e^{h\nu/kT}-1}\, d\nu\,. \tag{8.8}$$

Substitution of $x \equiv h\nu/kT$ and $d\nu \equiv kT/h\nu \cdot dx$ yields the integral

$$\frac{8\,\pi k^4 T^4}{c^3 h^3} \int_0^\infty \frac{x^3}{e^x - 1}\, dx\,, \tag{8.9}$$

that can be solved [Bra88] using

$$\int_0^\infty \frac{x^3}{e^x - 1}\, dx = \frac{\pi^4}{15} \tag{8.10}$$

resulting in

$$I_{total} = \frac{8\,\pi^5 k^4 T^4}{15\,h^3 c^3} = 3.93 \times 10^{-3} \frac{\mathrm{J}}{\mathrm{m}^3} \qquad \text{for T=2000 K}\,. \tag{8.11}$$

This value of 3.93×10^{-3} J/m^3 is the energy density of a blackbody at 2000 K. The situation in the storage ring is different, of course; here the omnipresent 300 K background is superimposed by a 2000 K field only in a small part of the ring and with a much smaller energy density, because only the thin filaments are emitting light at high temperatures. The length of the ring that is illuminated was estimated to 0.4 m, yielding a fraction of 0.4 m/55.4 m=7.2×10^{-2} of the ion orbit. Now a scaling factor for the 2000 K radiation field to account for the energy density created by the filaments has to be found. For that purpose we estimate the average power that reaches the walls of the beam pipe in the vicinity of the ion gauges to $P = 0.1$ Watt/cm^2. This average power P is related to the energy density by

$$P = I_{total} \cdot c = 0.1 \text{ Watt/cm}^2\,, \tag{8.12}$$

solving this equation for the energy density gives $I_{total} = 3.4 \times 10^{-6}$ J/m^3. That means that for an average radiation power of 0.1 Watt/cm^2 we have to scale down the original blackbody intensity at 2000 K (Eq. 8.11) by a factor of $3.4 \times 10^{-6}/3.93 \times 10^{-3} = 8.6 \times 10^{-4}$. Together with the fraction of 7.2×10^{-2} of the storage ring volume that is affected by the ion gauges we introduce an intensity scaling factor for the 2000 K radiation of $k_0 = 6.2 \times 10^{-5}$. The total spectral density acting on the ions is now assumed to be the

sum of the ambient room temperature ($T_1 = 300\,\mathrm{K}$) distribution and the scaled distribution ($T_2 = 2000\,\mathrm{K}$) caused by the ion gauges

$$\rho(\nu) = \frac{8\,\pi\nu^2}{c^3}\,\frac{h\,\nu}{e^{h\nu/kT_1} - 1} + k_0 \cdot \frac{8\,\pi\nu^2}{c^3}\,\frac{h\,\nu}{e^{h\nu/kT_2} - 1}\ . \tag{8.13}$$

In Fig. 8.11 this spectral distribution is compared to room temperature blackbody radiation alone. Note that here only the high energy region, relevant to the fast vibrational transitions is plotted (the peak of $\rho(\nu)$ for 300 K is $2.15 \times 10^{-19}\,\mathrm{J/m^3}$ at $570\,\mathrm{cm^{-1}}$). The opening of the first bending mode ($0,1^1$) at $2521\,\mathrm{cm^{-1}}$ is marked in the diagram, because – as seen in the last paragraph – bending mode transitions almost exclusively drive the reheating process. Obviously the 2000 K distribution contributes considerably for energies above the ($0,1^1$) threshold and therefore it seems appropriate to check how that influences

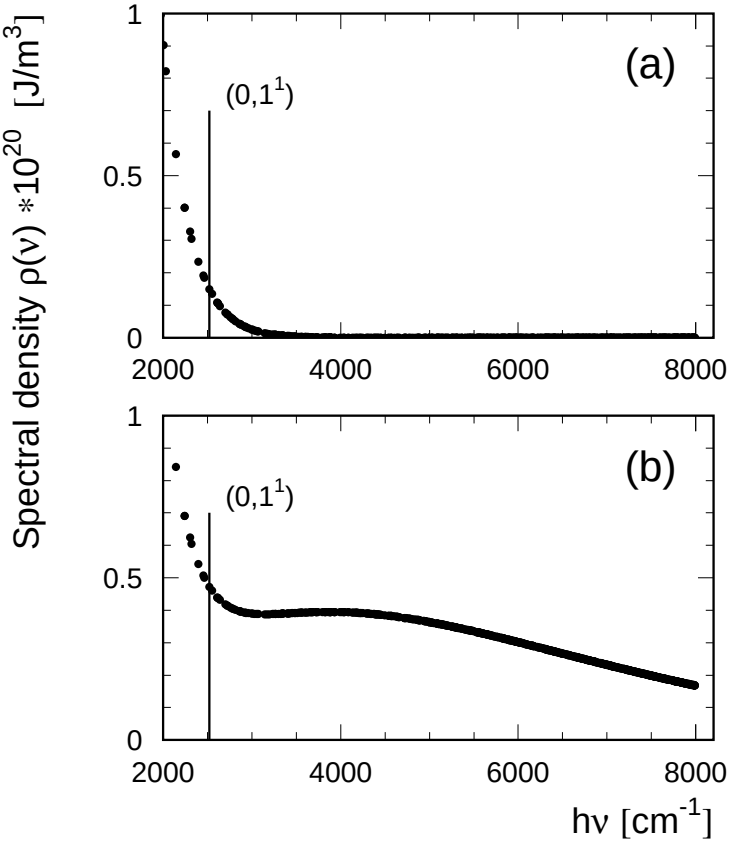

Figure 8.11: *Spectral density in the energy region relevant to vibrational excitation for a 300 K radiation field alone (a) and superimposed with a 2000 K component (b) scaled down by $k_0 = 6.2 \times 10^{-5}$ according to Eq. 8.13. The lines at 2521 cm^{-1} mark the opening of the first vibrational bending mode ($0,1^1$).*

the reheating times.

In Fig. 8.12 the radiative heating starting from an initial 100 K distribution (a) is depicted for three different times in analogy to Fig. 8.9. In comparison to the behaviour at room temperature, the heating process is significantly sped up. After 100 s the five lowest-lying states account for 92.1 % of the total population (compared to 98.1 % for 300 K radiation) and the next three rotational states have a fractional population between 1 % and 2.6 %. Still, 100 s of storage are hardly reached in a typical experiment and thus the influence of stray light from ion gauges is probably harmless. However, if the approach that was chosen would underestimate the light intensity systematically – e.g. no reflection on the walls of the beam pipe was considered and the filament temperature could not be measured – the

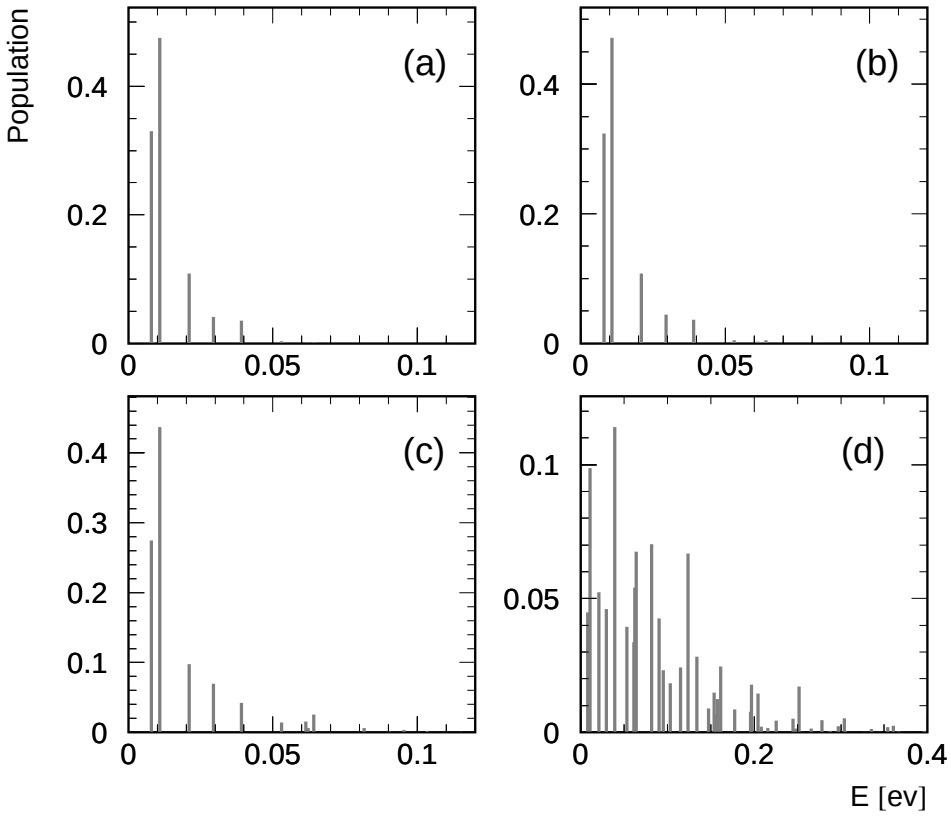

Figure 8.12: *Model calculations to estimate the possible influence of hot filament ion gauges on the reheating times. The initial distribution (a) represents a Boltzmann temperature of 100 K, furthermore the results of the model for exposure to 300 K radiation plus a 2000 K component according to Eq. 8.13 for 10 s (b), 100 s (c) and 1 hour (note that the abscissa has changed) are plotted.*

real heating might be faster.
Although the results demonstrate that any disturbances of DR experiments from ion gauges and other sources of stray light are rather unlikely, for measurements at longer storage times it should be kept in mind that these effects may exist. Experimental verification to exclude the influence of hot filament ion gauges on the measured DR rate coefficient is foreseen.

Part III

Development of a 22-Pole ion trap

Chapter 9
Introduction

The second part of this thesis demonstrated that H_3^+ is reluctant to cool via spontaneous emission. The lifetimes of rotational excitations are orders of magnitude longer than storage times that can be achieved in storage ring experiments, while the vibrational excitations decay within two seconds. Consequently, the published values for the H_3^+ DR rate coefficient at 300 K derived from storage ring measurements, are likely to be performed on vibrationally relaxed ions, while the mean rotational energy can be as high as several thousand Kelvin, depending on the ion source that was used.
Nonetheless for interstellar clouds the DR rate coefficient of the lowest rovibrational states is the most important, because the density of free electrons is much lower than the H_2 density, and thus H_3^+ will undergo many thermalizing collisions before it can recombine.
An ion storage ring with its ultra high vacuum is built to offer a collision free region and hence it is not the appropriate environment to cool down H_3^+. The idea that is presented in this last part of the thesis is to go one step further towards the creation of an interstellar analogue in the laboratory. To do so, one would have to let the H_3^+ ions undergo collisions with neutral H_2 gas at interstellar temperatures prior to the storage ring DR experiment. By this means, one would be able to measure reliable rate coefficients, since one could produce the same sequence occurring in the interstellar medium.
There are two principal approaches for collisional cooling, first the use of an expansion ion source; second utilizing buffer gas cooling in a cryogenic ion trap. We followed the latter path for it provides better control over the internal excitations.
Confinement of ions in small scale devices has a long history, milestones were the development of the so-called Penning trap with its roots already in the thirties and the Paul trap that originated from the mass filtering devices that were invented in the fifties, a review can be found in [Gos95]. Both concepts can not rely on electrostatic fields alone, since Earnshaw's theorem forbids the creation of a potential minimum solely with electric fields. The Penning trap overcomes this law by combining electric and magnetic fields

and the Paul trap uses time-varying fields at radio frequencies (RF) to create effective potential wells.

A novel approach was introduced recently by D. Zajfman [Zaj97], who demonstrated that ions *can* be trapped by static electric fields, as long as the ions themselves are moving with keV energies.

However, to cool down a larger sample of molecular ions to interstellar temperatures of 10 K, at first glance all three approaches do not appear to be well suited. To trap singly charged particles in a Penning trap very strong magnetic fields are required and since the ions are moving on circular trajectories all the time, buffer gas cooling to 10 K would probably be difficult if not impossible. The Zajfman trap is out of the race immediately, since the ions are bouncing back and forth at keV velocities. Hence the Paul trap is the best candidate, for it can easily trap singly charged molecular ions for long times without the necessity to send them on particular trajectories which is always adverse to collisional cooling. The problem arising from a standard Paul trap quadrupole design is the RF heating. The trapping potential of a quadrupole trap is that of a harmonic potential and therefore the ions are constantly pushed into the inner region of the trap unless they do not happen to dwell in the exact potential minimum. For many ions in the trap that means that they will frequently undergo collisions with the neutral buffer gas while they are being accelerated and thus energy may be carried into the system instead of being dissipated.

The remedy is that the trapping of charged particles in inhomogeneous RF fields does not depend upon the quadrupole geometry, in fact Gapanov and Miller realized early that "There are an unlimited number of possibilities for creating potential wells $\Phi(r)$. The simplest of these are realized in quasi-electrostatic multipole fields ..." [Gap58].

These possibilities were exploited in the last decades by D. Gerlich and coworkers, who could show that inhomogeneous RF fields are a perfect tool for the study of low energy collisions [Ger92]. We have adopted one of Gerlich's most successful designs, the 22-pole ion trap which overcomes the RF heating problem by the formation of a large field-free region in the middle of the trap. Further details will be given in the next chapters.

Chapter 10
Trapping and guiding of ions in inhomogeneous RF fields

In this chapter the effective potential approximation will be derived and the field properties of linear multipoles are discussed. The special application of the quadrupole geometry serving as a mass filter is described briefly, the more general adiabaticity principle is introduced and the functional properties of the 22-pole ion trap are explained.

10.1 The effective potential approximation

The derivation of the effective potential in this section follows the example given in the textbook of Landau and Lifshitz [Lan76] which is in the spirit of Kapiza [Kap51]. In general the force acting upon a particle of charge q in a electromagnetic field $\vec{E}(\vec{r},t), \vec{B}(\vec{r},t)$ obeys

$$\vec{F} = q\vec{E}(\vec{r},t) + q\dot{\vec{r}} \times \vec{B}(\vec{r},t)\,, \tag{10.1}$$

but since the maximum amplitude of the magnetic field scales as $B_0 = E_0/c$, it becomes important only if the particle velocity approaches the speed of light [Fri82], which is never the case in laboratory mass filters or ion traps. Therefore, the influence of magnetic fields is neglected throughout this description.
We will consider the motion of a particle of charge q in a static potential $V_0(\vec{r})$ superimposed with an oscillatory field

$$\vec{E}(\vec{r},t) = \vec{E}_0(\vec{r})\,\cos(\omega t)\,, \tag{10.2}$$

where ω is the angular frequency $\omega = 2\pi\nu$ and the amplitude $\vec{E}_0(\vec{r})$ depends only on the particle position. Furthermore, for the sake of simplicity, we will treat the problem in one

dimension x only, thus the equation of motion can be written

$$m\ddot{x} = -q\frac{d\,V_0}{dx} + q\,E(x,t)\,. \tag{10.3}$$

The motion of the particle is approximated by a smooth drift term $X(t)$ and a oscillatory term $\xi(t)$

$$x(t) = X(t) + \xi(t), \tag{10.4}$$

furthermore it is assumed that ξ is small enough that the static potential $V_0(x)$ and the amplitude of the oscillating field $E_0(x)$ can be regarded constant during one oscillation: $V_0(x) = V_0(X)$ and $E_0(x) = E_0(X)$. If we insert this ansatz into Eq. 10.3 and do a Taylor-Expansion around X, we get

$$m\ddot{X} + m\ddot{\xi} = -q\frac{d\,V_0}{dX} - q\xi\frac{d^2\,V_0}{dX^2} + qE(X,t) + q\xi\frac{\partial E(X,t)}{\partial X} + \ldots \tag{10.5}$$

Separating the oscillatory part of this equation yields

$$m\ddot{\xi} = -q\xi\frac{d^2\,V_0}{dX^2} + qE(X,t) + q\xi\frac{\partial E(X,t)}{\partial X}, \tag{10.6}$$

and since ξ is small, all terms multiplied by ξ are neglected and the oscillatory motion is dominated by the second term

$$m\ddot{\xi} = qE(X,t). \tag{10.7}$$

Using Eq. 10.2, this relation can be readily integrated

$$\xi = -\frac{qE(X,t)}{m\omega^2}\,, \tag{10.8}$$

and the amplitude ξ_0 of the micro-oscillation is given by

$$\xi_0 = -\frac{qE_0(X,t)}{m\omega^2}\,. \tag{10.9}$$

To derive a formula for the smooth motion, we average Eq. 10.5 over one period $2\pi/\omega$ of the oscillatory motion, the averaged terms are tagged by a bar, e.g. $\overline{x} = X(t)$; while slowly varying functions of $X(t)$ only – like $V_0(X)$ and $E_0(X)$ (see above) – are supposed to stay constant during one period of ξ. Consequently, first order terms of ξ and E vanish, because $\int_t^{t+2\pi/\omega} \cos\omega t\,dt = 0$ and we get

$$m\ddot{X} = -q\frac{d\,V_0}{dX} + q\overline{\xi\frac{\partial E(X,t)}{\partial X}} = -q\frac{d\,V_0}{dX} - \frac{q^2}{m\omega^2}\overline{E(X,t)\frac{\partial E(X,t)}{\partial X}}. \tag{10.10}$$

Now we can reduce the differential equation for the smooth motion to

$$m\ddot{X} = -\frac{dV_{\text{eff}}}{dX}, \tag{10.11}$$

with

$$V_{\text{eff}} = qV_0 + \frac{q^2}{2\,m\omega^2}\overline{E(X,t)^2} = qV_0 + \frac{q^2}{4\,m\omega^2}E_0(X)^2. \tag{10.12}$$

This *effective potential* V_{eff} described in Eq. 10.12 is time-independent and the new equation of motion (Eq. 10.11) for the smooth drift term $X(t)$ is much easier to solve than the original equation that contained time explicitly. Another result of this derivation can be seen, by considering the first integral of Eq. 10.12

$$\frac{1}{2}m\dot{X}^2 + qV_0 + \frac{q^2}{4\,m\omega^2}E_0(X)^2 = E_m\,, \tag{10.13}$$

where E_m is a constant of motion. Since the three terms on the left hand-side are identified as the kinetic energy and the energy in the static and effective potentials, respectively, this equation defines the conservation of total energy E_m (within the above approximation). It also shows that kinetic energy of the drift motion can be converted and stored in energy of the oscillatory motion and vice versa; thus the storage of a particle in a RF trap implies a frequent conversion of the particle's energy between the three different terms of Eq. 10.13.

10.1.1 Adiabaticity and stability

The concept of the effective potential depends upon the assumption that the particle motion can be separated into a smooth drift term and an oscillatory component. To examine the applicability of this approximation, usually a dimensionless parameter is introduced that compares the frequency of the RF field to some function of the drift motion. A typical requirement for particle trapping is that the macroscopic frequency Ω in the trap must be much smaller than the RF frequency, that means $\Omega \ll \omega$. We will chose a definition described in the comprehensive review of Gerlich [Ger92], demanding that over the full distance of a micro-oscillation $2\xi_0$ the change of the time-independent amplitude of the electric field $\vec{E_0}(\vec{r})$ be smaller than the field itself

$$|2(\xi\nabla)\vec{E_0}| < |\vec{E_0}|\,. \tag{10.14}$$

The so-called adiabaticity parameter η is now defined as the ratio

$$\eta = \frac{|2(\xi_0\nabla)\vec{E_0}|}{|\vec{E_0}|}, \tag{10.15}$$

by inserting Eq. 10.9 and using the vector analysis relation

$$(\vec{E_0}\nabla)\vec{E_0} = \frac{1}{2}\nabla\vec{E_0}^{\,2} - \vec{E_0}\times(\nabla\times\vec{E_0}) = \frac{1}{2}\nabla\,E_0^2\,, \tag{10.16}$$

the definition can be simplified

$$\eta = \frac{2q|\nabla E_0|}{m\omega^2}. \tag{10.17}$$

Since $E_0(\vec{r})$ is a function of the space coordinate $\vec{r}$, also η depends upon the position of the particle in the field, or $\eta = \eta(\vec{r})$, and thus restrictions on the maximum value $\eta_m = \max[\eta(\vec{r})]$ to secure adiabatic behaviour must be imposed on the full trajectories of the stored ions. Numerical simulations and experimental evidence showed [Tel74, Ger92] that the conservation of energy is a very good approximation if the working conditions are chosen such that

$$\eta_m < 0.3. \tag{10.18}$$

A second criterion for a stable motion inside an ion trap is that the particles can not collide with the electrodes. This requirement can be formulated by setting $\dot{X} = 0$ in Eq. 10.13, implying that the effective potential close to the electrodes is higher than the total energy E_m (which is constant if the adiabaticity condition $\eta_m < 0.3$ is fulfilled)

$$qV_0(\vec{r_m}) + \frac{q^2}{4\,m\omega^2} E_0(\vec{r_m})^2 \geq E_m\,, \tag{10.19}$$

where $\vec{r_m}$ marks the closest possible approach to the electrodes. To achieve an expression for the effective potential and calculate the adiabaticity parameter of a given electrode geometry, the Laplace equation for that particular arrangement has to be solved (neglecting the charge of the stored ions). In the next section the case of linear multipoles will be discussed.

10.1.2 Linear multipoles

The solution of Laplace's equation for multipole geometries can be found in [Fri82, Sza86], further details for practical applications are given in [Ger92]. The field of a cylindrically symmetrical multipole with two sets of n electrodes, connected to alternating potentials $-\Phi_0$ and $+\Phi_0$, with

$$\Phi_0 = V_0 - V_\sim \cos\,\omega t\,, \tag{10.20}$$

can be expressed in polar coordinates (r,φ) by

$$\Phi = \Phi_0 \left(\frac{r}{r_0}\right)^n \cos\,n\varphi\,, \tag{10.21}$$

where r_0 stands for the free inner circle of the electrode geometry. In Fig. 10.1 the static potentials of an ideal Quadrupole and a 22-pole field geometry are depicted. The electric field in polar coordinates can now be calculated

$$\vec{E} = -\left(\frac{\partial}{\partial r}\Phi, \frac{1}{r}\frac{\partial}{\partial \varphi}\Phi\right) = \frac{\Phi_0}{r_0} n \left(\frac{r}{r_0}\right)^{n-1} (-\cos\,n\varphi, \sin\,n\varphi)\,, \tag{10.22}$$

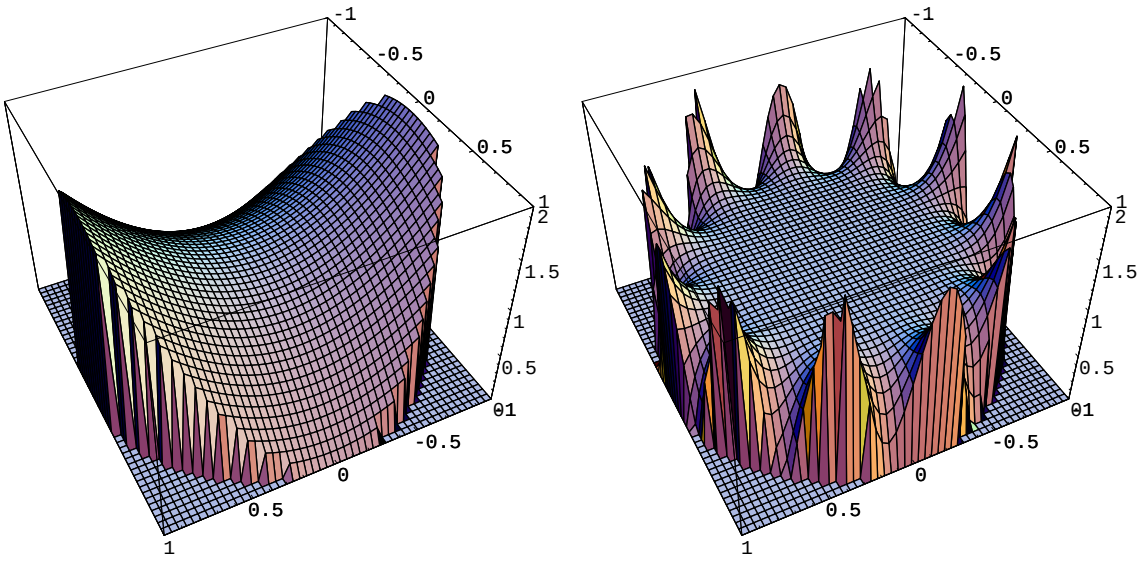

Figure 10.1: *Electrostatic potentials for Quadrupole (n=2) and 22-pole (n=11) geometries.*

and from this expression, it is apparent, that the absolute value of the oscillatory field does not depend on φ

$$|E| = \frac{E_0}{r_0} n \left(\frac{r}{r_0}\right)^{n-1} . \tag{10.23}$$

Inserting Eq. 10.23 into Eq. 10.12 yields the effective potential for linear multipoles

$$V_{\text{eff}} = \frac{1}{8}\frac{(q\,E_0)^2}{\epsilon}\left(\frac{r}{r_0}\right)^{2n-2} + qV_0\left(\frac{r}{r_0}\right)^{n} \cos\, n\varphi\,, \tag{10.24}$$

with the characteristic energy defined as

$$\epsilon = \frac{1}{2n^2}\, m\omega^2\, r_0^2. \tag{10.25}$$

This energy can be interpreted as the energy of a virtual ion cycling on the maximum radius r_0 in phase with the RF field [Ger92]. In reality, in order to achieve stable conditions, the energy of stored ions has to be substantially below ϵ.

For the quadrupole geometry, Eq. 10.24 reveals a harmonic potential, leading to special properties of the equation of motion, that will be discussed in the next section. One feature inherent to higher-order multipoles can already be seen in Fig. 10.1. Whereas in the r^2 quadrupole potential basically one field-free point can be found – namely the metastable saddle point in the middle of the structure – the potential of the 22-pole geometry shows a wide, essentially field-free region, enclosed by the steep fields close to the electrodes. This property is enhanced by adding more electrodes, as can be seen in Fig. 10.2, since the RF part of the effective potential (the first term on the right-hand side of Eq. 10.24) scales with $V_{\text{eff}} \sim r^{2n-2}$.

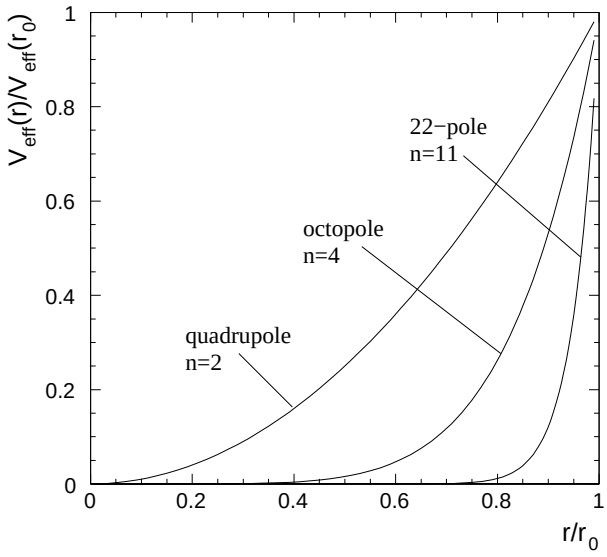

Figure 10.2: *Effective potentials for quadrupole, octopole and 22-pole geometries as a function of the distance from the symmetry axis*

To derive the adiabaticity parameter (Eq. 10.17), ∇E_0 has to be calculated

$$\nabla E_0 = \left(\frac{\partial}{\partial r}, \frac{1}{r}\frac{\partial}{\partial \varphi}\right) |\vec{E}_0| = \left(\frac{n(n-1)V_\sim}{r_0^2}\left(\frac{r}{r_0}\right)^{n-2},\ 0\right), \tag{10.26}$$

which has only a radial component, resulting eventually in an expression for the adiabaticity parameter

$$\eta = \frac{2q\,n(n-1)\,V_\sim}{m\omega^2\,r_0^2}\left(\frac{r}{r_0}\right)^{n-2}. \tag{10.27}$$

In the next two sections the motion of charged particles in two particular multipole fields will be discussed briefly.

10.2 The quadrupole mass filter

The quadrupole is the best characterized RF device and it has become the working horse of mass spectrometry in many areas of science. The ideal 4-pole potential is hyperbolic, in Cartesian coordinates it can be written

$$\Phi(x, y) = \frac{\Phi_0}{2r_0^2}(x^2 - y^2). \tag{10.28}$$

However, for many applications it is sufficient to approximate the hyperbolic shape by cylindrical rods, as depicted in Fig. 10.3. The potential Φ_0 consisting of a static voltage

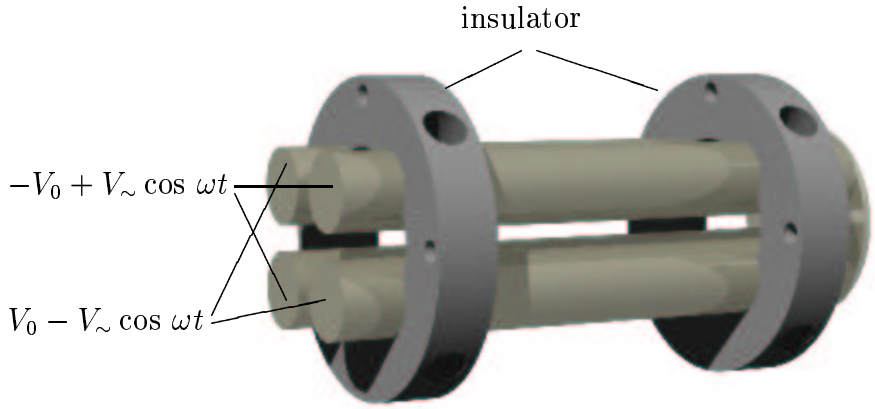

Figure 10.3: *The quadrupole mass filter used in the cryogenic ion source.*

V_0 and the oscillatory component with amplitude $V_\sim$

$$\Phi_0 = V_0 + V_\sim \cos\,\omega t \tag{10.29}$$

is applied with alternating signs to the two pairs of opposite rods. The equations of motion in x and y are

$$\ddot{x} + \frac{q}{mr_0^2}(V_0 + V_\sim \cos\,\omega t)x = 0\,, \tag{10.30}$$

$$\ddot{y} - \frac{q}{mr_0^2}(V_0 + V_\sim \cos\,\omega t)y = 0\,, \tag{10.31}$$

thus the motion in x- and y-directions are decoupled. By introducing the dimensionless parameters

$$a_2 = \frac{4qV_0}{mr_0^2\omega^2} \quad , \quad q_2 = \frac{2qV_\sim}{mr_0^2\omega^2} \quad , \quad \tau = \frac{1}{2}\omega t\,, \tag{10.32}$$

Eq. 10.30, 10.31 can be converted into the well-known *Mathieu differential equation*

$$\frac{d^2x}{d\tau^2} + (a_2 + 2q_2 \cos\,2\tau)x = 0\,, \tag{10.33}$$

$$\frac{d^2y}{d\tau^2} - (a_2 + 2q_2 \cos\,2\tau)y = 0\,, \tag{10.34}$$

that can be solved analytically [Mar89]. Comparison with Eq. 10.27 reveals that the q_2 parameter is identical with the more generally defined adiabaticity parameter η for $n = 2$. For all higher order multipoles, motion in x and y are coupled, and the equation of motion can only be treated numerically [Ger92]. The solutions of the Mathieu equation can be divided in two classes, depending on the values of the dimensionless parameters a_2 and q_2. The first class yields stable motion, defined by the distance to the middle axis staying

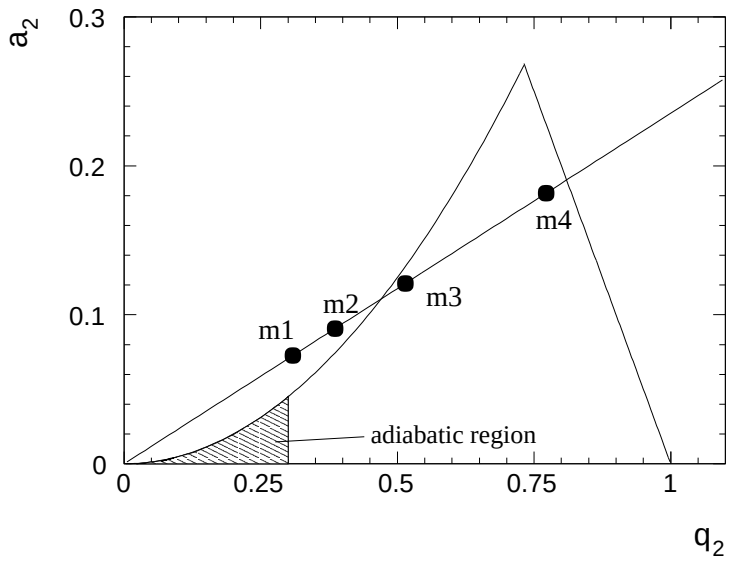

Figure 10.4: *Quadrupole stability diagram for the region close to the origin in the (a_2, q_2) plane; derived by solving the Mathieu equations describing the motion of charged particles in a time-varying linear 4-pole potential*

inside a certain interval that has to be smaller than r_0. In contrast, for the unstable solutions the amplitude of the oscillations increases exponentially, resulting in the loss of the ions once they leave the structure or hit the electrodes. To map out stable conditions of operation, a stability diagram in a_2 and q_2 can be drawn that shows where stable motion in both x- and y-direction can be achieved.

For practical purposes one usually limits the operation to the range of the stability diagram that is closest to the origin, which is depicted in Fig. 10.4. The stable region is that enclosed by the nearly triangular shape extending from the origin to $q_2 = 1$. To a good approximation it can described numerically by the two intersecting curves [Mar89, Ger92]

$$a_2 = \frac{1}{2}q_2^2 - \frac{7}{128}q_2^4 + \frac{29}{2304}q_2^6 \pm \ldots \tag{10.35}$$

$$a_2 = 1 - q_2 - \frac{1}{8}q_2^2 + \frac{1}{64}q_2^3 \pm \ldots \tag{10.36}$$

As pointed out before, q_2 corresponds to the adiabaticity parameter η and therefore the rule for safe operation that was established in the last section $\eta < 0.3$ would restrict the operational conditions to the small hatched area in Fig. 10.4. This mode can be chosen if the quadrupole is used as an ion guide, independent of the particle mass. However, since the equation of motion in quadrupole structures are unique in the sense that they are analytically fully understood, the majority of applications makes use of the mass separating properties at higher values of q_2.

To illustrate the mass filtering qualities, four different point masses of singly charged ions are plotted. As can be seen, whereas mass $m1$ and $m2$ are outside the stable region, $m3$ and $m4$ are inside and thus will be safely guided by the RF through the quadrupole structure. All masses are lying on a line with a slope that is defined by the ratio of the static voltage V_0 to the radio frequency amplitude $V_\sim$. In a typical mass scan implementation the ratio $V_0/V_\sim$ is kept fixed at a value where the mass line intersects the region of stability close to its maximum around $q_2 = 0.706$, $a_2 = 0.237$ (see Fig. 10.5) and then the absolute values of $V_\sim$ and V_0 are commonly ramped up. In this way the particular masses will move up along the mass line, and each mass will be inside the stable region for a certain interval of $V_\sim$. The closer one can get to the maximum tip of the stable region, the better the mass resolution will be.

In the next chapters both operational modes for quadrupoles will be used, ion guiding in the range of validity of the effective potential theorem and mass determination in the critical region of the stability diagram.

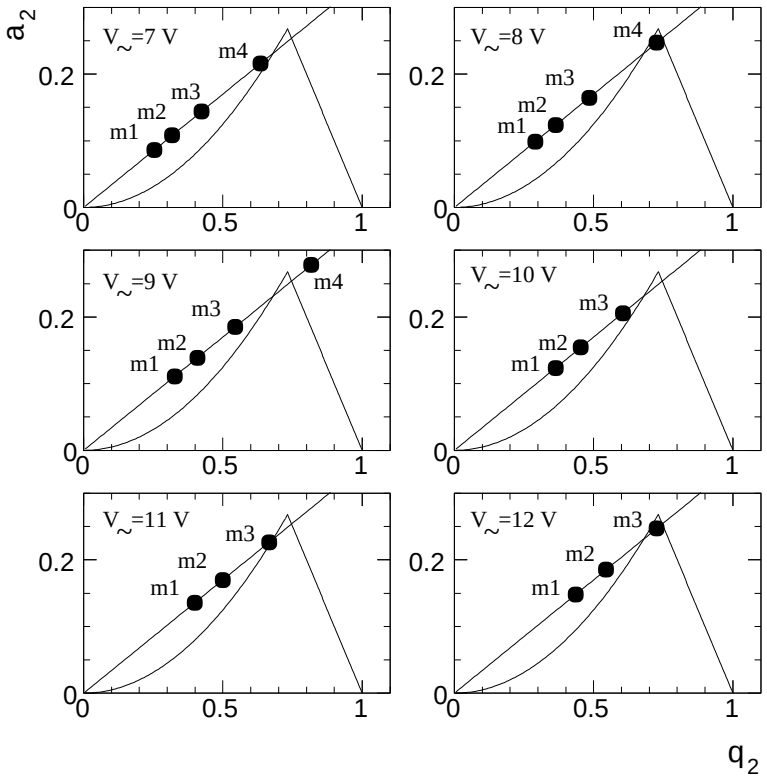

Figure 10.5: *Sketch of a mass filtering sequence. As the ratio $V_0/V_\sim = 0.34$ is kept fixed, the absolute values are ramped up. The RF amplitude $V_\sim$ is given in the insets, the masses correspond to atomic units. Further parameters are: $\omega/2\pi = 1.7\,Mhz$, $r_0 = 4.3\,mm$, V_0 varies proportional to $V_\sim$ between 2.38 V and 4.1 V.*

10.3 The 22-pole ion trap

The apparative use of higher order ($n > 2$) multipole geometries initially was motivated by the endeavor to scrutinize ion neutral collisions at low temperatures. The first realization of an octopole ion guide is described by Teloy and Gerlich [Tel74], further electrode geometries were implemented for various experimental purposes, as reported in [Ger92]. In this section the functional principle of the linear 22-pole ion trap will be explained, which was developed in Gerlich's group in the framework of the thesis of A. Sorgenfrei [Sor94]; Fig. 10.6 shows a drawing of the 22-pole trap. Eleven of the 22 stainless steel electrodes are alternatingly connected to one of the two copper side plates. The side plates on the other hand are electrically insulated with respect to the ground plate by thin sapphire sheets and supplied with the RF by external wiring (not depicted).

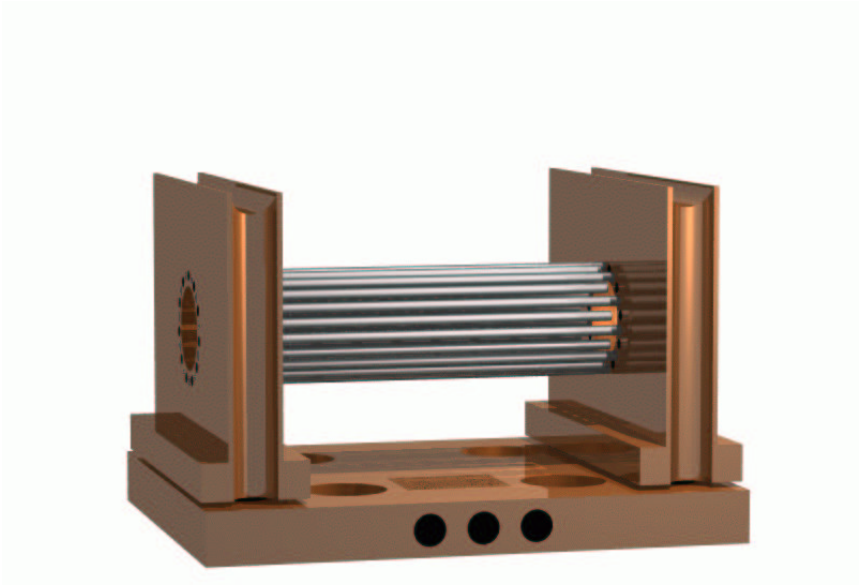

Figure 10.6: *Isometric view of the 22-pole ion trap. The diameter and length of the 22 rods is 1 mm and 40 mm, respectively.*

The main advantage of particle trapping in linear multipole fields of higher order is the shape of the effective potential, as seen in Fig. 10.2. The functional form of the effective potential scales with $n \sim r^{n-2}$ and thus for high n a large field-free region in the center of the trap is created (see also Fig. 10.1). The equipotential lines of ideal multipoles defined by Eq. 10.21 are hyperspherical, however, in practice the electrodes are usually made of circular rods. If the rod diameter d is to be adjusted to the radius of the potential curvature of the ideal multipole field, it is connected to the inner radius r_0 of the structure

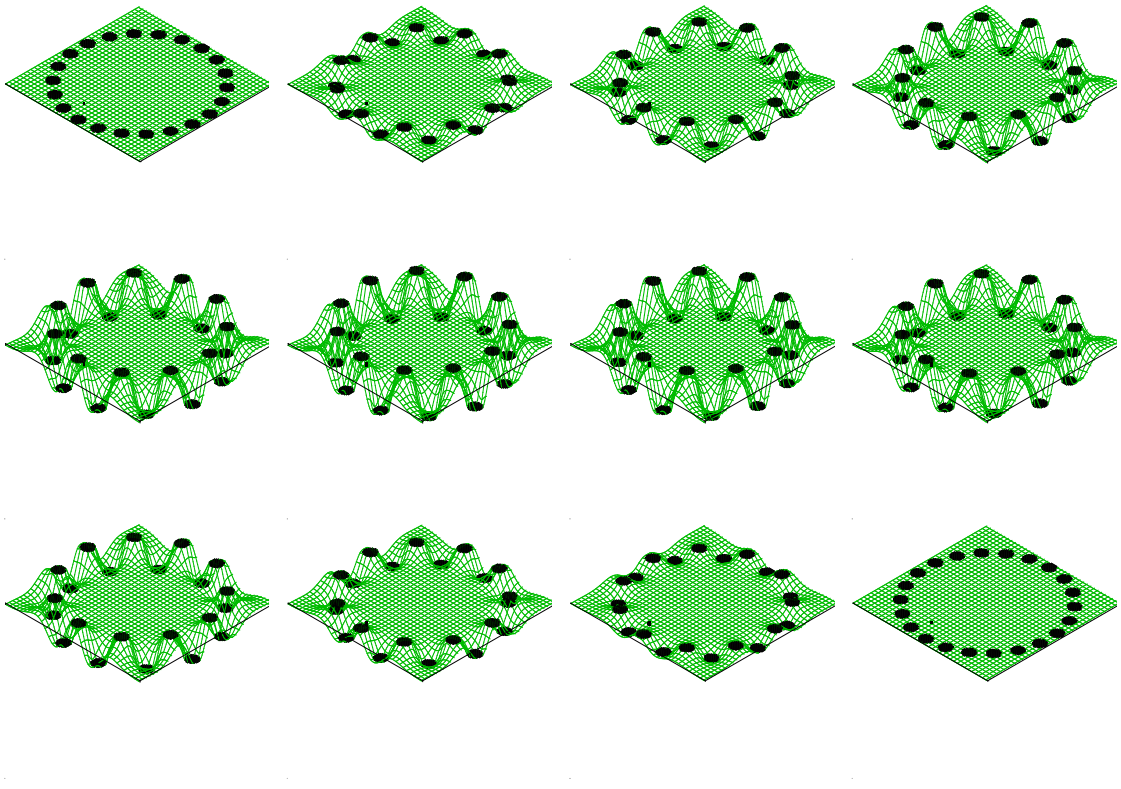

Figure 10.7: *Time evolution of the electric field in a 22-pole trap for one half-cycle of the radio frequency voltage, in arbitrary units (the sequence is to be read from left to right). The black areas represent cuts through the electrodes.*

by the simple relation[1] [Ger92]

$$r_0 = (n-1)\,\frac{d}{2}\,. \tag{10.37}$$

If one sets the rod diameter to $d = 1\,\mathrm{mm}$ and the trap diameter to $2r_0 = 1\,\mathrm{cm}$, the above formula yields $n = 11$ or 22 electrodes. Thus the number of 22 poles is in no way magical, it is rather a compromise between technical feasibility and experimental demand.

To illustrate the confinement of particles in radio frequency traps, usually a mechanical analogue is used. In this simple picture, the multipole potential is rotated around the symmetry axis, and a small globule is trapped inside the rotating potential [Pau89]. This type of mechanical traps can indeed by realized[2], but the actual time progression of the electric potential in a RF trap is of course different from a rotation; for the case of a 22-pole geometry and a sinusoidal RF voltage, the time-dependent potentials are plotted in Fig. 10.7.

1 for quadrupoles, corrections to this formula were derived by Dayton *et al.* [Day54]: $d/2 = 1.148\,r_0$.

2 On the occasion of his Nobel lecture, W. Paul used a plexiglas model that kept a small steel ball in position to demonstrate the functionality of his quadrupole trap [Pau89].

In order to derive the effective potential and the adiabaticity parameter for the trapping of H_3^+, we have to state realistic values for the various parameters. First we calculate the characteristic energy, according to Eq. 10.25. The two parameters $n = 11$ and $r_0 = 5\,\mathrm{mm}$ are given by the 22-pole structure, $m = 3\,m_{proton}$ is the mass of H_3^+ and the frequency ω of the oscillatory field is determined by the arrangement of the RF supply[3]. In our case (see next chapter) the resonance frequency was adjusted to $\omega/2\pi = 19.2\,\mathrm{MHz}$, no static potential is included ($V_0 = 0$). Under these conditions the characteristic energy amounts to $\epsilon \sim 1.2\,\mathrm{eV}$. Furthermore, to calculate the effective potential (Eq. 10.12), the charge of the ion $q = 1\,e$ and the RF amplitude $V_\sim$ are needed. The oscillatory circuit of the trap is not connected by any wires to the outside, and the RF is coupled in by induction, thus it is not trivial to measure its amplitude. However, by the use of a small antenna an estimate of $V_\sim \approx 30\,\mathrm{V}$ at regular operating conditions was obtained. With the inclusion of this value the effective potential depicted in Fig. 10.8 was derived.

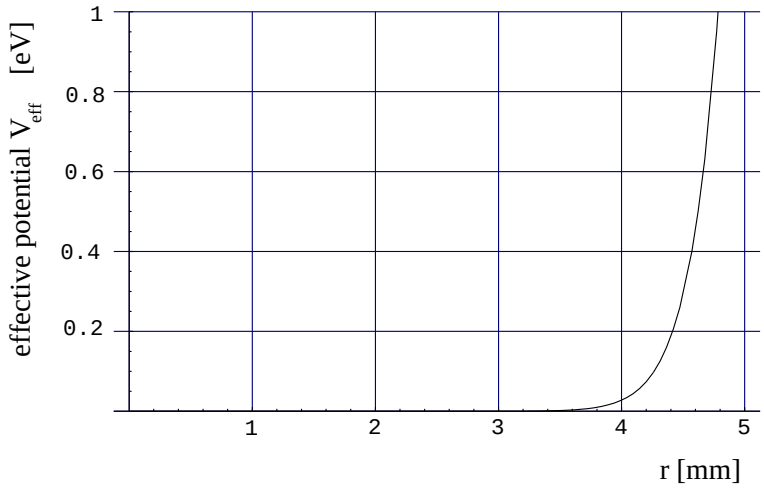

Figure 10.8: *Effective potential for an H_3^+ ion in the 22-pole trap as a function of the distance r from the trap axis. RF parameters are: $V_0 \approx 30\,V$, $\omega/2\pi = 19.2\,MHz$, $V_0 = 0$.*

It can be seen that the onset of the steep rise of the potential occurs close to the electrodes which are situated at 5 mm distance from the trap axis. The height of the effective potential is in the range of 1 eV, a value that is definitely high enough to trap particles at 10 K ($\sim$ 2.5 meV) and 300 K ($\sim$ 25 meV), nevertheless, one has to keep in mind, that most ions may come with much higher energies out of the ion source and have to be trapped before they are thermalized by collisions, thus a fair energy reserve in the effective potential is useful and necessary. With this requirement fulfilled, the next step

3 Actually it is determined by the resonance of the LC circuit, that consists of the ion trap (C) and a coil (L) that is used as an inductive RF coupling; the setup will be explained in the next chapter.

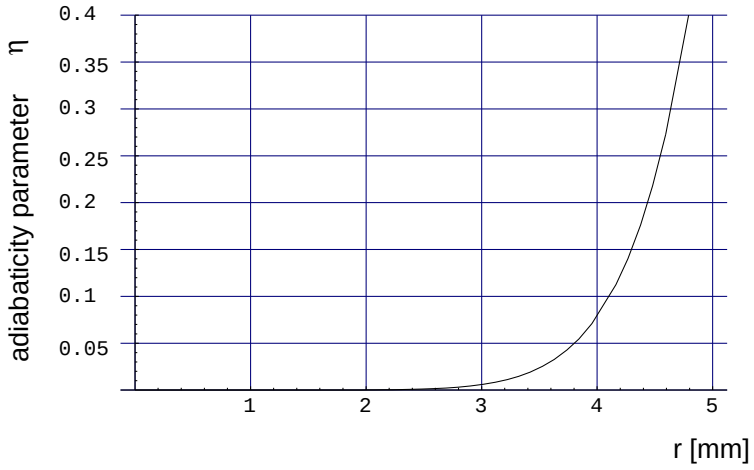

Figure 10.9: *Adiabaticity parameter for an H_3^+ ion in the 22-pole trap as a function of the distance r from the trap axis. RF parameters are: $V_\sim \approx 30$ V, $\omega/2\pi = 19.2$ MHz, $V_0 = 0$.*

is to evaluate the adiabaticity parameter η, to see whether safe operating conditions, characterized by $\eta < 0.3$, prevail in the trap.
Using the same parameters as above, Eq. 10.27 resulted in Fig. 10.9; it shows that η is below 0.3 practically in the whole trap volume, until the electrodes at $r = 5$ mm are reached. Comparing with the height of the potential (Fig. 10.8), one finds that more than 0.5 eV are needed to penetrate into regions with $\eta > 0.3$. Consequently, one may conclude that the operating conditions outlined above allow for the trapping of triatomic hydrogen ions in the 22-pole trap, and that due to the large region with essentially $V_{\text{eff}} = 0$ in the middle of the structure, even at low energies the ions will be able to fill the biggest part of the trap volume.

Numerical simulation of ion trajectories

Besides the use of the effective potential approximation, one can analyze the trapping properties of the 22-pole trap by performing numerical simulations of particle trajectories. For this purpose the `SIMION 3D` program suite [Dah00] was used, which is capable of evaluating ion orbits in time-varying electric fields in two- and three dimensions. In Fig. 10.10 the trajectory of a singly charged ion of mass three in a 22-pole trap is shown, under the RF conditions described above. In this picture two important aspects are visualized: first, the amplitude of the drift motion in the trap appears to be constant, implying that the total energy is conserved. Second, an avoided region is found in the middle of the trap, this effect is a consequence of angular momentum conservation, since the effective potential has rotational symmetry, the angular momentum of the particle with respect to

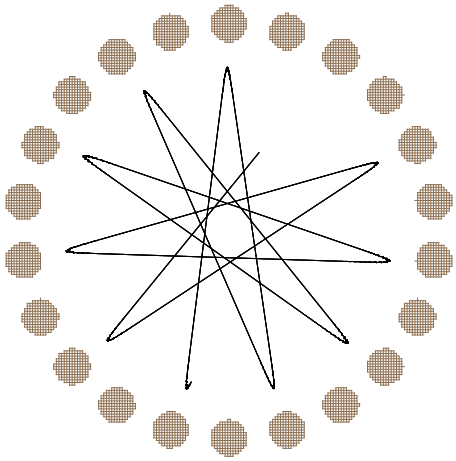

Figure 10.10: *Two-dimensional numerical simulation of the trajectory of a singly charged ion (mass 3) in a 22-pole trap. RF parameters as above, kinetic energy of the ion* $E_{\mathrm{kin}} = 7.5\,meV$ *(*$\sim 90\,K$*).*

the trap center will also be conserved.

This picture reflects the conclusions that were made considering the effective potential approximation, and it also supports the assumption established above, namely that this approximation holds practically in the whole trap volume. However, the smooth trajectories depicted in Fig. 10.10 may be misleading. Even within the favourable operating conditions chosen for these examples, the RF potential that is seen by the ion close to

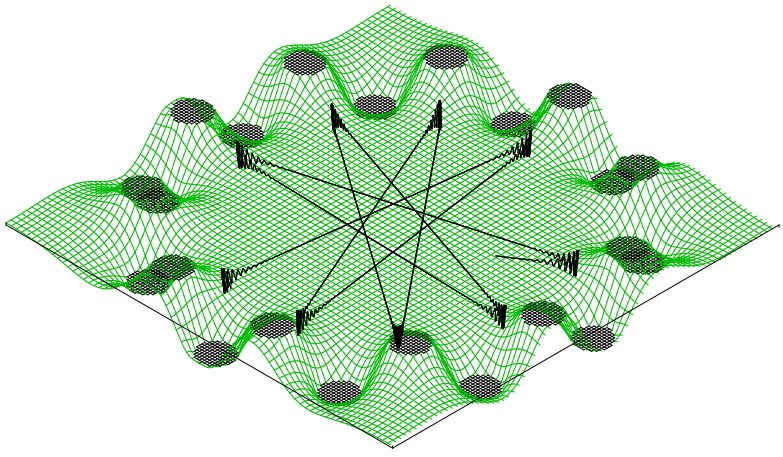

Figure 10.11: *Potential view of the ion's trajectory. The green surface represents a snapshot of the RF potential inside the trap, while the height of the trajectory corresponds to the potential that is seen by the ion at this position and time.*

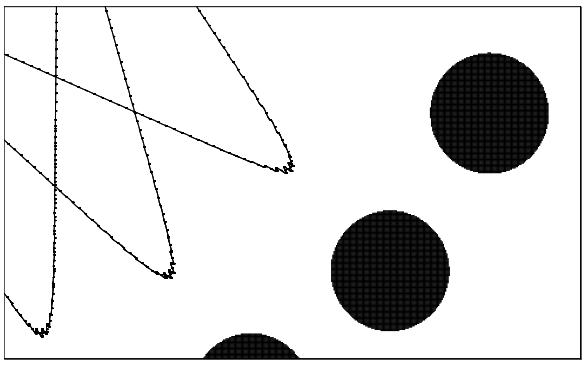

Figure 10.12: *Zoom into a region close to the electrodes. At the turning points the ion performs small wiggling motions under the influence of the radio frequency field.*

the electrodes can be as high as a few Volt (see Fig. 10.11). The small value of the adiabaticity parameter secures that the ions are too heavy to follow the potential, but small wiggling motions close to the rods are unavoidable (Fig. 10.12). If a collisions occurs at these positions the kinetic energy can be converted in internal energy and the ions may be heated rather than cooled by the buffer gas. One has to be aware of this effect especially in the light of the aim of this H_3^+ project. Once the trap will be operated in combination with the RFQ accelerator to deliver an ion beam for the TSR, it will be necessary to force as many ions as possible into the 22-pole, a total number of 10^5 to 10^6 H_3^+ molecules per trap filling is foreseen. Under these conditions a space charge potential is formed, that will make the ions spend more time in the outer parts of the trap, exactly where the risk of heating due to collisions under the influence of the RF is increased.

To evaluate the size of this effect, and the ultimate temperature that can be reached, we decided to rely on experiments rather than on more detailed simulations. One of the reasons for this decision is the fact, that it seems impossible to simulate precise conditions prevailing in the trap, since field inhomogeneities caused by imperfect machined parts or unwanted surface coatings can not be taken into account.

Eventually the simulations were extended to three dimensions to be able to analyze the loading and extraction from the trap. In reality for that purpose two circular end electrodes with a diameter of 8 mm are situated inside the openings of the side plates. These electrodes are responsible for the confinement of the particles along the trap axis and thus they can be used to fill and empty the trap, depending on the static voltage that is applied. In Fig. 10.13 a three-dimensional trajectory of an ion inside the trap is depicted. Here, the end electrodes are both set to 0.1 V to keep the ion inside. As can be seen,

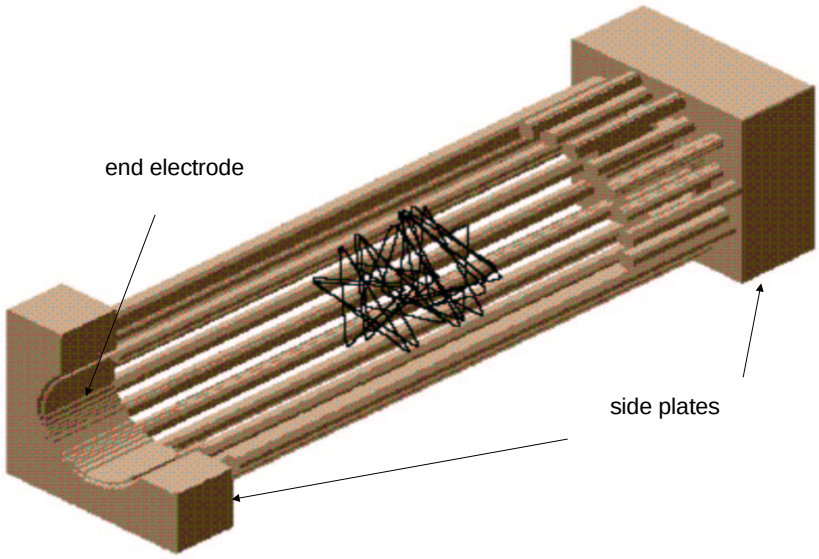

Figure 10.13: *Three-dimensional numerical simulation of the trajectory of a singly charged ion (mass 3) in a 22-pole trap. RF parameters as above, static voltages at the end caps* $+0.1\,V$*, kinetic energy of the ion* $E_{\mathrm{kin}} = 7.5\,meV$ *(*$\sim 90\,K$*). For clarity, only part of the side plates are drawn and the upper rods and part of one of the side plates with the end electrode inside is cut away.*

the ion is reflected at a significant distance from the end electrodes, apparently it sees already the small static end potentials at this point. This situation will naturally change with many ions in the trap, because they will try to keep their mutual distances as large as possible.

Chapter 11
Experimental setup

When the cryogenic 22-pole project was started, it was the aim right from the start to build a versatile apparatus that can be used as a molecule injector for the TSR as well as a stand-alone device for cold chemical reactions. Therefore, besides the infrastructure needed for the operation at the accelerator, an appropriate ion source and an efficient mass selective detector had to be implemented. The apparatus was designed with the help of D. Gerlich and collaborators from Technische Hochschule Chemnitz. The layout is shown in Fig. 11.1, it resembles very much the ion beam apparatus described in the thesis of W. Paul [Pau96] with a few simplifications and some strategic spots edited to meet the requirements imposed from future applications at the accelerator. Further references and descriptions of the 22-pole experiments in Chemnitz can be found in [Sch98, Ger02b, Ger02a, Sch02].

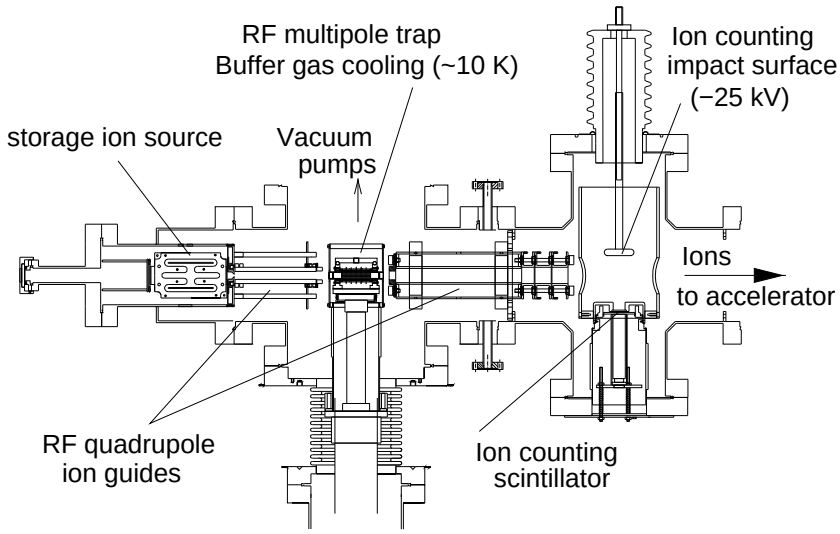

Figure 11.1: *Layout of the cold molecule injector using a RF ion source, the 22-pole ion trap mounted on a 10 K cold head and a Daly-type scintillation detector.*

The dimensions of the apparatus were severely restricted by the space that is available in the high voltage cage of the HSI accelerator (see Fig. 6.2), therefore the length of the setup was squeezed below 0.8 m. Furthermore, to meet the requirements of the RFQ structures of the HSI, on entrance of the accelerator the ions must have an energy of 4 keV per nucleon, and since the RFQs are at ground potential the whole trap including pumps and cryogenics has to be raised to 12 keV for H_3^+ and e.g. 24 keV for D_3^+. Consequently, a compact transportable design and high-voltage compatible remote control of all crucial parameters had to be planned.
The setup can be divided into three parts, the storage ion source including the quadrupole ion guide, the 22-pole trap and the mass selective detector consisting of a quadrupole and a Daly-type ion detector. In the following sections these three functional parts will be discussed separately.

11.1 The storage ion source

Although the production of H_3^+ is very simple (see chapter 3), a very elaborate ion source is used to feed the 22-pole trap. The reason for this is, that the trap is rather shallow and to achieve a good capture probability it is advantageous if the ions are precooled. Moreover, when the present setup was realized, the storage ion source was readily provided from D. Gerlich and thus no further efforts were necessary.
The first description of the storage ion source can be found in Gerlich's diploma thesis [Ger71], the refined construction used in our setup was built by R. Disch in Freiburg [Dis87]. In the eighties a campaign was started by Mitchell and coworkers to utilize the storage source for DR measurements of vibrationally cold molecular ions (including H_3^+) [Sen86a, Sen86b].
The central part of the source is a stack of molybdenum plates with several U-shaped channels. Each layer is insulated by small ruby spheres (see Fig. 11.2). The idea is to confine the ions between the plates in a high pressure environment until they diffuse out of the exit opening. For that purpose a RF voltage with alternating sign is applied to the plates. To prevent the ions from leaking out of the trap on the top or the bottom, end plates are used (not depicted in Fig. 11.2) that can be biased by a small DC voltage. Hence it is likely that an ion undergoes many collisions with the surrounding gas and thus thermalizes before it leaves the source. Ionization is achieved through electron bombardment from a rhenium filament (0.3 mm diameter) that is situated above one of the side channels, so that the ions have to travel through the structure until they come to the exit. The filament is heated with 15-30 W DC power and at the same time biased

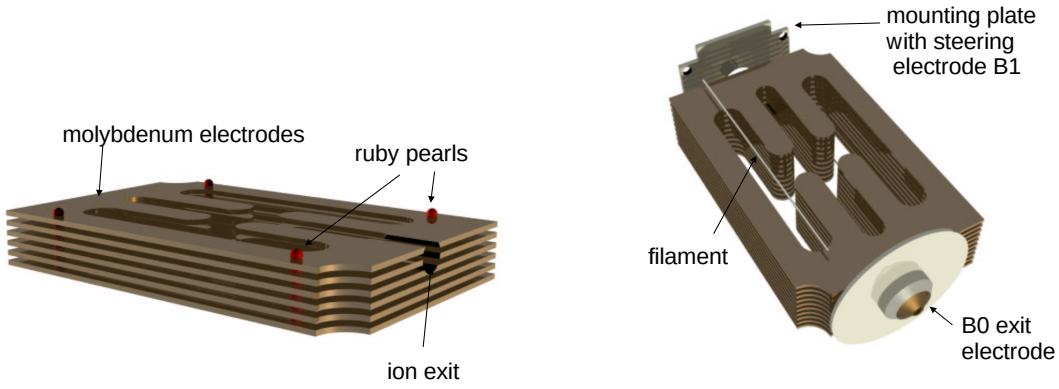

Figure 11.2: *Illustration of the construction principle of the storage ion source. A stack of molybdenum sheets with U-shaped recesses is insulated by small ruby spheres. Ions can be trapped inside the inner volume by an appropriate RF voltage applied to the plates with alternating sign. To control the flow out of the exit channel along the source axis, a steering electrode is placed at the backside (B1), and the exit electrode (B0) can be seen at the forefront.*

by 40-60 V with respect to the trap potential. By this means with the help of a focusing slit electrode and a repeller plate (see Fig. 11.3) the electrons are accelerated into the source volume to obtain maximum ion yield. At both ends of the source, apertures are mounted that allow the inner volume to be closed for the ions if a positive bias voltage is applied, or to produce a constant flow of ions if a negative voltage is used to create a field gradient penetrating into the exit region.
The source is mounted on a CF100 flange and enclosed by a metallic cover to built up

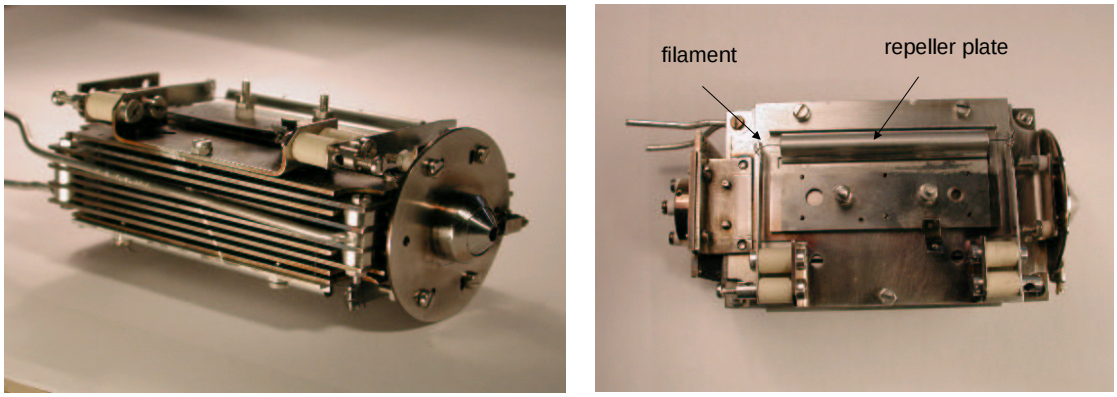

Figure 11.3: *Photographs of the storage ion source (taken in the Chemnitz laboratory). The first picture shows a side view, where the stack of molybdenum plates can be seen. In the top view on the right-hand side part of the rhenium filament is visible with the repeller plate that focuses the ions into the trap region.*

a high pressure inside, while the only opening to the vacuum system is the 3 mm exit aperture (B0). On one side of the cylindrical cover the reaction gas is let in by a stainless steel tubing that is connected to the outside by a Swagelock system. The gas flow can be adjusted by means of a sapphire precision valve that allows for leakage rates as low as 10^{-10} mbar l s^{-1}.

In our setup a small quadrupole of ~90 mm length with an inner radius of $r_0 = 4.3$ mm is attached to the source cover. It is used as an ion guide to transport the ions from the source to the 22-pole, reducing significantly the unwanted flow of neutral gas from the source into the ion trap compared to a direct connection. Moreover, in future experiments it can also serve as a mass filter if a particular species coming from the source has to be selected. If the source is operated with hydrogen, however, mass selection at this stage is hardly needed. The efficient formation reaction of H_3^+ which takes place almost at every collision with H_2 and the concept of long dwell times in the source renders it improbable for an H_2^+ ion to reach the source exit. In a first beamtime, testing the storage source alone at the accelerator, no current corresponding to mass 2 could be detected.

From experimental experience it is known [Ger01] that the best conditions for the storage of H_3^+ in the source are achieved at radio frequencies of $\omega/2\pi > 15$ Mhz and amplitudes of 150-200 V (which corresponds to up to 400 V between the plates). Because of the rather high capacity of the electrode stack of ~ 180 pF, the supply of such a high voltage and

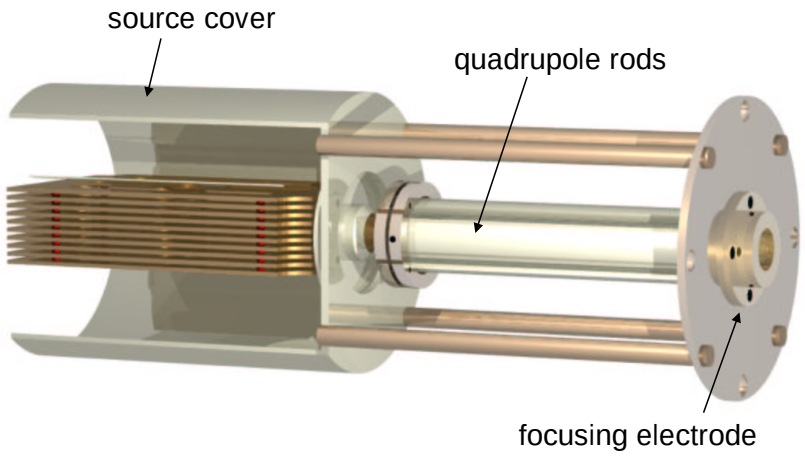

Figure 11.4: *Isometric view of the functional parts of the storage source with the small ion guide quadrupole attached to it.*

frequency to the circuit is not trivial. Transistor power supplies with powerful amplifiers are commercially available, nevertheless they are usually not capable of providing high voltages and thus an elaborate transformer for this high capacity would be needed. It is not by accident that tube amplifiers are still in operation at radio stations and other applications (e.g. the MPI post accelerator) where powerful RF signals at high voltage are needed. We also fell back upon an old tube oscillator provided by D. Gerlich, that had to be tuned to deliver the right output, which was a lengthy and cumbersome procedure since all the experience with tube amplifiers has deteriorated in the last decades and experts as well as spare parts are rare. Eventually we managed to adjust the oscillator to the right frequency and once this was accomplished, it affirmed the reputation that tube devices enjoy for their robustness and reliability.
Under regular operating conditions the source produces up to 30 nA of H_3^+ at the exit of the quadrupole. If the filament power is turned up to very high values, even more current can be achieved, which is not necessary if the arrangement is used to load the 22-pole trap; in fact, for that purpose a few nA are fully sufficient.

11.2 The cryogenic ion trap

The theoretical background and the principal geometry of the 22-pole trap was already discussed in the last chapter. In this section the setup of the trap will be explained in more detail and the features that are essential for the cooling and the RF supply will be presented.
In Fig. 11.5 a schematic drawing of the ion trap is shown. The side plates as well as the ground plate and the cover are made of copper for good thermal conductivity. For the

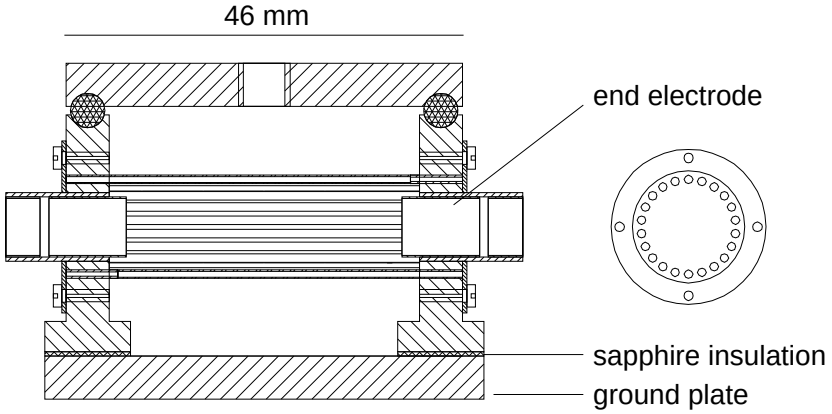

Figure 11.5: *Schematic drawing of the 22-pole trap.*

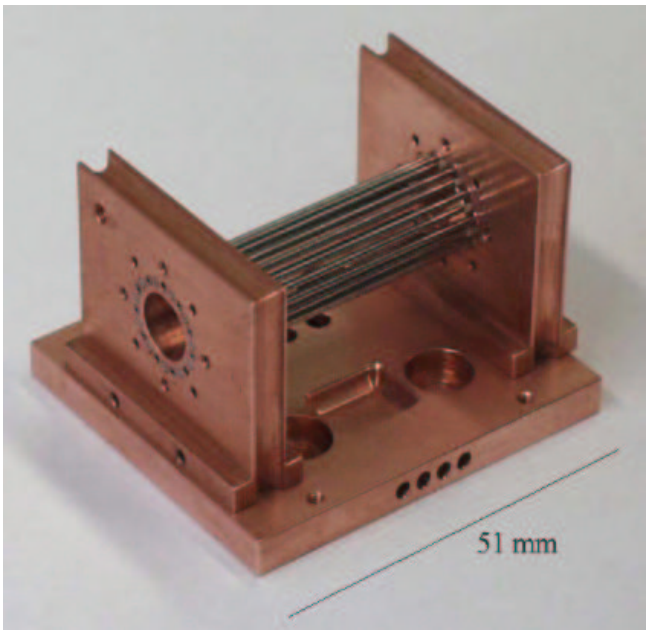

Figure 11.6: *Photograph of the basic 22-pole parts. The side plates are not yet fixed at the ground plate where holes can be seen which are thought to be used to fix the trap to the cold head and for feedthroughs of shaping electrodes that are currently not installed.*

first 22-poles that were built in Freiburg [Sor94], the 22 rods were shrunk into the side plates by cooling them to liquid nitrogen temperature while the copper side plates were heated slightly. This has to be done extremely thoroughly, since one mistake can ruin the whole piece, in addition the accuracy is limited. In our workshop a novel technique was developed by N. Schlicksupp, who manufactured a high precision guiding adapter that could be fastened on the side plates and allowed for safe planting of the rods into the material with unprecedented precision. By this way three 22-pole traps of equal quality were manufactured; two of them are currently being prepared for experiments by different groups in Chemnitz/Basel and Heidelberg/Freiburg, the third one (Fig. 11.6) is already operational and is the subject of this part of the thesis.

Cryogenics

The 22-pole was mounted on a 10 K cold head (Leybold Coolpower 2/10) with a nominal cooling power of 2 W at 10 K for the second stage and 12 W at $\sim$ 35 K for the first stage. During the operation, it is crucial that all parts that are seen by the buffer gas truly reach the cold head temperature, since the collisions between the neutral gas and the walls will eventually determine the internal temperature of the ions. In case of the side plates this imposes the requirement to completely insulate them electrically against their

surrounding, but at the same time they need to have good thermal contact to the cold head and they have to be aligned precisely. This is done by thin sapphire sheets between the side plates and the ground plate and cylindrical ceramic spacers that are used for insulation and alignment towards the trap cover (see Fig. 11.7). If one considers the thermal conductivity of sapphire $\kappa = 10\,\mathrm{W\,cm^{-1}\,K^{-1}}$ at 10 K [Pob96], it is nearly as good as that of mediocre copper (the conductivity of copper at 10 K is between 1-150 $\mathrm{W\,cm^{-1}\,K^{-1}}$, depending heavily upon its purity [Pob96]) and thus excellent thermal coupling between the ground plate and the trap can be reached. To push the contact to the maximum, the copper surfaces were manually adapted by a special grinding technique to the particular sapphire sheets which were uneven on a scale of several micrometers (work done at MPIK workshop, N. Schlicksupp). The thermal conductivity of the ceramic used at the top cover is distinctly lower (for pure Al_2O_3 – which is not exactly what is used in our version – it is about 850 $\mathrm{mW\,cm^{-1}K^{-1}}$ [Pob96]) and hence special care was taken that the copper cover and the ground plate have good contact since electrically they are both on ground potential.

Exposure of the trap to 300 K blackbody radiation would make it impossible to reach 10 K, since the surfaces of the trap are simply too big. Therefore an aluminium heat shield with openings only for the wiring, the gas inlets and the ion entrance and exit is

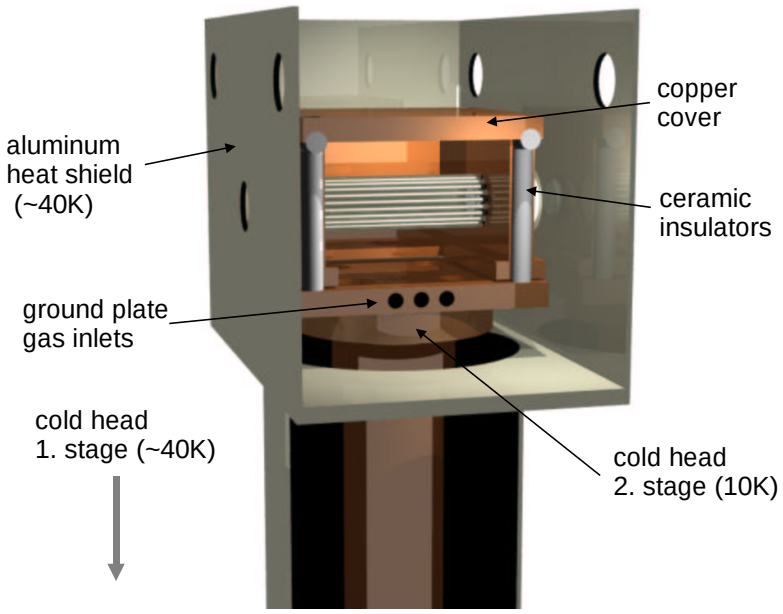

Figure 11.7: *Isometric view of the 22-pole ion trap mounted on the second stage of the cryogenic cold head. The aluminium heat shield and the copper cover are cut open to allow insight into the interior.*

built on the first stage of the cold had, enclosing the whole device (part of it can be seen in Fig. 11.7).

The buffer gas is let into the 22-pole through holes in the ground plate. This is done to cool the gas already before it enters the trap region. To further relief the second stage from the thermal strain the buffer gas tubes are U-shaped and tightly attached to the walls of the aluminium heat shield in order to be precooled (see Fig. 11.9).

However, for some experiments it might be necessary to work at higher temperatures, – because many reaction- or buffer gases freeze out at 10 K, and since the cold head can not be regulated, a dedicated means of heating had to be implemented. For that purpose a small capton coated heating foil is wound around the cold head and fixed there by a stainless steel clamp. The nominal power that this foil can tolerate is much higher than the power of the cold head, nevertheless it turned out that heating at low temperatures can be non-trivial. Simple model calculations show, that the thermal conductivity of synthetic insulators like capton at 10 K can be so low, that a temperature gradient of several hundred Kelvin can built up across 1 mm foil thickness. Consequently, the temperature of the heating wire inside can be far beyond the specifications although the outside of the foil is still around 10 K and is seemingly cooled very well. The remedy is to operate the foils distinctly below their specifications – which is still sufficient – and to change the heating power slowly, since with increasing temperature also the conductivity increases.

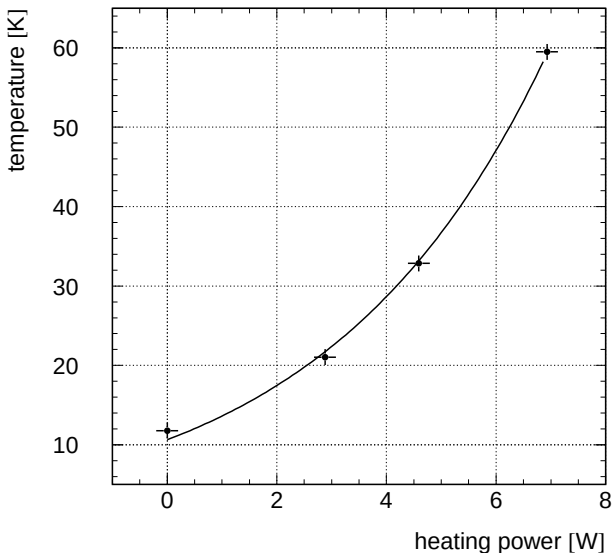

Figure 11.8: *Wall temperature of the 22-pole trap as a function of the power applied to a heating foil at the second stage of the cold head.*

Of course this understanding was gained not until the first heating foil had been grilled. The temperature of the walls of the trap can be measured by two silicon diodes of the type `Lakeshore DT-470-CU-11A` and `DT-471-CU` (accuracy $\pm 0.25\,\mathrm{K}$ and $\pm 1\,\mathrm{K}$, respectively) that were mounted to the cover and to one of the side plates (only in a preliminary setup, during operation the side plates are connected to the RF). When the trap was installed for the first time without gas inlets and electrical connections, a temperature of $\sim 8,5\,\mathrm{K}$ was reached. This value was raised to $\sim 12\,\mathrm{K}$ after all the wiring had been completed. The temperature as a function of the power applied to the heating foil is depicted in Fig. 11.8, it reaches equilibrium within seconds to minutes after a change has been made, depending on the size of the jump. The general behaviour is compatible with the refrigerating capacities of the cold head [Ley00].

RF connections

The radio frequency is inductively coupled to the 22-pole by a set of two concentric coils with different diameters. The ends of the larger coil extend into the aluminium shield and are eventually connected to the 22-pole (see Fig. 11.9). Thus the trap and the coil form an LC circuit with resonance frequency $\omega = \sqrt{(LC)^{-1}}$. Once the coil is tuned, the RF frequency is fixed and can not be altered without opening the vacuum system. In our case the resonance frequency was adjusted to $\omega/2\pi = 19.2\,\mathrm{MHz}$ which is an appropriate value for the experiments that are foreseen, as demonstrated in the last chapter.

The stimulation of the oscillation from the outside is done by applying a RF voltage to the small excitation coil. The arrangement has to be tuned carefully to minimize unwanted reflections that might influence the signal. Furthermore, silver coated copper wire of relatively large diameter is used to make the quality of the oscillating circuit as high as possible, in order to reduce ohmic heating of the coil which could be transfered to the trap.

During operation the RF power is supplied by a linear amplifier (`RFPA RF001100-8`, 8 W maximum) that is driven by a signal generator (`Marconi 2019A`). The forward- and reflected power is read out by a standard standing wave measuring unit, as used for radio applications. The difference between both values gives the effective power that is deposited inside the circuit and it has to be smaller than the 2 W refrigeration power of the cold head. It turned out, however, that less than 1 W forward power is needed to get an RF amplitude of ca. 30 V at the trap and less than 0.5 W stay inside the circuit and heat the system. Consequently, under normal conditions the RF does not influence the trap temperature perceptibly.

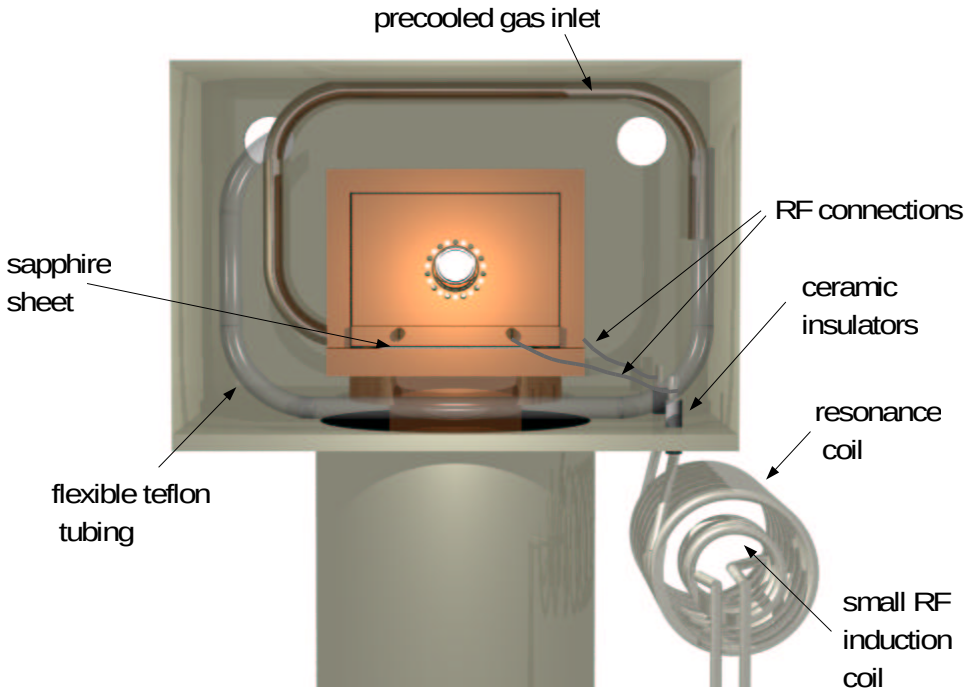

Figure 11.9: *Sketch of the 22-pole trap with the aluminium heat shield and the RF coil arrangement. The buffer gas tube is pressed to the aluminium cover and it ends in the copper ground plate.*

11.3 The Daly detector

In order to test the setup and the trap performance, a suitable ion detector was implemented. It had to serve two different purposes: first, as a sensitive detector for single ion counting, in case the trap is operated as an experimental device for cold reactions, second for rough current measurements to check the trap efficiency prior to installation at the accelerator. To account for these demands, a Daly-type detector is used, the layout is shown in Fig. 11.10. Its main parts are an aluminium stamp – the so-called converter – that is set to negative high voltage, and a scintillator that is read out by a photomultiplier which is located outside the vacuum chamber. Positive ions that are mass selected in the quadrupole are attracted by the high voltage and impinge at the converter where several secondary electrons are set free. These electrons are born in the potential gradient between the converter at -20 kV and the scintillator (ground potential) that is coated with a thin aluminium layer. Because the field in that region can be considered homogeneous, the electron trajectories will point along the field lines to the scintillator, if the position

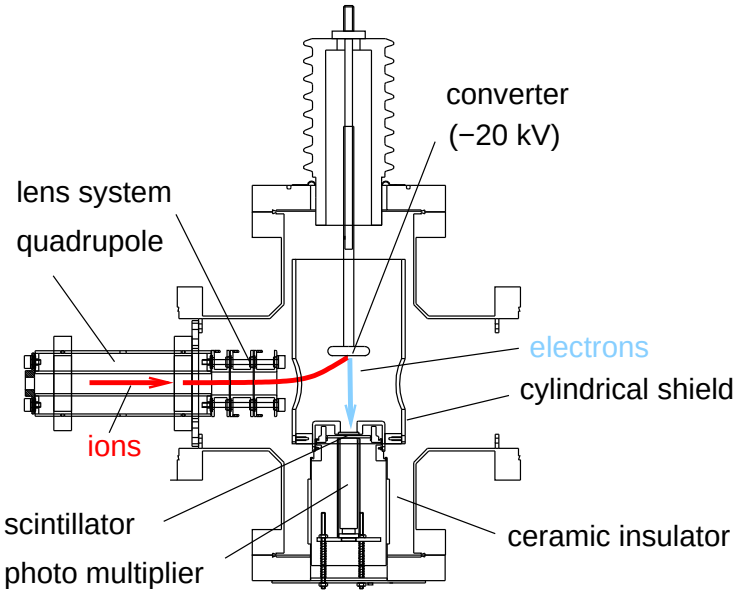

Figure 11.10: *Schematic drawing of the Daly detector.*

of the converter is properly adjusted.
This detection principle was first described by N.R. Daly [Dal60] as a diagnostics for high sensitivity mass spectrometry. It makes use of the ten times larger conversion efficiency of electrons compared to heavy ions for typical scintillators and the high secondary electron yield at the aluminium converter.
Today, the most commonly used ion detector in the keV- to MeV energy range is the micro channel plate (MCP). However, the Daly detector has a few advantages that convinced us to decide in favour of this design:

- the detection efficiency is close to unity, compared to 40-60% for an MCP,
- the in-vacuum parts (converter and scintillator) are practically unbreakable, also electron bombardment of the scintillator produces much less damage that ion impact,
- no part of the equipment has to be kept constantly under vacuum, if maintenance work at the apparatus is carried out (an MCP should not be exposed to atmosphere longer than $\sim$1 hour),
- the geometry allows for a quick change between detection and transport of the beam to the accelerator without any mechanical motion,
- the Daly detector can take very short ion pulses, corresponding to large currents without loosing its linearity (as will be seen below).

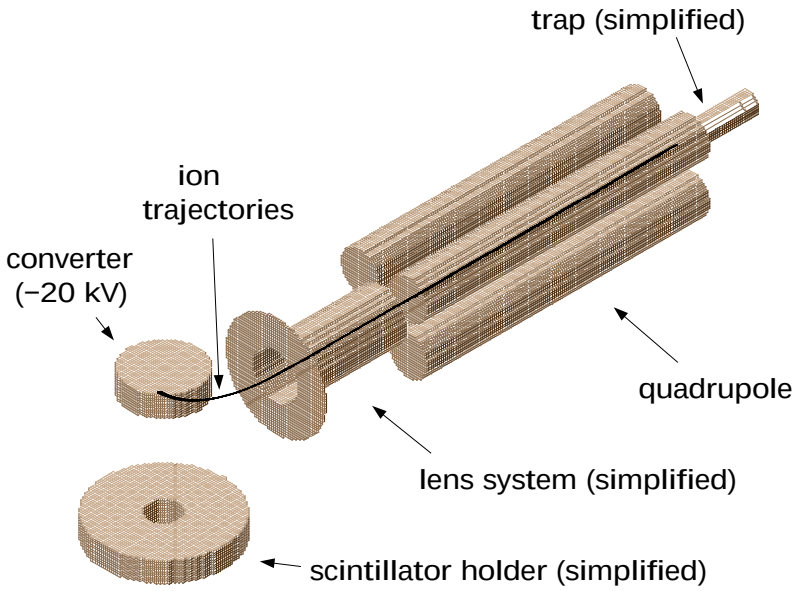

Figure 11.11: *Isometric view of the Daly detector with the second quadrupole.*

The most important parameter of the detector arrangement is the distance of the converter disc to the quadrupole axis. If the converter is too close to the beam, the particles hit the corner of the disc and the resulting electrons will not find their way to the detector window; if the disc is too far away they miss the scintillator and end up on the other side. To find the best position, a `SIMION` simulation of the detector including the mass selective quadrupole was performed. It showed that the absolute value of the high voltage as well

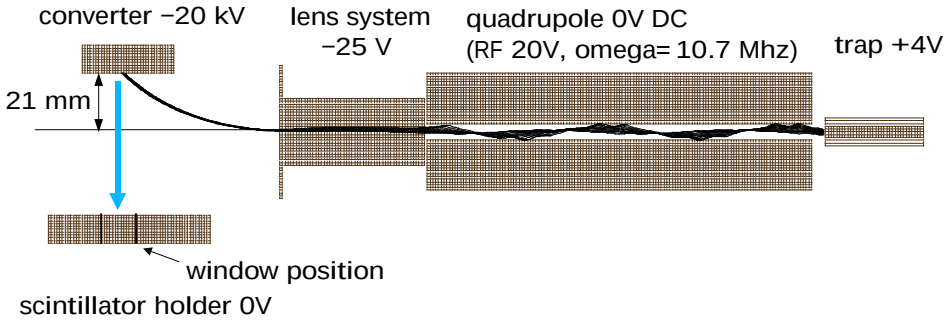

Figure 11.12: *Numerical simulation of several ion trajectories through the quadrupole onto the converter of the Daly-detector. The distance between the beam axis and the converter is adjusted to 21 mm. The ions (mass 3) have an initial kinetic energy of 1 eV, the azimuthal angle and the elevation angle vary between 0-20 degree, the initial position in x and y varies by 2 mm. Quadrupole RF parameters are* $\omega/2\pi = 1.7\,Mhz$, $V_{\sim}$=*20 V.*

as the voltages at the lens system have very little influence on the impact point of the ions at the converter disc. In order to optimize the impact position to the disc center, the distance from the disc to the quadrupole axis was adjusted to 21 mm (see Fig. 11.12). This adjustment was checked by using the ion beam from the storage source directly. For that purpose both quadrupoles as well as the 22-pole trap were operated as ion guides, with the RF switched on, and the ions were manouvred through the apparatus by small potential steps between the source (+0.5 V), the first quadrupole and the trap (ground potential) and the second quadrupole (-0.5 V). Consequently, the ions had a final kinetic energy of about 1 eV and the current reaching the second quadrupole was of the order of 1 nA. The photomultiplier was replaced by a CCD camera and pictures of the scintillator disc were taken for various converter voltages. In Fig. 11.13, it can be seen that the light spot created by the secondary electrons is well on the disc, although slightly decentered. The displacement is too small to justify further efforts and moreover it is in vertical direction, i.e. it is probably caused by gravity pulling down the converter which is kept in place by a small viton ring that is fitted into the big ceramic insulator and is secured by a small screw outside the vacuum chamber.

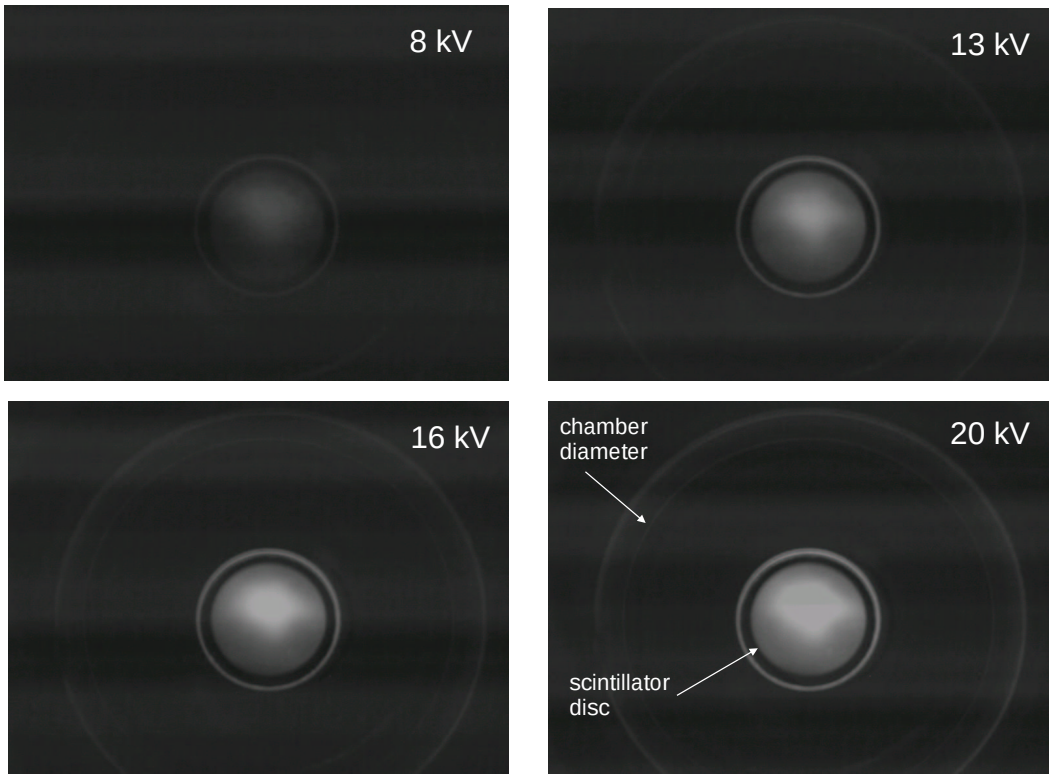

Figure 11.13: *Photographs of the light spots created at the scintillator of the Daly-detector by an H_3^+ beam of ca. 1 nA for various converter voltages.*

For single ion detection, the Daly detector is operated with a converter voltage of 20 kV. Further increase of the voltage did not increase the ion count significantly; this finding is supported by the dependence of the electron yield from ion impact on aluminium. Experiments performed in the fifties to scrutinize the influence of positive ions on the breakdown of vacuum systems, showed that the ratio of the secondary current (electrons) to the primary helium ion current hitting an aluminium surface was ∼7 for a voltage difference of 20 kV, while it increased only little further to ∼10 at 80 kV [Bou55].
In single ion mode, the photomultiplier is operated at 1000 V; the pulses are about 20 ns long and they are amplified by a timing filter amplifier, afterwards they are discriminated and counted by a 220 MHz universal counter which is read out by the data acquisition computer via GPIB. Since the pulses coming from the trap are usually about 200 μs long (see next chapter), this procedure works for ion counts up to several thousand ions per trap filling.
If more ions per pulse are to be measured, the detector is used in current mode. For that purpose the photomultiplier voltage is lowered to 500-600 V and the timing filter amplifier is replaced by a slow integrating amplifier. The voltage signal is read out by a digital scope which again communicates with the DAQ computer by GPIB. To a good approximation the peak signal height from the amplifier is proportional to the number of ions in the pulse.
Once the trap will be used at the accelerator it is foreseen to preaccelerate the ions at the end of the quadrupole to keV energies to be able to use standard ion optics. For this case, the head of the photomultiplier chamber is separated electrically from the vacuum chamber by a ceramic insulator and can be put to an independent potential (see Fig. 11.10). In addition a cylindrical shield can be attached to the photomultiplier chamber and a small drift tube will be inserted downstream in order to hide the potential of the vacuum chamber from the ions. These preparations are not yet tested in their final design.

11.4 Requirements for operation at the TSR

The use of the ion trap at the HSI accelerator as an injector for the TSR storage ring imposes certain requirements on the number of ions and the length of the extracted ion pulse.
It is instructive to calculate the count rate in a typical H_3^+ DR experiment in order to estimate the number of stored ions in the TSR that is needed to perform a meaningful DR measurement. The count rate R at the solid state detector (100 % detection efficiency) is given by the DR rate coefficient $\alpha = 6.8 \times 10^{-8}\,\mathrm{cm^3\,s^{-1}}$, the electron density

$n_e = 3 \times 10^6\,\mathrm{cm}^{-3}$, the length of the straight section of the electron cooler divided by the circumference of the storage ring $\eta = L_c/L = 0.027$ and the number of H_3^+ ions N_{ion} in the ring

$$R = \alpha\, n_e\, \eta\, N_{ion}. \tag{11.1}$$

If one assumes the number of stored H_3^+ ions to be $N_{ion} = 10^5$, the above equation yields a count rate $R = 550\,\mathrm{s}^{-1}$, which would be about the lower limit tolerable in a DR experiment (in regular beamtimes, if the source produces enough ions, the count rate is adjusted to 2 kHz).

To get an estimate of the number of ions that have to be extracted from the trap in order to achieve this amount of stored ions in the TSR, one has to consider the transmission from the trap to the storage ring. The transmission through the RFQ accelerator can be as high as 80 %, if it is thoroughly tuned; the flight through the postaccelerator to the injection section of the TSR usually reduces the current to 20 % if all focusing quadrupoles are optimized. Consequently these two stages – if carefully adjusted – reduce the ion current to 16 %. However, before the ions enter the accelerator they have to be preaccelerated to 4 keV/u, guided through the 60° magnet and out of the high voltage cage (see chapter 6.3). The loss processes in this part are difficult to estimate, because usually the magnet discrimates different charge states and masses coming out of a standard discharge source, therefore the ion current before and after the magnet can differ significantly. In contrast to that situation, the ion trap would deliver only H_3^+ ions and the low temperature of the ion sample would result in a vanishing energy spread and angular divergence provided the ion optics were adjusted accordingly.

Assuming that all ions extracted from the trap reach the accelerator, about 10^6 ions per trap filling would be needed for a DR measurement.

An additional restriction arises from the length of the time window resulting from the TSR multiturn injection scheme (see chapter 6.2). At typical energies of 500 keV/u, this window has a length of 200 μs; consequently the complete ion pulse extracted from the source should be shorter than this time interval.

Both requirements formulated above will be checked in chapter 12.

Chapter 12
First tests and measurements

12.1 Characterization of the RF storage source

The storage source used for the production of H_3^+ was described in the last chapter. The advantage of this type of source is the confinement of the ions in a high pressure region before they diffuse out of the exit aperture. As mentioned before, in the eighties a similar source design was used for a series of merged beam studies. Mitchell and coworkers inferred from collision-induced dissociation measurements with a crossed neutral beam that H_2^+ ions produced in the RF storage source were predominantly in $v = 0$ and $v = 1$, while H_3^+ was supposed to be completely relaxed to the $v = 0$ ground state [Sen86b, Sen86a, Sen87]. In subsequent DR measurements with H_3^+ and D_3^+ they found a dependence of the cross section on the source pressure and the extraction voltage, however the cross section was distinctly lower than measured with a usual hot RF ion source [Hus88, Van91].
Because of the progress that had been made at the TSR in monitoring vibrational and rotational excitation, it seemed worthwhile to make further tests to find out if the RF source alone is capable of producing cold H_3^+ ions. Although the source could not be cooled below room temperature, a DR measurement at 300 K would have been a major progress compared to the probably non-thermal distribution of 0.23 eV that had been observed with the CHORDIS ion source (see part II).
For a one-week beamtime the RF storage source was installed at the HSI accelerator. It was operated at pressures between 10 and 20 mbar and the small quadrupole was used to transport the ions slowly out of the high pressure region close to the aperture. The first measurement was performed with the Coulomb explosion setup, bypassing the storage ring and guiding the 1.43 MeV ions directly to the CEI beamline to test the initial vibrational population coming from the source. Fig. 12.1 shows the v_a velocity distribution connected to the breathing mode coordinate for two different source pressures and extraction voltages together with the distribution measured for the standard CHORDIS source.

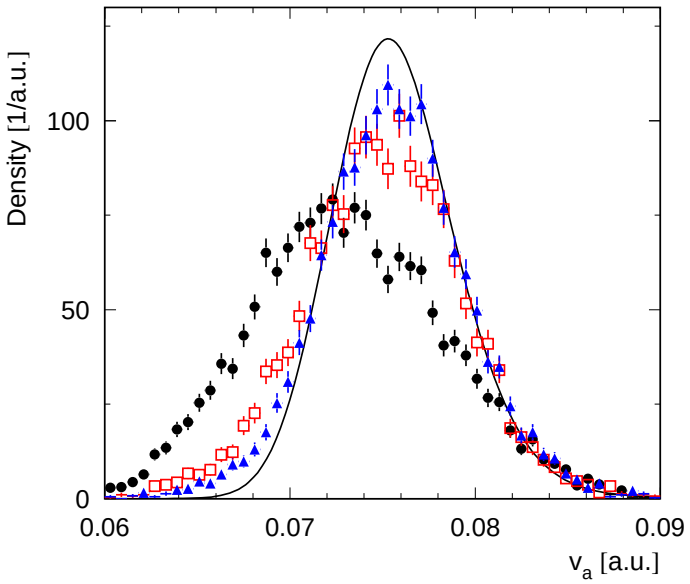

Figure 12.1: *Result of Coulomb explosion measurements for direct transfer of the H_3^+ beam from the accelerator to the CEI beamline. Plotted is the symmetric v_a distribution for the CHORDIS ion source (black dots), the RF storage source with a pressure of $p = 2 \times 10^{-4}$ mbar and a source potential of 6 V (open red squares), the RF storage source with $p = 5.7 \times 10^{-4}$ mbar at a source potential of 1 V (blue triangles) and the simulation of the ground vibrational state (solid black line).*

For comparison the simulated curve of the vibrational ground state is also plotted, the curves corresponding to the lowest two breathing mode excitations are depicted in Fig. 7.7.

For both settings the RF storage source is closer to the ground state than the CHORDIS source; nevertheless the plot shows that substantial vibrational excitation is present and consequently the ions are either not thermalized to the source temperature or they are excited during the extraction. The distribution that was observed for high pressure and low extraction voltage is obviously colder, revealing that more collisions are helpful. Further reduction of the extraction voltage to 0.1 eV did not improve the situation, further increase of the pressure was not possible due to limitations imposed by the turbomolecular pumps at the accelerator beamline. It is known that vibrations are more resistant to collisional cooling than rotations (see e.g. [Lev91]) and since the CEI experiments described in Part II of this thesis demonstrated that vibrational excitation can be removed by storage for more that two seconds, a DR fragment imaging experiment on a stored H_3^+ beam was carried out to examine the rotational excitation.

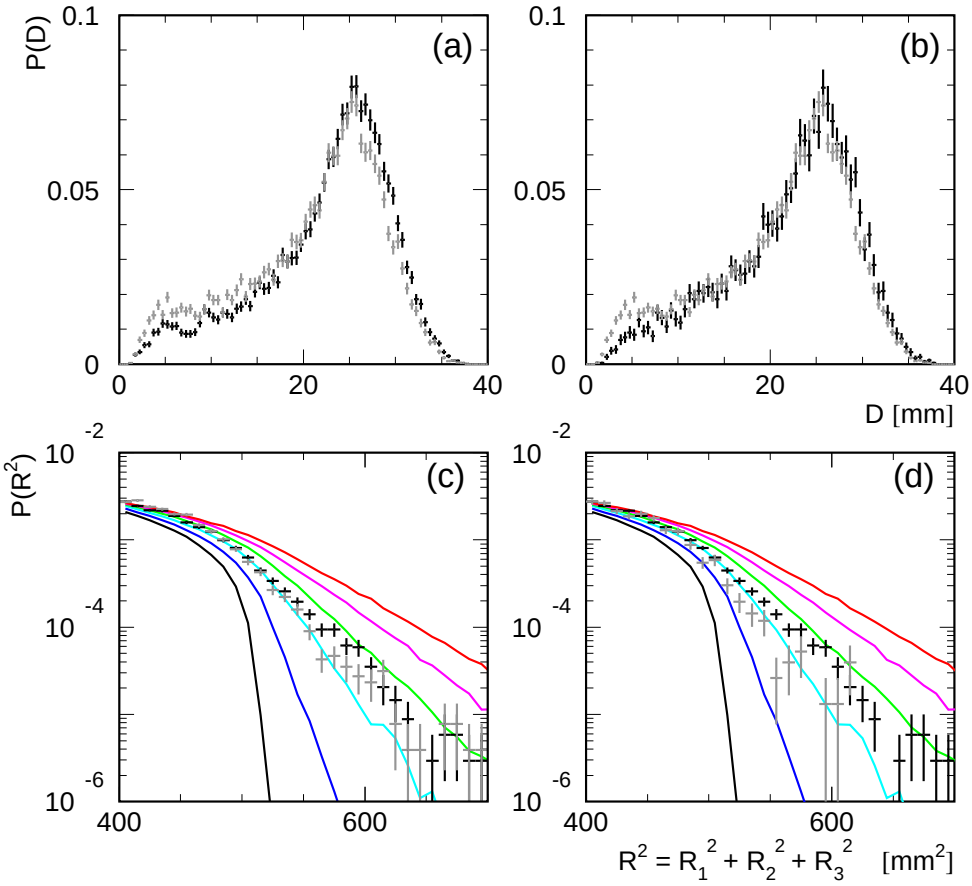

Figure 12.2: *Imaging results for two different settings of the RF storage source (black crosses) compared to the hot filament CHORDIS source (grey crosses). For (a),(c) the storage source was operated at low pressure (2×10^{-4} mbar outside) and a high source potential of 6 V, while for (b),(d) the pressure was higher (5.7×10^{-4} mbar outside) and the source potential was at 1 V. The solid lines represent simulations including various degrees of rotational excitation (in increasing order): black ≃ no rotations, blue ≃ 100 meV, cyan ≃ 200 meV, green ≃ 300 meV, magenta ≃ 400 meV, red ≃ 500 meV.*

The outcome of the DR imaging measurement is plotted in Fig. 12.2 for both two- and three-body breakup. In the two-body channel the shoulder that appears at low energies had been interpreted by the presence of H_3^+ ions with more than 0.96 eV internal energy that would allow to open the H(2s)+H_2 channel. The same shoulder can be seen for the measurement with the RF storage source at low pressure (a), while it vanishes for higher pressure (b). This effect clearly demonstrates that the bump has to do with internal excitation – ruling out experimental artefacts – and it strongly supports the above outlined

interpretation.
Furthermore the three-body DR fragment distributions reveal that the RF source produces slightly *colder* ions, although they are far from being cold enough to conform to our goals. While the excess energy in the tail of the high pressure distribution (d) corresponds to a little less than ∼200 meV rotational energy, the CHORDIS source lies between 200 and 300 meV, and consistently the low pressure setting (c) seems to produce more internal excitation, although the effect is very small.
One may conclude that the RF source is superior to standard ion sources, but that we could not tune it such that it would produce a thermalized ion sample, justifying a new DR rate coefficient measurement under well-defined conditions.

12.2 Lifetime and pulse shape measurements with the 22-pole trap

Before the 22-pole trap could be used and tested with H_3^+, the peripheral controls and electronics had to be installed. For the first test measurements, all the RF devices were used as ion guides without mass-selectivity, therefore no computer control of frequency or amplitude was necessary; the RF voltages and frequencies applied to the respective devices are given in Fig. 12.3. Since the apparatus is designed for the preparation of cold molecular ions with internal and translational energies of less then 1 eV, only small DC voltages of ±10 V are needed to steer the ions and direct them through the setup. Therefore all the time-critical voltages like the trap entrance- and exit electrodes and the source aperture could be controlled by a simple PCI analog output card (Adlink PCI-6308A) situated in the data acquisition PC. The voltage signals from this card have rise-times of about 10 μs, which is fast enough compared to typical trap timing schemes (see Fig. 12.3) that require only millisecond precision.
Modern personal computers are capable of providing millisecond timing without further efforts if a decent operating system is chosen, consequently we decided to implement a Labview interface running under a standard Linux operating system which was upgraded with a few real time extensions. By this way, the computer is responsible for the trap timing as well as for the data taking and storage and all crucial parameters can be adjusted and checked online.
Thus processing of the photomultiplier signal from the Daly detector was the only part where high precision electronics was needed. To do single ion counting, the signal (length ∼ 20 ns) is amplified by a fast timing filter amplifier, discriminated and then read out by

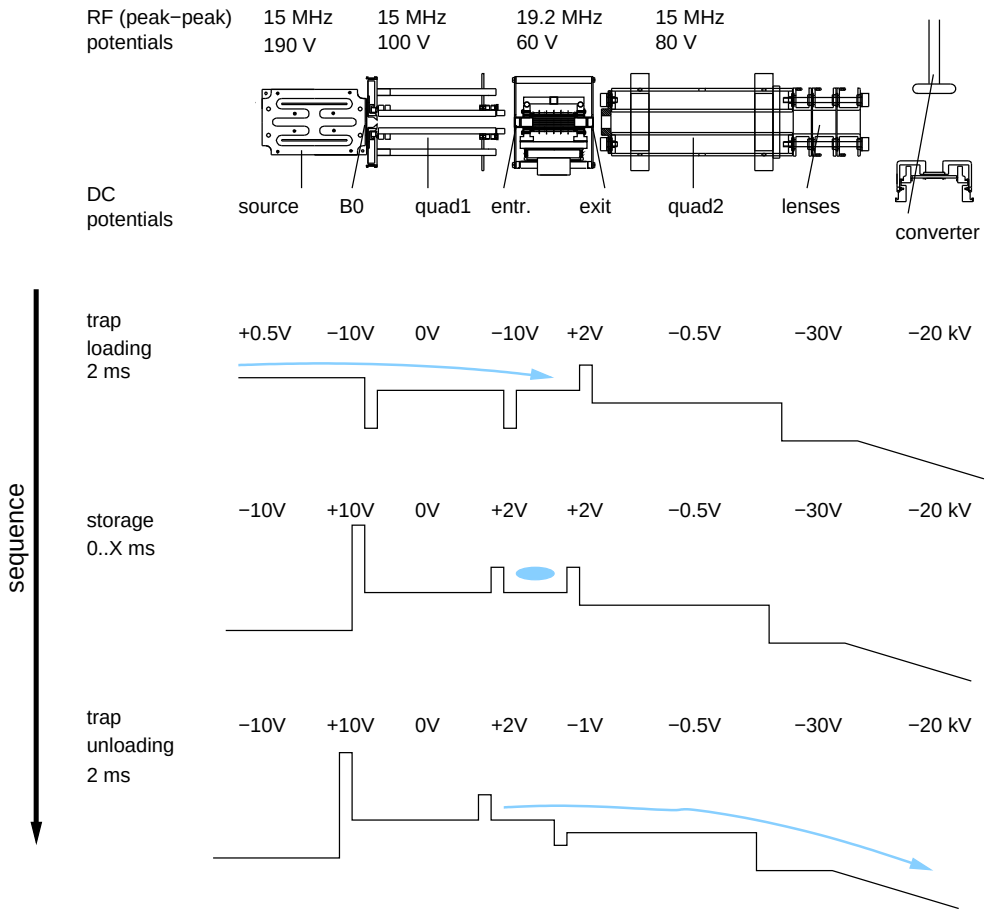

Figure 12.3: *Sketch of the timing scheme used to do lifetime and pulse shape measurements with the 22-pole trap.*

a universal counter (220 MHz) that is connected to the computer via GPIB. In order to suppress background events, the counter input is gated only for the unloading period of the trap, where the H_3^+ ions are expected to arrive at the detector. The counter does not provide any time information, however, in typical mass scan applications only the number of ions per trap filling is needed.

Determination of the lifetime

The timing scheme for the determination of the lifetime of H_3^+ in the trap is shown in Fig. 12.3. In the first step – the trap loading period – the ions travel from the source into the trap region until they reach the exit electrode, which is blocking most of them. Typical flight times from the source to the trap are several ten μs, consequently during the 2 ms loading period a constant flow of ions enters the source and is reflected at the exit electrode and the dwell time of the particles inside the source region is only a few μs.

This implies that the number of ions that can be caught would be saturated already at trap loading times of a few μs, which are too short to be realized by the computer system. The second step in the scheme is the trapping period, where the entrance electrode is raised to 2 V and the ions are kept inside the 22-pole for an adjustable time interval. It turned out that this voltage was not high enough to block all particles coming from the ion source, and in our first attempts we observed a constant increase of the number of ions in the trap with storage time. This disturbance was totally removed by lowering the source voltage to -10 V while the exit aperture was raised to +10 V during all times except for the trap loading period.

In the last step, the ions are extracted from the 22-pole and injected with an average kinetic energy of 0.5 eV into the second quadrupole that guides them towards the Daly detector. In Fig. 12.4 the number of H_3^+ ions measured by this procedure as a function of the storage time is plotted. The trap had a temperature of 12 K and the residual gas pressure in the vacuum chamber was $\sim 1 \times 10^{-8}$ mbar, while the H_2 pressure leaking out of the ion source amounted to 2×10^{-7} mbar. For these conditions an effective lifetime of 14.7 s was obtained that is likely to be dominated by reactions with the residual gas. In any case this lifetime is several orders of magnitude longer than storage times needed to cool down H_3^+ by buffer gas collisions. It should be noted that also a faster decay component

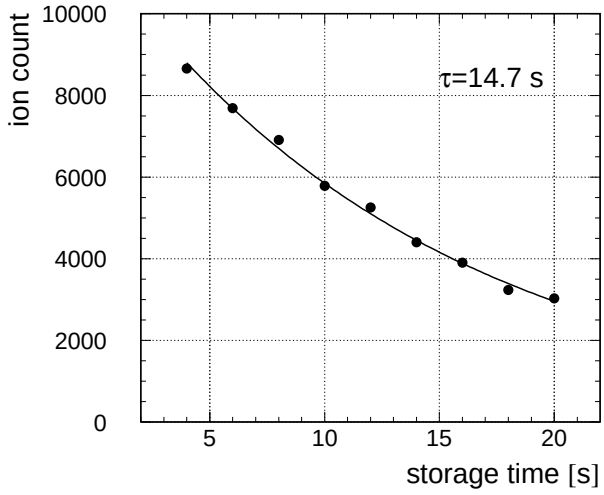

Figure 12.4: *Number of H_3^+ ions extracted from the 22-pole trap as a function of storage time. Several trap fillings ($\sim$ 50) were accumulated per storage time bin, while the source settings remained unchanged. The residual gas pressure in the trap chamber was $\sim 1 \times 10^{-8}$ mbar, the hydrogen pressure diffusing out of the source region was 2×10^{-7} mbar. The lifetime of the ions in the trap under these condition was determined to be $\tau = 14.7$ s.*

was observed at short storage times of less the 100 ms, which can be attributed to the escape of translationally hot ions from the trap, because no buffer gas was let in for this measurement.

Measurement of the extraction pulse shape

To get an understanding of the physics going on during the ion storage and the extraction, we were interested in the time that the ions need to reach the detector taken from the beginning of the unloading period. Since this time would depend on the velocity of the stored ions, it would give hints on the average translational energy in the trap. Furthermore we had to make sure that the whole pulse of ions is short enough to fit into the TSR injection window, that has a length of about 200 μs for typical energies of 500 keV per nucleon. For this measurement the counter was replaced by a digital scope that was

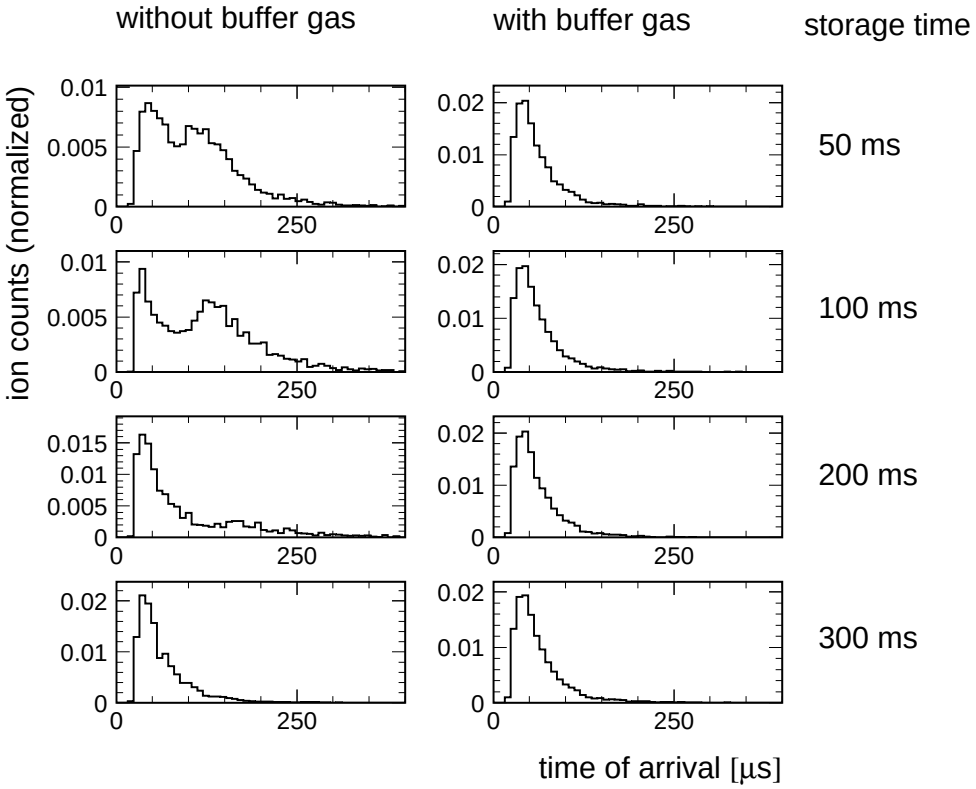

Figure 12.5: *Time distributions, showing the time of arrival of H_3^+ ions at the Daly detector after the exit electrode of the 22-pole trap has been put to negative voltage (−1 V). The ions have been stored at 12 K for variable storage times without buffer gas (left-hand side) and using H_2 buffer gas at a pressure of $\sim 5 \times 10^{-4}$ mbar (right-hand side). The potential difference between the trap and the second quadrupole was 0.5 eV, resulting in a minimal flight time of ca. 25 μs.*

triggered at the beginning of the unloading period and read out after the extraction pulse. Again this procedure was repeated for many trap fillings ($\sim$ 50 for each particular storage time) to gain statistics. The time scale and the number of ions per trap filling was adjusted such that a double event per digitizing bin at the scope was extremely unlikely. In Fig. 12.5 the time spectra recorded in this fashion are shown. One series of measurements was performed without buffer gas ($\sim 10^{-8}$ mbar rest gas pressure, $\sim 2 \times 10^{-7}$ mbar H_2 diffusing out of the source) and one series was taken with an estimated H_2 pressure of 2×10^{-4} mbar in the trap.

The spectra taken with buffer gas are all alike, but different from those without buffer gas, revealing that the translational temperature of the ions was thermalized by collisions already for the shortest storage time of 50 ms. The minimal flight time that the ions need to travel through the 140 mm quadrupole at an average energy of 0.5 eV amounts to 25 μs. This does not include the time needed to traverse the lens system, but in practice the -20 kV potential of the converter outreaches far into the lens system and even into the quadrupole, so that the real flight time is expected to be somewhat shorter.

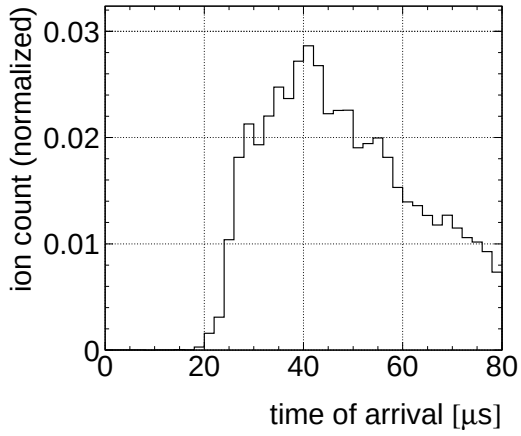

Figure 12.6: *Zoom into the short time region of the flight time spectra measured with buffer gas cooling.*

A zoom into the buffer-gas cooled pulses at shorter times (Fig. 12.6) shows that the onset of the signal is around 25 μs and the distribution peaks at 40 μs. This outcome is consistent with a relatively fast extraction of the cold ions out of the trap, followed by an average flight time through quadrupole and lens system of ca. 25 μs. The major implication of the measurement is, that the total length of the pulse is well below the 200 μs width of the TSR injection window, as required.

Nevertheless the spectra for storage without buffer gas were puzzling, since a second peak around 120 μs can be seen for short storage times. This peak decreases with increasing storage time and thus it was interpreted as being caused by hot ions that are escaping from the trap during the first 200 ms of storage. A lifetime measurement of the total number of ions extracted from the trap supported this interpretation, showing a fast initial decay

– reducing the number of extracted ions by about 50 % – with a similar time constant followed by a nearly constant plateau.
Without cooling the translational temperature of the particles in the 22-pole is determined by the ion source and the capture probability of the trap, but still it remains hard to understand why faster ions leave the trap later.
A likely explanation for this effect can be given by consideration of the angular momentum of the ions. It was mentioned already earlier, that the cylindrically symmetric effective potential of linear multipoles leads to the conservation of the angular momentum of the ions, this manifested itself in the avoided region in the center of the trap seen e.g. in Fig. 10.10. For ions with higher energy that happen to enter the trap close to the electrodes or may be pushed there by space charge, the angular momentum will force them on nearly circular trajectories close to the electrodes. If these ions are to be attracted towards the trap exit, a centrifugal barrier has to be overcome. This circumstance alone would not explain the observed behaviour, since a mechanism is needed to confine the ions in axial direction despite of the field gradient created by the entrance- and exit electrode. This mechanism is provided by the side plates of the 22-pole, which are also oscillating with the same frequency as the 22 rods and thus form an effective potential at the ends of the trap that can reflect particles approaching at large radii from the trap center, as discussed above.

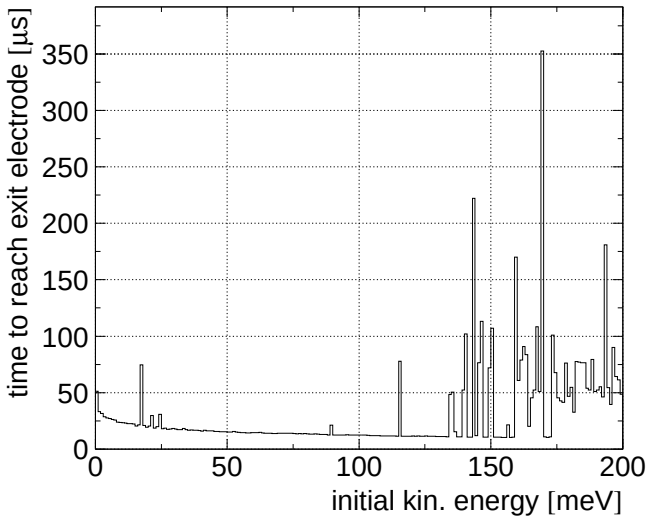

Figure 12.7: *Time needed for an ion in the 22-pole trap to reach the exit electrode (see Fig. 11.5) as a function of its initial kinetic energy. The results were derived from a* `SIMION` *simulation for ions with fixed starting position.*

In order verify this assertion qualitatively, a three-dimensional SIMION simulation of the extraction procedure was performed. Here, the time was taken that a singly charged particle of mass 3 needs to leave the trap as a function of the initial kinetic energy. The starting point was the same in all cases, located at a radius of 4 mm (leaving 1 mm distance to the next electrode) and the DC voltages at the entrance- and exit electrode were +1 V and −0.3 V, respectively. The velocity component of the initial velocity in radial direction was set to zero ($\vec{v_i} = r_i\, d\phi$), in order to create maximal angular momentum. A small constant azimuthal angle was introduced, so that the particles had a velocity component in axial direction, since a situation where a particle is stored in the central plane of the trap seems unrealistic. Fig. 12.7 shows the dwell time in the trap as a function of the kinetic energy of the ion, the maximum value for the energy being kept well below the trap depth of ∼1 eV. In this simulation the exit electrode was the lowest potential point and thus all particles ended at this electrode. It was found that the time to reach the exit decreased steadily for energies up to 130 meV (this is due to the small axial component of the steadily increasing initial velocity), while above this value the ions started to be reflected at the side plate several times, depending on the phase of the drift motion, until they could reach the electrode.
This effect provides a principal explanation of the observed behaviour and explains the occurence of the delayed extraction signals in Fig. 12.5; a detailed description including space charge and the not necessarily thermal distribution created by the ion source is beyond the scope of this work.

12.3 Deuteration

To accomplish the next step towards the application of the trap as a test chamber for cold reactions, the mass-selective capabilities of the second quadrupole were used. For the first tests no commercial quadrupole power supply was available, and the RF signal was provided by a simple oscillator (Digimess FG 100) that was controlled and integrated into the Labview desktop. The signal was amplified by a linear amplifier (RFPA 001220-25) and coupled to the quadrupole by a simple homemade transformer consisting basically of two big coils and a few capacitors and smaller inductivities to allow for the superposition of the DC potential needed for the mass scan (see chapter 10.2). With this arrangement peak-to-peak amplitudes up to 190 V at 1.7 MHz could be applied to the quadrupole rods. The DC voltage was supplied by a programmable power supply connected to the DAQ computer via serial bus.
It turned out however, that it is not trivial to obtain stability against thermal drifts during

the scan with such a simple setup, and to overcome this problem without implementing complicated analog feedback circuits, the RF amplitude is measured by a digital scope and iteratively corrected to the desired value by the computer. Since some of the data flow is sent through the low bandwidth serial bus, this procedure can take between one and a few seconds, slowing down the data taking severely. As a test system the deuteration reactions described in chapter 3.3.1 were chosen. The first reaction in the sequence

$$H_3^+ + HD \longrightarrow H_2D^+ + H_2 \quad + 232\,K, \tag{12.1}$$

$$H_2D^+ + HD \longrightarrow D_2H^+ + H_2 \quad + 189\,K, \tag{12.2}$$

$$D_2H^+ + HD \longrightarrow D_3^+ + H_2 \quad + 235\,K, \tag{12.3}$$

is the most important reaction for the deuterium fractionation in interstellar clouds, and

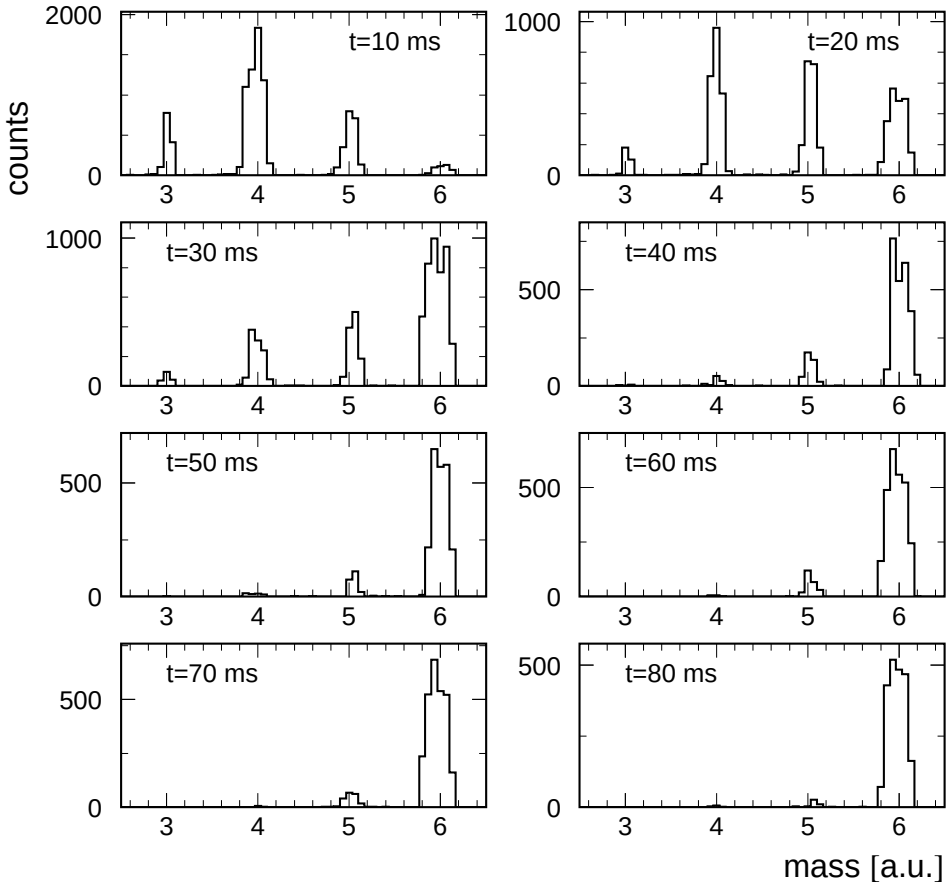

Figure 12.8: *Time-dependent mass scan, showing the deuteration of triatomic hydrogen ions stored in HD at a temperature of 12 K and at an estimated HD pressure of* 10^{-4} *mbar. After 80 ms of storage practically all the ions are fully deuterated to* D_3^+.

it has been studied in detail recently by D. Gerlich and coworkers [Ger02b].
All three reactions are exothermic by about 200 K and at low temperatures they are supposed to proceed rapidly, while the backward reactions are much slower if the ions thermalize between the reactions. To initiate this reaction chain, we produced H_3^+ ions in the storage source, and stored them in the 22-pole trap for various storage times at 12 K temperature, using HD buffer gas at an estimated pressure of 1×10^{-4} mbar. In Fig. 12.8 mass scans for storage times from 10-80 ms are plotted, showing that after 10 ms H_2D^+ is already the dominant ion in the trap and eventually after 80 ms all ions are fully deuterated to D_3^+. This rapid deuteration process is in agreement with earlier measurements and theoretical expectations. It should be noted however, that this is hardly surprising, since in this experiment the whole trap was flooded with HD gas, while only minor traces of H_2 were present. Hence for backward reactions, releasing one deuterium atom from the triatomic hydrogen ions, only HD collision partners are available, allowing for reactions of the type

$$H_2D^+ + HD \longrightarrow H_3^+ + D_2 \ , \tag{12.4}$$

which are endothermic by more than 1000 K and thus practically forbidden. In a more refined measurement one could use similar reactions (see chapter 13) to determine the ion temperature in the trap. Furthermore a laser assisted chemical probing experiment aiming to detect differences for the deuteration reactions using ortho- or para-H_2 as buffer gas is currently under development. At this stage the deuteration experiment served as a test of the trap setup including the electronics and DAQ system.

12.4 Maximal number of ions in the trap

It was seen above that the length of the ion pulse extracted from the source is well suited for use at the TSR storage ring. Another crucial number in that context is of course the total number of ions that can be achieved per trap filling. When the project was started it was stated that a minimum of the order of 10^5 ions in the storage ring is necessary for a decent DR cross section measurement; for Coulomb explosion or DR imaging experiments the restrictions are much less severe, there a few ten ions per second at the detector are sufficient.
To derive the maximum number of ions in the trap, the Daly detector can no longer be used in single ion mode, since an expected count rate of $> 10^5$ ions in a 200 μs pulse would saturate the bandwidth of all the electronic modules involved. As mentioned before, it is possible to operate the detector in DC or current mode, if the photomultiplier voltage is lowered and the voltage signal is integrated. In order to extract meaningful results

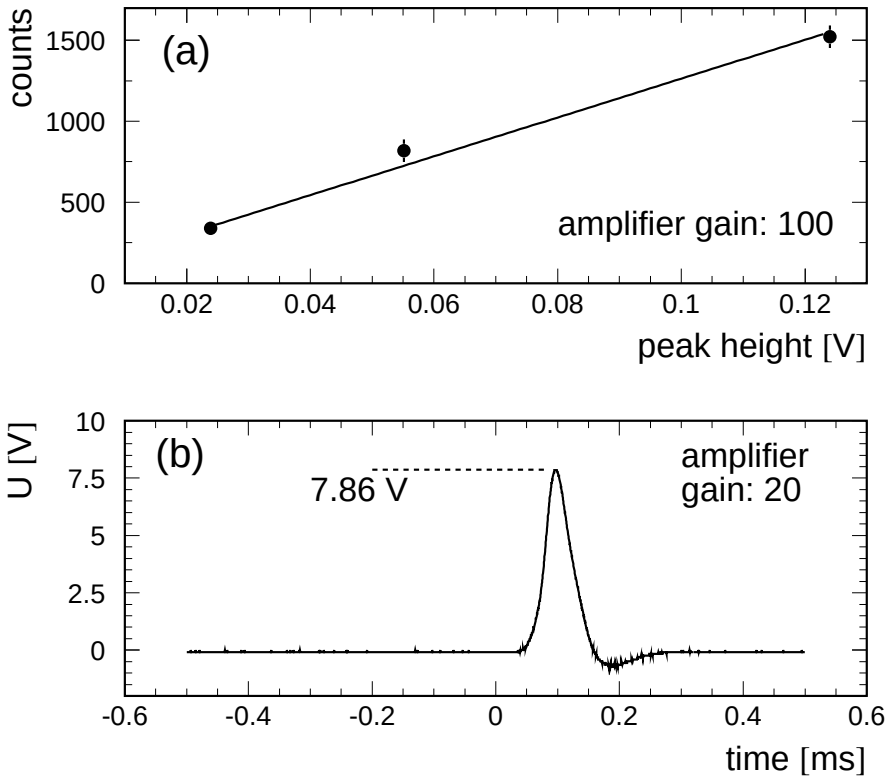

Figure 12.9: *(a) Calibration of the ion count rate vs. the signal height measured in DC mode with an amplifier gain of 100. The fit revealed a calibration factor of 11200 counts/Volt. (b) The maximum voltage signal that could be obtained. In order to avoid saturation of the integrating amplifier, the gain had to be reduced to 20. The maximum number of ions is given by:* $N_{max} \approx 11200 \cdot 7.86 \cdot 5 = 4.4 \times 10^5$.

in this manner, the DC signal has to be calibrated, i.e. a voltage-to-particle-number correspondence has to be established. This was done by adjusting the parameters such that a few hundred ions per trap filling were counted with single ion detection. Only small fluctuations in the signal were seen, once the source conditions had reached equilibrium. This signal was averaged over 64 trap fillings to derive the mean number of ions for this setting. In the second step all crucial parameters were left unchanged, only the Daly detector was switched to DC mode by reducing the photomultiplier voltage and replacing the amplifiers. Again the signal was averaged over 64 fillings and the comparison between both modes provides the necessary calibration information. To improve the statistical significance this procedure was repeated for three different settings, the result is plotted in Fig. 12.9(a). From the fit to the data a linear dependence of ~11200 ions/Volt (at an

amplifier gain of 20) was derived.
Now all the parameters were optimized for storage of a maximal number of ions. It turned out that a high buffer gas pressure and relatively low RF amplitude (the exact value of the RF amplitude can not be measured since the signal is stimulated inductively, however from an antenna signal a value of $V_{\sim} = 20\,\mathrm{V}$ was estimated) in the trap are favourable conditions. The high pressure helps to slow down and capture ions during the loading period, and the low RF voltage shifts the sharp rise of the effective potential to larger radii, effectively increasing the trap volume. The final adjustment that was reached was very stable and independent of the trap loading time and independent of small changes to source parameters as well, revealing that the ions indeed consumed the whole available phase space in the trap. The voltage signal for optimized settings is plotted in Fig. 12.9(b) showing a peak height of 7.86 V that indicates a maximum ion number of

$$N_{max} \approx 11200\,\frac{\mathrm{ions}}{\mathrm{Volt}} \cdot 7.86\,\mathrm{V} \cdot 5 = 4.4 \times 10^5 \text{ ions} , \tag{12.5}$$

where the factor five stems from the different amplifier gain values that had to be used during calibration and the final optimization. No non-linearities of any kind in the detection scheme were observed during operation. The uncertainty of this number is estimated to 10 %. However, if the detection efficiency of the Daly detector for some reason would be less than 1 or if the photomultiplier would be saturated, it would rather underestimate the real value.
It should be added here that it is not clear yet, how the optimization for ion yield affects the effective temperature of the ions. It is obvious that the space charge potential will push the ions outward towards the electrodes and thus it might induce RF heating. To which extent this will influence the internal ion temperature has to be tested experimentally.

Chapter 13
Conclusion and Perspectives

Since the early days of DR measurements, the standards and requirements have changed dramatically. Although it was well known that vibrational excitation heavily influences the DR process, the majority of experimental methods had no means to detect the initial state of the molecular ions directly. In more elaborate experiments, the preparation of ions in their vibrational ground state often represented a substantial part of the technical challenge. Nowadays, a new class of electron-ion recombination measurements is on the horizon, since the determination of state-selective cross sections may be possible in the near future even for molecules like H_3^+ and its deuterated relatives, which are of outstanding importance and at the same time notoriously difficult to handle and diagnose. This thesis dealt in detail with H_3^+ to understand its internal excitation in the dissociative recombination measurements at ion storage rings.

In Part II, the Coulomb explosion results were presented, which demonstrate that the vibrational excitation decays within a few seconds, a time scale that is easily accessible in ion storage rings. On the other hand the DR fragment spectra showed that rotational states up to 1 eV are populated after many seconds of storage and that the average excess energy remaining in the system is as high as 2700 K, if the ion beam is produced in a standard ion source. A comprehensive rovibrational relaxation model could give an unambigous qualitative explanation of the observed effects and even gave excellent quantitative agreement with the CEI experiment for the decay behaviour of the first breathing mode.

These findings make it particularly interesting to look at the history of measured H_3^+ DR rates in the last 50 years. In Fig. 13.1 the published thermal rate coefficients (300 K) for H_3^+ are plotted (except for the lowest value at $\sim 10^{-11}\,\mathrm{cm^3\,s^{-1}}$ [Smi87] that has been withdrawn in the meantime). If one considers for the moment only the values above the horizontal line, one finds a slow but steady trend towards smaller values, ending at the latest storage ring result from Stockholm at $6.8 \cdot 10^{-8}\,\mathrm{cm^3\,s^{-1}}$ [McC03]. This slope might

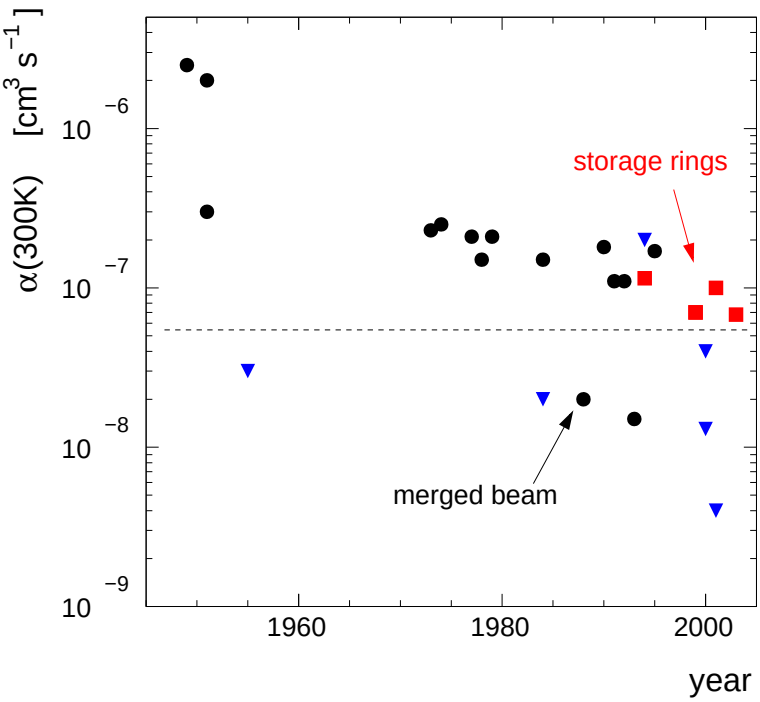

Figure 13.1: *Published DR rate coefficients (300 K) of H_3^+. The blue triangles represent upper limits, red squares stand for storage ring results. All values below the dashed horizontal line are indirect measurements, determining the rate coefficient by monitoring the presence of electrons, except for a merged beam result from 1988 which is especially marked. All references can be found in [Pla02].*

be explained by the increasingly better control of internal excitations, if one believes the experimental hints that excitations in general enhance the rate coefficient.

For the latest measurement from Stockholm an expansion ion source has been used that was tested spectroscopically in Berkeley. In absorption measurements the authors have seen two lines, one due to excitation of the lowest para-H_3^+ state and the other one from the lowest ortho state lying ~ 30 K above. From the ratio of these two lines a rotational temperature of 20-60 K is derived [McC03, Kok03]. However, it remains unclear why this ratio is supposed to represent a temperature, because for ortho-para transitions within the molecule a spin-flip would have to occur, hence they are forbidden and the two states in fact can not thermalize radiatively. The ortho-para ratio in the expansion source is likely to be governed by collisions with the surrounding normal H_2 gas (n-H_2 at 300 K is a mixture of 75 % ortho and 25 % para) – which are far from being understood – or other processes taking place in the expansion. As a matter of fact, cooling down H_3^+ to 10 K would not change the ortho-para ratio at all in the absence of some sort of catalyst initiating nuclear spin-relaxation.

All the values below the horizontal line were measured with indirect methods (except for the merged beam result that is especially tagged), i.e. not H_3^+ or the DR products were detected, but the decay of electrons in a plasma containing H_3^+. For most of these measurements many different chemical reactions have to be taken into account before the rate coefficient can be extracted so that the evaluation procedure tends to be less transparent than for the storage ring results. This may be the reason why, since the publication of the first CRYRING measurement, the storage ring values have found their way into interstellar chemistry models. Nevertheless, in the light of the recent TSR findings storage ring and plasma experiments can be considered complementary, for in the latter type of experiments the pressure is usually high enough to quench all rotational excitation, while vibrations are more difficult to cool collisionally, whereas in the storage rings, on the other hand, vibrations cool radiatively, but some rotations practically live forever.

None of the rate coefficients plotted above stems from experiments at the TSR, because the detailed excitation conditions of the ions are considered not be sufficiently well known. The cryogenic 22-pole trap can hopefully contribute in many ways in the near future, giving insight in collisions at interstellar temperatures and delivering rovibrationally well-defined samples of molecular ions.

Perspectives

Although the temperature of the walls of the 22-pole trap can be measured accurately, it has to be shown that the ions reach the temperature of the ambient buffer gas. Right now several pathways are pursued. First, an attempt will be made to detect rotational states of H_3^+ in the trap with laser excitation followed by chemical probing of the excited states. For this purpose it is planned to store H_3^+ in a mixture of helium and argon gas and to use an infrared laser to excite ions from various low-lying rotational states to the $\nu_2 = 3$ vibrational bending excitation; these transitions will deposit about 0.93 eV in the molecule. With this energy available, the reaction

$$H_3^+(v = 3) + Ar \longrightarrow ArH^+ + H_2 \ , \tag{13.1}$$

which is endothermic by 0.57 eV is supposed to be rapid. Detection of ArH^+ with a mass spectrometer during the trap unloading period therefore should give a background-free signal for the laser resonance. There are several difficulties that have to be overcome if this measurement is going to be realized

- the argon vapour pressure is vanishingly small at 10 K, thus for measurements below 40 K the argon inlet will have to be pulsed,

- the argon pressure has to be high enough for the collision rate to compete with the spontaneous decay of the $v = 3$ states,

- the presence of H_2 in the trap (e.g. leaking out of the source) might destroy ArH^+ due to the backwards reaction of Eq. 13.1.

Tests of this simple detection scheme will be performed in a collaboration with J. Glosik from Charles university Prague.
Independent from this approach we are planning to examine the deuterium fractionation in the trap and especially the role of para- and ortho-H_2. In a logical extension of a work recently published by Gerlich [Ger02b] we plan to influence the production of H_2D^+ by utilizing the natural deuterium content in H_2 together with a para hydrogen generator. Again we will try to use laser induced vibrational transitions to shift the equilibrium fraction of the deuterated ion H_2D^+ in the trap. Both measurements could help to determine the actual ion temperature, and if they are successful the chemical probing can provide a new route to do spectroscopy of H_3^+, since for absorption measurements a powerful laser system and high number densities are needed.
Also a third type of reactions may serve as a thermometer, namely the temperature-dependence of hydrogen cluster formation. If H_3^+ is stored in hydrogen at high densities and low temperatures, H_n^+ clusters will form in ternary collisions. The reaction rates are temperature-dependent and thus can be used to determine the ion temperature. In fact, a prototype experiment has already been carried out and the formation of hydrogen clusters up to H_{17}^+ (which was the limit of the mass spectrometer) in the 22-pole was observed; however, to derive rate coefficients the mass spectrometer and the pressure measurement in the trap have to be improved.
Beside the construction of novel ion sources, developments at the TSR are underway that will trigger the next generation of electron-ion collision experiments in both atomic and molecular physics. A new electron target has been manufactured in the last years and in April of 2003 it was implemented in the storage ring and successfully used to cool an ion beam already in the first beamtime [Spr03]. Apart from a substantial improvement of the energy resolution in DR measurements with the new target, the availability of two electron beams will greatly enhance the experimental situation, a detailed account being beyond the scope of this work. In parallel, a novel detector for molecular recombination measurements was developed at the Weizmann Institute of Science. It will provide the

opportunity to perform fully three-dimensional DR fragment imaging measurements in a new dedicated beamline.

Altogether, many open questions remain regarding H_3^+ electron recombination, but considering the progress of experiment and theory in the last years, the understanding of the situation is greatly improving. Regarding the situation at the TSR in particular, the present investigation shows up a path towards new experimental developments which will soon become operational.

Appendix

A Influence of internal kinetic energy

In this section the normal mode oscillations will be considered in the harmonic oscillator approximation. The total energy in the three modes (see chapter 7)

$$E_a = (\nu_1 + \frac{1}{2})\,\hbar\omega_a \qquad , \quad E_x = E_y = (\nu_2 + \frac{1}{2})\,\hbar\omega_{xy}\,, \tag{A.1}$$

can be divided into kinetic and potential energy for each normal mode (here denoted by k)

$$E_k = E_{kin} + E_{pot}. \tag{A.2}$$

The time-averaged values of the potential and kinetic energies are equal and thus the mean value of the kinetic energy per atom for the normal mode k is

$$\langle E_{kin,k}\rangle = \frac{1}{6}\,E_k = \frac{1}{2}m\langle \mathtt{v}_\mathtt{k}^2\rangle \tag{A.3}$$

The aim is to determine the impact of the averaged initial velocities $\langle \mathtt{v}_\mathtt{k}^2\rangle$ (for k=a,x,y) that are induced by zero point oscillations, on the distribution of the asymptotic velocities v_a, v_x and v_y.

Influence of initial kinetic energy in the breathing mode

In the case of the symmetric stretch motion, the initial velocity vectors $\vec{\mathtt{v}}_{||}$ are parallel to the Coulomb force (see Fig. A.1) that eventually accelerates the fragments to $v_1 = v_2 = v_3 = v_0 = 0.0257$ (a.u.) as calculated above (Eq. 7.7).

Because of energy conservation the net velocity for each atom is given by

$$v = \sqrt{v_0^2 + \mathtt{v}_{||}^2}\,. \tag{A.4}$$

Neglecting terms of higher than quadratic order in $\frac{\mathtt{v}_{||}}{v_0}$ and considering the time-averaged velocities, one finds the new approximate expectation value for the asymptotic breathing mode velocity

$$\langle v_a^a\rangle \approx 3\,v_0\left(1 + \frac{1}{2}\frac{\langle \mathtt{v}_{||}^2\rangle}{v_0^2}\right), \tag{A.5}$$

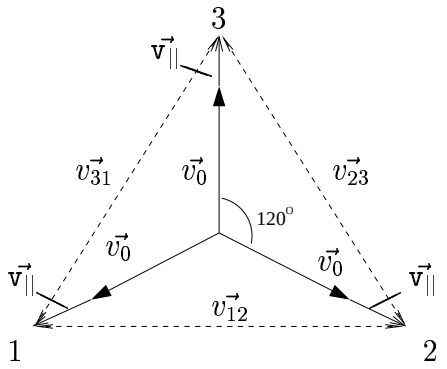

Figure A.1: *Symmetric Coulomb explosion with additional breathing mode kinetic energy resulting in initial velocities* $\mathtt{v}_{||}$.

that can be expressed in terms of energies by substituting

$$\langle \mathtt{v}_{||}^2 \rangle = \frac{2\,E_{kin,a}}{m} \quad \text{and} \quad v_0^2 = \frac{2\,E_0}{3\,m}, \tag{A.6}$$

where E_0 is equal to the potential energy that is set free in the Coulomb explosion $E_0 = 49.5\,\text{eV}$ that was calculated above (Sect. 7.2.2). The resulting modified breathing mode velocity

$$v_a^a = \frac{1}{\sqrt{3}}(v_{12} + v_{23} + v_{31})\,, \tag{A.7}$$

together with Eq. 7.8 and A.4 can be expressed

$$v_a^a = 3\,v = 3\sqrt{v_0^2 + \mathtt{v}_{||}^2} = 3\,v_0 \left(1 + \frac{1}{2}\frac{\mathtt{v}_{||}^2}{v_0^2} - \frac{1}{8}\frac{\mathtt{v}_{||}^4}{v_0^4} \pm \ldots\right)\,, \tag{A.8}$$

Thus the corrected value for the mean of the breathing mode velocity is given by

$$\langle v_a^a \rangle = v_a^0 \left(1 + \frac{3\,E_{kin,a}}{E_0}\right)\,. \tag{A.9}$$

Here $3\,v_0$ is replaced by v_a^0, the "undisturbed" asymptotic value of the breathing mode coordinate. To evaluate the term in brackets that represents the correction factor one needs to estimate the zero point energy E_a of the breathing oscillation. The ν_1 fundamental has an energy of $3240\,\text{cm}^{-1}$ [Pol99] or $0.4\,\text{eV}$ that yields for the zero point energy $E_a \approx 0.2\,\text{eV}$. According to Eq. A.3 the value for $E_{kin,a} = 1/6\,E_a \approx 0.033\,\text{eV}$ and thus

$$\langle v_a^a \rangle = v_a^0 \cdot 1.002\,. \tag{A.10}$$

Consequently the kinetic energy E_a will shift the breathing mode distribution by $0.2\,\%$, a change that is below the resolution of the CEI experiment.
The next step is to consider the change in the width of the distribution which (according to the harmonic picture) is given by the variance

$$(\sigma_a^a)^2 = \langle (v_a^a)^2 \rangle - \langle v_a^a \rangle^2, \tag{A.11}$$

with

$$\langle (v_a^a)^2 \rangle = \langle 9(v_0^2 + \mathtt{v}_{||}^2) \rangle = 9\,v_0^2 + 9\,\langle \mathtt{v}_{||}^2 \rangle, \tag{A.12}$$

and

$$\langle v_a^a \rangle^2 = 9\,v_0^2 \left(1 + \frac{1}{2}\left\langle \frac{\mathtt{v}_{||}^2}{v_0^2} \right\rangle - \frac{1}{8}\left\langle \frac{\mathtt{v}_{||}^4}{v_0^4} \right\rangle \pm \ldots\right)^2 \tag{A.13}$$

$$= 9\,v_0^2 \left(1 + \frac{\langle \mathtt{v}_{||}^2 \rangle}{v_0^2} - \frac{1}{4}\frac{\langle \mathtt{v}_{||}^4 \rangle}{v_0^4} + \frac{1}{4}\frac{\langle \mathtt{v}_{||}^2 \rangle^2}{v_0^4} \pm \ldots\right), \tag{A.14}$$

one obtains for the additional width

$$(\sigma_a^a)^2 = \frac{9\,v_0^2}{4\,v_0^4}\left(\langle \mathtt{v}_{||}^4\rangle - \langle \mathtt{v}_{||}^2\rangle^2\right) \ . \tag{A.15}$$

To simplify this equation further one has to determine the moments of the harmonic oscillator basis function, which is given by

$$P(v_k^n) = \frac{1}{\sqrt{2\,\pi}\ \sigma}\ e^{-\frac{v_k^2}{2\,\sigma^2}}. \tag{A.16}$$

The moments of the Gaussian distribution can be expressed in terms of the Γ-function [Bro89]

$$\langle v_k^n\rangle = \frac{1}{\sqrt{2\,\pi}\ \sigma}\int_{-\infty}^{\infty} v_k^n\ e^{-\frac{v_k^2}{2\,\sigma^2}}\ dv_k \tag{A.17}$$

$$= \frac{1}{\sqrt{2\,\pi}\ \sigma}\ \frac{\Gamma\left(\frac{n+1}{2}\right)}{\left(\frac{1}{2\,\sigma^2}\right)^{\left(\frac{n+1}{2}\right)}} \tag{A.18}$$

$$= \frac{1}{\pi}\,\Gamma\left(\frac{n+1}{2}\right)\ (2\,\sigma^2)^{(n/2)} \ . \tag{A.19}$$

By using $\Gamma(\frac{3}{2}) = \frac{\sqrt{\pi}}{2}$ and $\Gamma(\frac{5}{2}) = \frac{3\sqrt{\pi}}{4}$, the second and the fourth moment can be derived

$$\langle v_k^2\rangle = \sigma_k^2 \qquad , \qquad \langle v_k^4\rangle = 3\,\sigma_k^4, \tag{A.20}$$

and inserted into Eq. A.15

$$(\sigma_a^a)^2 = \frac{9\,v_0^2}{2}\frac{\langle \mathtt{v}_{||}^2\rangle^2}{v_0^4}, \tag{A.21}$$

that gives after conversion of the velocities into energies

$$\sigma_a^a = v_a^0\frac{3}{\sqrt{2}}\frac{E_{kin,a}}{E_0} \approx 1.1\cdot 10^{-4}\,\text{a.u.} \tag{A.22}$$

This width is added quadratically to the width that stems from the shape of the wave function. The distribution in Fig 7.6(a) has a RMS of 3.4×10^{-3} a.u., hence the effective broadening due to the contribution of σ_a^a is less than 0.1 %.
The contribution of kinetic energy in the breathing mode to the asymmetric distributions is zero, because the triangular shape is unaltered

$$\langle v_x^a\rangle = 0 \qquad , \qquad \sigma_x^a = 0, \tag{A.23}$$

$$\langle v_y^a\rangle = 0 \qquad , \qquad \sigma_y^a = 0. \tag{A.24}$$

Influence of initial kinetic energy in the bending mode v_x

Kinetic energy in bending coordinates creates a more complex situation (see Fig. A.2), since the Coulomb repulsion is no longer parallel to the initial velocities and thus the relative velocities are not equal $v_{13} = v_{23} \neq v_{12}$. To calculate the value of the modified relative velocities, one has to determine the angles $\beta_1 = \beta_2$ with the help of the geometrical relations

$$\mathtt{v}_\perp = \mathtt{v}_1 \sin(60°) = \frac{\sqrt{3}}{2}\mathtt{v}_1 \qquad , \qquad \sin\beta_1 = \frac{\mathtt{v}_\perp}{v} = \frac{\sqrt{3}}{2}\frac{\mathtt{v}_1}{v}, \tag{A.25}$$

the relative velocities are (keeping in mind that the absolute values of the three particle velocities due to energy conservation are equal $v_1 = v_2 = v_3 = v$)

$$v_{12}^2 = 2\,v^2\,[1 - \cos(120° - 2\,\beta_1)] \ , \tag{A.26}$$

$$v_{23}^2 = 2\,v^2\,[1 - \cos(120° + \beta_1)] \ . \tag{A.27}$$

Now the modified breathing mode coordinate can be written

$$v_a^x = \sqrt{\frac{2}{3}}\,v\left\{\sqrt{1 - \cos(120° - 2\,\beta_1)} + 2\sqrt{1 - \cos(120° + \beta_1)}\right\}, \tag{A.28}$$

using the trigonometric relations $[\cos 2x = \cos^2 x - \sin^2 x]$ and for the second step $[\sin(x \pm y) = \sin x \cos y \pm \cos x \sin y]$ and $[\cos(x \pm y) = \cos x \cos y \mp \sin x \sin y]$, one obtains

$$v_a^x = \sqrt{\frac{2}{3}}\,v\left\{\sqrt{2}\sin(60° - \beta_1) + 2\sqrt{2}\sin(60° + \beta_1/2)\right\}. \tag{A.29}$$

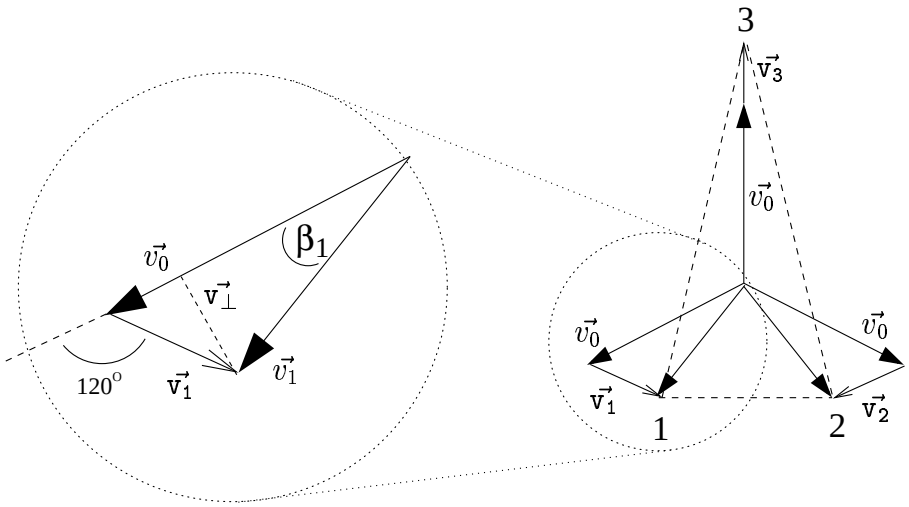

Figure A.2: *Coulomb explosion with initial velocities* $\mathtt{v}_1$, $\mathtt{v}_2$, $\mathtt{v}_3$, *corresponding to kinetic energy in the bending mode* v_x.

$$= \frac{2}{\sqrt{3}}\, v \left\{ \frac{\sqrt{3}}{2} \cos\beta_1 - \frac{1}{2} \sin\beta_1 + \sqrt{3} \cos(\beta_1/2) + \sin(\beta_1/2) \right\}. \qquad \text{(A.30)}$$

With a series expansion of the sine and cosine terms up to fourth order this transforms into

$$v_a^x = 3\, v \left(1 - \frac{1}{4}\beta_1^2 - \frac{1}{\sqrt{3}\,12}\, \beta_1^3 + \frac{1}{64}\beta_1^4 \right). \qquad \text{(A.31)}$$

Replacing $v = \sqrt{v_0^2 + \mathtt{v}_1^2}$ by the approximation $v{=}v_0(1 + \frac{\mathtt{v}_1^2}{v_0^2})$ gives

$$v_a^x = 3\, v_0 \left(1 + \frac{\mathtt{v}_1^2}{v_0^2} \right) \left(1 - \frac{1}{4}\beta_1^2 - \frac{1}{\sqrt{3}\,12}\, \beta_1^3 + \frac{1}{64}\beta_1^4 \right), \qquad \text{(A.32)}$$

Now β_1 has to be replaced by $\mathtt{v}_1$ and v_0; this can be done by remembering that before the explosion, the components of the initial velocity $\mathtt{v}$ are

$$\mathtt{v}_{||} = \mathtt{v}_1 \cos\,\alpha\,, \qquad \text{(A.33)}$$

$$\mathtt{v}_{\perp} = \mathtt{v}_1 \sin\,\alpha\,, \qquad \text{(A.34)}$$

while after the explosion

$$\sin\,\beta_1 = \frac{\mathtt{v}_{\perp}}{v_1} = \frac{\mathtt{v}_1 \sin\,\alpha}{v} \approx \frac{\mathtt{v}_1 \sin\,\alpha}{v_0} \qquad \text{(A.35)}$$

and since in this case (see Fig. A.2) $\alpha = 120°$, β_1 can be approximated by

$$\sin\,\beta_1 = \sqrt{\frac{3}{4}}\, \frac{\mathtt{v}_1}{v_0} \qquad \Longrightarrow \qquad {\beta_1}^2 \approx \frac{3}{4}\frac{\mathtt{v}_1^2}{v_0^2}. \qquad \text{(A.36)}$$

Inserting this relation into Eq. A.32 and taking only terms up to quadratic order in $\mathtt{v}_1/v_0$ yields

$$\langle v_a^x \rangle \approx 3\, v_0 \left(1 + \frac{5}{16}\frac{\mathtt{v}_1^2}{v_0^2} \right), \qquad \text{(A.37)}$$

that is related to the average undisturbed breathing mode velocity v_a^0 by

$$\langle v_a^x \rangle = v_a^0 \left(1 + \frac{5}{32}\frac{E_b}{E_0} \right). \qquad \text{(A.38)}$$

The ν_1 fundamental has an energy of $2521\,\mathrm{cm}^{-1}$ or $0.32\,\mathrm{eV}$ that yields a zero point energy of $0.16\,\mathrm{eV}$. With this value the corrected breathing mode velocity is

$$\langle v_a^x \rangle \approx v_a^0 \cdot 1.0005\,, \qquad \text{(A.39)}$$

and thus distinctly below the CEI resolution.

To estimate the influence on the width of the v_a distribution, we have to calculate

$$(\sigma_a^x)^2 = \langle (v_a^x)^2 \rangle - \langle v_a^x \rangle^2, \tag{A.40}$$

where according to Eq. A.32

$$(v_a^x)^2 = 9\left(v_0^2 + \mathtt{v}_1^2\right)\left(1 - \frac{1}{4}\beta_1^2 - \frac{1}{\sqrt{3}\,12}\,\beta_1^3 + \frac{1}{64}\beta_1^4\right)^2 , \tag{A.41}$$

and by the inserting the same replacements used above

$$(v_a^x)^2 = 9\,v_0^2\left(1 + \frac{\mathtt{v}_1}{v_0}\right)\left(1 - \frac{3\mathtt{v}_1^2}{8\,v_0^2} + \frac{\mathtt{v}_1^3}{\sqrt{3}\cdot 6\,v_0^3} + \frac{27\,\mathtt{v}_1^4}{512\,v_0^4}\right) , \tag{A.42}$$

one obtains after averaging

$$\langle (v_a^x)^2 \rangle = 9\,v_0^2\left(1 + \frac{5\langle \mathtt{v}_1^2 \rangle}{8\,v_0^2} + \frac{27\langle \mathtt{v}_b^4 \rangle}{512\,v_0^4}\right). \tag{A.43}$$

The second term in Eq. A.40 can be derived by accomplishing the multiplication in Eq. A.32

$$\langle v_a^x \rangle^2 = 9\,v_0^2\left(1 + \frac{5{\mathtt{v}_1}^2}{16\,v_0^2} - \frac{23\mathtt{v}_1^4}{1024\,v_0^4}\right)^2 , \tag{A.44}$$

$$= 9\,v_0^2\left(1 + \frac{5\langle \mathtt{v}_1^2 \rangle}{8\,v_0^2} - \frac{23\langle \mathtt{v}_1^4 \rangle}{512\,v_0^4} + \frac{25\langle \mathtt{v}_1^2 \rangle^2}{256\,v_0^4} \pm \ldots\right). \tag{A.45}$$

Inserting both equations into Eq. A.40 yields

$$(\sigma_a^x)^2 = 9\,v_0^2\left(\frac{25\langle \mathtt{v}_1^4 \rangle}{512\,v_0^4} - \frac{25\langle \mathtt{v}_1^2 \rangle^2}{256\,v_0^4}\right), \tag{A.46}$$

that can be simplified by using Eq. A.20, resulting in the approximated contribution to the width of the breathing mode caused by zero point oscillation in v_x

$$\sigma_a^x \approx v_a^0 \frac{25\,E_x}{256\,E_0}. \tag{A.47}$$

Now the influence of internal energy in the v_x mode on the v_x distribution itself will be considered

$$v_x^x = \frac{1}{\sqrt{6}}(2\,v_{12} - v_{23} - v_{31}) = \frac{2}{\sqrt{6}}(v_{12} - v_{23}) , \tag{A.48}$$

$$= \frac{2\sqrt{2}}{\sqrt{6}} v \left([1 - \cos(120° - 2\,\beta_1)]^{1/2} - [1 - \cos(120° + \beta_1)]^{1/2}\right) , \tag{A.49}$$

$$= 2\sqrt{\frac{2}{3}} v \left(\sin(60° - \beta_1) - \sin(60° + \beta_1/2)\right) , \tag{A.50}$$

$$= 2\sqrt{\frac{2}{3}} v \left(\frac{\sqrt{3}}{2}\cos\,\beta_1 - \frac{1}{2}\sin\,\beta_1 - \frac{\sqrt{3}}{2}\cos\,(\beta_1/2) - \frac{1}{2}\sin\,(\beta_1/2)\right) , \tag{A.51}$$

and using a series expansion of sine and cosine terms, one obtains

$$v_x^x = 2\sqrt{\frac{2}{3}}v\left(-\frac{3}{4}\beta_1 - \frac{3\sqrt{3}}{16}\beta_1^2\right) \ , \tag{A.52}$$

that can be further simplified by applying the approximations $v \approx v_0$ and $\beta_1 = \sqrt{3/4}\,\frac{\mathtt{v}_b}{v_0}$

$$v_x^x = -\frac{3}{2\sqrt{2}}\mathtt{v}_x\left(1 + \frac{3\,\mathtt{v}_x}{8\,v_0}\right), \tag{A.53}$$

averaging eliminates the first term in the bracket and converting the velocities to energies yields

$$\langle v_x^x\rangle = -\frac{3}{32\sqrt{2}}v_a^0\frac{E_x}{E_0}\,. \tag{A.54}$$

With this result, it is easy to determine the effect on the width of the distribution

$$(\sigma_x^x)^2 = \langle (v_x^x)^2\rangle - \langle v_x^x\rangle^2\,, \tag{A.55}$$

since $\langle v_x^x\rangle = 0$, the second term is zero and

$$(\sigma_x^x)^2 = \frac{9\,v_0^2}{8}\frac{\langle \mathtt{v}_1^2\rangle}{v_0^2}\,, \tag{A.56}$$

resulting in

$$\sigma_x^x = \frac{1}{4}v_a^0\sqrt{\frac{E_x}{E_0}}. \tag{A.57}$$

With Eq. A.54 and Eq. A.57, one can calculate the effect of initial energy in the v_x bending mode on the v_x distribution, in the experiment however, the particles are randomly tagged and thus the asymmetric v_x and v_y distributions are exchange-symmetrized in order to take all possible permutations into account. That means that the additional contributions $v_x^x\prime$, $v_x^x\prime\prime$ and $\sigma_x^x\prime$, $\sigma_x^x\prime\prime$ have to be included to obtain the effective values $\langle v_{x,eff}^x\rangle$ and $\sigma_{x,eff}^x$

$$v_x^x\prime = \frac{1}{\sqrt{6}}\left(2v_{23} - v_{12} - v_{31}\right)\,, \tag{A.58}$$

$$v_x^x\prime\prime = \frac{1}{\sqrt{6}}\left(2v_{31} - v_{12} - v_{23}\right)\,, \tag{A.59}$$

$$\Longrightarrow \quad v_x^x\prime = v_x^x\prime\prime = \frac{1}{\sqrt{6}}\left(v_{23} - v_{12}\right) = -\frac{1}{2}v_x^x\,, \tag{A.60}$$

revealing that the shift of the mean value is eliminated

$$\langle v_{x,eff}^x\rangle = \left(\langle v_x^x\rangle + \langle v_x^x\prime\rangle + \langle v_x^x\prime\prime\rangle\right)/3 = 0\,, \tag{A.61}$$

while the symmetrization of the width

$$\sigma_x^x\prime = \sigma_x^x\prime\prime = \frac{1}{4\sqrt{2}}v_a^0\sqrt{\frac{\langle \mathtt{v}_1\rangle^2}{v_0^2}} = \frac{1}{8}v_a^0\sqrt{\frac{E_x}{E_0}}\,, \tag{A.62}$$

results in an effective width of

$$\sigma^x_{x,eff} = v^0_a\sqrt{\frac{E_x}{E_0}}\left(\frac{1}{16}+\frac{1}{64}+\frac{1}{64}\right)^{1/2}, \tag{A.63}$$

$$\sigma^x_{x,eff} = \sqrt{\frac{3}{2}}\,\frac{1}{4}v^0_a\sqrt{\frac{E_x}{E_0}}. \tag{A.64}$$

The numerical values describing the effect of internal energy in the v_x coordinate can now be summarized

$$\langle v^x_a\rangle = \langle v^0_a\rangle\left(1+\frac{5}{32}\frac{E_x}{E_0}\right) = v^0_a\cdot 1.0005 \tag{A.65}$$

$$\sigma^x_a = v^0_a\frac{25}{256}\frac{E_x}{E_0} = v^0_a\cdot 3.14\times 10^{-4}, \tag{A.66}$$

$$\langle v^x_{x,eff}\rangle = 0, \tag{A.67}$$

$$\sigma^x_{x,eff} = v^0_a\sqrt{\frac{3}{2}}\,\frac{1}{4}\sqrt{\frac{E_x}{E_0}} = v^0_a\cdot 0.0174. \tag{A.68}$$

Comparison with the velocity distributions of chapter 7 shows, that the only sizable contribution is the last one $\sigma^x_{x,eff}$.
In a similar fashion, it can be shown, that the zero point oscillations of the vy mode have the same effect on the v_a and v_b distribution, that the v_b mode oscillations have

$$\langle v^y_a\rangle = v^0_a\left(1+\frac{5}{32}\frac{E_b}{E_0}\right) = v^0_a, \tag{A.69}$$

$$\sigma^y_a = v^0_a\frac{25\,E_x}{256\,E_0}, \tag{A.70}$$

$$\langle v^c_{x,eff}\rangle = 0, \tag{A.71}$$

$$\sigma^c_{x,eff} = \sqrt{\frac{3}{2}}\,\frac{1}{4}v^0_a\sqrt{\frac{E_x}{E_0}}. \tag{A.72}$$

with these expressions, the influence of the initial energies on the v_a and v_x distributions can be described; we desist from calculating the effects of the various zero point energies on the v_y distribution and assume that they are equal to the v_b case, since neither would one expect the two degenerate modes to show different behaviour theoretically, nor is a difference between the two modes seen in the experiment.
The result of this calculation can be applied to the simulated CEI distributions to verify whether the zero point oscillations can explain the discrepancies between experiment and theory. The outcome of the comparison is shown in Tab. 7.1.

References

[Ada84] Adams N.G., Smith D., Alge E., *Measurements of dissociative recombination coefficients of H_3^+, HCO^+, N_2H^+ and CH_5^+ at 95 and 300 K using the FALP apparatus* , J. Chem. Phys. **81** (1984), 1778.

[Ama88] Amano T., *Is the dissociative recombination of H_3^+ really slow? A new spectroscopic measurement of the rate constant*, Astrophys. J. **329** (1988), L121.

[Ami96] Amitay Z., Zajfman D., Forck P., Hechtfischer U., Seidel B., Grieser M., Habs D., Repnow R., Schwalm D., Wolf A., *Dissociative recombination of CH^+: Cross section and final states*, Phys. Rev. A **54** (1996), 4032.

[Ami98] Amitay Z., Baer A., Dahan M., Knoll L., Lange M., Levin J., Schneider I.F., Schwalm D., Suzor-Weiner A., Vager Z., Wester R., Wolf A., Zajfman D., *Dissociative Recombination of HD^+ in Selected Vibrational Quantum States*, Science **281** (1998), 75.

[Ami99] Amitay Z., Baer A., Dahan M., Levin J., Vager Z., Zajfman D., Knoll L., Lange M., Schwalm D., Wester R., Wolf A., Schneider I.F., Suzor-Weiner A., *Dissociative recombination of vibrationally excited HD^+: State-selective experimental investigation*, Phys. Rev. A **60** (1999), 3769.

[Ani86] Anicich V.G., Huntress W.T. Jr., *A survey of bimolecular ion-molecule reactions for use in modeling the chemistry of planetary atmospheres, cometary comae, and interstellar clouds*, Astrophys. J. Suppl. **62** (1986), 553.

[Bar70] Bardsley J.N., Biondi M.A., *Dissociative recombination*, Adv. At. Mol. Phys. **6** (1970), 1.

[Bat50a] Bates D.R., *Dissociative recombination*, Phys. Rev. **78** (1950), 492.

[Bat50b] ———, *Electron recombination in helium*, Phys. Rev. **77** (1950), 718.

[Bat94] ———, *Dissociative recombination: crossing and tunneling modes*, Adv. At. Mol. Opt. Phys. **34** (1994), 427.

[Bio49] Biondi A.M., Brown C., *Measurement of electron-ion recombination*, Phys. Rev. **76** (1949), 1697.

[Bis90] Bisoffi G., Grieser M., Jaeschke E., Krämer D., Noda A., *Radiofrequency stacking experiments at the Heidelberg test storage ring*, Nucl. Instr. Methods A **287** (1990), 320.

[Bla98] Black J.H., *Molecules in harsh environments*, Faraday Discuss. **109** (1998), 257.

[Bla00] ———, *The abundance and excitation of interstellar H_3^+*, Phil. Trans. R. Soc. Lond. A **358** (2000), 2515.

[Bor27] Born M., Oppenheimer R., *Zur Quantentheorie der Molekeln*, Ann. Physik **84** (1927), 457.

[Bor51] Born M., *Kopplung der Elektronen- und Kernbewegung in Molekeln und Kristallen*, Nachr. Ges. Wiss. Göttingen **6** (1951), 654.

[Bou55] Bourne H.C. Jr., Cloud R.W., Trump J.G., *Role of positive ions in high-voltage breakdown in vacuum*, J. of Applied Phys. **26** (1955), 596.

[Bra88] Bransden B.H., Joachain C.J., *Physics of atoms and molecules*, Longman, Harlow, 1988.

[Bro89] Bronstein I.N., Semendjajew K.A., *Taschenbuch der Mathematik*, 24 ed., Teubner, Leipzig, 1989.

[Buh02] Buhr H., *Studies of target polarization effects in Coulomb explosion imaging of light molecular ions*, Diplomarbeit, Universität Heidelberg, 2002.

[Bun98] Bunker P.R., Jensen P., *Molecular Symmetry and Spectroscopy*, 2 ed., NRC Research Press, 1998.

[Car74] Carney G.D., Porter R.N., *H_3^+: Geometry dependence of electronic properties*, J. Chem. Phys. **60** (1974), 4251.

[Car76] ———, *H_3^+: Ab initio calculation of the vibration spectrum*, J. Chem. Phys. **65** (1976), 3547.

[Car80] ———, *Ab initio prediction of the rotation-vibration spectrum of H_3^+ and D_3^+*, Phys. Rev. Lett. **45** (1980), 537.

[Cen98] Cencek W., Rychlewski J., Jaquet R., Kutzelnigg W., *Sub-microhartree accuracy potential energy surface for H_3^+ including adiabatic and relativistic effects. I. Calculation of the potential points*, J. Chem. Phys. **108** (1998), 2831.

[Chr64] Christofferson R.E., Hagstrom S., Prosser F., *H_3^+ ion. Its structure and energy*, J. Chem. Phys. **40** (1964), 236.

[Con93] Connery J.E.P., Baron R., Satoh T., Owen T., *Images of excited H_3^+ at the foot of the Io flux tube in Jupiter's atmosphere*, Science **262** (1993), 1035.

[Con00] Connery J.E.P., Satoh T., *The H_3^+ ion: a remote diagnostic of the Jovian magnetosphere*, Phil. Trans. R. Soc. Lond. A **358** (2000), 2359.

[Cos88] Cosby P.C., Helm H., *Experimental determination of the H_3^+ bond dissociation energy*, Chem. Phys. Lett. **152** (1988), 71.

[Cou35] Coulson C.A., *The electronic structure of H_3^+*, Proc. Camb. Phil. Soc. **31** (1935), 244.

[Dah00] Dahl, D.A., *Simion 3D version 7.0 user's manual*, Idaho national engineering and environmental laboratory, Idaho Falls, 2000.

[Dal53] Dalitz R.H., *On the analysis of τ-meson data and the nature of the τ-meason*, Phil. Mag. **44** (1953), 1068.

[Dal60] Daly N.R., *Scintillation type mass spectrometer ion detector*, Rev. Sci. Instr. **31** (1960), 264.

[Dal94] Dalgarno A.G., *Terrestrial and Extraterrestrial H_3^+*, Advances in atomic, molecular, and optical physics **32** (1994).

[Day54] Dayton I.E., Shoemake F.C., Moeseley R.F., Rev. Sci. Instr. **25** (1954), 485.

[Dem98] Demtröder W., *Laser Spectroscopy*, 2 ed., Springer, Heidelberg, 1998.

[Din92] Dinelli B.M., Miller S., Tennyson J., *Bands of H_3^+ up to $4\nu_2$: Rovibrational Transitions from First Principles Calculations*, J. Mol. Spectrosc. **153** (1992), 718.

[Din95] Dinelli B.M., Polyansky O.L., Tennyson J., *Spectroscopically determined Born-Oppenheimer and adiabatic surfaces for H_3^+, H_2D^+, D_2H^+, and D_3^+*, J. Chem. Phys. **103** (1995), 433.

[Din97] Dinelli B.M., Neale L., Polyansky O.L., Tennyson J., *New assignments for the infrared spectrum of H_3^+*, J. Mol. Spectrosc. **181** (1997), 142.

[Dis87] Disch R., Diplomarbeit, Universität Freiburg, 1987.

[Dul84] Duley W.W., Williams D.A., *Interstellar Chemistry*, Academic Press, London, 1984.

[Ers94] Erskine G.A., *RRKSTP: first-order differential equations (Runge-Kutta)*, Cern Program Library D200 (1994).

[For93] Forck P., Grieser M., Habs D., Lampert A., Repnow R., Schwalm D., Wolf A., Zajfman D., *Dissociative recombination of cold HD^+ at the Test Storage Ring*, Phys. Rev. Lett. **70** (1993), 426.

[Fri82] Friedmann M.H., Yergey A.L., Campana J.E., *Fundamentals of ion motion in electric radio-frequency multipole fields*, J. Phys. E.: Sci. Instrum. **15** (1982), 53.

[Gai78] Gaillard M.J., Gemmell D.S., Goldring G., Levine I., Pietsch W.J., Poizat J.C., Ratkowski A.J., Remillieux J., Vager Z., Zabransky B.J., *Experimental determination of the structure of H_3^+*, Phys. Rev. A **17** (1978), 1797.

[Gap58] Gapanov A.V., Miller M.A., *Potential wells for charged prticles in a high-frequency electromagnetic field*, J. Exptl. Theoret. Phys. (U.S.S.R.) **34** (1958), 242.

[Gar00] Garcia-Molina R., Abril I., Denton C.D., Arista N.R., *Exit angle, energy loss and internuclear distance distributions of H_2^+ ions dissociated when traversing different materials*, Nucl. Instr. Meth. B **164** (2000), 310.

[Geb96] Geballe T.R., Oka T., *Detection of H_3^+ in interstellar space*, Nature **384** (1996), 334.

[Geb99] Geballe T.R., McCall, B.J., Hinkle H.K., Oka T., *Detection of H_3^+ in the diffuse interstellar medium: the Galactic center and Cygnus OB2 Number 12*, Astrophys. J. **510** (1999), 251.

[Gem75] Gemmell D.S., Remillieux J., Poizat J.C., Gaillard M.J., Holland R.E., Vager Z., *Evidence for an alignment effect in the motion of swift ion clusters through solids*, Phys. Rev. Lett. **34** (1975), 1420.

[Ger71] Gerlich D., Diplomarbeit, Universität Freiburg, 1971.

[Ger92] ———, *Inhomogeneous RF fields: a versatile tool for the study of processes with slow ions*, Adv. in Chem. Phys. **LXXXII** (1992), 1.

[Ger01] ———, 2001, private communication.

[Ger02a] ———, *Molecular ions and nanoparticles in RF and AC traps*, Hyperfine Interactions, special issue APAC conference Århus, 2002.

[Ger02b] Gerlich D., Herbst E., Roueff E., *$H_3^+ + HD \longrightarrow H_2D^+ + H_2$: Low-temperature laboratory measurements and interstellar implications*, Planetary and Space Science **50** (2002), 1275.

[Giu80] Giusti A., *A multichannel quantum defect approach to dissociative recombination*, J. Phys. B **13** (1980), 3867.

[Gos95] Gosh P.K., *Ion traps*, Clarendon Press, Oxford, 1995.

[Gou95] Gougousi T., Johnson R., Golde M.F., *Recombination of H_3^+ and D_3^+ ions in a flowing afterglow plasma*, Int. J. Mass Spectrom. Ion Proc. **149/150** (1995), 131.

[Gub94] Gubermann S.L., *Dissociative recombination without curve crossing*, Phys. Rev. A. **49** (1994), R4277.

[Har72] Harris N.C., Hemmerling E.M., *Introductory applied physics*, McGraw-Hill, New York, 1972.

[Her27] Herzberg G., *Über die Spektren des Wasserstoffs (nach Versuchen mit der elektrodenlosen Ringentladung)*, Ann. Phys. **84** (1927), 565.

[Her50] ———, *I. Molecular spectra and molecular structure*, Van Nostrand Reinhold, 1950.

[Her73] Herbst E., Klemperer W., *The formation and depletion of molecules in dense interstellar clouds*, Astrophys. J. **185** (1973), 505.

[Her79] Herzberg G., *A spectrum of triatomic hydrogen*, J. Chem. Phys. **70** (1979), 4806.

[Her00] Herbst E., *The astrochemistry of H_3^+*, Phil. Trans. R. Soc. Lond. A **358** (2000), 2523.

[Hil56] Hildebrand F.B., *Introduction to numerical analysis*, McGraw-Hill, New York, 1956.

[Hir38] Hirschfelder J.O., J. Chem. Phys. **6** (1938), 795.

[Hol00] Hollis J.M., Lovas F.J., Jewell P.R., *Interstellar Glycolaldehyde: the first sugar*, Astrophys. J. Lett. **540** (2000), 107.

[Hou62] Hougen J.T., *Classification of rotational energy levels for symmetric-top molecules*, J. Chem. Phys **37** (1962), 1433.

[Hou63] ———, *Classification of rotational energy levels II*, J. Chem. Phys **39** (1963), 358.

[Hus88] Hus H., Yousif F., Sen A., Mitchell J.B.A., *Merged beam studies of the dissociative recombination of H_3^+ ions with low internal energy*, Phys. Rev. A **38** (1988), 658.

[Inu98] Inui T., Tanabe Y., Onodera Y., *Group theory and Its Applications in physics*, 3 ed., Springer, 1998.

[Jae88] Jaeschke E., Krämer D., Arnold W., Bisoffi G., Blum M., Friedrich A.. Geyer C., Grieser M., Habs D., Heyng H.W., Holzer B., Ihde R., Jung M., Matl K., Neumann R., Noda A., Ott W., Pohv B., Repnow R., Schmitt F., Steck M., Steffens E., *The Heidelberg Test Storage Ring for heavy ions TSR*, 1st Europ. Part. Acc. Conf. (Rome), 1988, p. 365.

[Jan90] Jansen, G.H., *Coulomb interactions in particle beams*, Adv. in electronics and electron physics, supplement **21** (1990).

[Jan99] Janev R.K., *Role of dissociative recombination and related molecular processes in fusion edge plasmas*, Dissociative recombination, theory, experiment and applications (Stockholm), vol. 4, 1999, p. 40.

[Jaq98] Jaquet R., Cencek W., Kutzelnigg W., Rychlewski J., *Sub-microhartree accuracy potential energy surface for H_3^+ including adiabatic and relativistic effects. II. Rovibrational analysis for H_3^+ and D_3^+*, J. Chem. Phys. **108** (1998), 2831.

[Kap31] Kaplan J., *The light of the night sky*, Phys. Rev. **38** (1931), 1048.

[Kap51] Kapiza P.L., Zn. Eksperim. i. Teor. Fiz. **21** (1951), 588.

[Kel89] Keller R., Nielsen B.R., Torp B., *Metal beam production using a high current ion source*, Nucl. Instr. Meth. B **37** (1989), 74.

[Ket89] Ketterle W., Messmer H.-P., Walther H., *The v_1 vibration of H_3^+ and autoionizing Rydberg states of H_3*, Europhys. Lett. **8** (1989), 333.

[Kno97] Knoll L., *Direkte Abbildung und Berechnung räumlicher Molekülstrukturen*, Diplomarbeit, Universität Heidelberg, 1997.

[Kok01] Kokoouline V., Greene C.H., Esry B.D., *Mechanism for the destruction of H_3^+ ions by electron impact*, Nature **412** (2001), 891.

[Kok03] Kokoouline V., Greene C.H., *Theory of dissociative recombination of D_{3h} triatomic ions applied to H_3^+*, Phys. Rev. Lett. **90** (2003), 133201.

[Kre00] Kreckel H., *Coulomb explosion imaging von H_3^+*, Diplomarbeit, Universität Heidelberg, 2000.

[Kre02] Kreckel H., Krohn S., Lammich L., Lange M., Levin J., Scheffel M., Schwalm D., Tennyson J., Vager Z., Wester R., Wolf A., Zajfman D., *Vibrational and rotational cooling of H_3^+*, Phys. Rev. A **66** (2002), 052509.

[Kro92] Kroto H.W., *Molecular rotation spectra*, Dover Publications, 1992.

[Kro02] Krohn S., *Inelastic collisions and recombination betweeen electrons and molecular ions*, Ph.D. thesis, Universität Heidelberg, 2002.

[Kul79] Kulander K.C., Guest M.F., *Excited electronic states of H_3 and their role in the dissociative recombination of H_3^+*, J. Phys. B **12** (1979), L501.

[Lam04] Lammich L., *to be published*, Ph.D. thesis, Universität Heidelberg, 2004.

[Lan76] Landau L.D., Lifschitz E.M., *Mechanik*, Akademie-Verlag, Berlin, 1976.

[Lan99] Lange M., *Verzweigungsverhältnisse und Winkelabhängigkeit der dissoziativen Rekombination von HD^+-Ionen*, Diplomarbeit, Universität Heidelberg, 1999.

[Lan02] ———, *Competition between reaction channels in electron collisions of the hydrogen molecular ion HD^+*, Ph.D. thesis, Universität Heidelberg, 2002.

[Lar93] Larsson M., Danared H., Mowat J.R., Sigray P., Sundström G., Broström L., Filevich A., Källberg A., Mannervik S., Rensfeld K.G., Datz S., *Direct High-Energy Neutral-Channel Dissociative Recombination of Cold H_3^+ in an ion storage ring*, Phys. Rev. Lett. **70** (1993), 430.

[Lar96] Larsson M., Lepp S., Dalgarno A., Strömholm C., Sundström G., Zengin V., Danared H., Källberg A., af Ugglas M., Datz, S., *Dissociative recombination of H_2D^+ and the cosmic abundance of deuterium*, Astron. Astrophys. **309** (1996), L1.

[Lar00] Larsson M., *The astrochemistry of H_3^+*, Phil. Trans. R. Soc. Lond. A **358** (2000), 2433.

[LeS92] Le Sueur C.S., Miller S., Tennyson J., *On the use of variational wavefunctions in calculating vibrational band intensities*, Mol. Phys. **76** (1992), 1147.

[LeP98] Le Padellec A., Larsson M., Danared H., Larson Å., Peterson J.R., Rośen S., Semaniak J., StrÓmholm C., *A storage ring study of dissociative excitation and recombination of D_3^+*, Phys. Scripta **57** (1998), 215.

[LeT00] Le Teuff Y.H., Millar, T.J, Marwick A.J., *The UMIST database for astrochemistry 1999*, Astron. Astrophys. Suppl. Ser. **146** (2000), 157.

[Leu73] Leu M.T., Biondi M.A., Johnsen R., *Measurements of Recombination of electrons with H_3^+ and H_5^+ ions*, Phys. Rev. A **8** (1973), 413.

[Lev91] Levine R.D., Bernstein R.B., *Molekulare Reaktionsdynamik*, Teubner, Stuttgart, 1991.

[Lev00] Levin J., Knoll L., Scheffel M., Schwalm D., Wester R., Wolf A., Baer A., Vager Z., Zajfman D., Liechtenstein V.K., *Application of ultrathin diamond-like-carbon targets to Coulomb explosion imaging*, Nucl. Instrum. Methods B **168** (2000), 268.

[Ley00] Leybold, 2000, Coolpower 2/10, operating instructions.

[Lie97] Liechtenstein V.K., Ivkova T.M., Olshanski E.D., Feigenbaum I., DiNardo R., Doebeli M., *Preparation and evaluation of thin diamond-like carbon foils for heavy-ion tandem accelerators and time-of-flight spectrometers*, Nucl. Instrum. Methods A **397** (1997), 140.

[Lin01] Lindsay C.M., McCall B.J., *Comprehensive Evaluation and Compilation of H_3^+ Spectroscopy*, J. Mol. Spectrosc. **210** (2001), 60.

[Lis02] Lis D.C., Roueff E., Gerin M., Phillips T.G., Coudert L.H., van der Tak F.F.S., Schilke P., *Detection of triply deuterated ammonia in the barnard 1 cloud*, Astrophys. J. **571** (2002), L55.

[Mar89] March R.E., Hughes R.J., *Quadrupole storage mass spectrometry*, Chemical Analysis, vol. 102, John Wiley & Sons (New York), 1989.

[May97] Mayer-Kuckuk T., *Atomphysik*, 5 ed., Teubner, Stuttgart, 1997.

[McC98] McCall B.J., Geballe T.R., Hinkle K.H., Oka T., *Detection of H_3^+ in the diffuse interstellar medium toward Cygnus OB2 No. 12*, Science **279** (1998), 1910.

[McC01] McCall B.J., *Spectroscopy of H_3^+ in laboratory and astrophysical plasmas*, Ph.D. thesis, University of Chicago, 2001.

[McC03] McCall B.J., Huneycutt A.J., Saykally R.J., Geballe T.R., Djuric N., Dunn G.H., Semaniak J., Novotny O., Al-Khalili A., Ehlerding A., Hellberg F., Kalhori S., Neau A., Thomas R., Österdahl F., Larsson M., *An enhanced cosmic-ray flux towards ζ Persei inferred from a laboratory study of the H_3^+-e^- recombination rate*, Nature **422** (2003), 500.

[McN95] McNab I.R., *The spectroscopy of H_3^+*, Adv. in Chem. Phys **89** (1995), 1.

[Mey86] Meyer W., Botschwina P., Burton P.G., *Ab initio calculation of near-equilibrium potential and multipole moment surfaces and vibrational frequencies of H_3^+ and its isotopomers*, J. Chem. Phys. **84** (1986), 891.

[Mic84] Michels H.H., Hobbs R.H., *Low-temperature dissociative recombination of $e + H_3^+$*, Astrophys. J. **286** (1984), L27.

[Mil90] Miller S., Tennyson J., Sutcliffe B.T., *Forbidden rotational and ro-vibrational transitions in H_3^+: first principles calculations*, J. Mol. Spectrosc. **141** (1990), 104.

[Mil92] Miller S., Tennyson J., Lepp S., Dalgarno A., *Identification of features due to H_3^+ in the infrared spectrum of supernova SN1987A*, Nature **355** (1992), 420.

[Mil00] Millar T.J., Roberts H., Markwick A.J., Charnley S.B., *The role of H_2D^+ in the deuteration of interstellar molecules*, Phil. Trans. R. Soc. Lond. A **358** (2000), 2535.

[Mit83] Mitchell J.B.A, Forand J.L., Ng C.T., Levac D.P., Mitchell R.E., Mul P.M., Claeys W., Sen A., McGowan J.Wm., *Measurement of the branching ratio for the dissociative recombination of $H_3^+ + e^-$*, Phys. Rev. Lett. **51** (1983), 885.

[Mow95] Mowat J.R., Danared H., Sundström G., Carlson M., Andersen L.H., Vejby-Christensen L., af Ugglas M., Larsson M., *High resolution, low-Energy dissociative recombination spectrum of $^3HeH^+$.*, Phys. Rev. Lett. **74** (1995), 50.

[Mül99a] Müller U., Cosby P.C., *Three-body decay of the 3s $^2A_1'$ (N=1,K=0) and 3d $^2E''$ (N=1, G=0, R=1) Rydberg states of the triatomic hydrogen molecule H_3*, Phys. Rev. A **59** (1999), 3632.

[Mül99b] Müller U., Eckert Th., Braun M., Helm H., *Fragment correlation in the three-body breakup of triatomic hydrogen*, Phys. Rev. Lett. **83** (1999), 2718.

[Nea96] Neale L., Miller S., Tennyson J., *Spectroscopic properties of the H_3^+ molecule: a new calculated line list*, Astroph. J. **464** (1996), 516.

[Oka80] Oka T., *Observation of the infrared spectrum of H_3^+*, Phys. Rev. Lett. **45** (1980), 531.

[Oka99] ———, *H_3^+ in the diffuse interstellar medium: the enigma related to dissociative recombination*, Dissociative recombination, theory, experiment and applications (Stockholm), vol. 4, 1999, p. 13.

[Ore93] Orel A.E., Kulander K.C., *Resonant dissociative recombination of H_3^+*, Phys. Rev. Lett. **71** (1993), 4315.

[Pau89] Paul. W., *Electromagnetic traps for charged and neutral particles*, 1989, Nobel Lecture, Stockholm.

[Pau96] Paul W., *Reaktionsdynamik schwach gebundener ionischer Cluster*, Ph.D. thesis, Technische Universität Chemnitz-Zwickau, 1996.

[Pev01] Peverall R., Rosen S., Peterson J.R., Larsson M., Al-Khalili A., Vikor L., Semaniak J., Bobbenkamp R., Le Padellec A., Maurellis A.N., van der Zande W.J., *Dissociative recombination and excitation of O_2^+: Cross sections, product yields*

and implications for studies of ionospheric airglows, J. Chem. Phys. **114** (2001), 6679.

[Pla02] Plašil R., Glosik J., Poterya V., Kudrna P. Rusz J., Tichý M., Pysanenko A., *Advanced integrated stationary afterglow method for experimental study of recombination of processes of H_3^+ and D_3^+ ions with electrons*, Int. J. Mass Spectrom. **218** (2002), 105.

[Pob96] Pobell F., *Matter and methods at low temperatures*, Springer, Berlin, 1996.

[Pol99] Polyansky O.L., Tennyson J., *Ab initio calculation of the rotation-vibration energy levels of H_3^+ and its isotopomers to spectroscopic accuracy*, J. Chem. Phys. **110** (1999), 5056.

[Pol00] Polyansky O.L., Prosmiti R., Klopper W., Tennyson J., *An accurate, global* ab initio *potential energy surface for the H_3^+ molecule*, Mol. Phys. **98** (2000), 261.

[Por68] Porter R.C., Stevens R.M., Karplus M., *Symmetric H_3^+: a semiempirical and ab initio study of a simple Jahn-Teller system*, J. Chem. Phys. **49** (1968), 5163.

[Pro97] Prosmiti R., Polyansky O.L., Tennyson J., *A global potential energy surface for the H_3^+ molecule*, Chem. Phys. Lett. **273** (1997), 107.

[Roe94] Roehse R., Kutzelnigg W., Jaquet R., Klopper W., *Potential energy surface of the H_3^+ ground state in the neighborhood of the minimum with microhartree accuracy and vibrational frequencies derived from it*, J. Chem. Phys. **101** (1994), 2232.

[Sar94] Sarpal B.K., Tennyson J. Morgan L.A., *Dissociative recombination without curve crossing: study of HeH^+*, J. Phys. B **27** (1994), 5943.

[Sch74] Schaad L.J., Hicks W.V., *Gaussian basis configuration interaction calculations on twenty electronic states of H_3^+. A bound $^3\Sigma_u^+$ level*, J. Chem. Phys. **61** (1974), 1934.

[Sch98] Schlemmer S., Kuhn T., Lescop E., Gerlich D., *Laser excited N_2^+ in a 22-pole ion trap: experimental studies of rotational relaxation processes*, Int. J. Mass Spectrom. Ion Processes **185/186/187** (1998), 589.

[Sch99] Scheffel M., *Untersuchung orts- und zeitauflösender Mehrteilchen-Detektoren mit Laserpulsen*, Diplomarbeit, Universität Heidelberg, 1999.

[Sch00] Schneider I.F., Orel A.E., Suzor-Weiner A., *Channel mixing effects in the dissociative recombination of H_3^+ with slow electrons*, Phys. Rev. Lett. **85** (2000), 3785.

[Sch02] Schlemmer S., Lescop E., von Richthofen J., Gerlich D., Smith M., *Laser induced reactions in a 22-pole ion trap: $C_2H_2^+ + h\nu_3 + H_2 \longrightarrow C_2H_3^+ + H$*, J. Chem. Phys. **117** (2002), 2068.

[Sem96] Semaniak J., Rosén S., Sundström G., Strömholm C., Datz S., Danared H., af Ugglas M., Larsson M., van der Zande W.J., Amitay Z., Hechtfischer U., Grieser M., Repnow R., Schmidt M., Schwalm D., Wester R., Wolf A., Zajfman D., *Product-state distributions in the dissociative recombination of $^3HeD^+$ and $^4HeH^+$*, Phys. Rev. A **54** (1996), R4617.

[Sen86a] Sen A., Mitchell J.B.A., *Production of H_3^+ ions with low internal energy for studies of dissociative recombination*, J. Phys. B **19** (1986), L544.

[Sen86b] ———, *Production of vibrationally cold ions using a radio-frequency storage ion source*, Rev. Sci. Instr. **57** (1986), 754.

[Sen87] Sen A., McGowan J.W., Mitchell J.B.A., *Production of low-vibrational-state H_2^+ ions for collision studies*, J. Phys. B **20** (1987), 1509.

[Sid92] Sidhu K.S., Miller S., Tennyson J., *Partition functions and equilibrium constants for H_3^+ and H_2D^+*, Astron. Astrophys. **255** (1992), 453.

[Smi87] Smith D., Adams N.G., *Ionic reactions in thermal plasmas*, J. Chem. Soc. Faraday Trans. II **83** (1987), 148.

[Smi93a] Smith D., Španel P., *Dissociative recombination of H_3^+ and some other interstellar ions: a controversy resolved*, Int. J. Mass Spectrom. Ion Proc. **129** (1993), 163.

[Smi93b] ———, *Dissociative recombination of H_3^+. Experiment and theory reconciled*, Chem. Phys. Lett. **211** (1993), 454.

[Sor94] Sorgenfrei A., Ph.D. thesis, Universität Freiburg, 1994.

[Spr03] Sprenger F., *to be published*, Ph.D. thesis, Universität Heidelberg, 2003.

[Str01a] Strasser D., Lammich L., Krohn S., Lange M., Kreckel H., Levin J., Schwalm D., Vager Z., Wester R., Wolf A., Zajfman D., *Two- and three-body kinematical*

correlation in the dissociative recombination of H_3^+, Phys. Rev. Lett. **86** (2001), 779.

[Str01b] Strasser D., Levin J., Pedersen H.B., Heber O., Wolf A., Schwalm D., Zajfman D., *Branching ratios in the dissociative recombination of polyatomic ions: the H_3^+ case*, Phys. Rev. A **65** (2001), 010702.

[Str02] Strasser D., Lammich L., Kreckel H., Krohn S., Lange M., Naaman A. Schwalm D., Wolf A., Zajfman D., *Breakup dynamics and isotope effect in H_3^+ and D_3^+ dissociative recombination*, Phys. Rev. A **66** (2002), 032719.

[Str03] Strasser D. *et al.* , *in preparation*, 2003.

[Str04] Strasser D., *to be published*, Ph.D. thesis, Weizman Institute of Science, Rehovot Israel, 2004.

[Sun94] Sundström G., Mowat J.R., Danared H., Datz S., Broström L., Filevich A., Källberg A., Mannervik S., Rensfelt K.G., Sigray P., af Ugglas M., Larsson M., *Destruction rate of H_3^+ by low-energy electrons measured in a storage ring experiment*, Science **263** (1994), 785.

[Sut87] Sutcliffe B.T., Tennyson J., *Variational methods for the calculation of rovibrational energy levels of small molecules*, J. Chem. Soc. Faraday Trans. **83** (1987), 1663.

[Sza86] Szabo I., *New ion-optical devices utilizing oscillatory electric fields. I. Principles of operation and analytical theory of multipole devices with two-dimensional electric fields*, Int. J. Mass Spectrom. Ion Processes **73** (1986), 197.

[Tan93] Tanabe T., Katayama I., Inoue N., Chida K., Arakaki Y., Watanabe T., Yoshizawa M., Ohtani S., Noda K., *Dissociative recombination of HeH^+ at large center-of-mass energies*, Phys. Rev. lett. **70** (1993), 422.

[Tel74] Teloy E., Gerlich D., *Integral cross sections for ion-molecule reactions: the guided beam technique*, Chem. Phys. **4** (1974), 417.

[Ten95a] Tennyson J., *Spectroscopy of H_3^+: planets, chaos and the Universe*, Rep. Prog. Phys. **57** (1995), 421.

[Ten95b] Tennyson J., Henderson J.R., Fulton N.G., *DVR3D: for the fully pointwise calculation of ro-vibrational spectra of triatomic molecules*, Comp. Phys. Comm. **86** (1995), 175.

[Ten01] Tennyson J., *private communication*, 2001.

[Tho11] Thomson J.J., *Rays of positive electricity*, Phil. Mag **21** (1911), 225.

[Vag76a] Vager Z., Gemmell D.S., *Polarization induced in a solid by the passage of fast charged particles*, Phys. Rev. Lett. **37** (1976), 1352.

[Vag76b] Vager Z., Gemmell D.S., Zabransky B.J., *Dissociation of fast HeH^+ ions traversing thin foils*, Phys. Rev. A. **14** (1976), 638.

[Van91] Van der Donk P., Yousif F., Mitchell J.B.A., *Dissociative recombination and excitation of D_3^+*, Phys. Rev. A **43** (1991), 5971.

[Var96] Varandas A.J.C., *Energy switching approach to potential surfaces: An accurate single-valued function for the water molecule*, J. Chem. Phys. **105** (1996), 3524.

[vHa98] von Hahn R, Cee R., Grieser M., Koessler V., Madert M., Papureanu S., Podlech H., Repnow R., Schwalm D., Kleffner C.-M., Habs D., Schemp A., *The High Current Injector at the MPI für Kernphysik in Heidelberg*, European Particle Accelerator Conference (Stockholm), 1998.

[Wag98] Wagner M., *Gruppentheoretische Methoden in der Physik*, 5 ed., Vieweg, Braunschweig, Wiesbaden, 1998.

[Wat84] Watson J.K.G., *High-Order vibration-rotation energies of the X_3 molecule*, J. Chem. Phys. **103** (1984), 350.

[Wat00] ———, *An introduction to the spectroscopy of H_3^+*, Phil. Trans. R. Soc. Lond. A **358** (2000), 2371.

[Wes96] Wester R., *Erste Untersuchungen zur Coulomb-Explosion kalter gespeicherter Molekülionen*, Diplomarbeit, Universität Heidelberg, 1996.

[Wes98] Wester R., Albrecht F., Grieser M., Knoll L., Repnow R., Schwalm D., Wolf A., Baer A., Levin J., Vager Z., Zajfman D., *Coulomb explosion imaging at the heavy ion storage ring TSR*, Nucl. Instrum. Methods A **413** (1998), 379.

[Wil80] Wilson E.B., Decius J.C., Cross P.C., *Molecular vibrations*, Dover Publications, 1980.

[Wil02] Williams D.A., Herbst E., *It's a dusty universe: surface science in space*, Surface Science **500** (2002), 823.

[Win74] Winnewisser G., *Interstellar molecules*, Topics in current chemistry, vol. 44, 1974.

[You89] Yousif F.B., Mitchell J.B.A., *Recombination and excitation of HeH^+*, Phys. Rev. A. **40** (1989), 4318.

[Zaj90] Zajfman D., Both G., Kanter E.P., Vager Z., *Multiple scattering of MeV atomic and molecular ions traversing ultrathin films*, Phys. Rev. A **41** (1990), 2482.

[Zaj92a] Zajfman D., Graber T., Kanter E.P., Vager Z., *Influence of multiple scattering on the Coulomb explosion imaging of fast molecules*, Phys. Rev. A **46** (1992), 194.

[Zaj92b] Zajfman D., Kanter E.P., Graber T., Vager Z., Naaman R., *Quantitative molecular spectroscopy using Coulomb explosions*, Nucl. Instrum. Methods B **67** (1992), 22.

[Zaj95] Zajfman D., Amitay Z., Broude C., Forck P., Seidel B., Grieser M., Habs D., Schwalm D., Wolf A., *Measurement of branching ratios for the dissociative recombination of cold HD^+ using fragment imaging*, Phys. Rev. Lett. **75** (1995), 814.

[Zaj97] Zajfman D., Heber O., Vejby-Christensen L., Ben-Itzhak I., Rappaport M., Fishman R., Dahan M., *Electrostatic bottle for long-time storage of fast ion beams*, Phys. Rev. A **55** (1997), R1577.

[Zur65] Zurmühl R., *Praktische Mathematik für Ingenieure und Physiker*, 5 ed., Springer, Berlin, 1965.

Dankeschön

Diese Arbeit wurde nur möglich durch die tatkräftige Hilfe vieler Personen.
Zuallererst gilt mein Dank meinen Betreuern Prof. Andreas Wolf und Prof. Dirk Schwalm, die in ihrer Gruppe ein angenehmes Arbeitsklima schaffen durch ihre Diskussionsbereitschaft und ihr eigenes Engagement. Sie lassen eigenverantwortliche Arbeit zu, sind aber auch stets sofort bereit zu unterstützen, wenn es einmal irgendwo hakt.
Weiterhin möchte ich allen Mitgliedern der Molekül-Gruppe für die gute Zusammenarbeit danken. Vor allem Lutz Lammich sorgt immer wieder dafür, daß ich nicht zu viel Chaos anrichte. Außerdem hat er die Simulation für die DR Imaging Daten geschrieben und Bilder bereitgestellt, die in diese Arbeit eingeflossen sind. Dankeschön.
Vielen Dank auch all den anderen Strahlzeit- und Nachtschicht-Gefährten: Sven Krohn, Michael Lange, Yasha Levin, Henrik Buhr, Simon Altevogt, Vola Andrianarijaona, Henrik Pedersen, Peter Witte, Ulrich Hechtfischer, Marcus Scheffel, Lars Knoll, und natürlich Roland Wester, der mir einerseits den Coulomb Explosions-Aufbau vererbt hat, und jetzt nach seiner Rückkehr aus Berkeley wieder an entscheidender Stelle – nämlich bei der Inbetriebnahme der Falle – mitwirkte.
Prof. Daniel Zajfman und Daniel Strasser, unsere israelischen Partner, bringen immer wieder neue Ideen und eine Menge Schwung aus dem Heiligen Land mit.
Andreas Hillenbach gebührt Dank, da er als Diplomand am Aufbau der 22-Pol Falle beteiligt war, und so manche Schraube mit mir gesucht hat. Susanne Klages hat als Praktikantin ebenfalls engagiert mitgeschraubt.
Ganz entschieden beigetragen zum Aufbau der Falle haben natürlich Prof. Dieter Gerlich und seine Gruppe in Chemnitz. Von dort kamen nicht nur die Pläne für den 22-Pol, sondern auch die Speicherquelle und unzählige Ratschläge. Vor allem Doreen Kunte hat immer wieder prompt und kompetent auf meine vielen Fragen geantwortet.
Bei der technischen Umsetzung ist Norbert Schlicksupp, der Leiter unserer Mechanischen Ausbildungswerkstatt, über sich hinausgewachsen und hat seine langjährige Erfahrung eingebracht. Die Tatsache, daß die Falle nun tatsächlich bei tiefen Temperaturen arbeitet, ist vor allem sein Verdienst.
Thomas Wagner und Roland Holoch gilt Dank für die Entwicklung der Radiofrequenz-Generatoren und die Unterstützung im Umgang mit dieser "schwarzen Magie".
Volker Mallinger und seinem Team von der Hauptwerkstatt möchte ich dafür danken, daß sie mich nicht gleich herausgeworfen haben, wenn ich wieder einmal mit einem dringenden Auftrag kam.
Der Beschleunigerwerkstatt um Karl Hahn gilt Dank für all die Arbeiten und Hilfestel-

lungen “vor Ort”, sowohl im Bereich des Speicherrings und der Extraktions-Beamline, als auch an der Falle.
Besonders dankbar bin ich natürlich Manfred Grieser und Kurt Horn, die immer wieder viel Mühe mit unseren Molekülstrahlen haben, und den Auftrag bekommen Unmögliches in die Tat umzusetzen.
Oliver Koschorrek und Holger Schneider danke ich für die Hilfe mit aller Art von Elektronik und Computer-Ansteuerung und für die Berreicherung unserer Kaffee-Tisch-Diskussionsrunde.
Vielen Dank auch an Roland Repnow und all die Operateure, die sich mit uns die Nächte um die Ohren geschlagen haben.
Dank gebührt Robert von Hahn, Volker Kößler und Manfred König, dem Team vom RFQ Bechleuniger, für die Flexibilität beim Einsatz all der verschiedenen Ionen-Quellen für die Molekül-Strahlen.
Danken möchte ich Gernot Vogt, der mir viele Artikel besorgt hat, die beim Verfassen dieser Arbeit hilfreich waren.
Doris Cerny und Helga Krieger danke ich für alle Tipps und Ratschläge, wenn es darum geht, möglichst wenig Umwege zu machen.
Mein Physik-Lehrer in der zehnten Klasse hat mir die Empfehlung für einen Leistungskurs verweigert; er war der Meinung, daß ich nicht genug Motivation hätte, um mich die nächsten drei Jahre mehrere Stunden pro Woche mit Physik zu beschäftigen. Ihm bin ich immer noch nicht besonders dankbar.
Letzlich danke ich natürlich meiner Familie, vor allem meinen Eltern, die mir stets geholfen haben wo sie nur konnten, und die ihren sämtlichen drei Söhnen ein Studium ermöglicht haben.
Meiner Freundin Simone danke ich sehr für ihre Geduld und Nachsicht, denn die viele Zeit die ich um den Speicherring herumgelaufen bin, geht natürlich auch auf ihre Kosten.